



**University of Minho**  
School of Engineering

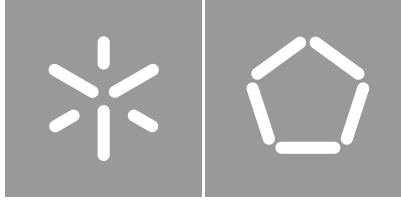
Luis Miguel Pinto de Matos

**Integrated Mixed-Mode Fracture  
Model for the Design of 2D Steel Fibre  
Reinforced Concrete Structures**

**Integrated Mixed-Mode Fracture Model for the Design  
of 2D Steel Fibre Reinforced Concrete Structures**

Luis Miguel Pinto de Matos





**University of Minho**

School of Engineering

Luís Miguel Pinto de Matos

**Integrated Mixed-Mode Fracture  
Model for the Design of 2D Steel Fibre  
Reinforced Concrete Structures**

Doctorate Thesis

Doctorate in Civil Engineering

Work developed under the supervision of:

**Professor Doctor Joaquim António Oliveira Barros**

**Professor Doctor António Ventura-Gouveia**

**Professor Doctor Rui Artur Bártolo Calçada**

## **COPYRIGHT AND TERMS OF USE OF THIS WORK BY A THIRD PARTY**

This is academic work that can be used by third parties as long as internationally accepted rules and good practices regarding copyright and related rights are respected.

Accordingly, this work may be used under the license provided below.

If the user needs permission to make use of the work under conditions not provided for in the indicated licensing, they should contact the author through the RepositoriUM of Universidade do Minho.

### ***License granted to the users of this work***



### **Creative Commons Attribution-NonCommercial-ShareAlike 4.0 International CC BY-NC-SA 4.0**

<https://creativecommons.org/licenses/by-nc-sa/4.0/deed.en>

# Acknowledgements

This Thesis represents thousands of hours of work carried out throughout the past 5 years. I gave it my best, had help from the best and I hope it represents a relevant contribution to the field.

Firstly, I would like to express my deepest gratitude to my supervisor, Professor Joaquim Barros, for his guidance, teaching, availability, countless hours of enriching discussions and friendship during these past years. A true Scientist whom I truly admire. Also, to Professor António Ventura-Gouveia, co-supervisor of this work, I would like to express my sincere gratitude for the availability, patience and all the help provided in crucial aspects of the work. Finally, to Professor Rui Calçada, I would like to thank for the opportunity and for his contributions to the work. To them, my profound gratitude, it was a pleasure working with you!

To my colleagues at UMinho and FEUP, thank you for all the shared moments during these years. Also, I thank Tiago Valente and Christoph de Sousa from CiviTest for the help provided in many occasions.

I would also like to acknowledge the financial support provided by Fundação para Ciência e Tecnologia (FCT) through the grants PD/BD/135174/2017 and COVID/BD/151997/2021.

Finally, to the ones that are always there for better or for worse:

To all my friends with whom I have shared unforgettable moments and helped turning this journey into a smoother and happier ride, a big thank you! Also, I would like to address a special thank you to my dear friend José Neto, for the comradeship during all these years, for the countless hours of conversations, funny moments and friendship that I will never forget.

To my family, thank you for the unconditional love and support in everything I do, anywhere I am, always. I would not be who I am today without you.

And lastly, to my Mariana, my friend, my partner and love of my life, thank you for being the beacon in this sometimes troubled, sometimes calm sea, that life is. If I did not have you in my life where would I find my happiness?

### **STATEMENT OF INTEGRITY**

I hereby declare having conducted this academic work with integrity. I confirm that I have not used plagiarism or any form of undue use of information or falsification of results along the process leading to its elaboration.

I further declare that I have fully acknowledged the Code of Ethical Conduct of the Universidade do Minho.

Guimarães, 29th October 2022

A handwritten signature in black ink, appearing to read 'Luís Miguel Pinto de Matos', written in a cursive style.

---

(Luís Miguel Pinto de Matos)

*“Love and compassion are necessities, not luxuries. Without them, humanity cannot survive.” (Dalai Lama)*

*In memory of my dear mother who I miss every day.*

# Abstract

## Integrated Mixed-Mode Fracture Model for the Design of 2D Steel Fibre Reinforced Concrete Structures

The research work presented in this Thesis aims at contributing to the field of numerical simulation and analysis of fibre reinforced concrete (FRC) structures by developing and implementing numerical tools in a computer code designated FEMIX, which is a general purpose finite element software. Initially, the existing multi-fixed smeared crack model approach in the FEMIX software is used in combination with the constitutive models currently available to conduct a set of numerical case studies of FRC elements failing in bending and shear to analyse the influence the fracture mode I/II parameters of the constitutive models. Subsequently, a generalised approach to compute the crack band width (CBW) is presented and its implementation in the FEMIX computer code is detailed. Furthermore, the extension of this approach to the integration point (IP) level was also conducted and its application made available for plane stress, shell and solid finite elements. The referred approach is analysed by means of a numerical case study where distinct mesh configurations are used to investigate the impact of the CBW in the results. Subsequently, an approach for deriving the fracture mode I parameters of FRC from experimental results of three-point notched beam bending test (3PNBBT) and round panel tests supported on three points (RPT-3PS) is proposed and implemented with C programming language. The developed inverse analysis (IA) approach is based on a nonlinear least squares algorithm coupled with an automatic parameter updating procedure in which the optimised variables are modified based on the deviation between numerical and experimental response. The numerical response is simulated by means of analytical models eliminating the need for a finite element (FE) model significantly reducing the computational time. The developed methodology provides very accurate predictions of the experimental responses both for 3PNBBT and RPT-3PS results. Furthermore, the automatic updating procedure of the input parameters ensures that the final results are practically insensitive to the initial guess of the variables provided by the user. Finally, the developed tool is used to derive the fracture mode I parameters of a real-scale fibre reinforced concrete (FRC) beam and the results are discussed. Finally, the development and implementation of a two dimensional mixed-mode fracture smeared crack model (MMFSCM) in the FEMIX software is detailed. The model is based on the combination of the aggregate interlock and fibre pullout resisting mechanisms, using the rough crack model (RCM) and the contact density Model (CDM) for the aggregate interlock component, and the P<sub>fyl</sub>, simplified diverse embeddment model (SDEM) and universal variable engagement model (UVEM) for simulating the fibre pullout contribution. The model is appraised by means of numerical case studies, addressing both mode I and mode II fracture dominant mechanisms. Furthermore, modifications to the original fibre pullout models formulation are proposed in order to enhance the predictive performance of the MMFSCM. The predictive performance of the MMFSCM is analysed and discussed by comparing numerical and experimental results gathered from the literature.

**Keywords:** Finite element analysis, mixed-mode fracture smeared crack model, aggregate interlock, fibre pull-out, inverse analysis, FRC structures



# Resumo

## Modelo Integrado de Fratura em Modo Misto para o Dimensionamento de Estruturas 2D em Betão Reforçado com Fibras

O trabalho de investigação apresentado nesta Tese visa contribuir para a área da mecânica computacional e análise de estruturas em betão reforçado com fibras (BRF) através do desenvolvimento e implementação de ferramentas numéricas no software de elementos finitos designado FEMIX. Assim, analisam-se inicialmente um conjunto de casos de estudo numéricos de elementos em BRF cuja rotura se dá por flexão e por corte. Os casos apresentados são analisados através de modelos multifendas fixas de fendilhação distribuída disponíveis no FEMIX, sendo o impacto da variação dos parâmetros que simulam o modo I e II analisado através de um estudo paramétrico. Apresenta-se também neste trabalho uma abordagem genérica para o cálculo do comprimento característico (CC). A metodologia é aplicada ao nível do EF, usando a geometria de todo o elemento para efetuar o seu cálculo, tendo sido também estendida ao nível do PI, usando para o efeito a sua área tributária. Ambas as abordagens são implementadas no software FEMIX e a sua utilização analisada através de casos de estudo numéricos. A metodologia referida foi implementada para elementos de estado plano de tensão, elementos de casca e também elementos sólidos. Seguidamente é proposta uma nova metodologia de análise inversa (AI) para obtenção dos parâmetros de fratura em modo I de elementos em BRF tendo por base ensaios experimentais comumente utilizados nomeadamente ensaios de flexão sob três pontos de carga em vigas entalhadas e ensaios de painéis circulares apoiados em três pontos. A metodologia baseia-se num procedimento de regressão de mínimos quadrados não-linear acoplado a um processo automático de otimização das variáveis de entrada. A resposta numérica é calculada através de modelos analíticos em vez de modelos de EF, eliminando por um lado a necessidade de construção de um modelo de elementos finitos e por outro lado o custo computacional do cálculo da resposta numérica. A abordagem proposta é implementada na linguagem de programação C sendo o seu bom desempenho avaliada através de resultados numéricos e experimentais. Por fim, o desenvolvimento de um modelo integrado de fendilhação distribuída em modo de fratura misto é detalhado. O modelo proposto tem em consideração os mecanismos resistentes que se desenvolvem durante o processo de fendilhação de elementos em BRF, usando para o efeito modelos constitutivos de arrancamento das fibras e também modelos micromecânicos para simulação do efeito do embricamento dos agregados. São utilizados três modelos constitutivos para simular o arrancamento das fibras, nomeadamente o modelo proposto por PfyL, o SDEM e o UVEM, e dois modelos para simulação do efeito de embricamento dos agregados, nomeadamente o RCM e CDM. O modelo integrado é implementado no software FEMIX, estudando-se por um lado o impacto das variáveis envolvidas na sua definição e por outro lado a sua capacidade preditiva, em roturas governadas pelo modo de fratura I e II. Para o efeito são levadas a cabo várias simulações numéricas utilizando o modelo proposto, e os resultados numéricos obtidos comparados com resultados experimentais encontrados na literatura.

**Palavras-chave:** Análise de EF, modelo de fendilhação distribuída em modo de fratura misto, embricamento de agregados, arrancamento de fibras, análise inversa, estruturas BRF

# Contents

<b>List of Figures</b>	<b>xii</b>
<b>List of Tables</b>	<b>xx</b>
<b>Glossary</b>	<b>xxii</b>
<b>Acronyms</b>	<b>xxiii</b>
<b>Symbols</b>	<b>xxvi</b>
<b>1 Introduction</b>	<b>1</b>
1.1 Motivation . . . . .	1
1.2 Objectives . . . . .	2
1.3 Thesis outline . . . . .	3
<b>2 Literature Review</b>	<b>5</b>
2.1 Introduction . . . . .	5
2.2 Crack formation and propagation in FRC elements . . . . .	5
2.3 Pullout behaviour of steel fibres . . . . .	7
2.4 Importance of fibre orientation and distribution . . . . .	11
2.4.1 Main factors and definitions . . . . .	11
2.4.2 Concept of orientation factor . . . . .	13
2.4.3 Measuring fibre orientation and distribution . . . . .	15
2.5 Classification of the tensile behaviour of FRC . . . . .	16
2.5.1 Potential use of FRC technology in railway infrastructures . . . . .	17
2.6 Simulation of the nonlinear behaviour of FRC elements . . . . .	23
2.6.1 Analytical-based models for simulating the nonlinear behaviour of FRC elements	23
2.6.2 FEM-based models for simulating the nonlinear behaviour of FRC . . . . .	29
2.7 Determining the fracture parameters of FRC . . . . .	33
2.8 Summary and Conclusions . . . . .	35

<b>3</b>	<b>Modelling and Simulation of FRC Elements</b>	<b>37</b>
3.1	Introduction . . . . .	37
3.2	Modelling the cracked behaviour of FRC elements . . . . .	37
3.3	Numerical simulations using the MFSCM approach . . . . .	41
3.3.1	Three-Point Notched Beam Bending Test (3PNBBT) . . . . .	41
3.3.2	FRC shear panels . . . . .	45
3.3.3	FRC railway sleeper . . . . .	50
3.4	A generalised approach to compute the crack band width . . . . .	54
3.4.1	Implementation in FEMIX v4.0 . . . . .	57
3.4.2	Issues and modifications to Oliver’s approach . . . . .	60
3.4.3	Extending Oliver’s method to the integration point level . . . . .	64
3.4.4	Appraisal of the implemented CBW calculation approach . . . . .	65
3.5	Summary and Conclusions . . . . .	76
<b>4</b>	<b>A New Inverse Analysis Approach To Derive The Fracture Mode I Parameters of FRC</b>	<b>78</b>
4.1	Introduction . . . . .	78
4.2	Proposed inverse analysis approach . . . . .	79
4.2.1	General overview of the developed tool . . . . .	79
4.2.2	Strategy for simulating the response of 3PNBBT and RPT-3PS . . . . .	84
4.3	Assessment and validation of the developed approach . . . . .	89
4.3.1	Introduction . . . . .	89
4.3.2	Three-point notched beam bending tests (3PNBBT) . . . . .	89
4.3.3	Round panel tests (RPT-3PS) . . . . .	94
4.3.4	Impact of the initial guess for the stress-crack width relationship . . . . .	97
4.4	Application of the proposed IA approach to the analysis of a real-scale FRC beam . . . . .	98
4.4.1	Introduction . . . . .	98
4.4.2	Geometry and experimental setup . . . . .	98
4.4.3	Assessment of the Mode I fracture parameters . . . . .	99
4.4.4	Beam FE mesh, loading and support conditions . . . . .	99
4.4.5	Constitutive laws to simulate the nonlinear behaviour of the materials . . . . .	100
4.4.6	Results and discussion . . . . .	103
4.5	Summary and Conclusions . . . . .	104
<b>5</b>	<b>Two-Dimensional Integrated Mixed-Mode Smeared Crack Model</b>	<b>106</b>
5.1	Introduction . . . . .	106
5.2	General overview . . . . .	106
5.3	Constitutive model description . . . . .	108

5.3.1	Introduction . . . . .	108
5.3.2	Fibre resisting mechanisms . . . . .	109
5.3.3	Models for simulating the aggregate interlock resisting mechanism . . . . .	114
5.3.4	Coupling the fibre and aggregate interlock resisting mechanisms . . . . .	116
5.3.5	Parametric study . . . . .	117
5.4	Assessment of the predictive performance of the model . . . . .	128
5.5	Modification of the aggregate interlock resisting mechanism . . . . .	133
5.6	Summary and Conclusions . . . . .	136
<b>6</b>	<b>Implementation of the Two-Dimensional Mixed-Mode Smeared Crack Model</b>	<b>138</b>
6.1	Introduction . . . . .	138
6.2	Two dimensional mixed-mode fracture smeared crack model . . . . .	139
6.2.1	Introduction . . . . .	139
6.2.2	General description of the model . . . . .	139
6.2.3	Model implementation in FEMIX V4.0 . . . . .	140
6.2.4	Model validation . . . . .	146
6.3	Assessment of the model's predictive performance . . . . .	150
6.3.1	Introduction . . . . .	150
6.3.2	Three-point notch beam bending tests (3PNBBT) . . . . .	150
6.3.3	Shear panel tests . . . . .	163
6.3.4	Mixed-mode test . . . . .	168
6.4	Summary and Conclusions . . . . .	170
<b>7</b>	<b>Conclusions</b>	<b>172</b>
7.1	General conclusions . . . . .	172
7.2	Recommendations for future works . . . . .	175
	<b>Bibliography</b>	<b>176</b>
	<b>Annexes</b>	
<b>I</b>	<b>Annex 1 Aggregate interlock and fibre pullout models expressions</b>	<b>199</b>
<b>II</b>	<b>Annex 2 Determination of the <math>D^{cr}</math> coefficients</b>	<b>203</b>

# List of Figures

1	Basic fracture modes: I - opening mode (tensile), II - sliding mode (in-plane shear) and III - tearing mode (out-of-plane shear). . . . .	6
2	Schematic representation of the fracture process in uni-axial tension and correspondent stress-crack opening relationship [16]. . . . .	6
3	Schematic representation of the effect of aggregates and fibres in FRC [16]. . . . .	7
4	Typical pullout relationship between end-slip and load for smooth fibre (adapted from Löfgren [16] and Cunha [17]). . . . .	8
5	Typical pullout relationship between end-slip and load for smooth and end-hooked fibre (adapted from Löfgren [16] and Cunha [17]). . . . .	8
6	Schematic representation of the ITZ (adapted from Bentur and Mindess [30]). . . . .	10
7	Bending and shearing action of and inclined fibre during the pullout process (a) before and (b) after concrete spalling (adapted from Cunha [17]). . . . .	10
8	Pullout response of end-hooked steel fibres at different inclination angles [26]. . . . .	11
9	Influencing factors affecting fibre orientation and structure. . . . .	12
10	Effect of boundary conditions in fibre distribution (adapted from Álvarez [40]). . . . .	12
11	Explanation for fibre orientation due to nonlinear velocity profile and wall-effect [42]. . . . .	13
12	Two-dimensional fibre orientation system. . . . .	14
13	Three-dimensional fibre orientation system: (a) randomly orientated fibres in three dimensions and (b) average projected length in xy plane. . . . .	14
14	Cross-section of beam considered in Dupont and Vandewalle [39] study with the three distinct orientation zones. . . . .	15
15	Schematic representation of tensile softening and hardening behaviour of FRC (adapted from Löfgren [16]). . . . .	17
16	Schematic representation of the ballasted track configuration. . . . .	18
17	(a) Twin-block and (b) prestressed monoblock sleeper [4]. . . . .	19
18	(a) Longitudinal cracking [94], (b) crack due to impact loads [95], and (c) rail-seat abrasion [96]. . . . .	19
19	Schematic representation of a slab track system configuration. . . . .	21

20	Families of slab track systems grouped by rail support type. . . . .	22
21	FCM model: (a) schematic representation of the process zone; (b) stress-crack relationship (adapted from Hillerborg et al. [111] and Vandewalle et al. [114]). . . . .	24
22	CBM model: (a) stress-distribution in the crack band proposed by Bazant and (b) stress-strain relationship smeared on crack band width [116]. . . . .	25
23	Distribution of the curvature around the nonlinear hinge [119]. . . . .	26
24	Nonlinear hinge model proposed by Pedersen and Stang [118]: (a) Schematic representation of the kinematic assumption of the nonlinear hinge; (b) nonlinear hinge subjected to axial force and bending moment and the assumed stresses distribution with the resultant forces. . . . .	26
25	Distribution of normal stresses in the nonlinear hinge section [120]. . . . .	27
26	Model proposed by Maalej and Li [120]: superposition of crack mouth opening displacement (CMOD) (adapted from Spasojevic [122]). . . . .	28
27	Nonlinear hinge model presented by Olesen [121]. (a) Geometry, loading and deformation of cracked incremental horizontal layer of the hinge; (b) Bilinear stress-crack opening relationship [121]. . . . .	28
28	Nonlinear hinge concept for a beam with reinforcement [16]. . . . .	29
29	Propagation of crack in early discrete crack model [125]. . . . .	32
30	Constitutive relationships used in the scope of the present work: (a) trilinear and (b) quadrilinear diagrams used for simulating mode I ( $\sigma_{n,1}^{cr} = f_{ct}$ , $\sigma_{n,2}^{cr} = \alpha_1 \sigma_{n,1}^{cr}$ , $\sigma_{n,2}^{cr} = \alpha_1 \sigma_{n,1}^{cr}$ , $\sigma_{n,3}^{cr} = \alpha_2 \sigma_{n,2}^{cr}$ , $\sigma_{n,4}^{cr} = \alpha_3 \sigma_{n,3}^{cr}$ , $\epsilon_{n,2}^{cr} = \xi_1 \epsilon_{n,u}^{cr}$ , $\epsilon_{n,3}^{cr} = \xi_2 \epsilon_{n,u}^{cr}$ , $\epsilon_{n,4}^{cr} = \xi_3 \epsilon_{n,u}^{cr}$ ) [115, 201]. . . . .	39
31	Shear softening constitutive relationship to simulate the shear stress transferring capacity degradation [141]. . . . .	39
32	Constitutive relationships used in the scope of the present work: (a) multi-linear branch diagram for modelling the conventional steel reinforcement [201] and (b) bond-slip relationship for modelling the bond between finite elements (FEs). . . . .	40
33	Relationships for modelling the compressive behaviour according to the plastic-damage multidirectional smeared crack (PDSC): (a) plasticity model, (b) damage model and (c) constitutive relationship of the compressive behaviour [202]. . . . .	40
34	Geometry, mesh, loading and support conditions of the 3PNBBT numerical model (all dimensions in mm). . . . .	41
35	Results of the parametric study of the governing parameters of the fracture mode I: (a) quadrilinear diagrams defined according to the values specified in Table 5 (b) impact of varying the tensile strength ( $f_{ct}$ ), (c) effect of varying $G_{f,I}$ and (d) effect of the shape of the quadrilinear diagram. . . . .	43
36	(a) Comparison between the previous quadrilinear diagrams and the relationship obtained after conducting inverse analysis (IA) and (b) corresponding numerical and experimental results comparison. . . . .	44

37	Schematic representation of the shear FRC panels tested by Susetyo et al. [204]. . . . .	45
38	Geometry, FE mesh ( $\approx 27 \times 27$ mm), loading and support conditions of the numerical model. Dimensions in mm. . . . .	46
39	Effect of varying the mode II governing parameters: (a) slope of the initial shear branch ( $\beta$ ), (b) mode II fracture energy and (c) maximum shear strength. . . . .	48
40	(a) Experimental and (b) numerical crack pattern comparison. . . . .	49
41	(a) Sleeper geometry and (b) cross-sectional details of the rail-seat/centre sections[100].	50
42	Schematic representation of the static bending tests setup: (a) rail-seat section and (b) centre section [100]. . . . .	50
43	Geometry, loading, support conditions and FE mesh adopted in the simulation: (a) centre section and (b) rail-seat section (dimensions in mm) . . . . .	51
44	Comparison between numerical and experimental results at (a) centre section and (b) rail-seat section. . . . .	53
45	(a) Experimental and (b) numerical crack patterns at failure of the centre section sleeper simulation. . . . .	53
46	(a) Experimental and (b) numerical crack patterns at failure of the rail-seat section sleeper simulation. . . . .	54
47	Schematic representation of the projection distance concept of the CBW for an inclined crack.	55
48	(a) Crack entity represented by the singular band encompassed by two singular lines and (b) displacement field across the singular band (adapted from Oliver and Idelsohn [205]). . . . .	55
49	Singular band approximated by finite element discretization (adapted from [205]). . . . .	56
50	(a) 4-noded element with a $2 \times 2$ Gauss-Legendre integration scheme and (b) the same finite element with normalised isoparametric coordinates. . . . .	57
51	Algorithm to compute the CBW according to Oliver's approach. . . . .	59
52	Schematic representation of a 4-noded FE with a $2 \times 2$ G-L integration scheme. . . . .	60
53	CBW value obtained at each IP considering the value of $\theta_{cr}$ ranging between $[-90^\circ, 90^\circ]$	60
54	Schematic representation of the geometric meaning of the methodology proposed by [205].	61
55	Discontinuity situation of CBW for the IP1 crack scenario. . . . .	61
56	Comparison between the original and modified version of the approach proposed by Oliver and Idelsohn [205]. . . . .	62
57	Schematic representation of the obtained CBW values for the original and modified methodology. . . . .	63
58	Modified CBW computation algorithm considering the smoothing function proposed by Govindjee et al. [206]. . . . .	63
59	Algorithm of the extended Oliver's approach to compute the CBW at the IP level with schematic representation of each step for a 4-noded element with a $2 \times 2$ G-L integration scheme. . . . .	64
60	Scaling process of width and height of the isoparametric FE by the corresponding IP's weights. . . . .	65

61	Translation process of the virtual scaled IP to the correct position. . . . .	65
62	Geometry, loading, support conditions and finite element meshes (a) M40 (40mm), (b) M20 (20mm) and (c) M10(10mm). All dimensions are in millimeters. . . . .	66
63	Comparison between the experimental and numerical force-displacement curves obtained for the meshes (a) M40, (b) M20 and (c) M10, and considering different computation methodologies of the CBW. . . . .	68
64	Comparison of the crack patterns, obtained for the mesh M40, considering different CBW computation approaches: (a) experimental pattern, (b) $\sqrt{FE}$ , (c) $\sqrt{IP}$ , (d) Oliver FE and (e) Oliver IP. . . . .	69
65	Comparison of the crack patterns, obtained for the mesh M20, considering different CBW computation approaches: (a) experimental pattern, (b) $\sqrt{FE}$ , (c) $\sqrt{IP}$ , (d) Oliver FE and (e) Oliver IP. . . . .	70
66	Comparison of the crack patterns, for the mesh M10, considering different CBW computation approaches: (a) experimental pattern, (b) $\sqrt{FE}$ , (c) $\sqrt{IP}$ , (d) Oliver FE and (e) Oliver IP. . . . .	71
67	Schematic representation of the mosaic meshes configuration: (a) mesh MO1 and mesh (b) MO2. All dimensions are in millimeters. . . . .	72
68	Comparison between experimental and numerical force-displacement curves for the meshes (a) MO1 and (b) MO2 considering different CBW computation approaches. . . . .	73
69	Comparison between (a) the experimental failure mode and the crack patterns obtained for the mesh MO1, considering the (b) $\sqrt{FE}$ , (c) $\sqrt{IP}$ , (d) $Ol_{FE}$ and (e) $Ol_{IP}$ methodologies to estimate the CBW. . . . .	74
70	Comparison between (a) the experimental failure mode and the crack patterns obtained for the mesh MO2, considering the (b) $\sqrt{FE}$ , (c) $\sqrt{IP}$ , (d) $Ol_{FE}$ and (e) $Ol_{IP}$ methodologies to estimate the CBW . . . . .	75
71	Comparison between the crack patterns according to the crack width value obtained for the mesh MO2, considering the (a) $\sqrt{FE}$ and (b) $Ol_{FE}$ methodologies. . . . .	76
72	Global overview of the proposed IA algorithm. . . . .	80
73	Algorithm of the parameter updating module. . . . .	81
74	$w_m$ mapping between the $\sigma_{ct} - w_{cmod,m}$ relationship and global response. . . . .	83
75	Numerical sampling approaches implemented in COFIT: (a) uniform sampling approach and (b) custom method with specification of different sampling in different regions of the response. . . . .	84
76	Schematic representation of the nonlinear hinge model subjected to bending: hinge deformed configuration and layered cross sectional model on the left and right, respectively (adapted from [194]). . . . .	85
77	Tensile constitutive model of FRC in tension: (a) pre-preak stress-strain, and (b) post-peak multi-linear stress-crack width diagram [194]. . . . .	85



78	Idealization of nonlinear mechanisms in a three-point notched beam bending tests (3PNBBT) for the prediction of its deflection: (a) elastic and (b) plastic components of the beam deflection. . . . .	87
79	Schematic representation of the crack tip opening displacement (CTOD) and CMOD entities.	88
80	Analysis of the crack rotation kinematic mechanism [194]. . . . .	88
81	Results of the inverse analysis: (a) experimental results of 3PNBBT in terms of force-deflection [216] and (b) in terms of force-CMOD [217], (c) and (d) obtained $\sigma_n^{cr} - w_n^{cr}$ for the results shown in (a) and (b), respectively. . . . .	90
82	Results of the inverse analysis: (a)/(c) comparison between experimental and numerical responses for RSFRC/ISFRC specimens and (b)/(d) the corresponding $\sigma_n^{cr} - w_n^{cr}$ relationship.	91
83	(a) FE mesh, loading and support conditions adopted in the simulation and (b) quadrilinear diagram used to simulate the material nonlinear behaviour of FRC ( $\sigma_{n,1}^{cr} = f_{ct}$ , $\sigma_{n,2}^{cr} = \alpha_1 \cdot \sigma_{n,1}^{cr}$ , $\sigma_{n,3}^{cr} = \alpha_2 \cdot \sigma_{n,1}^{cr}$ , $\sigma_{n,4}^{cr} = \alpha_3 \cdot \sigma_{n,1}^{cr}$ , $\varepsilon_{n,2}^{cr} = \xi_1 \cdot \varepsilon_{n,u}^{cr}$ , $\varepsilon_{n,3}^{cr} = \xi_2 \cdot \varepsilon_{n,u}^{cr}$ , $\varepsilon_{n,4}^{cr} = \xi_3 \cdot \varepsilon_{n,u}^{cr}$ ).	92
84	Results of the IA using FEM and COFIT approaches: (a) comparison in terms of force-CMOD, (b) comparison in terms of the tensile stress vs crack width. . . . .	93
85	Results of the inverse analysis for the round panel tests supported on three points (RPT-3PS) of the experimental results obtained by Montaignac et al. [186]: (a)/(c) numerical and experimental force-central deflection curves and (b)/(d) the obtained $\sigma_n^{cr} - w_n^{cr}$ relationships.	95
86	Results of the inverse analysis for the RPT-3PS of the experimental results obtained by Frazão et al. [218]: (a)/(b) Force-central deflection curve fitting and (c)/(d) the obtained $\sigma_n^{cr} - w_n^{cr}$ relationship. . . . .	96
87	Impact of the initial $\sigma_n^{cr} - w_n^{cr}$ relationship: (a) initial guesses for the post-peak multi-linear diagram, (b) optimised relationships and (c) results in terms of global fitted response. . .	97
88	Geometry of the beam: (a) cross section and (b) lateral view (dimensions in mm). . . .	98
89	Experimental setup and location of linear voltage differential transducers (LVDTs) for measuring the deflection and concrete strain at the longitudinal reinforcement level. . . . .	99
90	(a) Experimental envelope, average and 5% fractile force-CMOD curves, (b) results of the IA for 5% fractile curve and (c) $\sigma_n^{cr} - w_n^{cr}$ relationship derived by cofit. . . . .	100
91	Geometry, loading, support conditions and finite element mesh adopted in the simulation (FE of $\approx 25 \times 25$ mm). Dimensions in mm. . . . .	100
92	Constitutive model used to simulate the nonlinear material behaviour of the conventional steel reinforcement [220]. . . . .	101
93	Shear softening diagram used to simulate the decrease of shear transferring capacity [141].	101
94	Representation of the regions assigned with confined and unconfined bond-slip properties.	102
95	(a) Bond shear stress-slip relationship and (b) bond-slip relationship for the confined and unconfined regions considering bad bond conditions. . . . .	103

96	(a) Comparison between numerical and experimental results in terms of force-deflection curve, (b) crack pattern (magenta: fully open cracks; red: opening cracks; green: closing cracks; blue: closed cracks; cyan: reopening cracks;) and (c)/(d) experimental crack pattern at failure. . . . .	104
97	Schematic representation of a crack opening ( $w_n^{cr}$ ) and sliding ( $w_t^{cr}$ ), crack displacement ( $w^{cr}$ ), and fibre embedment length ( $l_{bf}$ ). . . . .	108
98	Concept of intervals of active and inactive fibres regarding the loading direction. . . . .	110
99	Fibre orientation and bending angle definition according to Htut and Foster [222]. . . . .	111
100	Crack morphology according to the rough crack model (RCM) [246]. . . . .	114
101	Crack contact idealisation: (a) direction of contact stress in the crack face and (b) local normal and tangential displacement in the contact plane according to Li et al. [248]. . . . .	115
102	Concept of mixed-mode fracture smeared crack model: (a) crack opening and sliding displacement representation, (b) aggregate interlock contribution and (c) equivalent fibre pullout contribution. . . . .	116
103	First order and total sensitivity indices for the input parameters considering the RCM (a,b,e,f) and CDM (c,d,g,h) aggregate interlock models. . . . .	120
104	Comparison of results in terms of (a) normal and (b) shear stresses, obtained with the RCM and CDM aggregate interlock models for different crack opening widths. . . . .	121
105	Results of the parametric study considering the RCM aggregate interlock model. . . . .	122
106	Results of the parametric study considering the CDM aggregate interlock model. . . . .	123
107	Aggregate interlock and fibre contribution in terms of (a) normal and (b) shear stresses considering the RCM and (c), (d) relative contribution of fibres and aggregate interlock. . . . .	124
108	Aggregate interlock and fibre contribution in terms of (a) normal and (b) shear stresses considering the CDM and (c), (d) relative contribution of fibre and aggregate interlock. . . . .	125
109	Fibre/total stress ratio in terms of normal and shear stresses considering the RCM. A ratio of 1 means only fibre contribution. . . . .	126
110	Fibre/total stress ratio in terms of normal and shear stresses considering the CDM. A ratio of 1 means only fibre contribution. . . . .	127
111	Schematic representation of the experimental setup used by Khanlou et al. [241]. . . . .	128
112	Experimental and numerical results comparison for two fibre dosages [241]. $f_c = 45$ MPa, $l_f = 60$ mm, $l_f/d_f = 80$ , $D_{max} = 13$ mm. . . . .	129
113	Experimental and numerical results comparison considering different fibre pull-out models and the RCM. $f_c = 45$ MPa, $l_f = 60$ mm, $l_f/d_f = 80$ , $D_{max} = 13$ mm. . . . .	130
114	Geometry and loading configuration of the specimen [231]. . . . .	131
115	Comparison between experimental and numerical results: (a) shear stress - sliding displacement and (b) shear stress - opening displacement. $l_f = 30$ mm, $l_f/d_f = 80$ , $V_f = 1.125\%$	131

116	Comparison between experimental and numerical results considering different fibre pull-out models in combination with the RCM. $l_f = 30$ mm, $l_f/d_f = 80$ , $V_f = 1.125\%$ . . . . .	132
117	Comparison of the experimental and numerical results: $l_f = 30$ mm, $l_f/d_f = 80$ , $D_{max} = 7$ mm. . . . .	133
118	Comparison of the numerical predictions obtained using different fibre pull-out models.	134
119	Effect of varying the coefficients (a) $b$ and (b) $c$ in Equation (5.32). . . . .	134
120	Comparison of the results given by the original and modified RCM/contact density model (CDM) and the experimental results obtained by (a), (b) Khanlou et al. [241] and (c), (d) Soltanzadeh et al. [231]. . . . .	135
121	Comparison of the results given by the original and modified RCM/CDM and the experimental results obtained by Soetens and Matthys [245]. . . . .	136
122	Schematic representation of possible crack status a crack can assume in (a) mode I and (b) mode II. . . . .	145
123	Mesh geometry, loading and support conditions of the single element simulation. . . . .	146
124	Results of the single element simulation: (a) $\sigma_n^{cr} - w_n^{cr}$ considering the RCM, (b) $\tau_t^{cr} - w_t^{cr}$ considering the RCM, (c) $\sigma_n^{cr} - w_n^{cr}$ considering the CDM, (d) $\tau_t^{cr} - w_t^{cr}$ considering the CDM, (e) $w_n^{cr} - w_t^{cr}$ relation in the LCS. . . . .	148
125	Results break down by resisting mechanism i.e. matrix, aggregate interlock and fibre pullout contribution in the N.R-S case: (a) $\sigma_n^{cr} - w_n^{cr}$ relation at the crack LCS, (b) $\tau_t^{cr} - w_t^{cr}$ relation at the crack LCS. . . . .	149
126	Geometry, mesh, loading and support conditions of the 3PNBBT numerical model (all dimensions in mm). . . . .	151
127	Results of the 3PNBBT simulations: (a) Force-CMOD curve and (b) crack pattern at CMOD=5mm obtained using the Pfyl model (red: opening cracks; green: closing cracks;). . . . .	152
128	Results in the integration point of the first element above the notch: (a) using Pfyl's, (b) UVEM and (c) SDEM model, respectively. . . . .	153
129	Schematic representation of the proposed modification to the Pfyl's fibre pullout model. . . . .	154
130	Comparison between the original formulation of the Pfyl's model and the modified version proposed in the present work. Pfyl - original formulation; Pfyl Mod. - linear pre-peak phase; Pfyl Mod. ( $l_f/4$ ) - linear pre-peak phase and $w_{ult}^{cr} = l_f/4$ ; Pfyl Mod. ( $p=3$ ) - linear pre-peak phase, $w_{ult}^{cr} = l_f/4$ and $p = 3$ . . . . .	155
131	Assessment of the effect of the modified version of the Pfyl's model on the structural behaviour of the 3PNBBT FEM simulation. . . . .	155
132	Comparison between the original UVEM model and the modified version including the $w_{ult}$ parameter and different $\tau_{b0}$ values. . . . .	156
133	Comparison between the original and modified UVEM model in the results of the 3PNBBT FEM simulation. . . . .	157

134	Plot by resisting component (straight portion and hooked-end part of the fibre) of the SDEM model using the properties indicated in Table 23 . . . . .	158
135	Comparison between the original and modified version of the SDEM model using the properties indicated in Table 23. . . . .	159
136	Comparison between the original and modified SDEM model in the results of the 3PNBBT FEM simulation. . . . .	159
137	Numerical results for the 3PNBBT series considering the modified fibre pullout models (properties listed in Table 24). . . . .	161
138	Multi-linear mode I constitutive model implemented in the MMFSCM. . . . .	162
139	Assessment of the multi-linear branch model performance in the 3PNBBT simulations. . . . .	163
140	(a) Experimental test setup and (b) schematic representation of the shear FRC panels tested by Susetyo et al. [204]. Dimensions in mm. . . . .	164
141	Geometry, FE mesh, loading and support conditions of the numerical model. Dimensions in mm. . . . .	164
142	Constitutive model used to simulate the nonlinear material behaviour of the conventional steel reinforcement [220]. . . . .	165
143	Comparison between the experimental and numerical results of the SFRC panels, in terms of $\tau_{xy} - \gamma_{xy}$ . . . . .	166
144	Comparison between experimental and numerical results considering only the contribution of the aggregate interlock resisting mechanism. . . . .	167
145	Comparison between the fibre pullout contribution at a given crack of the panel C1F3V3. . . . .	168
146	Geometry, mesh, support and loading conditions of the mixed-mode test conducted by Arrea and Ingrassia [268] (all dimensions in mm). . . . .	168
147	(a) Force (B) - crack mouth sliding displacement (CMSD) and (b) crack pattern obtained using the RCM model. . . . .	169

# List of Tables

1	Steel fibre profiles [17]. . . . .	9
2	Destructive and non-destructive methods for measuring fibre orientation [40, 51]. . . . .	16
3	Summary table of the components and functions of the superstructure and substructure.	18
4	Types of finite elements used in the simulations conducted throughout this study [143]. .	38
5	Material properties and parameters used to define the concrete constitutive model in the 3PNBBT simulations. . . . .	42
6	Material properties and parameters used to define the concrete constitutive model in the 3PNBBT simulations after conducting IA. . . . .	44
7	Parameters used to define the steel reinforcement constitutive model. . . . .	46
8	Material properties and parameters used to define the quadrilinear and shear softening diagrams in the shear panels simulations. . . . .	47
9	Parameters used to define the concrete constitutive model. . . . .	52
10	Parameters used to define the steel constitutive model for prestressing strands [100]. . .	52
11	Values adopted to define the bond-slip behaviour of the interface elements. . . . .	52
12	Parameters used to define the steel constitutive model for top and transversal reinforcements, and glass fibre reinforced polymer (GFRP) bars for the bottom reinforcement. . .	67
13	Parameters used to define the concrete constitutive model. . . . .	67
14	Time elapsed during the IA process for 3PNBBT cases using COFIT. . . . .	94
15	Time elapsed during the IA process for RPT-3PS cases using COFIT. . . . .	96
16	Parameters used to define the steel constitutive model for top, transversal reinforcements, and bottom reinforcement. . . . .	101
17	Parameters used to define the concrete constitutive model. . . . .	102
18	Parameters of the bond-slip confined and unconfined relationship. . . . .	103
19	Input factors, description and range of variation considered in the SA. . . . .	118
20	List of the selected variables for the parametric study. . . . .	121
21	Average values of the coefficients $b$ and $c$ of Equation (5.32). . . . .	135

22	Parameters used to define the MMFSCM model in the single FE simulations. . . . .	147
23	Parameters used to define the MMFSCM model in the 3PNBBT simulations. . . . .	151
24	Parameters used to define the MMFSCM model in the additional series of the 3PNBBT simulation. . . . .	160
25	Parameters used to define the MMFSCM model in the shear panel test simulations [204].	165
26	Parameters used to define the steel reinforcement constitutive model. . . . .	166
27	Parameters used to define the MMFSCM model in the mixed-mode test conducted by [268].	169
1	Summary of the main equations of the RCM and CDM aggregate interlock models. . . .	199
2	Summary of the main equations of the Pfyf's model. . . . .	200
3	Summary of the main equations of the UVEM model. . . . .	201
4	Summary of the main equations of the SDEM model. . . . .	202

# Glossary

- CiviTest** Portuguese Civil Engineering company with strong focus on the development of new construction materials, testing and design of singular infrastructures.
- COFIT** Inverse analysis software for determining the fracture mode I parameters from 3PNBBT and RPT-3PS experimental results in an automatic and optimised fashion.
- FEMIX V4.0** An in-house developed FEM based software.
- Shift2Rail** European initiative fostering railway technology by means of research and innovation (R&I) promoting the competitiveness of the European rail industry (<https://shift2rail.org/about-shift2rail/>).

# Acronyms

**3PNBBT** three-point notched beam bending tests

**CBM** crack band model

**CBW** crack band width

**CDA** continuum damage approach

**CDM** contact density model

**CMOD** crack mouth opening displacement

**CSL** concrete support layer

**CT** computerized tomography

**CTOD** crack tip opening displacement

**CWR** continuous welded rail

**DCM** discrete crack model

**DEM** diverse embedment model

**DSS** double shear specimen

**DTT** direct tensile test

**FCM** fictitious crack model

**FE** finite element

**FEA** finite element analysis

**FEM** finite element method

**FPL** frost protection layer

**FPZ** fracture process zone

**FRC** fibre reinforced concrete

**FSCM** fixed smeared crack model

**G-L** Gauss-Legendre



<b>G-Lo</b>	Gauss-Lobatto
<b>GCS</b>	global coordinate system
<b>GFEM</b>	generalised finite element method
<b>GFRP</b>	glass fibre reinforced polymer
<b>GGBFS</b>	ground granulated blast furnace slag
<b>HBL</b>	hydraulically bonded layer
<b>HPFRC</b>	high performance fibre reinforced concrete
<b>IA</b>	inverse analysis
<b>IP</b>	integration point
<b>IP3</b>	innovation programme 3
<b>ISFRC</b>	industrial steel-fibre reinforced concrete
<b>ITZ</b>	interfacial transition zone
<b>JSCE</b>	Japanese Society of Civil Engineers
<b>KRS</b>	Korean Railway Standard (TR 0008)
<b>LCS</b>	local coordinate system
<b>LEFM</b>	linear elastic fracture mechanics
<b>LMA</b>	Levenberg-Marquardt algorithm
<b>LVDT</b>	linear voltage differential transducer
<b>MFSCM</b>	multi-fixed smeared crack model
<b>MMFSCM</b>	mixed-mode fracture smeared crack model
<b>N-R</b>	Newton-Raphson
<b>NA</b>	neutral axis
<b>NLSQ</b>	nonlinear least-squares fitting
<b>OAT</b>	one-at-a-time
<b>PDSC</b>	plastic-damage multidirectional smeared crack
<b>PP</b>	polypropilene
<b>PUM</b>	partition of unity method
<b>PVA</b>	polyvinyl alcohol

<b>RCM</b>	rough crack model
<b>RPT-3PS</b>	round panel tests supported on three points
<b>RSCM</b>	rotating smeared crack model
<b>RSF</b>	recycled steel fibres
<b>RSFRC</b>	recycled steel-fibre reinforced concrete
<b>SA</b>	sensitivity analysis
<b>SCC</b>	self-compacting concrete
<b>SCM</b>	smeared crack model
<b>SDEM</b>	simplified diverse embedment model
<b>SED</b>	strong embedded discontinuities
<b>SERA</b>	single European rail system
<b>SFRC</b>	steel-fibre reinforced concrete
<b>SFRSCC</b>	steel-fibre reinforced self-compacting concrete
<b>TC</b>	traditional concrete
<b>TD</b>	technical demonstrator
<b>UVEM</b>	unified engagement model
<b>VEMI</b>	variable engagement model I
<b>VEMII</b>	variable engagement model II
<b>WED</b>	weak embedded discontinuities
<b>XFEM</b>	extended finite element method

# Symbols

$A_f$	cross-sectional area of a fibre
$\alpha_i$	tensile strength factor used to define the trilinear/quadrilinear diagrams
$A_{sec}$	cross-sectional area of the FRC element
$\beta$	shear retention factor
$\beta_1$	coefficient that defines the shape of the pre-peak branch of the bond-slip relation
$\beta_2$	coefficient that defines the shape of the post-peak branch of the bond-slip relation
$\chi_c$	curvature in a cracked concrete section
$\chi_e$	curvature in an elastic concrete section
$\chi_m$	average curvature of the cracked and elastic concrete sections
$D_{max}$	crack stiffness matrix
$\hat{D}^{cr}$	derivative of the crack stiffness matrix
$\delta_0$	slip at the end of the linear branch of the bond-slip diagram
$\delta_m$	peak bond slip
$d_f$	fibre diameter
$D_{max}$	maximum aggregate diameter
$E_c$	concrete modulus of elasticity
$\ell_b$	crack band width
$\ell_c$	crack band width in compression
$\eta_\theta$	fibre orientation factor to account for the fibre effectiveness
$\varepsilon_n^{cr}$	crack normal strain
$\varepsilon_{n,ult}^{cr}$	ultimate crack normal strain
$f_c$	concrete compressive strength

$f_{ct}$	concrete tensile strength
$F_{err}$	maximum force deviation error between numerical and experimental responses
$F_{Exp}^i$	$i^{\text{th}}$ interpolated experimental data point
$F_{Num}^i$	$i^{\text{th}}$ predicted numerical data point
$F_{toler}$	force deviation tolerance between the numerical and experimental responses
$\Gamma^+$	right region of the singular band
$\Gamma^-$	left region of the singular band
$G_{fI}$	concrete fracture energy in tension
$G_{f,c}$	concrete fracture energy in compression
$G_{f,s}$	mode II fracture energy
$h$	width of the singular band
$K_n$	normal stiffness of the interface element
$l_f$	fibre length
$N_f$	number of fibres per unit area
$N_{\perp}$	component of the pullout force normal to the embedded portion of the fibre
$N_{\parallel}$	component of the pullout force aligned with the embedded portion of the fibre
$nIter$	number of global fitting iterations
$N_{nodes}$	number of corner nodes of the finite element
$nParams$	number of optimisation parameters
$OL_{FE}$	crack band width computed based on the Oliver's approach at FE level
$OL_{IP}$	crack band width computed based on the Oliver's approach at IP level
$\phi$	value assigned to the nodes on the right and left of the crack in the Oliver's approach
$\phi_{min}$	minimum value assigned to the nodes on the right and left of the crack in the Oliver's approach
$P_{toler}$	parameter (i.e. of the stress-crack width relationship) deviation tolerance between the fitting cycles
$\underline{P}$	fitting variables vector
$R$	local compression reaction in the matrix at the fibre exit point
$\sigma_n^{cr}$	crack normal stress

$\sigma_{n,ai}^{cr}$	crack normal stress due to the aggregate interlock
$\sigma_{n,cf}^{cr}$	crack normal stress due to the fibre pullout
$\sigma_{n,c}^{cr}$	crack normal stress due to the matrix
$S$	interfacial stresses between the fibre and the matrix medium
$\sqrt{FE}$	crack band width computed based on the area of the FE
$\sqrt{IP}$	crack band width computed based on the tributary area of the IP
$\tau_0$	bond stress at the end of the linear branch of the bond-slip diagram
$\tau_{t,ai}^{cr}$	crack shear stress due to the aggregate interlock
$\tau_{t,cf}^{cr}$	crack shear stress due to the fibre pullout
$\tau_{t,p}^{cr}$	maximum crack shear stress
$\tau_m$	peak bond stress
$\theta_{cr,j}$	crack orientation angle
$\theta_f$	fibre angle in regards to the crack surface
$\theta_w$	pullout loading direction angle
$\vec{u}_{cr}$	crack normal vector
$\vec{v}_{xG,i}$	vector from the centre of the element to the current node i
$V_f$	fibre contents in volume ratio
$w^{cr}$	crack displacement
$w_n^{cr}$	crack opening displacement
$w_t^{cr}$	crack sliding displacement
$\xi_i$	ultimate crack strain factor used to define the trilinear/quadrilinear diagrams

# 1 Introduction

## 1.1 Motivation

The use of concrete as a construction material dates back thousands of years and it is still one of the most popular material used in the civil engineering industry today. Despite its brittle behaviour and weak tensile capacity, different technologies have emerged by combining concrete with other materials as load carrying mechanisms to successfully overcome its inherent brittleness, originating a competitive, resistant and reliable structural material with a wide range of potential applications.

The idea of employing fibres as reinforcement to increase the tensile capacity of binder materials dates back to ancient Egypt, when dry bricks were bound together using a mixture of straw and mud [1]. Similarly, the Romans used to employ horse hair in their concrete mixtures to reduce shrinkage. However, it was only in the 1960s that the attention of the scientific community was drawn to the real potential applications of fibre reinforced concrete (FRC) in the construction industry. Higher energy absorption capacity, ductility, reduced crack widths and enhanced resistance to dynamic, fatigue and impact loading are some of the appealing characteristics provided by the fibre reinforcing mechanisms [2, 3]. Several types of fibres can be used namely steel fibres, glass fibres, synthetic or natural fibres, however in general, steel fibres are typically preferred due to their mechanical and geometric properties resulting in better structural performance.

The railway industry is one of the sectors that can take advantage of the enhanced structural performance of FRC due to its exigent structural requirements and frequent exposure to heavy loads. In fact, the European Commission is promoting a modal shift from road to railway, by fostering railway technology by means of research and innovation (R&I) under the Shift2Rail project, promoting not only the competitiveness of the European railway industry, but also contributing to the development of the necessary technology to complete the single European rail system (SERA). The Shift2Rail project aims at the duplication of the capacity of the European railway system, increase reliability and service quality by 50% while reducing by half the life-cycle costs.

Hence, considering the interest of the European community in high-speed lines and high axle load corridors, the current ballasted track solution will soon exceed its performance capacity if the system is not modernized. The sleepers are of key importance in the structural behaviour of the ballasted track system

and higher axle loads and speeds contribute to the premature failure and degradation of these elements, rising maintenance costs. An alternative to the ballasted track configuration is the slab track system. In comparison with the ballasted solution, the slab track system has lower maintenance requirements, higher service life time, increased lateral and longitudinal resistance, and better performance in high speed tracks (elimination of ballast churning at high-speed) [4–6]. However, higher initial cost, uncertainties about the serviceability performance and lack of studies on the life cycle cost of such systems are some of the current disadvantages of these solutions. Several authors identified the most common damage factors of concrete sleepers and slab track systems as concrete degradation beneath the rail, longitudinal cracking, fatigue damage and accelerated degradation due to exposure to high impact loads as the most relevant ones which could potentially be minimised by using FRC technology.

Despite the advantages of FRC technology, the design of structural elements using this material poses complex challenges. The highly material nonlinear behaviour of FRC due to the combination of materials with different stiffness and properties, leads to challenging modelling and analysis approaches, often involving sophisticated computer programs based on the finite element method (FEM). The selection of appropriate constitutive models, specification of the parameters to be used in these constitutive models, and ensuring that these values are representative of the behaviour of the actual structure are some of the key challenges faced by engineers when designing FRC structures.

Hence, this PhD research aims at contributing to the field of numerical simulation of FRC by enhancing the approaches in the FEMIX V4.0 computer code and by proposing and implementing a new constitutive model for analysing FRC elements. This PhD thesis is aligned with the objectives of Shift2Rail project, more precisely with the innovation programme 3 (IP3) - Cost Efficient and Reliable High Capacity Infrastructure under the technical demonstrator (TD) 3.3/3.4 - Optimized and Next Generation Track Systems, in the sense that the herein presented research applies to FRC structural elements in general including railway infrastructural components such as sleepers or slab track systems.

## **1.2 Objectives**

In the past decades, several approaches to analyse and simulate FRC elements were proposed based on continuous smeared and discrete crack approaches. However, a unified consensual methodology to accurately simulate the behaviour of FRC elements does not yet exist. The herein presented work aims at contributing with the development of numerical tools and models that improve simulation reliability of FRC elements as well as to provide a better understanding of the resisting mechanisms involved in the fracture process of FRC. Hence, the main objectives of the present work can be summarised in the following key-points:

- Contribute to the enhancement of the current approaches to simulate FRC, in the present case the multi-fixed smeared crack model (MFSCM) approach available in FEMIX V4.0 computer code, by

implementing a generalised approach (applicable to all finite elements available in FEMIX V4.0) to compute the crack band width (CBW) parameter;

- The development and implementation of an automatic, robust and reliable inverse analysis (IA) tool for deriving the fracture mode I parameters of FRC from three-point notched beam bending tests (3PNBBT) and round panel tests supported on three points (RPT-3PS) experimental tests;
- Propose a mechanically-based mixed-mode constitutive model that integrates the fracture mode I and II by coupling the fibre pullout and aggregate interlock resisting mechanisms;
- Implementation and assessment of the proposed constitutive model in the FEMIX V4.0 computer code;

### **1.3 Thesis outline**

Chapter 2 presents an overview on the fundamental concepts regarding the fracture behaviour of FRC elements. For this purpose, a brief description on the crack formation and propagation phenomena is provided as well as a review on the fibre pullout behaviour of steel fibres with emphasis on the different pullout stages and main influential aspects on fibre effectiveness to the tensile behaviour of FRC. In addition, the most popular approaches for simulating the nonlinear material behaviour of this type of elements are provided, where the advantages and disadvantages of each approach are discussed. Finally, a review on the main procedures for deriving the fracture mode I parameters of FRC is provided.

In Chapter 3 a set of numerical case studies of FRC elements failing in bending and shear are presented, and a parametric study involving the fracture mode I/II parameters is performed by analysing their impact on the results at the structural level. In addition, a generalised approach to compute the CBW is presented and its implementation in the FEMIX V4.0 computer code is detailed. The original methodology is based on the dimension of the entire finite element (FE), however its extension to the integration point (IP) level by considering only the tributary area of the IP is also implemented. The methodology is available for plane stress elements, shell elements and solid elements. The impact on the results of the referred methodology is assessed by means of a numerical case study involving different mesh sizes and configurations.

Chapter 4 presents the development of a novel IA approach for deriving the fracture mode I parameters of FRC in an automatic and optimised fashion by using experimental results of 3PNBBT and RPT-3PS. The proposed methodology was implemented using C programming language and its predictive performance is assessed by means of experimental results from 3PNBBT and RPT-3PS retrieved from the literature. In addition, the developed tool is applied in the analysis of real-scale steel-fibre reinforced concrete (SFRC) beam, where the fracture parameters were derived using the proposed IA methodology.

In Chapter 5 a new integrated mixed-mode fracture constitutive model is detailed and its predictive capacity for simulating FRC structures is analysed. In this chapter, the potentialities of the combination of the main resisting mechanisms involved in the fracture process of FRC are explored, through the integration of well-established fibre pullout and aggregate interlock constitutive models. A parametric study involving



the main variables that define the proposed constitutive model is conducted to analyse the impact of these parameters in the output results. Also, the predictive performance of the model is assessed by comparing the results of the analytical expressions to experimental results gathered from the literature.

In Chapter 6, the implementation of the proposed constitutive model (mixed-mode fracture smeared crack model (MMFSCM)) in FEMIX V4.0 is described and its adequacy for simulating FRC structures is assessed. The predictive performance of the MMFSCM is analysed by comparing the numerical and experimental experimental results of several simulations presented in this chapter.

Finally, Chapter 7 summarises the conclusions and main contributions of the PhD research as well as recommendations for future studies.

# Literature **2** Review

## **2.1 Introduction**

*In this chapter a literature review is conducted regarding the most relevant concepts of the fracture behaviour and modelling approaches of fibre reinforced concrete (FRC) elements. Hence, a general overview on the mechanism of fracture propagation in FRC is provided, followed by a review on the pullout behaviour of steel fibres, where the main phases of the pullout process are detailed. In addition, an overview on the effect of fibre distribution and orientation on the global tensile behaviour of FRC is also included, as well as the main factors affecting fibre structure and typical approach to account for its distribution. The most popular approaches for simulating the nonlinear material behaviour of FRC using analytical and numerical approaches are provided, where the advantages and disadvantages of each approach are discussed. Finally, a review on the main procedures for deriving the fracture mode I parameters of FRC is provided.*

## **2.2 Crack formation and propagation in FRC elements**

Fracture mechanics is the science that studies the forces associated with the rupture of solid body, in particular, with the balance of energies involved with the propagation of a crack [7]. The applicability of fracture mechanics to metals and other brittle materials, such as glass, is well known and extensively documented in the literature. Its principles are based on the linear elastic theory combined with different techniques to take energy absorption, plasticity and other phenomena at crack tip into consideration [8].

For a given defect, a crack can develop under tensile (mode I), sliding (mode II) or tearing mode (mode III) [9, 10], as illustrated in Figure 1, or in a combination of these three modes (mixed-modes). Mode I is the most common fracture mode, consisting in normal separation of the crack faces due to tensile stresses. Mode II and III are originated by shearing actions, residing the main difference in the fact that in the former the action is normal to the leading edge of the crack plane, whereas in the latter the action is parallel to the edge of plane.

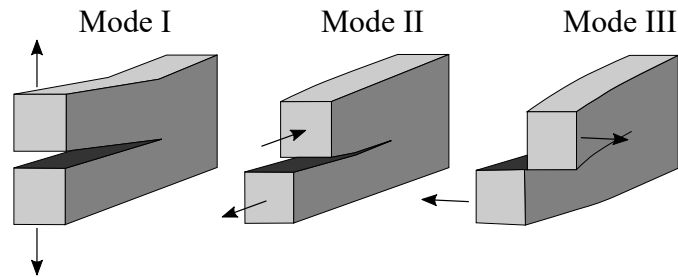


Figure 1: Basic fracture modes: I - opening mode (tensile), II - sliding mode (in-plane shear) and III - tearing mode (out-of-plane shear).

Crack formation and propagation have a major impact in the performance of plain and reinforced concrete. The first studies regarding the fracture mechanism of concrete elements were conducted by Kaplan [11] by applying the linear elastic fracture mechanics (LEFM) concepts. However, concrete is a quasi-brittle material, or in other words has some residual load-carrying capacity after reaching the tensile strength. Thus, despite showing small plastic deformation, concrete exhibits a relatively large zone in front of the crack tip where the stress-strain relationship is nonlinear [8, 12]. This zone is known as fracture process zone (FPZ), and these characteristic rules out the applicability of LEFM principles, since the nonlinear zone cannot be neglected and does not concentrate in a point at the crack tip [12, 13].

Hence, the FPZ is an inelastic region where the damage is accumulated as the crack progresses. In case of plain concrete, the FPZ is formed by coalescent microcracks, bond cracks between aggregates and the matrix and frictional pull-out of aggregates (aggregate interlock). When subjected to stress, the pre-existing microcracks within the concrete due to shrinkage and thermal deformations [14–16], start to propagate through the concrete (point A in Figure 2) until the peak stress is reached (C) resulting in the formation of unstable micro-cracks which ultimately lead to the propagation of macro-cracks, finally culminating in the stress-drop observed at point D.

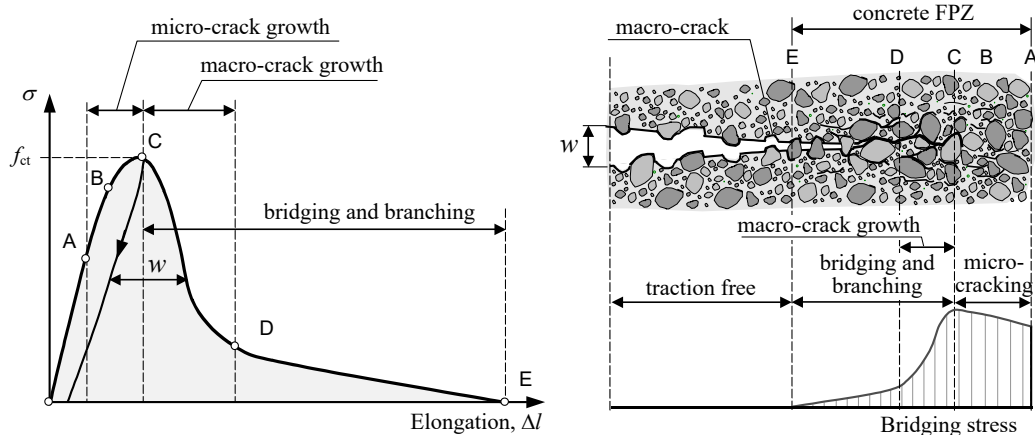


Figure 2: Schematic representation of the fracture process in uni-axial tension and correspondent stress-crack opening relationship [16].

On the other hand, in case of FRC, the FPZ is composed of a fibre-bridging zone and a combination of the former and the aggregate interlock effect, where the latter has a less representative impact, due to

the relatively larger crack width bridged by the fibres. The tensile post-cracking behaviour of FRC is related to the mechanisms that arise at matrix/fibre interface such as fibre debonding, matrix fracture/spalling, post-debonding friction between fibre and matrix (fibre pullout), fibre rupture, and fibre yielding, which impact depends on factors such as the quality of cementitious matrix, geometry and fibre material [16, 17]. Thus, for FRC elements a combined effect of aggregate and fibre bridging arises, as illustrated in Figure 3, as the fibre bridging mechanism is gradually activated upon a certain crack width value. In Figure 3, three distinct zones can be identified, namely, a traction-free zone (with relatively large crack widths), a bridging zone where fibre and aggregate bridging take place and a zone of microcrack growth.

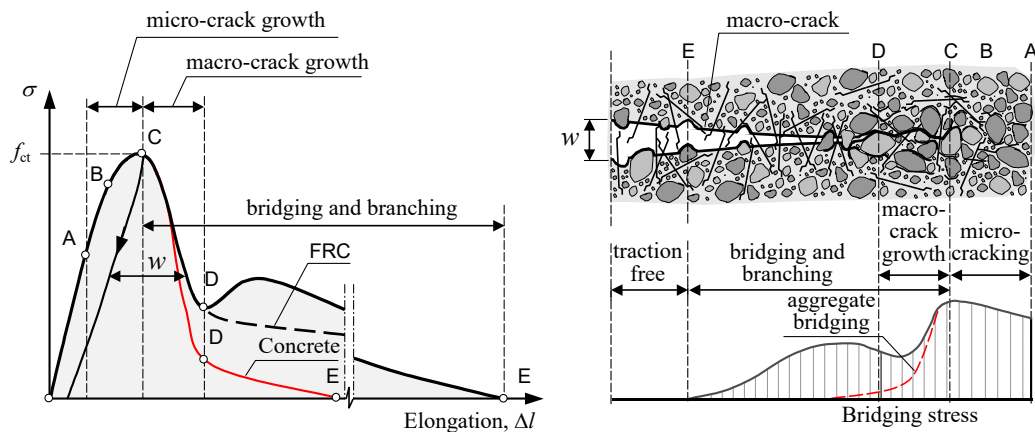


Figure 3: Schematic representation of the effect of aggregates and fibres in FRC [16].

## 2.3 Pullout behaviour of steel fibres

The addition of steel fibres to concrete has a major effect in brittleness and crack width control, since the mechanisms that arise after crack initiation, such as crack bridging, dissipate a considerable amount of energy during the fibre pullout process. The crack bridging capacity provided by the fibres is attained as a result of bond-slip mechanisms such as adhesion, friction, mechanical and fibre interlock with the surrounding matrix. In fact, bond mechanism plays a major role in the composite action of FRC [18, 19].

The overall mechanical behaviour of smooth steel fibres results from a combination of adhesion and friction with the surround matrix during the pullout process. The pullout behaviour of an aligned smooth fibre is presented in Figure 4. The first branch of the curve corresponds to a linear force-slip relationship due to the elastic bond originated by the physical and chemical adhesion of the fibre to the surrounding matrix [20]. After reaching point A, the debonding process starts to develop until the peak load is attained at point B and the fibre is fully debonded. After reaching the peak, the load starts to decrease, with the correspondent increase in slip due to the damage propagation at the fibre-matrix interface zone that decreases its frictional resistance. Finally, the C-D branch is governed by the frictional slip of the fibre, until maximum slip is achieved [17].

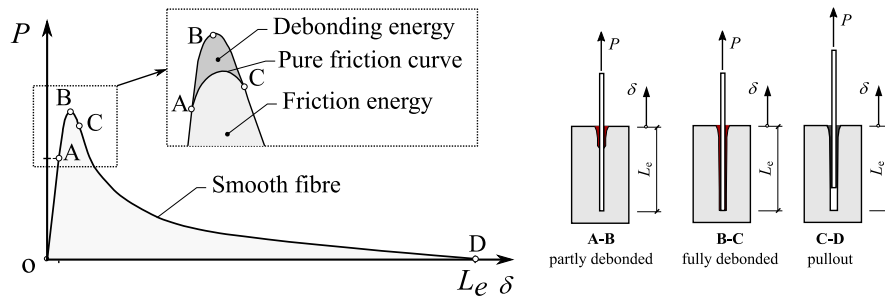


Figure 4: Typical pullout relationship between end-slip and load for smooth fibre (adapted from Löfgren [16] and Cunha [17]).

The behaviour of an end-hooked fibre is similar to the one of smooth fibre (Figure 4), as it is also composed by a debonding and frictional phase. However, after the debonding process is complete, the frictional phase is complemented with a mechanical bond mechanism originated by the mechanical interlock and plastic deformation of the end-hook. A comparison between the pullout behaviour of a smooth and hooked fibre is presented in Figure 5.

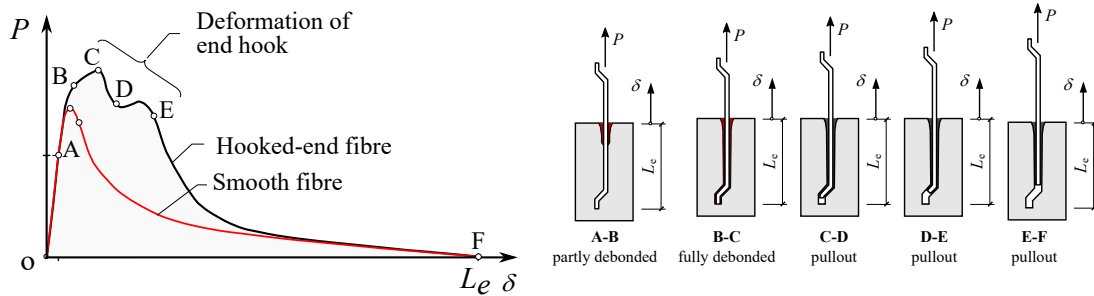


Figure 5: Typical pullout relationship between end-slip and load for smooth and end-hooked fibre (adapted from Löfgren [16] and Cunha [17]).








As depicted in Figure 5, the linear branch is very similar in both fibres, however, after the debond process is complete an increase in the pullout load (B-C) is observed, as a result of the contribution of the mechanical anchorage mechanism provided by the hook. As the end-hook becomes progressively deformed, a decrease in the load is observed (D), however, until the fibre does not attain a fully straightened shape, another peak load is observed. Finally, after the fibre is completely straight, the pullout process occurs (E-F) under frictional resistance, similarly to smooth fibres.

The peak pullout force and amount of energy dissipated depends on several factors namely, the mechanical properties and geometry of the fibres, fibre inclination and orientation (see Section 2.4), fibre embedment length and mechanical properties of the matrix.

Currently, all steel fibres have an enhanced bond capacity provided by mechanical “deformations” (e.g. crimping, indenting, end-hooks/buttons/paddles). As referred previously, a smooth fibre relies mainly on the breakdown of chemical adhesion and friction mechanisms involving the surrounding matrix, however, if a mechanical deformation is induced, the bond effect due to adhesion can be neglected since physical bond has a considerably higher impact on the pullout behaviour [21]. In fact, according to Banthia

and Trottier [22] and Li and Stang [23], deforming the fibre is the most effective approach to improve bond-slip characteristics of steel fibres in cementitious matrices. Some typical profiles of steel fibres commonly used in FRC are presented in Table 1.

Table 1: Steel fibre profiles [17].

Longitudinal profile	Cross section
 (a) Smooth	Round, flat or any shape
 (b) Indented/etched/roughened	
 (c) Flat-ended	Round or flat
 (d) Buttons-ended	Round
 (e) Hooked-ended	
 (f) Crimped/corrugated	Round, flat or any shape
 (g) Polygonal twisted	Polygonal (triangular or rectangular)

Besides fibre geometry, embedment length also constitutes an important parameter in the pullout performance of the fibres. Increasing the embedment length translates into a larger contact surface area with the surrounding matrix, leading to enhanced pullout response, which is specially important when smooth fibres are used [23]. In case of fibres with deformations along its length (e.g. indented, etched, roughened, crimped/corrugated), a better performance is obtained, since the larger embedment length mobilises more mechanical anchorages, as stated in the works of Chanvillard [24] and Groth [25]. However, the use of fibres with mechanical anchorages in its extremities, such as end-hooked fibres, seem to be less affected by larger embedment lengths, since the performance of this kind of fibres is conferred mainly by the grade of mobilisation of the anchorage system and not by the larger bond surface [18, 26].

When fibres are added to concrete, the mixture of aggregates, cement past and fibres are bonded together through the hydration process and development of the matrix microstructure. This results in the formation of the so-called interfacial transition zone (ITZ), which separates the fibre from the bulk cement paste (see Figure 6). From a microscopic point of view, the morphology of this zone is mainly characterised by the existence of a significantly porous layer, and the presence of an increased amount of calcium-hydroxide (CH) crystals, resulting in substantially lower strength when compared to the bulk

cement paste [27, 28]. Thus, matrix properties influence the pullout performance of the fibres, since the bond quality is affected by the microstructure of the ITZ. Several authors state that lower water/binder ratios leads to higher pullout loads, due to the densification of the ITZ and correspondent improved bond strength [22, 25, 29]. However, lower w/b ratios also increases the stiffness and strength of the bulk cement paste which results in lower toughness values [22] and potentially leads to fibre rupture, compromising the desired post-cracking performance.

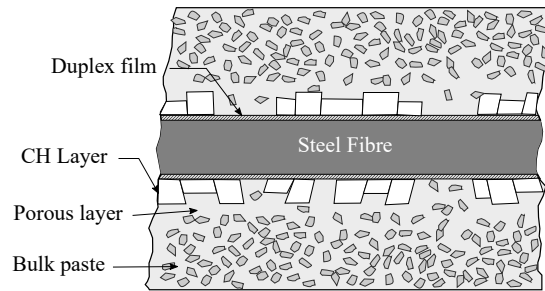


Figure 6: Schematic representation of the ITZ (adapted from Bentur and Mindess [30]).

When an inclined fibre at an angle,  $\theta_f$ , is subjected to a pullout force, a similar behaviour to the case of aligned fibres is observed, however, additional mechanisms are also activated, mainly at the fibre exit point. Firstly, the debonding of the fibre/matrix interface occurs, followed by sliding of the fibre over the debonded interface. However, due to the inclination angle, bending and shearing actions arise, originating local compression and push off of the matrix in the vicinity of the crack faces (Figure 7). The pullout force,  $N$ , can be decomposed in two components,  $N_{\parallel}$  and  $N_{\perp}$ . The component  $N_{\parallel}$  is responsible for fibre debonding which is sustained by interfacial stresses,  $S$ , whereas  $N_{\perp}$  originates a bending effect, which is counteracted by the reaction,  $R$ , originated by the local compression of the matrix. Hence, the matrix strength is of key importance since a weak matrix is prone to damage in the compressed area, potentially leading to concrete spalling.

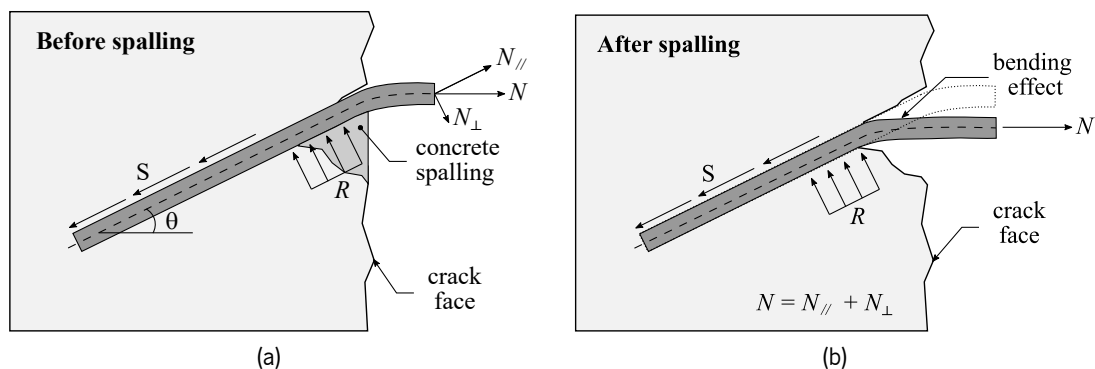


Figure 7: Bending and shearing action of an inclined fibre during the pullout process (a) before and (b) after concrete spalling (adapted from Cunha [17]).

The combination of the aforementioned mechanisms usually results in higher pullout resistance, especially for inclinations ranging between 10 to 30° [17, 22, 26, 31]. Higher inclination angles originate

higher stress levels in the fibres due to bending effect which potentially increases the risk of fibre rupture, jeopardizing the benefits of fibre addition [32]. The influence of fibre inclination in the pullout response is illustrated in Figure 8.

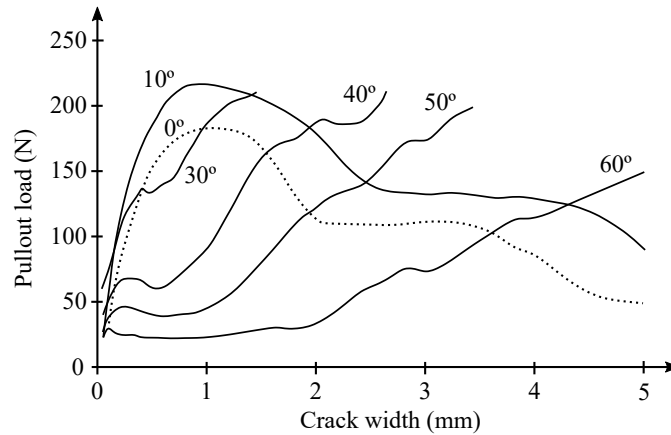


Figure 8: Pullout response of end-hooked steel fibres at different inclination angles [26].

## 2.4 Importance of fibre orientation and distribution

Fibre orientation and distribution plays an important role in the mechanical performance of FRC [33]. The desired post-cracking behaviour of steel-fibre reinforced concrete (SFRC) arises from fibre effectiveness in crack-width control, which severely depends on global performance granted by the individual contribution of each fibre bridging the crack. The distribution and orientation of fibres within the matrix seldom presents an optimal arrangement and the same efficiency in all directions. In the present section, the main factors affecting fibre orientation, current approaches to quantify the impact of fibre orientation and the existing techniques to measure the orientation of fibres are presented.

### 2.4.1 Main factors and definitions

In Section 2.3 the efficiency of a single fibre was described in terms of pullout performance for both aligned and inclined cases. According to the definition stated by Kameswara Rao [34], *fibre efficiency* consists in the performance of an individual fibre in function of its orientation relative to the pullout direction. On the other hand, *fibre effectiveness* gives the average value of the efficiency obtained for all possible orientations that the fibre can present.

Fibre effectiveness is affected by two main groups of factors, the first is related with the variables involved in the increasing of bond capacity (as described in Section 2.3) and the latter related with fibre structure itself. Fibre structure and morphology can be influenced by several aspects that may, or may not, favour the optimal alignment of the fibres. These factors (Figure 9) include fibre length, wall-effects, specimen size, casting direction, compaction method, mixture composition and rheological properties, and existence of rebars or other obstacles [17, 35].



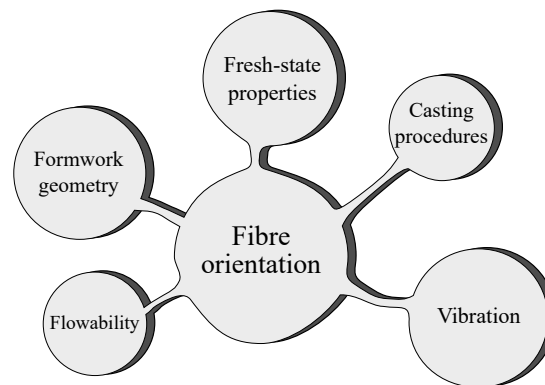


Figure 9: Influencing factors affecting fibre orientation and structure.

According to Laranjeira [36], amongst the referred aspects, the wall-effects introduced by the formwork and fresh-state properties of SFRC are the most relevant factors affecting the fibre structure. If the spread of fresh FRC is not restricted by boundaries (mainly due to the molds), the arrangement of the fibre structure is considered random without the occurrence of any preferential orientation. However, when geometric boundaries are introduced, fibres tend to align parallel to them as depicted in Figure 10. This phenomenon is known as wall-effect, and its impact increases as the volume is exposed to more boundaries [37–39].

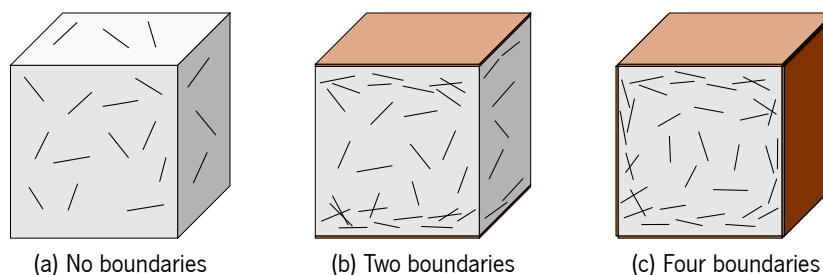


Figure 10: Effect of boundary conditions in fibre distribution (adapted from Álvarez [40]).

In addition, the volume affected by the wall-effect depends on the ratios between the dimensions of the mould and fibre length. According to Kooiman [38] and Soroushian and Lee [41], the effect of constrained orientation of fibres is relevant in cases when the dimensions of specimen/structure is less than five times the length of the fibres.

The flow property of fresh concrete is also identified as a major factor in fibre orientation, especially in self-compacting concrete (SCC). This is due to the fact that fibres tend to align perpendicularly to the cast direction. Furthermore, fibre alignment in SCC is subjected to both wall-effect and the nonlinear velocity profile of the concrete flux. The latter is originated by the frictional resistance offered by the walls of the mould [42]. A schematic representation of a possible explanation for the nonlinear velocity profile in concrete flux is depicted in Figure 11.

Vibration of a conventional concrete is another factor that affects fibre orientation. According to the

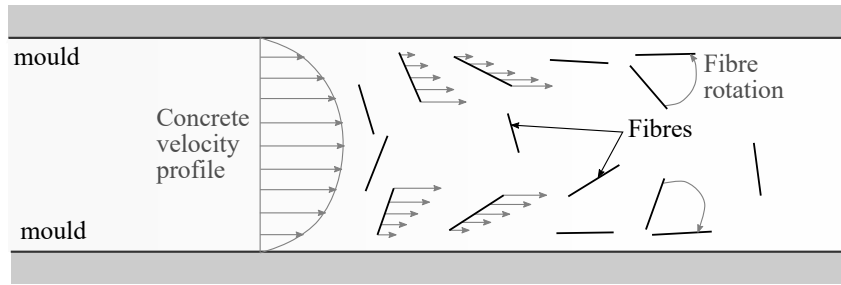


Figure 11: Explanation for fibre orientation due to nonlinear velocity profile and wall-effect [42].

works of Kooiman [38] and Barragán [43], compaction achieved through table vibration tends to produce planar random orientation perpendicular to the direction of such vibration. Furthermore, the use of immersion vibrator is not advisable since it leads to a fibre reduction in the insertion area [44].

### 2.4.2 Concept of orientation factor

Usually, the average fibre orientation in a certain direction is evaluated through the so-called *orientation factor*,  $\eta_\theta$  [45]. This parameter is given by the average projected length of all fibres, along a given direction, divided by the total fibre length. As a consequence, the value of this factor ranges from 0 to 1, when fibre alignment is parallel or orthogonal to the analysed cross-section, respectively. Thus, it is expected that fibre efficiency and post-cracking response decreases as  $\eta_\theta$  tends to 0, and on the contrary, increases as  $\eta_\theta$  approaches unity [46, 47].

The number of fibres bridging a crack is obtained by means of Equation (2.1) which includes  $\eta_\theta$  as a parameter [45],

$$N_f = \frac{A_{sec}}{A_f} \cdot V_f \cdot \eta_\theta \quad (2.1)$$

where  $N_f$  is the number of fibres per unit area,  $A_{sec}$  is the cross-sectional area of the FRC element,  $A_f$  is the cross-sectional area of a single fibre,  $V_f$  and  $\eta_\theta$  are the fibre content in volume and the orientation factor, respectively.

#### One-dimensional case

In one-dimensional systems the fibres are inevitably aligned with the direction of the applied load, which leads to optimal efficiency of fibres and ultimately to a theoretical fibre effectiveness of 1 [35, 38, 48].

#### Two-dimensional case

The situation changes when a two-dimensional space is considered, due to the fact that fibre orientation can range between 0 and  $\pi$ , relatively to the crack face ( $x$  axis in Figure 12). Fibre orientation is assumed to be random, with equal probability in the plane. Figure 12 illustrates the position of a randomly orientated fibre in a 2D system.  $\eta_\theta$  is obtained by projecting the mean fibre length on the axis that represents the direction of the tensile stress ( $y$  axis in Figure 12). Thus, according to Kameswara Rao [34]

fibre effectiveness can be computed using Equation (2.2).

$$\eta_{\theta 2D} = \int_0^\pi \frac{\sin \theta \cdot d\theta}{\pi} = \frac{2}{\pi} \quad (2.2)$$

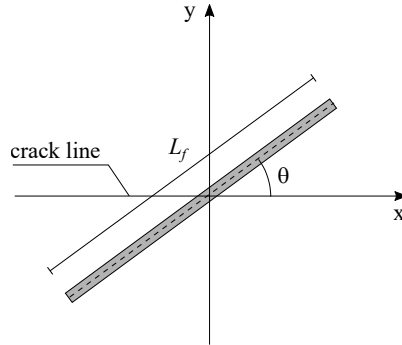


Figure 12: Two-dimensional fibre orientation system.

### Three-dimensional case

In the three-dimensional space, fibres can have any orientation and their end points cover the circumference of a sphere with a diameter equal to the fibre length,  $l_f$ , as depicted in Figure 13a. Assuming a randomly uniform distribution of fibres, Romualdi and Mandel [49] used Equation (2.3) to calculate the 3D fibre effectiveness. This expression relied on the fact that all fibre orientations have the same probability of occurrence. However Stroeven [50] proved this was not correct by computing the spatial-random effectiveness based on the geometric probability theory.

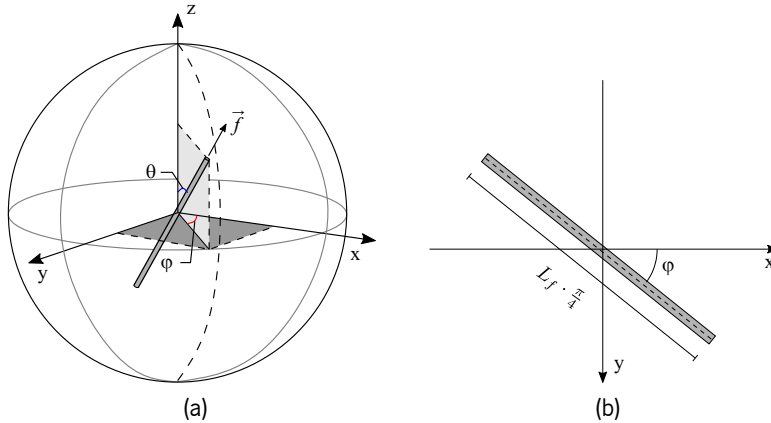


Figure 13: Three-dimensional fibre orientation system: (a) randomly orientated fibres in three dimensions and (b) average projected length in xy plane.

$$\eta_{\theta 3D} = \frac{\int_0^\pi \int_0^\pi \sin \varphi \cdot \sin \theta \cdot d\varphi \cdot d\theta}{\pi^2} = \frac{4}{\pi^2} \quad (2.3)$$

According to Stroeven [50] the contributions of the fibres formed a circular shape that depends on the angle of inclination,  $\theta$ , and therefore, are not independent of the fibre length. This resulted in an average projection length on the xy plane equal to  $L_f \cdot \pi/4$  (Figure 13b). Stroeven [50] then computed the

orientation factor by employing the same approach as Kameswara Rao [34] for the two-dimensional case. Considering the  $xy$  plane as the crack plane and the  $z$  axis coincident with the tensile stress direction, the orientation factor for a three-dimensional case is obtained using Equation (2.4).

$$\eta_{\theta 3D} = \frac{\int_0^\pi \frac{\pi}{4} \cdot \sin \varphi \cdot d\varphi}{\pi} = \frac{1}{2} \quad (2.4)$$

The aforementioned expressions arise from the assumption that fibres can orient freely in 2D or 3D space. However, this holds true only if fibres are located away from geometrical boundary surfaces of the specimen/structure avoiding wall-effects [38]. Dupont and Vandewalle [39] divided the cross-section of a beam into three distinct orientation zones as illustrated in Figure 14. Zone 1 represents the bulk in which a 3D-orientation is assumed whereas zone 2 and 3 represent areas with 1 and 2 boundaries, respectively. Hence, the average orientation factor over the cross-section can be obtained using Equation (2.5).

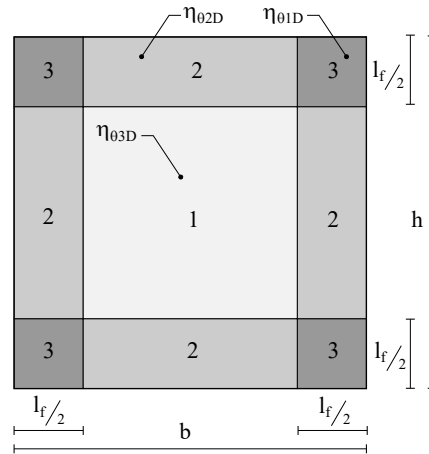


Figure 14: Cross-section of beam considered in Dupont and Vandewalle [39] study with the three distinct orientation zones.

$$\eta_\theta = \frac{\left[ \eta_{\theta 1D} \cdot (b - l_f) (h - l_f) + \eta_{\theta 2D} \cdot \left[ (b - l_f) l_f + (h - l_f) l_f \right] + \eta_{\theta 3D} \cdot l_f^2 \right]}{b \cdot h} \quad (2.5)$$

### 2.4.3 Measuring fibre orientation and distribution

Steel fibre orientation can be characterized by means of destructive or non-destructive techniques, and based on direct or indirect measurements. During the past years significant research was conducted in order to investigate fibre orientation in fibre-reinforced composites. Several methodologies exist (see Table 2) ranging from the use of expensive equipment, to cumbersome procedures and from destructive to post-test methodologies.

Fibre counting on cut specimens/elements constitutes the most simple and intuitive technique to measure the orientation factor. This procedure presents a simple and fast way to determine the number of fibres intersecting the cross-section, however, for a high volume of fibre content the procedure

rapidly becomes cumbersome and subjected to higher risk of fibre miscount. Direct approaches such as the X-ray method or computerized tomography (CT) scans provide very accurate measurements of fibre positioning, however, these methodologies are expensive, time-consuming and are mainly applicable to laboratory-size specimens, restricting its use to research purposes only. Other non-destructive methods have been developed in the last years such as the alternating current-impedance spectroscopy, open coaxial transmission line, dielectric waveguide antennas and others, based on electrical properties of SFRC. A detailed description of such methods can be found in the references provided in Table 2.

Table 2: Destructive and non-destructive methods for measuring fibre orientation [40, 51].

Method Type		Technique	References
Destructive	Indirect	Manual counting + theoretical expression by Krenchel [45]	[39, 41, 44, 52–56]
		Mechanical testing	[38, 48, 57–63]
	Direct	Image analysis	[48, 64–68]
		X-ray method	[37, 44, 69–71]
		Computerized tomography	[42, 72–76]
Non-destructive	Direct	Alternating current-impedance spectroscopy (AC-IS)	[77, 78]
		Translucent fluid	[79]
		Open coaxial transmission line	[80]
		Dielectric waveguide antennas	[81]
		Electrical resistivity methods	[82]
		Magnetic monitoring	[78, 83, 84]
		Electromagnetic and inductive methods	[85, 86]

## 2.5 Classification of the tensile behaviour of FRC

The addition of fibres to concrete drastically affects the tensile behaviour of the material with ductility being the main affected property depending on the fibre type and content [44]. Depending on the post-cracking behaviour of cement based materials, such as FRC, the uniaxial tensile behaviour can be classified as strain softening or strain hardening behaviour where the typical behaviour for each type is depicted in Figure 15 [87].

Strain softening behaviour is characterised by the formation of a dominant crack that leads to a progressive reduction of the load bearing capacity immediately after the peak-load is attained, accompanied by an increase in crack width. The main benefits that arise from the use of FRC with softening behaviour

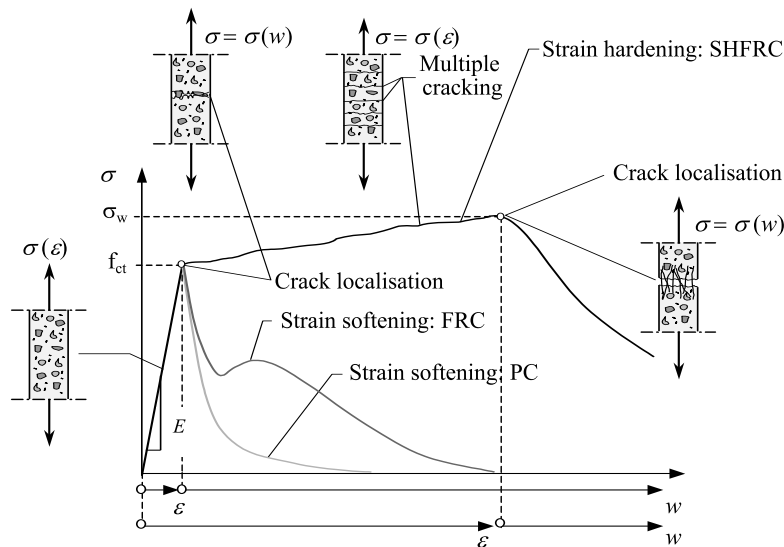


Figure 15: Schematic representation of tensile softening and hardening behaviour of FRC (adapted from Löfgren [16]).

resides in the significant energy dissipation capacity and the much tougher post-cracking behaviour [32, 88].

On the contrary, strain hardening behaviour is defined by an increase in load bearing capacity, after the tensile strength of the matrix,  $f_{ct}$ , is attained. After this value is reached, multiple cracks arise throughout the specimen accompanied by a gradual increase in the load capacity, until the critical value,  $\sigma_w$ , is achieved. After this point, a localised crack initiates and starts to widen and consequently a softening behaviour is observed, as illustrated in Figure 15.

## 2.5.1 Potential use of FRC technology in railway infrastructures

### 2.5.1.1 FRC Railway Sleepers

The ballasted track system, also known as ‘classical track’ or ‘conventional track’, consists of a flat structure formed by rails and sleepers supported on ballast. The ballast layer rests on a sub-ballast layer that ultimately transfers the loads to the underlying foundation layers. A schematic representation of the typical ballasted track configuration is presented in Figure 16.

Hence, the ballasted track configuration can be divided in two main groups, the superstructure (rail, fastening system, sleepers and ballast layer) and the substructure (sub-ballast, formation and base layers). Table 3 presents a summary of the track components and corresponding main functions.

As referred in Table 3 the sleepers are of utmost importance in the structural behaviour of the ballasted track, providing support to the rails, sustaining and distributing loads with acceptable stresses to the ballast, granting lateral stability and preserving track gauge. In the past, most of sleepers were made of timber, however due to its susceptibility to mechanical and biological degradation, short life span (25-30 years [4, 89]) and reduced lateral resistance, owed to its low weight, the use of this material has decreased

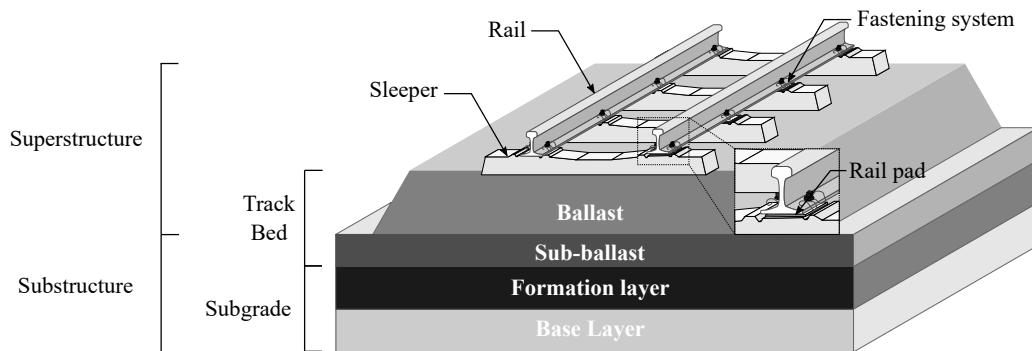


Figure 16: Schematic representation of the ballasted track configuration.

Table 3: Summary table of the components and functions of the superstructure and substructure.

Component	Functions
a) Rail	<ul style="list-style-type: none"> <li>Accommodate and distribute the wheel loads to the sleepers</li> <li>Provide wheel-rail guidance (ensured by the shape of the rail head and wheels)</li> <li>Distribute accelerating and braking forces by means of adhesion</li> </ul>
b) Fastening system	<ul style="list-style-type: none"> <li>Absorb rail forces and transfer them to the sleeper</li> <li>Ensure proper fixation in order to maintain track gauge and rail inclination</li> <li>Provide electrical insulation between the rail and the sleepers</li> </ul>
c) Rail pad	<ul style="list-style-type: none"> <li>Filter high frequency vibrations of the rail reducing load impact transmission to the sleepers</li> </ul>
d) Sleeper	<ul style="list-style-type: none"> <li>Provides support to the rails by means of the fixation system</li> <li>Sustain and distribute the loads uniformly to the ballast layer</li> <li>Provide lateral stability to the track and preserve track gauge</li> </ul>
e) Ballast layer	<ul style="list-style-type: none"> <li>Grant adequate support to the sleepers by limiting the displacements in vertical, transversal and longitudinal directions</li> <li>Reduce the stresses on the underlying layers by means of degradation of the forces transmitted by the sleepers</li> <li>Provide drainage capacity to the track, as well as lateral stability</li> </ul>
f) Sub-ballast layer	<ul style="list-style-type: none"> <li>Avoid degradation of the foundation layers due to the ballast grains</li> <li>Prevent fine soil particles migration to the overlying ballast layer</li> <li>Prevent water from reaching the foundation layers</li> <li>Filter the ascension of water from the foundation to the superstructure but avoiding the fine soil particles to migrate to the ballast layer</li> <li>Grant protection against freezing thawing cycles</li> </ul>
g) Subgrade	<ul style="list-style-type: none"> <li>Provide adequate support conditions to the overlying layers and accommodate stresses transmitted by the superstructure</li> </ul>

considerably. Moreover, the scarcity of wood after the Second World War, and technological developments such as the introduction of the continuous welded rail (CWR) and improvements in concrete prestressing technology [4], led countries such as Germany, England, Russia and Mexico to include concrete sleepers in their railway lines [90]. Concrete sleepers can be categorised in two main groups, the reinforced twin-block sleeper and the prestressed monoblock sleeper (Figure 17). The latter is the most used type of concrete sleeper due to easier handling, lower price and lower susceptibility to cracking, and currently extensively used in high speed railway lines.

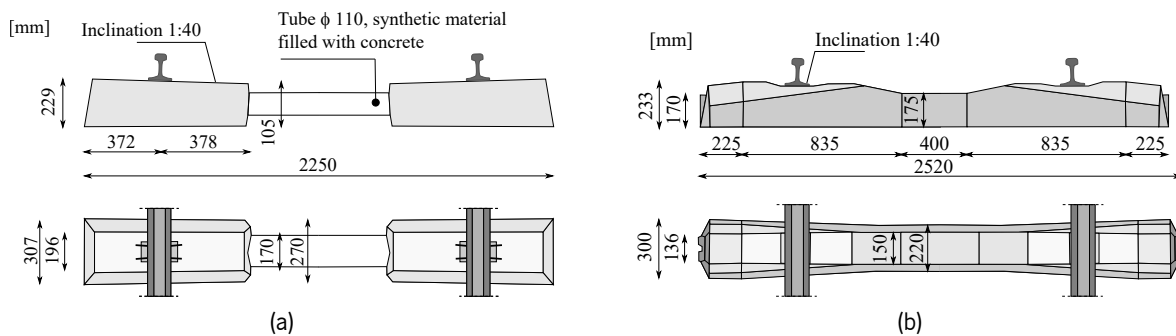


Figure 17: (a) Twin-block and (b) prestressed monoblock sleeper [4].

For the last decades, many researchers reported and investigated the most common failure modes in monoblock prestressed sleepers. Van Dyk et al. [91] ranked the most common failure modes of sleepers and fastening systems based on North American and worldwide surveys, identifying deterioration of concrete material beneath the rail, shoulder/fastening system wear or fatigue, as the main failure modes, and installation or tamping damage as the main failure mode internationally. Ferdous and Manalo [92] also reported rail-seat deterioration and longitudinal cracking as two major modes of failure in concrete sleepers. Furthermore, fatigue damage and exposure to impact loads, due to repeated loading and wheel/rail irregularities during their life cycle also contribute to premature failing and subsequent need for replacement [93]. Figure 18 presents the identified failure modes.

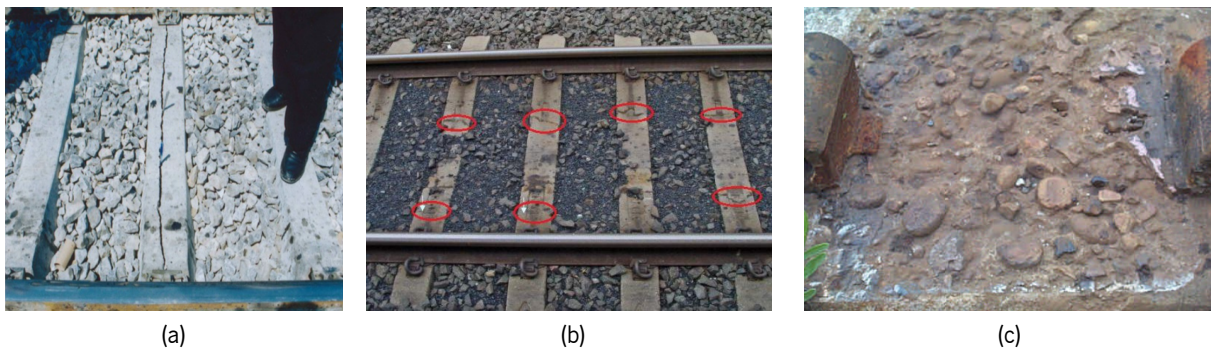


Figure 18: (a) Longitudinal cracking [94], (b) crack due to impact loads [95], and (c) rail-seat abrasion [96].

Hence, the necessity to develop solutions for the stated premature failures of concrete sleepers, along



with the increasing demands for high speed railway tracks, many research efforts have been conducted for the last years in an attempt to investigate the most durable, strongest and cost effective material to replace, or enhance, existing sleeper solutions.

It has been shown, in recent studies, that the tensile strength, flexural strength, energy absorption capacity, and resistance to cracking can be improved by means of the addition of fibres to concrete sleepers. Sadeghi et al. [97] conducted an experimental study on the application of steel fibres in prestressed sleepers, in order to investigate the benefits in terms of load-carrying capacity and energy absorption. This experimental research involved testing 30 sleepers, similar to the one presented in Figure 17, with 4, 6 and 8 prestressing wires and 0, 0.3, 0.5, 0.7 and 1.0% fibre volume ratio. The authors concluded that the addition of steel fibres led to the improvement of flexural strength, cracking resistance, energy absorption capacity and service life. Furthermore, the specimen with 6 prestressing wires and 0.5% fibre volume ratio performed optimally, when compared with the conventional sleeper, showing an increase in compressive strength, energy absorption capacity and lower construction costs.

As referred previously, sleepers are subjected to hundreds of axle loads per train, resulting in millions of load cycles during their life time. Hence, fatigue and impact damage are of extreme importance when assessing the adequacy of a sleeper. Hwang et al. [98] studied the performance of steel FRC prestressed sleepers with 0.75% fibre volume ratio under repeated loading. Results revealed that the SFRC prestressed sleepers successfully passed 3 million cycles of loading without failure, and showed increased flexural load in comparison with the wooden sleepers.

Likewise, Parvez and Foster [99] also examined the fatigue behaviour of SFRC sleepers subjecting 8 specimens with two different fibre contents (0.25 and 0.50%) to cyclic loading. The results indicate that the sleepers with 0.5% fibre volume have sustained higher static loads, fatigue life and residual strength. Furthermore, when compared with the conventional sleeper, the former had lower deflections and smaller crack widths, indicating better serviceability performance. However, the sleepers with 0.25% fibre volume revealed large variability in fatigue life, leading to the conclusion that a minimum dosage of fibres is fundamental for efficient performance of steel fibre reinforced sleepers.

In addition, concerns about the CO<sub>2</sub> emissions produced by the cement industry led some authors to partially replace the cement used in the manufacturing of the prestressed concrete sleepers by ground granulated blast furnace slag (GGBFS), besides the addition of steel fibres [100, 101]. Nonetheless, Yang et al. [100] conducted pull-out tests of rail fastening shoulder, static bending tests at rail and centre sections, as well as fatigue tests at rail seat section on a set of 40 prestressed concrete sleepers. The sleepers were designed in accordance with the Korean Railway Standard (TR 0008) (KRS) which is equivalent to the EN13230-2 [102], and involved conventional concrete sleepers partially replaced with concrete sleepers, including and not including 0.75% fibre volume ratio. The results indicate that the use of steel fibres and cement partially replaced with GGBFS, leads to higher loads at first cracking, adequate crack widths and fatigue life, in respect to KRS and [102].

Similarly, Shin et al. [101] conducted an impact experimental programme using a drop-weight impact test machine on a set of sleepers, with the same characteristics as the ones used by Yang et al. [100].

Shin et al. [101] concluded that the use of fibres and partially replaced cement by GGBFS, leads crack width reduction and limited propagation, decreased number of cracks and prevention of concrete spalling. The use of fibres also showed increased flexural strength.

In conclusion, considering the existing research, the use of steel fibres in prestressed concrete sleepers reveal several advantages, namely:

- i) Increase in flexural strength;
- ii) Higher load at first crack;
- iii) Reduced crack width;
- iv) Improved service life (less damage due to cracking, lower deflections);
- v) Increased energy absorption capacity;
- vi) Adequate impact and fatigue behaviour;

Nonetheless, further studies are necessary to better understand the behaviour, life cycle cost and design approach of these elements. In fact, the use of numerical tools capable of accurately simulate the structural behaviour of SFRC sleepers can ultimately contribute to the achievement of such objectives.

### 2.5.1.2 FRC Slab Track Modules

Another potential application of FRC technology is the Slab track, or ballastless track system. Similarly to the ballasted track, the slab track components can be grouped in the superstructure and substructure. The first group is formed by the rails, fastening system, rail pads, sleepers (if existent) and the concrete slab, while the latter usually comprises the hydraulic bonded layer, frost protection layer and the subgrade. Figure 19 presents a schematic representation of a typical slab track configuration. It should be noted however, that there are several slab track systems and not all require the use of sleepers or conventional fastening systems.

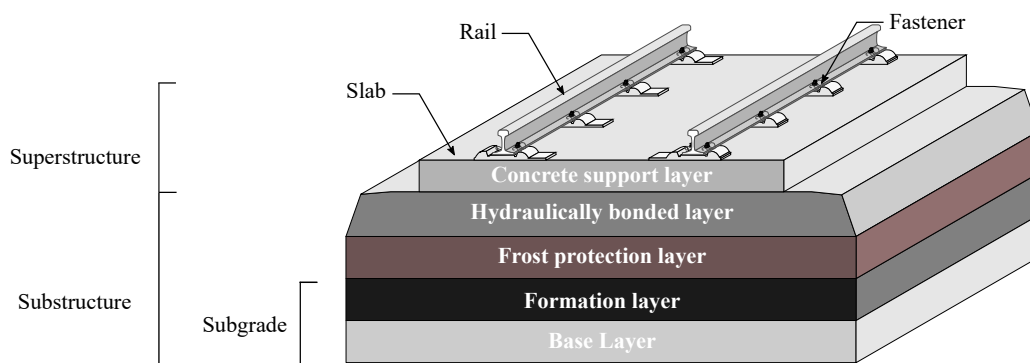


Figure 19: Schematic representation of a slab track system configuration.

In the slab track system, the support structure is mainly characterized by the (i) concrete support layer (CSL), (ii) hydraulically bonded layer (HBL), (iii) frost protection layer (FPL) and finally the (iv) subgrade.

i) The CSL consists of a reinforced concrete slab with equivalent functions to the ballast layer of transferring the loads uniformly to the underlying layers with acceptable stress level.

ii) The HBL consists of coarse granular material combined with an hydraulic binder (usually cement). The HBL is the first layer of the substructure, and similarly to the CSL, presents a major function in distributing the stresses to the foundation layers below [103].

iii) The FPL separates the trackbed from the subgrade and has a major function regarding the hydraulic protection against freeze/thaw cycles and increasing water levels.

iv) The subgrade characteristics and functions are the same as the conventional ballasted track (Table 3).

In the first ballastless track solutions the ballast layer was simply replaced by a concrete slab, preserving the sleepers in its original position. However, new systems progressively started to incorporate the sleepers into the slab, allowing for prefabrication and prestress application [104]. Figure 20 presents the main families of slab track systems, grouped by the nature of the support layer (concrete/asphalt) and type of rail support. It should be noted however, that slab track systems can be classified according to other criteria such as execution process (*in situ* or precast), number of resilient levels and foundation nature [105]. The examples shown in Figure 20 have been reviewed in the work of several authors [4, 103, 106, 107].

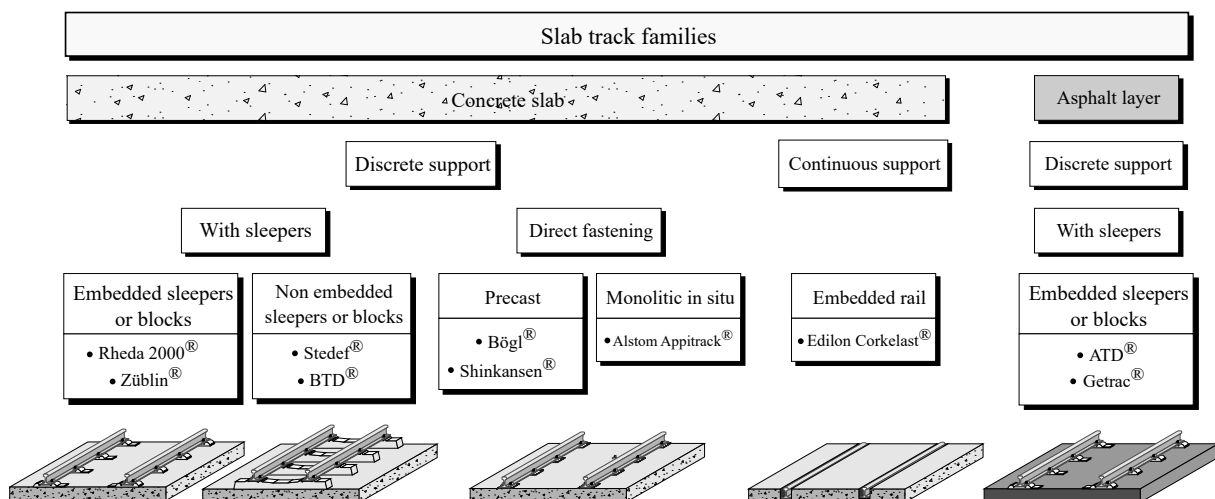


Figure 20: Families of slab track systems grouped by rail support type.

The advantages of adding steel fibres to concrete arise from the reinforcement mechanisms provided by the fibres bridging the cracks. This results in a higher level of stress redistribution, providing increased deformation capacity between crack onset, and structural failure. This aspect is especially relevant in structures with redundant support conditions [108], which is the case of slab track systems.

Despite the several applications of SFRC the use of such material is still scarce in railway structures, particularly in slab track systems. To the author knowledge limited research has been conducted in this field.

Takahashi et al. [109] investigated the possibility of replacing the conventional reinforcement in the JSlab system by non-corrodible short fibres (polypropilene (PP) and polyvinyl alcohol (PVA)). The experimental study involved compression, direct tensile and bending tests in specimens with different fibre

volume ratios (0.0, 0.5%, 1.0%, 1.5%, 2.0%, 2.5% and 3.0%). In addition, static bending tests and bending fatigue tests were performed on an actual size specimen with 2.0% fibre volume ratio. A bending fracture load of 80 kN was achieved in the static bending test of the actual size specimen, which corresponds to  $\approx 1.83$  times the design load (43.6 kN), showing increased bending capacity. Moreover, the elastic properties of a specimen reinforced with 2.0% PVA fibre volume ratio did not suffer significant alteration after being subjected to a 300 cycle freezing/thawing test, indicating adequate durability.

Besides the mechanical advantages already presented for the case of FRC sleepers (see Section 2.5.1.1), the use of fibres provides enhanced durability to the track, due to the diffuse crack pattern and limited crack width granted by the fibre bridging mechanisms. Furthermore, the use of such material would also increase construction speed, since when well conceived, fibre reinforcement can replace totally, or partly, conventional reinforcement [110].

Despite the aforementioned advantages, it should be noted however, that the lack of practical design methodologies, and robust and accurate numerical strategies to conduct reliable structural analysis limits the dissemination of such technologies. Thus, it is the author opinion that the development/improvement of numerical tools capable of better simulating the nonlinear behaviour of FRC can ultimately contribute to a better understanding and development of design guidelines for this kind of railway structures.

## **2.6 Simulation of the nonlinear behaviour of FRC elements**

### **2.6.1 Analytical-based models for simulating the nonlinear behaviour of FRC elements**

Several methods for analysing the bending capacity of FRC sections have been proposed during the past years, and are based on different assumptions regarding either kinematic or constitutive models for simulating the behaviour of FRC.

The fictitious crack model (FCM) [111] and the crack band model (CBM) [112] are probably the most popular fracture mechanic-based models to simulate the cracking behaviour of concrete. Despite the original purpose of these models to be used in combination with a FEM tool, these approaches can also be incorporated in simpler analytical models.

#### Fictitious crack model

The FCM was originally proposed by Hillerborg et al. [111] and Hillerborg [113]. This model is based on the principle that the stress transfer mechanism over the crack provided by the fibres is achieved by means of the so-called,  $\sigma - w$ , relationship.

In this model, the crack is assumed to propagate when the stress at the crack tip attains the tensile strength, however, when the crack initiates, the stress is not assumed to drop to zero, but instead to decrease gradually as the crack opens. The stress decay between the crack tip and the stress-free crack face corresponds to a microcracked zone where some residual stress transferring capacity still exists (FPZ).

Figures 21a and 21b illustrates the fracture zone and the stress-crack width relationship, respectively.

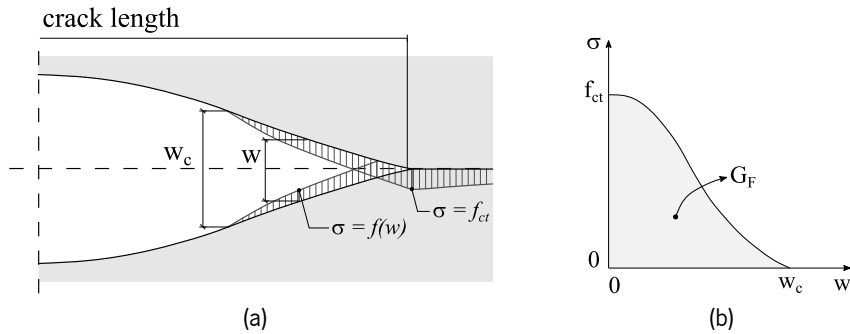


Figure 21: FCM model: (a) schematic representation of the process zone; (b) stress-crack relationship (adapted from Hillerborg et al. [111] and Vandewalle et al. [114]).

The area under the curve depicted in Figure 21b is known as fracture energy,  $G_{fI}$  (Equation (2.6)), and represents the energy consumed during the fracture process per unit area.

$$G_F = \int_0^{w_c} \sigma_w(w) \cdot dw \quad (2.6)$$

### Crack band model

The CBM [112] on the other hand, characterises the material behaviour in the FPZ, in a smeared manner through a strain-softening relation. In fact, this constitutes the main difference between the two aforementioned approaches. The CBM replaces the crack line with a band, of width  $\ell_b$  in which the nonlinear tensile deformation is uniformly smeared. Due to this fact, the CBM model requires an additional parameter, the crack band width (CBW), which corresponds to the length in which the tensile strain is smeared. Bažant [112] assumed this value to range between 1 to 6 times the maximum aggregate size.

The CBW should be dependent on the characteristics of the finite element mesh in order to avoid mesh dependency of the results and assure that the energy dissipated per unit length equals the fracture energy [115]. Figure 22 illustrates the concept of crack band width and the converted stress-strain relationship, with the strain smeared on the crack band width.

#### **2.6.1.1 Nonlinear hinge models**

Cross-sectional analysis can be conducted using nonlinear fracture mechanics concepts and based on the assumptions of the FCM, by means of a stress-crack opening relationship, in which the cracked section is described as a nonlinear hinge. Such approach has been presented by several authors [117–121].

The nonlinear hinge models presented herein are based on different kinematic and constitutive conditions. Nevertheless, the main principles associated with these models can be summarised as follows [114, 122]:

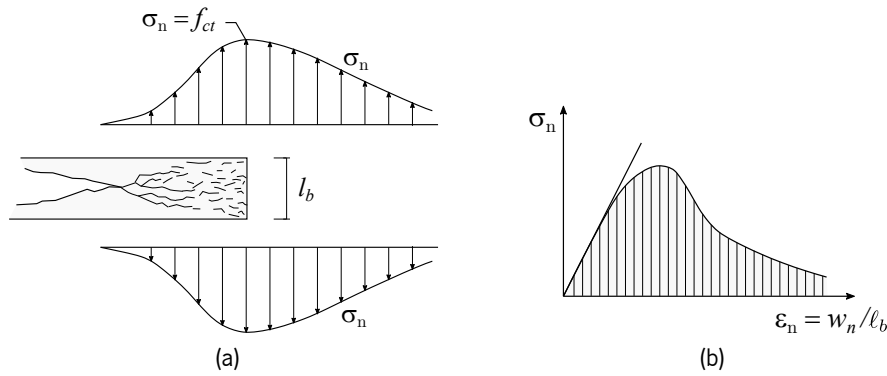


Figure 22: CBM model: (a) stress-distribution in the crack band proposed by Bazant and (b) stress-strain relationship smeared on crack band width [116].

i) The nonlinear behaviour is concentrated in the nonlinear hinge zone of length,  $s$ . This parameter has to be assumed, however according to Ulfkjær et al. [117] the length of the hinge can be approximately half of the beam height.

ii) The fictitious crack surfaces remain plane and the crack opening angle is equal to the overall angular deformation of the nonlinear hinge [118].

iii) The fictitious crack surfaces remain plane and the crack opening angle is equal to the overall angular deformation and the curvature of the elastic and cracked faces of the hinge are linked by means of a parabolic variation of the curvature [119].

iv) The crack surfaces do not remain plane, being the deformation dictated by the stress-crack opening relationship as well as the crack length and overall angular rotation of the hinge.

#### Casanova's approach

The approach proposed by Casanova and Rossi [119] considers the existence of proportionality between the angular rotation,  $\varphi$ , and the crack length,  $a$  (Equation (2.7)) and the formation of two different curvatures,  $\chi_e = 12M/Ebh^3$  and  $\chi_c = \varepsilon_c/x_0$ , respectively. The first represents the elastic curvature, whereas the latter represents the curvature in the cracked section.

$$\varphi = \frac{w_{cmod}}{a} \quad (2.7)$$

Moreover, the length of the nonlinear hinge ( $\Delta f$ ) is assumed to be dependent on the crack length,  $a$ , by means of expression 2.8.

$$\Delta f = 2 \cdot a \quad (2.8)$$

The curvature in the uncracked and cracked part of the hinge can be linked through the average curvature,  $\chi_m$  (Equation (2.9)), by assuming a parabolic variation of the curvature as depicted in Figure 23.

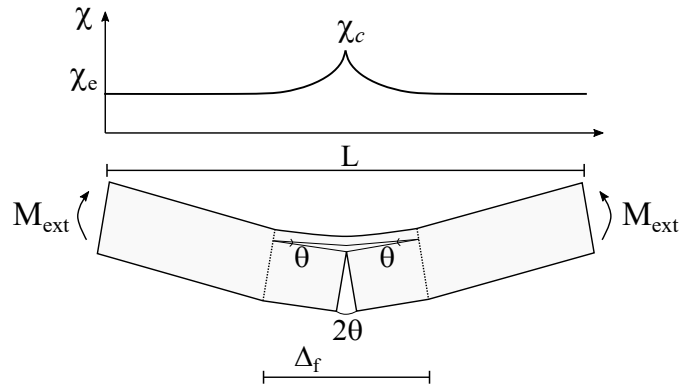


Figure 23: Distribution of the curvature around the nonlinear hinge [119].

$$\chi_m = \frac{2\chi_e + \chi_c}{3} \quad (2.9)$$

The relation between the average curvature and  $w_{cmod}$  is given by expression 2.10

$$w_{cmod} = 2\chi_m a^2 = 2 \left( \frac{2\chi_1 + \chi_2}{3} \right) a^2 \quad (2.10)$$

#### Pedersen's approach

The simplified approach proposed by Pedersen and Stang [118] is based on the kinematic hypothesis that the fictitious crack surfaces remain plane and the crack opening angle is equal to the overall angular deformation of the nonlinear hinge, as depicted in Figure 24a. The element is assumed to behave accordingly to classic Bernoulli beam theory up to attain the cracking strain in the most tensioned concrete surface. Considering a nonlinear hinge with rectangular cross-section and a height,  $h$ , subjected to an external axial force and bending moment per width, the distribution of stresses is assumed to develop as represented in Figure 24b.

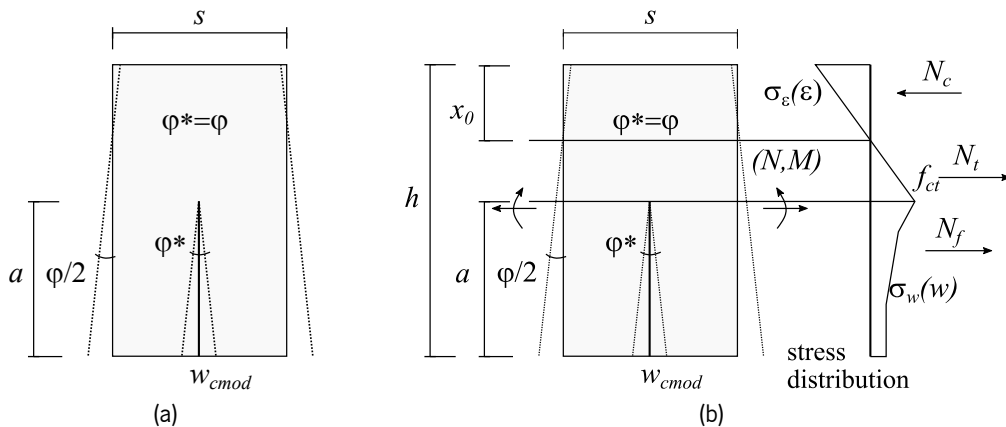


Figure 24: Nonlinear hinge model proposed by Pedersen and Stang [118]: (a) Schematic representation of the kinematic assumption of the nonlinear hinge; (b) nonlinear hinge subjected to axial force and bending moment and the assumed stresses distribution with the resultant forces.

The nonlinear hinge is related to the crack mouth opening displacement,  $w_{cmod}$ , by means of Equation (2.11),

$$h - x_0 = \frac{1}{\varphi} \cdot \left( \frac{f_{ct}}{E_c} \cdot s + w_{cmod} \right) \quad (2.11)$$

where  $s$  is the length of the nonlinear hinge,  $x_0$  is the position of the neutral axis,  $a$  is the crack length,  $\varphi$  is the rotation of the cross-section and  $f_{ct}$  and  $E_c$  are the tensile strength and modulus of elasticity, respectively.

#### Maalej and Li approach

Another approach was presented by Maalej and Li [120] by studying the flexural strength of FRC based on the FCM concept, relating the flexural strength of these elements to the material tension softening property. The stress distribution on a rectangular cross-section with a depth,  $d$ , and subjected to a bending moment is illustrated in Figure 25.

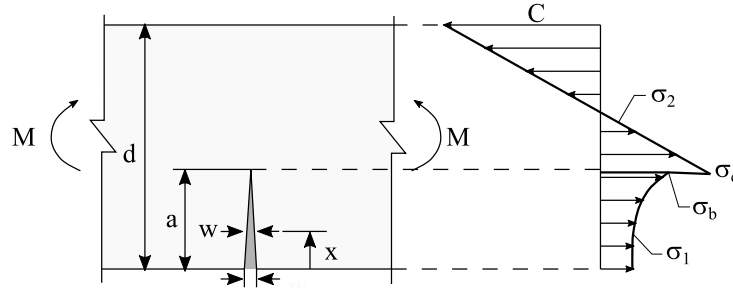


Figure 25: Distribution of normal stresses in the nonlinear hinge section [120].

The tension softening relationship developed within the fracture process zone was related to the crack width,  $w$ , at any point,  $x$ , of the fictitious crack by means of Equation (2.12),

$$\sigma(w) = \sigma_b \left[ 1 - 2k \left( \frac{w}{w_c} \right) + p \left( \frac{w}{w_c} \right)^2 \right] \quad (2.12)$$

where  $w_c$  represents the crack width at which the stress is null,  $\sigma_b$  is the post-cracking strength of the composite,  $k$  and  $p$  are coefficients that govern the shape of the slope of the tension softening curve. If a linear tension softening curve is assumed,  $k$  and  $p$  are equal to  $1/2$  and  $0$ , respectively.

The method presented is based on the idea of superposition in which the crack mouth opening displacement (CMOD),  $w$ , corresponds to the sum of a CMOD,  $w_1$  of a stress-free crack of length,  $a$ , caused by a bending moment,  $M$ , and the closing CMOD,  $w_2$ , caused by cohesive stress,  $\sigma(x)$ , as illustrated in Figure 26. A more detailed explanation is given elsewhere (see Maalej and Li [120] and Li et al. [123]).

#### Stang & Olesen's approach

Ulfkjær et al. [117] modelled the failure in bending of concrete beams by including the development of a fictitious crack in an elastic layer with a thickness proportional to the beam depth. Pedersen and Stang [118] extended this simplified approach by adding a normal force to the original formulation. The



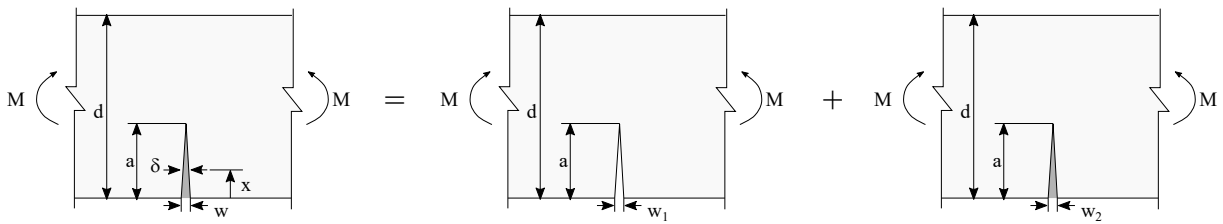


Figure 26: Model proposed by Maalej and Li [120]: superposition of CMOD (adapted from Spasojevic [122]).

nonlinear hinge model presented by Olesen [121] modelled the bending failure in the same way, however, a bilinear stress-crack opening relationship is considered. Furthermore, the model also includes the effect of an axial force.

In terms of kinematic assumptions, Olesen [121] considered that the boundaries of the nonlinear hinge remain plane, while the fictitious crack plane deformation is given by the stress-crack opening relationship, and the overall angular deformation and the length of the fictitious crack. Thus, the hinge is modelled as incremental layers of independent spring elements without transferring shear between each other [114, 121]. Figure 27a illustrates the propagation of the fictitious crack through the nonlinear hinge and the deformation of a cracked incremental horizontal strip of hinge. A representation of the bilinear stress-crack relation is also presented (Figure 27b).

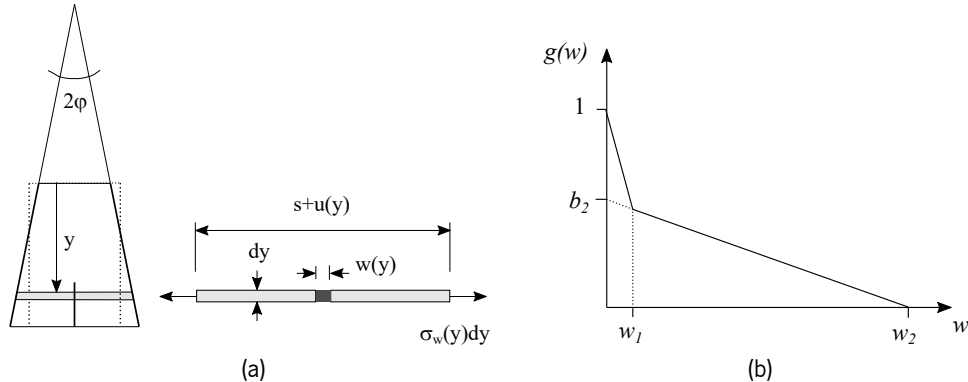


Figure 27: Nonlinear hinge model presented by Olesen [121]. (a) Geometry, loading and deformation of cracked incremental horizontal layer of the hinge; (b) Bilinear stress-crack opening relationship [121].

### Löfgren's approach

Löfgren [16, 124] further expanded the model proposed by Olesen [121] by considering a nonlinear stress-strain behaviour in compression, a multi-linear stress-crack opening relationship and a multi-linear strain-hardening relationship for conventional reinforcement. Furthermore, the author considered that the cross-section was subjected to a bending moment,  $M$ , and a normal force,  $N$  and that the average strain in the reinforcement is related to the elongation of the nonlinear hinge at the reinforcement level. Moreover, the kinematic assumption is that the crack surfaces remain plane and the crack opening angle is equal to the overall angular deformation of the hinge. The length of the nonlinear hinge corresponds to the average crack spacing.

According to Löfgren [16] the sectional forces can be written as follows,

$$\frac{N}{b} = \int_0^{h-a} \sigma_c(\varepsilon(y)) \cdot dy + \int_{h-a}^h \sigma_f(w(y)) \cdot dy + \sigma_s \cdot A_s \quad (2.13)$$

$$\frac{M}{b} = \int_0^{h-a} \sigma_s(\varepsilon(y)) \cdot \left(y - \frac{h}{2}\right) \cdot dy + \int_{h-a}^h \sigma_f(w(y)) \cdot \left(y - \frac{h}{2}\right) \cdot dy + \sigma_s \cdot A_s \cdot \left(d_1 - \frac{h}{2}\right) \quad (2.14)$$

where the parameters presented in Equations (2.13) and (2.14) are illustrated in Figure 28

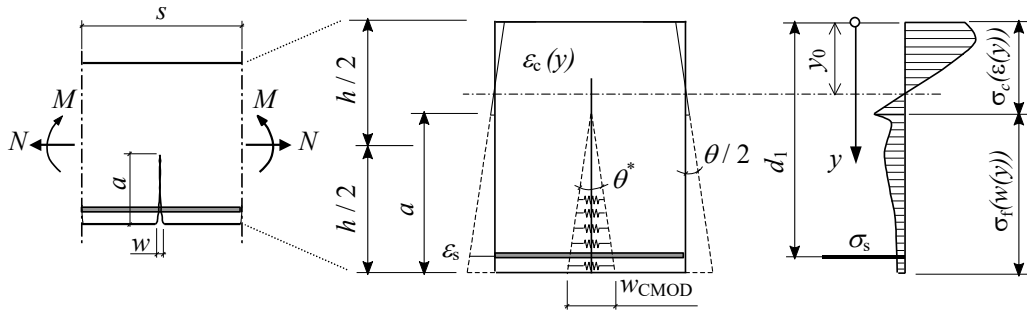


Figure 28: Nonlinear hinge concept for a beam with reinforcement [16].

## 2.6.2 FEM-based models for simulating the nonlinear behaviour of FRC

Currently, several finite element approaches are available to simulate the nonlinear behaviour of concrete structures exhibiting quasi-brittle failure modes, however, a unified, robust and accurate approach does not still exist.

The most popular models to simulate the fracture process of concrete may be grouped in two main categories: discrete crack model (DCM) and smeared crack model (SCM). The DCM approach aims at the simulation of initiation and propagation of dominant cracks by introducing a geometric entity in the finite element mesh representing the actual crack, either by means of interface elements allowing the separation of the continuum or by means of embedded strong discontinuities where discontinuities are introduced in the displacement field. On the contrary, in the SCM approach the individual cracks are not actually numerically resolved, but instead smeared out in the material volume associated with the integration point. Thus, the deterioration process of concrete is captured by means of a constitutive relationship [125]. During the past years, other approaches such as hybrid models have also been proposed. These models make use of both concepts inherent to the discrete and smeared approaches applying them in a simultaneous fashion. In the following sections, an overview of the discrete, smeared and hybrid crack models is presented.

### 2.6.2.1 Overview of the Smeared Crack Model (SCM) approach

In the past decades, several approaches to analyse and simulate FRC elements were proposed based on continuous smeared and discrete crack approaches. The SCM [126, 127] approach is one of the

most commonly and widely used strategy for simulating FRC structures. In this approach the cracks are smeared out within a band of material, in which the damage evolution is captured through the use of constitutive laws assigned to the material. Hence, this approach is very convenient from an implementation standpoint and is able to capture with good accuracy the main relevant structural behavioural aspects, mainly for ultimate limit state conditions, as long as the constitutive models simulate adequately the behaviour of the intervenient materials.

One of the main disadvantage of SCM is the dependency of the results on the mesh size and orientation, however, several authors proposed regularisation techniques to mitigate this effect and obtain mesh-independent results [125, 128]. Furthermore, due to the continuous nature of the displacement field in a finite element (FE) assumed in the SCM, the strains, stresses and the crack widths are also difficult to predict with the rigor that DCM potentially has. The SCM can be further categorised in rotating, fixed and multidirectional fixed smeared crack models [129–131]. In case of rotating smeared crack models the local coordinate system allocated to a given crack rotates in order to preserve coaxiality between the principal strains and stresses, resulting in lower stiffness and load carrying capacity than the corresponding values registered experimentally [132, 133].

In fixed and multidirectional fixed smeared crack models the coordinate system remains fixed throughout the analysis process, where in the latter approach multiple cracks with independent fixed coordinate systems at different fracture stages may originate in the same integration point. While in the rotating SCM the crack shear stress transfer is not defined by the user, being imposed by the formulation in order to assure coaxiality of principal strains and stresses, in the fixed and multidirectional fixed SCMs another user-dependent information is required, namely the process of modelling the crack shear stress transfer, which introduces additional difficulties of high relevance in structures failing in shear [134].

In the context of the SCM approach, the mode I fracture behaviour of FRC is typically simulated using constitutive models based on exponential or multi-linear segment softening diagrams governed by input parameters that are usually determined by conducting inverse analysis (IA) of experimental results of three-point notched beam bending tests (3PNBBT) or round panel tests supported on three points (RPT-3PS) [135–137]. On the other hand, the shear behaviour is often accounted by means of a shear retention factor, which is frequently assumed constant or dependent on other entities involved in the fracture process [127, 138, 139], or alternatively by means of a shear softening diagram [140, 141] where the parameters are, in general, difficult to estimate with confidence.

In the SCM approach, cracks are conceptualized as a series of parallel cracks distributed along a predetermined portion of material. In this way, the effect of an initiating crack at an integration point translates into a degradation of the current stiffness and strength at that integration point, by means of a tensile-softening relation [125]. Thus, this kind of models do not implicate the need for mesh topology alteration, nor inherent restrictions to crack orientation exist [115].

SCMs can be further classified into rotating smeared crack model (RSCM) and fixed smeared crack model (FSCM). When the specified criterion, e.g. the maximum principal stress,  $\sigma_I$ , reaches the tensile strength,  $f_{ct}$ , a crack is formed, normal to direction of  $\sigma_I$ , and distributed in the representative area (or

volume in case of solid finite elements) of the integration point, with local  $s$ - $n$  axes. The  $n$  axis is oriented in the normal direction to the crack plane, and the  $s$  axis aligned in the tangential direction to the crack plane. In fixed crack models, the local coordinate system allocated to the crack remains the same during the entire analysis, contrary to rotating crack models where the local coordinate systems varies in accordance with the direction of the principal tensile stress [142].

Since the direction of the principal tensile stress may vary during loading, due to the mechanisms involved in the fracture process (i.e. aggregate interlock and dowel action of the reinforcement) another approach was proposed, the multi-fixed smeared crack model (MFSCM). In this case, the formation of multiple smeared cracks at the same integration point is possible, depending on the crack initiation criterion, i.e. the angle of the new direction of  $\sigma_I$ , relatively to the already existing cracks (the direction of each one defined by the orthogonal to its plane) crack normal is greater than a predefined threshold angle and  $\sigma_I$  attains the tensile strength at less than an assumed tolerance [129, 143].

In the first SCMs [144, 145], normal and shear stiffness of concrete across the crack were set to zero, disregarding the effect of Poisson's coefficient [125]. However, due to the sudden drop of stiffness, convergence issues along with distorted crack patterns arose [146]. In an attempt to solve this issues, the concept of shear retention factor,  $\beta$ , was introduced along with the normal stiffness reduction factor,  $\mu$ . The former represents the shear resistance originated by the mechanisms that arise during the cracking process [147, 148], whereas the latter characterises the degradation of stiffness in normal direction to the crack plane.

The coefficients  $\beta$  and  $\mu$  can be seen as damage variables, that characterise the stiffness degradation of concrete in both tangential and normal directions to the crack plane. Thus, the material behaviour may be simulated by means of distinct damage evolution laws. The shear sliding process is usually tackled either by using a constant shear retention factor [146] or by adopting a local strain-softening law [140, 141].

Plasticity theory has also been widely used for modelling concrete behaviour, especially under compressive stress states [143]. Originally, Borst and Nauta [129] introduced the concepts of plasticity theory in a multi-fixed non-orthogonal crack model, by separating the elastic and plastic strain fields allowing for the simulation of the elasto-plastic behaviour of concrete between cracks [115]. More recently, other authors have also applied the concepts of plasticity theory to model concrete behaviour under multiaxial stress states [149–152].

These models are based on yield functions that characterize the concrete behaviour under compression, tension or compression and tension. However, this approaches fail to characterise the experimentally observed micro-scale damage process due to crack initiation and propagation. Consequently, several authors proposed continuum damage approach (CDA) in an attempt to accurately simulate the loss of strength and stiffness of concrete [153–156].

Nonetheless, these models are not capable of addressing irreversible deformations and the inelastic volume expansion of concrete in compression [157]. In an attempt to further improve the existing approaches, several authors proposed a combination of plasticity theory with CDA models, the so-called

*plastic-damage models* [158–162]. In this way, the strength and stiffness degradation and occurrence of irreversible deformations can be taken into consideration allowing for improved predictability of the nonlinear behaviour of concrete.

### 2.6.2.2 Discrete and hybrid crack approaches

#### Discrete crack models

The DCM is based on the fact the crack itself is modelled as a geometric discontinuity in the finite element mesh. Originally, cracks were modelled by means of the separation between element edges [163, 164]. Thus, as the nodal force, at the node in the vicinity of the crack tip, attained the tensile strength, the node was split into two nodes and subsequently letting the crack progress to the next node. Figure 29 presents a schematic representation of the aforementioned process.

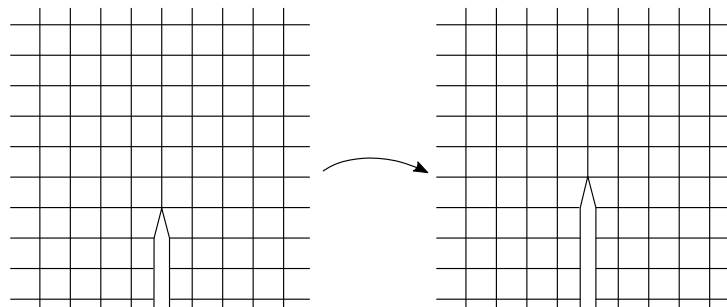


Figure 29: Propagation of crack in early discrete crack model [125].

Such an approach possesses several disadvantages. Firstly, the introduction of additional nodes to simulate crack propagation, changes nodal connectivity requiring the recalculation of the global stiffness matrix. Furthermore, the crack is constrained to a predetermined path, since it is forced to propagate along element edges, which is not known in the majority of structural analysis. In order to overcome these drawbacks, Ingraffea and Saouma [165] developed automatic remeshing procedures with the intent to adapt the finite element mesh topology to the crack progression. However, the complexity of such algorithms and inherent high computational time constrain the use of such techniques to situations where a small number of predominant cracks arise.

Alternatively the kinematics of the material separation can be simulated by directly embedding discontinuities in the finite elements eliminating the need for remeshing techniques [166, 167] and allowing arbitrary crack propagation. The appearance of such techniques gave rise to two main formulations, weak embedded discontinuities (WED) [168, 169] and strong embedded discontinuities (SED) [170–176] where the main difference resides in the fact that in the first approach the discontinuities are simulated through the use of softening bands, whereas in the strong discontinuities approach the displacement field becomes truly discontinuous. Another popular formulation within the DCM approach is the nodal enrichment of the conventional finite elements by introducing additional degrees of freedom over the ordinary mesh nodes, allowing the modelling of continuous jumps over the elements boundaries. This approach is

known in the literature as the extended finite element method (XFEM), generalised finite element method (GFEM) [177] or partition of unity method (PUM) [178, 179].

The main advantages of these methods over the SCMs is the higher accuracy in predicting crack width and spacing and the fact that the stress distribution in the vicinity of crack area is more realistically captured [133].

#### Hybrid crack models

In hybrid approaches, both smeared and discrete methodologies are combined, so that the initial micro-cracking phase is simulated by means of a smeared crack approach. When the material has reached a highly damage state, where the effect of material separation becomes more relevant, a transition to a discrete crack model approach is made. Thus, the transition threshold between these formulations is a key aspect for which a reliable solutions is still a challenging task in the computational mechanics domain [180].

## **2.7 Determining the fracture parameters of FRC**

The post-cracking behaviour of FRC can be characterised by means of the tensile versus crack width relationship (henceforth referred to as  $\sigma_n^{cr}$ - $w_n^{cr}$  relationship). It is well known that the direct tensile test (DTT) is the most adequate experimental procedure for estimating the post-cracking tensile relationship of FRC, however, this test requires very specialised equipment, is complex and costly to execute [181]. Alternatively, the fracture mode I parameters can be derived by IA by considering the experimental results of simpler test configurations such as 3PNBBT [182] or RPT-3PS [183].

To successfully conduct IA, the experimental procedure is simulated by FE analysis or analytical approaches, and the numerical response is fitted to the experimental curve with the minimum error as possible. In this regard, the two curves are approximated by modifying the fracture parameters used in the FE or analytical model until the difference between the curves is below a given tolerance.

In the past decades, many researchers attempted to perfect and develop IA approaches, however a consensual methodology has not yet been established in the literature. The work of Nanakorn and Horii [184] was pioneer in the development of a methodology to derive the  $\sigma_n^{cr}$ - $w_n^{cr}$  relationship of FRC using the experimental force-deflection curve obtained from 3PNBBT. In this study, the  $\sigma_n^{cr}$ - $w_n^{cr}$  relationship consists of a piecewise-linear diagram, and each new point is obtained in a sequential manner. The methodology employs a FE model using the “cracked element” formulation to simulate the numerical force-deflection curve. Hence, for a given deflection increment, the tangential slope of the subsequent linear branch of the  $\sigma_n^{cr}$ - $w_n^{cr}$  relationship is determined in such a way that the slope of the load/deflection increment equals the value from the experimental response.

Almost at the same time, Kitsutaka [185] proposed a similar approach consisting of a stepwise IA procedure, where each point in the post-cracking relationship is determined based on the error between the numerical and experimental curve. In this work, the author also used a FE approach to simulate the

numerical response. Other authors such as Montaignac et al. [186] adopted the same stepwise strategy to derive the  $\sigma_n^{cr} - w_n^{cr}$  relationship of SFRC. However, instead of using a FE model to simulate the response, these authors used analytical models to predict the behaviour of 3PNBBT and RPT-3PS. Nour et al. [187] have also proposed an IA procedure based on a “window-by-window” strategy in which the experimental curve is subdivided in three main regions, and the numerical response is fitted to the experimental results in each region of the curve. In this way, each point fitted to the experimental response allows the determination of a point in the  $\sigma_n^{cr} - w_n^{cr}$  relationship. Recently, Vorel and Kabele [188] developed a stepwise IA methodology based on the work of Nanakorn and Horii [184], however, in this study the sequentially linear analysis approach is used to derive the post-cracking relationship, instead of the nonlinear FE approach, and contrary to Nanakorn and Horii, the authors use zero-thickness cohesive interface elements in the FE model to simulate the crack propagation. This technique was also used in the work of Czernuschka et al. [189]. The main drawback of stepwise approaches are related to the possible accumulation of errors in the derived  $\sigma_n^{cr} - w_n^{cr}$  diagram, since a new point is determined adopting a configuration of the  $\sigma_n^{cr} - w_n^{cr}$  up to the previous point that is predicting the experimental results with a certain error.

Hence, several authors attempted approaches considering pre-defined multi-linear post-cracking tensile diagrams. In the work of Oliveira e Sousa and Gettu [190] a global fitting approach is adopted for the determination of the governing parameters of the post-cracking tensile relationship. In this case, the numerical response is simulated by means of the cracked hinge model proposed by Ulfkjær et al. [117] and later enhanced by Pedersen [191] and Stang and Olesen [192, 193]. A brief overview on the most popular hinge models is provided in Section 2.6.1.1. Also, four  $\sigma_n^{cr} - w_n^{cr}$  diagrams can be selected by the user, namely the Hordijk model, a sloped-constant diagram, a bilinear and trilinear diagram. The IA process makes use of a weighting function in order to assign higher importance to different regions of the experimental curve. However, the use of a weighting function introduces an additional layer of complexity that may hinder the robustness of the process. Another restriction is related to limited number of branches of the trilinear diagram that might prove insufficient for more complex force-deflection responses.

Salehian et al. [194] also developed an IA procedure where a multi-linear  $\sigma_n^{cr} - w_n^{cr}$  relationship is defined a-priori and the parameters defining this relationship are adjusted until an acceptable tolerance between the numerical and experimental force-deflection curves is achieved. These authors proposed analytical approaches to derive the force-deflection response of 3PNBBT and RPT-3PS based on a numerical model for deriving the moment-curvature response of the cross section of a SFRC member subjected to bending and axial forces [195]. Mazaheripour [196] used a 2D FE model combined with a “crack range windows” IA approach to obtain the post-cracking behaviour of high performance fibre reinforced concrete (HPFRC). In this work, an optimisation strategy based on three “range windows” is adopted in which the experimental response is divided in three CMOD ranges (0 to 0.2 mm, 0.2 to 1 mm and 1 to 5 mm, respectively). For this purpose, a multi-linear diagram is initially defined and in each range the slope of the linear branches is varied until a satisfactory (controlled by a tolerance) deviation between the numerical and experimental curves is obtained.

Lameiras [197] used a FE model and a simplified graphical IA methodology to estimate the post-cracking parameters based on 3PNBBT results. The IA approach used by this author is also based on a “window-by-window” approach, in which the post-cracking parameters of the tensile diagram are modified in a sequential manner. Alberti et al. [198] also successfully conducted IA using FE models, based on the cohesive crack fracture concept instead of the SCM approach, and trilinear softening diagrams to characterise FRC with polyolefin fibres.

More recently, Jepsen et al. [135, 199] proposed an IA methodology based on a global fitting procedure, relying on an analytical nonlinear hinge model to simulate the 3PNBBT response, in which an initial bilinear  $\sigma_n^{cr}-w_n^{cr}$  is assumed and additional points are inserted sequentially in the relationship based on the error curve computed between the numerical and experimental response. However, this author uses an even discretisation of the experimental curve, which might require a high number of points, if the maximum measured CMOD is relatively high, in order to obtain a good resolution of the main regions of the curve. Stephen et al. [136] explored a similar concept of global optimisation, and nonlinear hinge model, in combination with weighting functions for assigning different importance to the regions of the experimental curves.

## **2.8 Summary and Conclusions**

In this Chapter an overview on the fundamental concepts that govern the fracture behaviour of FRC was presented. The behaviour of FRC depends heavily on the fibre and concrete properties and the advantages of using fibres as reinforcing are now well established in literature. The addition of fibres has a major effect in brittleness and crack width control due to the resisting mechanisms that arise upon crack formation leading to smaller crack widths, higher load-carrying capacity, ductility and energy absorption capability of FRC structures.

The pullout resisting mechanism of steel fibres is governed by two key components, the bond between the fibres and the matrix and the mechanical anchorage of hook when hooked-end fibres are used. Hooked-end fibres exhibit a higher pullout load capacity and energy absorption during the pullout due to the different mechanisms that need to be exhausted after the fibre-matrix bond has been broken (hook deformation and pullout). One effective strategy to improve that bond capacity is to introduce deformations along the fibres and/or increase the bond length.

Another key aspect in the tensile capacity of FRC is fibre orientation and distribution within the matrix. The distribution and orientation of the fibres rarely present an optimal arrangement and efficiency in all directions affecting the individual contribution of each fibre to the overall desired post-cracking behaviour. Several factors can affect fibre effectiveness namely, fibre length, wall-effects, specimen size, casting direction, compaction method, mixture composition and rheological properties and existence of rebars or other obstacles. The effectiveness of the fibres can be taken into consideration in the design of FRC by means of the fibre orientation factor which consists in multiplying the overall fibre contribution to the



tensile of FRC by a factor ranging between 0 and 1.

Depending the fibre type and dosage different tensile behaviours can be obtained, namely, strain softening or strain hardening behaviour. In the first case, when the tensile capacity of the composite is attained, dominant cracks are formed and a soft decay in the tensile behaviour is observed. On the other hand, in a strain hardening behaviour, after the tensile strength is reached, several micro-cracks are formed throughout the specimen with a corresponding increase in load bearing capacity until dominant cracks take over the crack propagation mechanism and a softening behaviour occurs.

FRC technology has a wide range of applications in the construction industry namely, buildings, bridges, tunnels etc. One potential application of such technology is the railway sector due to its extension and economic impact. In fact, small improvements in the maintenance and/or service life of such infrastructures likely result in significant long term effects in terms of cost, labour and economic performance. Several studies involving the use of FRC in railway sleepers and slab track systems have shown an increase in structural capacity, increase in impact and fatigue performance and improvements in service life due to lower cracking and deformation. Nonetheless, the lack of design guidelines and tools that facilitate the use of FRC still hinders the application of FRC. Hence, the development of numerical tools to aid the dissemination and normalisation of FRC technology is a crucial factor to the future of the construction sector.

The most popular finite element method (FEM) approaches to simulate the fracture process of concrete may be grouped in two main categories: DCMs and SCMs. The DCM approach aims at the simulation of initiation and propagation of dominant cracks by introducing a geometric entity in the finite element mesh representing the actual crack. On the contrary, in the SCM approach the individual cracks are not actually numerically resolved, but instead smeared out in the material volume associated with the integration point. Thus, the deterioration process of concrete is captured by means of a constitutive relationship. During the past years, other approaches such as hybrid models have also been proposed. These models make use of both concepts inherent to the discrete and smeared approaches applying them in a simultaneous fashion.

The fracture parameters of FRC can be determined by means of DTTs or IA. The first approach is costly and complex to execute, and therefore IA is typically the go-to approach for deriving the fracture mode I properties of FRC. Throughout the past years several methodologies were proposed to conduct IA, some based on point-by-point strategies and other based on a global approaches. In point-by-point methodologies no *a-priori* knowledge of the stress-crack width relation is required and the relationship is determined iteratively where each point is determined based on the previous ones. On the contrary, in global approaches the stress-crack width relationship is initially defined and its governing parameters modified until the numerical response is sufficiently close to the experimental response.

# Modelling and Simulation of FRC Elements

# 3

## 3.1 Introduction

*The present chapter is comprised of two main parts, the first provides an overview on the simulation of fibre reinforced concrete (FRC) elements using the multi-fixed smeared crack model (MFSCM) approach, and in the second part a generalised methodology to compute the crack band width (CBW) parameter is detailed and implemented in the FEMIX V4.0 computer code. Hence, in the first part, a set of numerical case studies of FRC elements failing in bending and shear are presented, and a parametric study involving the fracture mode I/II parameters is performed by analysing their impact on the results at the structural level. One of the key parameters of the smeared crack model (SCM) approach is the CBW. This parameter allows the results to be mesh independent by assuring adequate fracture energy consumption depending on the size of the finite elements (FEs). In the second part of the chapter, a generalised approach to compute the CBW is presented and its implementation in the FEMIX V4.0 computer code detailed. The referred approach is analysed by means of a numerical case study where distinct mesh configurations are used to investigate the impact of the CBW in the overall results and crack pattern configurations.*

## 3.2 Modelling the cracked behaviour of FRC elements

During the past decades, several models have been proposed to simulate cementitious based materials. Consequently, several finite element approaches were developed to simulate the nonlinear behaviour of concrete structures exhibiting quasi-brittle failure modes that attempt to accurately predict crack initiation and propagation.

The most popular approaches to simulate the fracture process of concrete may be grouped in two main categories:



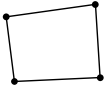
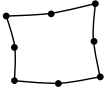

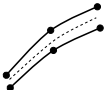
- Discrete Crack Models (DCM)
- Smeared Crack Models (SCM)

The discrete crack model (DCM) approach aims at the simulation of the initiation and propagation of dominant cracks, by introducing a geometric entity in the finite element mesh representing the actual crack. In this approach the crack is modelled as a geometric entity introducing an actual discontinuity in the displacements field. However, this approach is not the nature of the displacements method, since this method is based upon the continuity of the medium.

On the contrary, in the SCM approach, the individual cracks are not physically modelled, but instead, they are smeared out over some tributary area/volume of material associated with the integration point, the so-called characteristic length or crack band width (CBW). Thus, the deterioration process of the concrete is captured by means of a constitutive relationship [125] instead of a an actual discontinuity in the material. This approach is very convenient from an implementation standpoint and is able to capture with good accuracy the main relevant structural behavioural aspects, mainly for ultimate limit state conditions, as long as the constitutive models simulate adequately the behaviour of the intervenient materials.

Throughout the present study several numerical simulations are conducted using the FEMIX V4.0 [200] computer code, adopting for each case specific element types and constitutive models for modelling the structures in the most suitable manner. In addition, the MFSCM approach is used in all conducted simulations. Hence, the FE types and constitutive models available in FEMIX V4.0 and used in this study are briefly described in this section, however, for a more detailed description the reader is referred to the works of Barros [115], Ventura-Gouveia [141], and Sena-Cruz [201]. The FE types used in the context of the present work are the following: i) 2D plane stress elements (mainly for simulating concrete elements), ii) 2D embedded cable elements (conventional steel reinforcement) and iii) 2D line interface elements (model the bond behaviour between the reinforcing steel and the surrounding matrix). The aforementioned element types are schematically depicted in Table 4.

Table 4: Types of finite elements used in the simulations conducted throughout this study [143].

Use case	Description	Representation
Embedded cable (2D)	Linear 2-nodes	
	Quadratic 3-nodes	
Plane stress (2D)	Lagrangian 4-nodes	
	Serendipity 8-nodes	
Line interface (2D)	Linear 4-nodes	
	Quadratic 6-nodes	

For simulating the nonlinear material behaviour of FRC, different constitutive models are used to account for the contribution of the resisting mechanisms that govern the tensile and shear behaviour. Hence, to simulate the damage induced by the crack opening and propagation, the tensile softening trilinear/quadrilinear diagrams depicted in Figure 30 are used. As shown in this figure, the diagrams are defined by the parameters  $\alpha_i$  and  $\xi_i$  that are used to define each branch of the constitutive relationship.

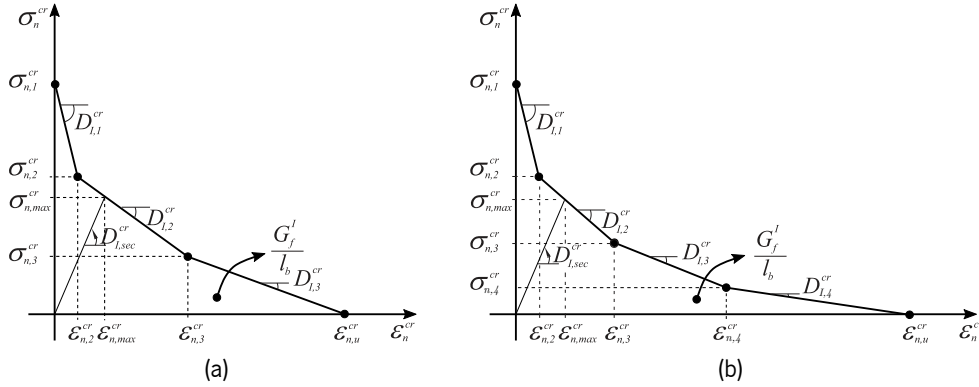


Figure 30: Constitutive relationships used in the scope of the present work: (a) trilinear and (b) quadrilinear diagrams used for simulating mode I ( $\sigma_{n,1}^{cr} = f_{ct}$ ,  $\sigma_{n,2}^{cr} = \alpha_1 \sigma_{n,1}^{cr}$ ,  $\sigma_{n,3}^{cr} = \alpha_2 \sigma_{n,2}^{cr}$ ,  $\sigma_{n,4}^{cr} = \alpha_3 \sigma_{n,3}^{cr}$ ,  $\epsilon_{n,2}^{cr} = \xi_1 \epsilon_{n,u}^{cr}$ ,  $\epsilon_{n,3}^{cr} = \xi_2 \epsilon_{n,u}^{cr}$ ,  $\epsilon_{n,4}^{cr} = \xi_3 \epsilon_{n,u}^{cr}$ ) [115, 201].

The degradation of the shear transferring capacity is simulated by means of the shear-softening diagram proposed by Ventura-Gouveia [141] and depicted in Figure 31. The diagram is constituted by one ascending linear branch up to the maximum shear stress ( $\tau_{t,p}^{cr}$ ) followed by a softening branch. The slope of the ascending branch depends on the shear retention factor ( $\beta$ ), and the slope of softening branch depends on the mode II fracture energy parameter ( $G_{f,s}$ ).

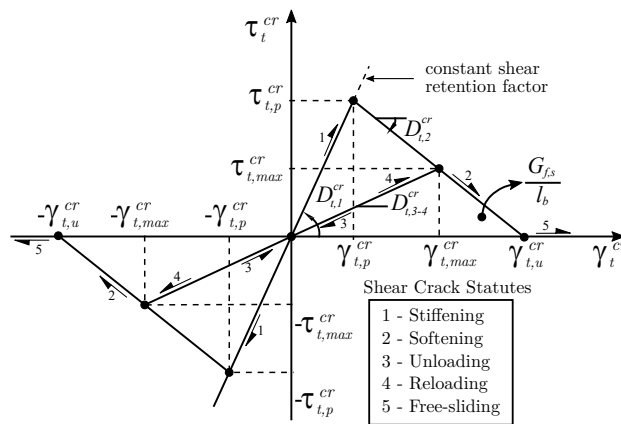


Figure 31: Shear softening constitutive relationship to simulate the shear stress transferring capacity degradation [141].

For modelling the contribution of the conventional steel reinforcement, the constitutive relationship shown in Figure 32a is used. The diagram is comprised by four branches, defined by the points PT1, PT2 and PT3 and the parameter  $p$  that governs the shape of the third branch. In addition, a bond-slip

constitutive diagram is also used to simulate the bond behaviour between the reinforcing bars and the surrounding matrix by means of interface elements. For this purpose the diagram shown in Figure 32b is used, where the parameters  $\beta_1$  and  $\beta_2$  govern the shape of the nonlinear pre-peak and post-peak branches and  $\tau_0$ - $\delta_0$  and  $\tau_m$ - $\delta_m$  the points that define the end of the linear branch and the maximum bond strength, respectively.

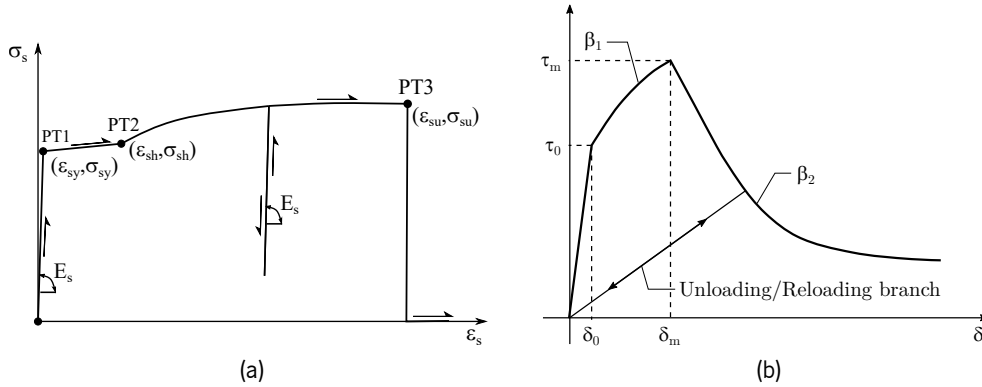


Figure 32: Constitutive relationships used in the scope of the present work: (a) multi-linear branch diagram for modelling the conventional steel reinforcement [201] and (b) bond-slip relationship for modelling the bond between FEs.

In cases where failure is governed by significant concrete inelastic compressive behaviour, the plastic-damage multidirectional smeared crack (PDSC) model available in FEMIX V4.0. The referred constitutive model is based on the combination of plasticity and damage theories by coupling the hardening law depicted in Figure 33a and the damage evolution function shown in Figure 33b that leads to the constitutive relationship presented in Figure 33c. The parameters  $G_{f,c}$  and  $l_c$  represent the fracture energy and characteristic length in compression, respectively, in which  $l_c$  is assumed equal to  $l_b$  in tension.

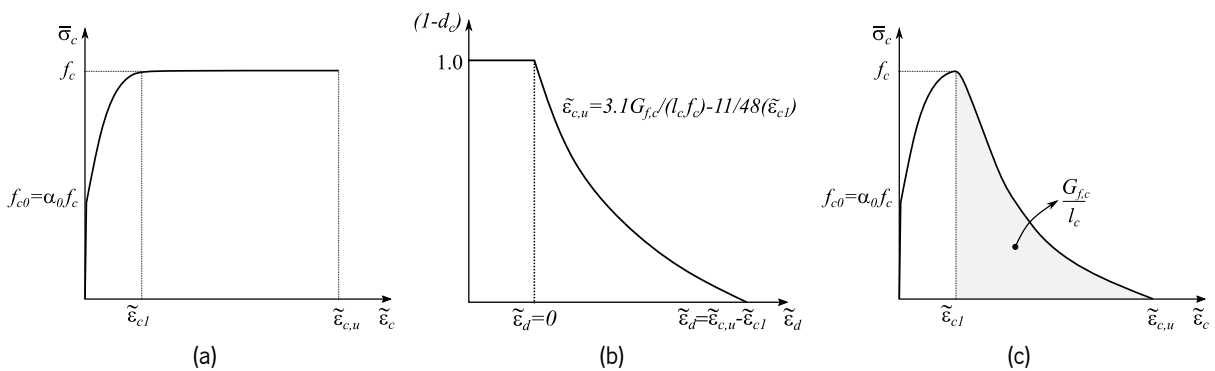


Figure 33: Relationships for modelling the compressive behaviour according to the PDSC: (a) plasticity model, (b) damage model and (c) constitutive relationship of the compressive behaviour [202].

### 3.3 Numerical simulations using the MFSCM approach

#### 3.3.1 Three-Point Notched Beam Bending Test (3PNBBT)

In this section the simulation of a three-point notched beam bending tests (3PNBBT) using the MFSCM approach available in FEMIX V4.0 is conducted and the influence of the parameters used to define the fracture mode I constitutive model is analysed and discussed. The material properties as well as the experimental results used in the present section were kindly provided by Portuguese Civil Engineering company CiviTest.

The configuration of the experimental setup is defined as per the recommendations of Model Code 2020 [203]. The geometry of the specimens is 550x150x150 mm, which was simulated by means of 4 node plane stress FEs, considering a 2x2 Gauss-Legendre (G-L) integration scheme except for the elements directly above the notch which were assigned a 2x1 G-L scheme limiting the propagation of cracks along the symmetry axis as typically observed in experimental tests. The numerical simulations were performed using the Newton-Raphson (N-R) method and by controlling the relative horizontal displacement between the nodes at the notch extremity. The adopted mesh, loading and support conditions are presented in Figure 34.

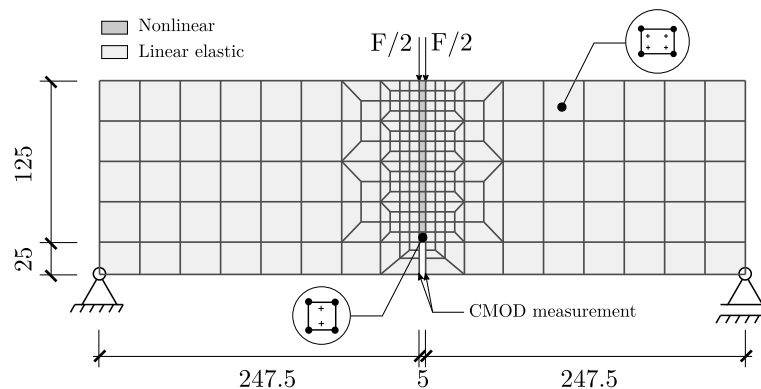


Figure 34: Geometry, mesh, loading and support conditions of the 3PNBBT numerical model (all dimensions in mm).

The FEs above the notch were assigned a nonlinear material behaviour, by adopting the quadrilinear constitutive model presented in Figure 30b, while the remaining elements were attributed a linear elastic behaviour. To analyse the impact of the parameters that govern the fracture mode I namely, the concrete tensile strength ( $f_{ct}$ ), fracture energy ( $G_{fI}$ ), and shape of the constitutive diagram, different values were adopted for the referred parameters and the results in terms of structural response (Force - crack mouth opening displacement (CMOD)) compared. The material properties adopted for defining the aforementioned parameters and the remaining material properties are listed in Table 5.

Hence, considering the parameters listed in Table 5, several simulations were conducted to analyse: i) the effect of varying the concrete tensile strength, ii) the effect of varying the mode I fracture energy and iii) the impact of the shape of the quadrilinear constitutive model (see Figure 30b).

Table 5: Material properties and parameters used to define the concrete constitutive model in the 3PNBBT simulations.

Property	Value
Poisson's ratio ( $\nu$ )	0.20
Young's modulus ( $E_c$ )	29430 N/mm <sup>2</sup>
Compressive strength ( $f_c$ )	55.7 N/mm <sup>2</sup>
Tensile strength ( $f_{ct}$ )	2.76 N/mm <sup>2</sup> ; 3.94 N/mm <sup>2</sup> ; 5.13 N/mm <sup>2</sup>
Crack band width	$\sqrt{A_{FE}}$ *
Threshold angle	30°
Maximum number of cracks per integration point	2
Quadrilinear diagram I	$\xi_1 = 0.01; \alpha_1 = 0.50;$ $\xi_2 = 0.10; \alpha_2 = 0.40;$ $\xi_3 = 0.30; \alpha_3 = 0.20;$
Quadrilinear diagram II	$\xi_1 = 0.01; \alpha_1 = 0.80;$ $\xi_2 = 0.05; \alpha_2 = 1.20;$ $\xi_3 = 0.20; \alpha_3 = 0.30;$
Quadrilinear diagram III	$\xi_1 = 0.01; \alpha_1 = 0.95;$ $\xi_2 = 0.05; \alpha_2 = 0.90;$ $\xi_3 = 0.20; \alpha_3 = 0.70;$
Fracture energy ( $G_{fI}$ )	3.50 N/mm; 6.00 N/mm; 8.00 N/mm;
Parameter defining the mode I fracture energy available to the new crack	2

\* Square root of the area of the finite element;

The results of the simulations considering several parameter scenarios are presented in the plots of Figures 35b to 35d, regarding the effect of varying  $f_{ct}$ ,  $G_{fI}$ , and shape of the quadrilinear diagram, respectively. In Figure 35a the quadrilinear diagrams presented in Table 5 are also plotted to facilitate the analysis of the results.

Regarding the effect of varying the tensile strength, the results presented in Figure 35b show that this parameter has a significant impact in the maximum load attained at the structural level, as expected, with a deviation of  $\approx 25\%$  from the average curve for a corresponding decrement/increment of 30% in the  $f_{ct}$  value. It is also noteworthy the fact that higher  $f_{ct}$  values lead to faster degradation of the post-peak response when compared to lower values. This is due to the fact that the  $G_{fI}$  is constant and higher  $f_{ct}$  values lead to a reduction of the ultimate tensile strain resulting in steeper drops in the branches that define the  $\sigma_n^{cr} - \varepsilon_n^{cr}$  diagram and consequently a faster load carrying capacity degradation.

In what concerns the fracture energy variation and the results shown in Figure 35c it is possible to observe that higher fracture energy values leads on one hand to slight increase in the peak load and on the other hand to an increased post-peak load carrying capacity with a much smoother decay in the force as CMOD increases. This behaviour was expected since the increase in  $G_{fI}$  leads to a greater ultimate

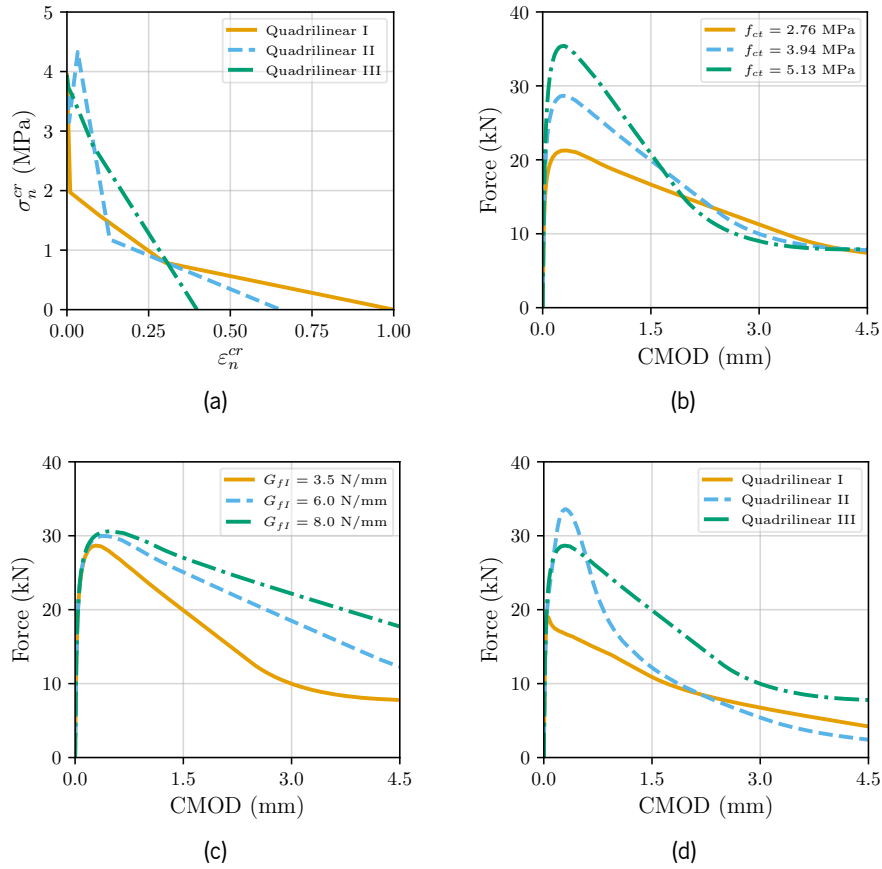


Figure 35: Results of the parametric study of the governing parameters of the fracture mode I: (a) quadrilinear diagrams defined according to the values specified in Table 5 (b) impact of varying the tensile strength ( $f_{ct}$ ), (c) effect of varying  $G_{f,I}$  and (d) effect of the shape of the quadrilinear diagram.

crack normal strain ( $\epsilon_{n,ult}^{cr}$ ) when compared to lower  $G_{f,I}$  values originating an increase in the load carrying capacity as shown in the results.

Regarding the effect of the configuration of the quadrilinear diagram (Figure 35d) the results show that the load carrying capacity and the overall trend of the structural response is directly associated with the configuration of the constitutive relationship. Considering the quadrilinear diagram I, shown in Figure 35a, and the corresponding result in Figure 35d, it is possible to observe that the maximum attained load is lower than the results obtained with diagrams II and III. This is explained by the fact that the first branch of the diagram is a steep drop in terms of tensile capacity, whilst diagram II exhibits a small reduction followed by an increase of the tensile capacity justifying the higher peak load. The results obtained using diagram III exhibit the greater load carrying capacity in the post-peak load phase when compared to the remaining diagrams, explained by the soft decay of the  $\sigma_n^{cr} - \epsilon_n^{cr}$  relationship.

As shown in the results of Figure 35 the fracture mode I parameters involved in the definition of the constitutive models used to simulate FRC have a significant impact in the overall results. Consequently, an accurate estimation of these parameters is of utmost importance to conduct a reliable analysis of the behaviour of FRC elements. To determine the post-cracking behaviour of FRC and consequently extract



the fracture parameters, two main approaches are used, namely direct tensile test (DTT) and inverse analysis (IA) approaches. The DTT approach is the most adequate procedure to directly determine the tensile behaviour of FRC, however, this approach is expensive and complex to execute. An alternative approach, which is typically the used one, is to derive the post-cracking behaviour indirectly through an IA procedure based on the experimental results of simpler and cheaper experimental tests configurations such as 3PNBBT. One possible approach to conduct IA is to perform a finite element analysis (FEA) of the experimental setup and iteratively approximate the numerical and experimental responses by modifying the fracture parameters that govern the numerical results until a satisfactory deviation is achieved.

Hence, the aforementioned IA approach was conducted by manually adjusting the  $f_{ct}$ , and the parameters of the quadrilinear diagram and  $G_{fI}$  until a reduced deviation between numerical and experimental response was obtained. The parameters obtained from this procedure are presented in Table 6 and the obtained results in terms of Force - CMOD are presented in Figure 36.

Table 6: Material properties and parameters used to define the concrete constitutive model in the 3PNBBT simulations after conducting IA.

Property	Value
Tensile strength ( $f_{ct}$ )	3.74 N/mm <sup>2</sup>
Quadrilinear diagram I	$\xi_1 = 0.000667$ ; $\alpha_1 = 0.59$ ; $\xi_2 = 0.023$ ; $\alpha_2 = 1.10$ ;
Fracture energy ( $G_{fI}$ )	$\xi_3 = 0.17$ ; $\alpha_3 = 0.50$ ; 19.5 N/mm;

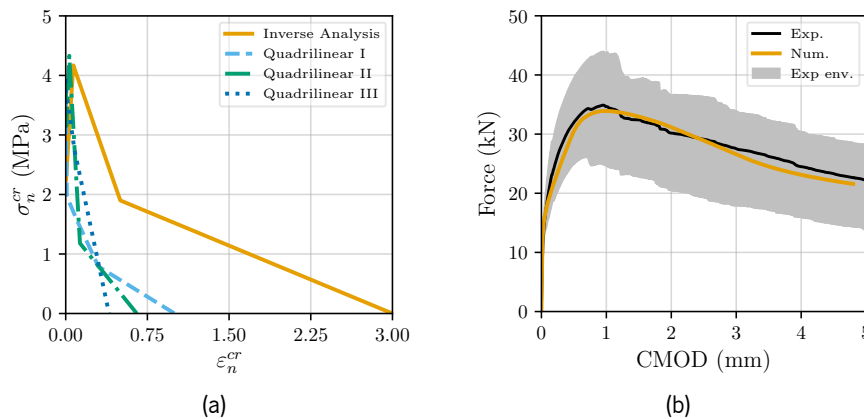


Figure 36: (a) Comparison between the previous quadrilinear diagrams and the relationship obtained after conducting IA and (b) corresponding numerical and experimental results comparison.

As shown in the results of Figure 36, the IA procedure was successfully conducted. However, the manual approach used in the context of this study is cumbersome, time consuming and operator dependent. Hence, the development of an automatic, robust, and fast tool for conducting IA is of utmost importance for a faster and more reliable finite element method (FEM) simulations of FRC elements.

### 3.3.2 FRC shear panels

In this section the MFSCM approach is used to simulate and analyse FRC elements failing in shear. For this purpose an steel-fibre reinforced concrete (SFRC) panel subjected to pure shear loading condition is simulated using the available constitutive models in FEMIX V4.0. In addition, the influence of the parameters that govern the shear softening diagram (see Figure 31), namely i) the slope of the ascending branch of the diagram controlled by  $\beta$ , ii) the maximum shear strength ( $\tau_{t,p}^{cr}$ ) and iii) the mode II fracture energy ( $G_{f,s}$ ), is investigated. Finally, the predictive capacity of the MFSCM is appraised by comparing the numerical results to experimental results available in the literature.

The numerical case study consists of the SFRC panels investigated by Susetyo et al. [204] in the context of an experimental campaign that aimed at analysing on one hand the importance of the concrete material properties in terms of shear strength capacity and on the other hand the influence of the fibre type and dosage in the structural response of the specimens. In terms of geometry, the specimens are 890 x 890 mm with a 70 mm thickness and reinforced with conventional reinforcement in one direction ( $\rho = 3.31\%$ ) as depicted in Figure 37a. The specimens are subjected to an in-plane pure-shear monotonic loading condition by means of vertical and horizontal actuators connected to steel keys embedded in the concrete as depicted in Figure 37b.

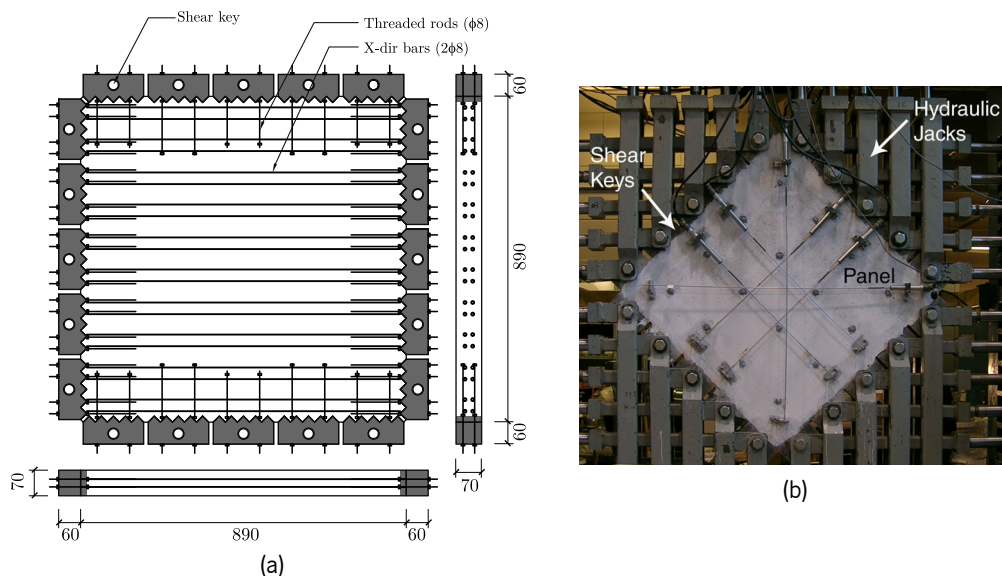


Figure 37: Schematic representation of the shear FRC panels tested by Susetyo et al. [204].

The numerical simulations were conducted using 8-node serendipity plane stress elements with a 3x3 G-L integration scheme to simulate the concrete and steel plates. For simulating the conventional steel reinforcement 3-node embedded cable elements with 3 G-L integration scheme were used considering a perfect bond behaviour with the surrounding matrix. The panel is supported in the vertical and horizontal direction in the lower left corner and in the vertical direction in the opposite lower right corner. The load is applied along the edges of the panel, in the centre of the steel plates, in order to replicate the pure shear

loading condition of the experimental test. Figure 38 shows the geometry, FE mesh, loading and support conditions adopted in the simulations.

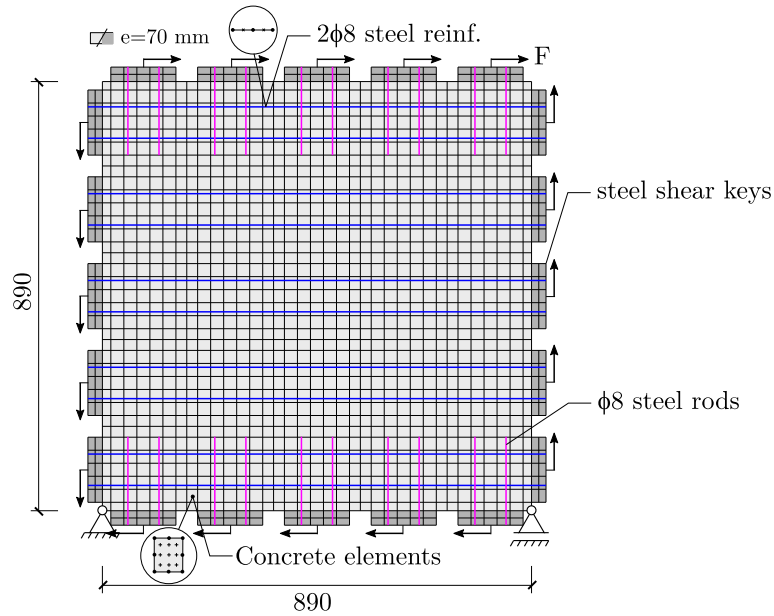


Figure 38: Geometry, FE mesh ( $\approx 27 \times 27$  mm), loading and support conditions of the numerical model. Dimensions in mm.

For simulating the material nonlinear behaviour of the panels the quadrilinear diagram for modelling the fracture mode I was adopted (see Figure 30b), and for simulating the behaviour in mode II, the linear shear softening relationship depicted in Figure 31 was used. The behaviour of the conventional steel reinforcement was defined by means of the constitutive relationship depicted in Figure 32a. The parameters used to define the referred relationship are listed in Table 7.

Table 7: Parameters used to define the steel reinforcement constitutive model.

$\phi$ (mm)	$A_s$ (mm <sup>2</sup> )	$\epsilon_{sy}$	$\sigma_{sy}$ (N/mm <sup>2</sup> )	$\epsilon_{sh}$	$\sigma_{sh}$ (N/mm <sup>2</sup> )	$\epsilon_{su}$	$\sigma_{su}$ (N/mm <sup>2</sup> )	$\rho$
8	50.27	2.457e-3	552	1.0e-2	552	0.1	647	1

The material properties and the parameters used to define the constitutive relationships are listed in Table 8. In addition, the values adopted for the parametric study regarding the governing parameters of the shear softening diagram are presented in this table.

Table 8: Material properties and parameters used to define the quadrilinear and shear softening diagrams in the shear panels simulations.

Property	Value
Poisson's ratio ( $\nu$ )	0.20
Young's modulus ( $E_c$ )	31243 N/mm <sup>2</sup>
Compressive strength ( $f_c$ )	53.4 N/mm <sup>2</sup>
Tensile strength ( $f_{ct}$ )	3.46 N/mm <sup>2</sup>
Crack band width	$\sqrt{A_{FE}}$ *
Threshold angle	30°
Maximum number of cracks per integration point	2
Parameter defining the mode I fracture energy available to the new crack	2
Quadrilinear tension-softening diagram (softening)	$\xi_1 = 0.0075; \alpha_1 = 0.75;$ $\xi_2 = 0.030; \alpha_2 = 0.80;$ $\xi_3 = 0.075; \alpha_3 = 0.80;$
Fracture energy ( $G_{f,I}$ )	12.0 N/mm
Shear softening diagram	
Shear stiffness ( $\beta$ )	$\beta = 0.10; \beta = 0.50^\dagger; \beta = 0.80$
Shear strength (MPa)	$\tau_{t,p}^{cr} = 1.0; \tau_{t,p}^{cr} = 2.75^\dagger; \tau_{t,p}^{cr} = 4.0$
Fracture energy $G_{f,s}$ (N/mm)	$G_{f,II} = 0.50; G_{f,II} = 1.5^\dagger; G_{f,II} = 2.5$

\* Square root of the area of the finite element;

† Base case scenario values;

The results of the numerical simulations considering i) the variation of the slope of the first branch ( $\beta$ ), ii) the effect of varying the mode II fracture energy ( $G_{f,s}$ ) and iii) the impact of varying the maximum shear strength ( $\tau_{t,p}^{cr}$ ) are presented in Figures 39a to 39c respectively.

Regarding the results shown in Figure 39a it is possible to observe that higher values of  $\beta$  leads to an increase in the shear capacity when compared to lower values. In addition, the load drop observed in the results occurs earlier for  $\beta = 0.8$  when compared to the remaining values. This is due to the fact that greater  $\beta$  values force the  $\tau_{t,p}^{cr}$  to be attained for lower shear strains (see Figure 31) and consequently the existing cracks enter the softening branch of the constitutive diagram at an earlier stage when compared to a lower  $\beta$  leading to a faster degradation of the shear transferring capacity.

As for the effect of varying  $G_{f,s}$  (Figure 39b), the results show that lower fracture energy values lead to a lower load carrying capacity due to earlier failure occurrence, when compared to higher fracture energy values as shown in Figure 39b. This is shown by the red curve (circle markers) where an earlier and sudden drop in the shear transferring capacity is observed when compared to the blue and teal curves which exhibit a much softer decay. This was expected since a higher fracture energy will increase the area under the softening branch of the shear softening diagram and consequently lead to on one hand a softer capacity decay and on the other hand higher ultimate shear strain values.

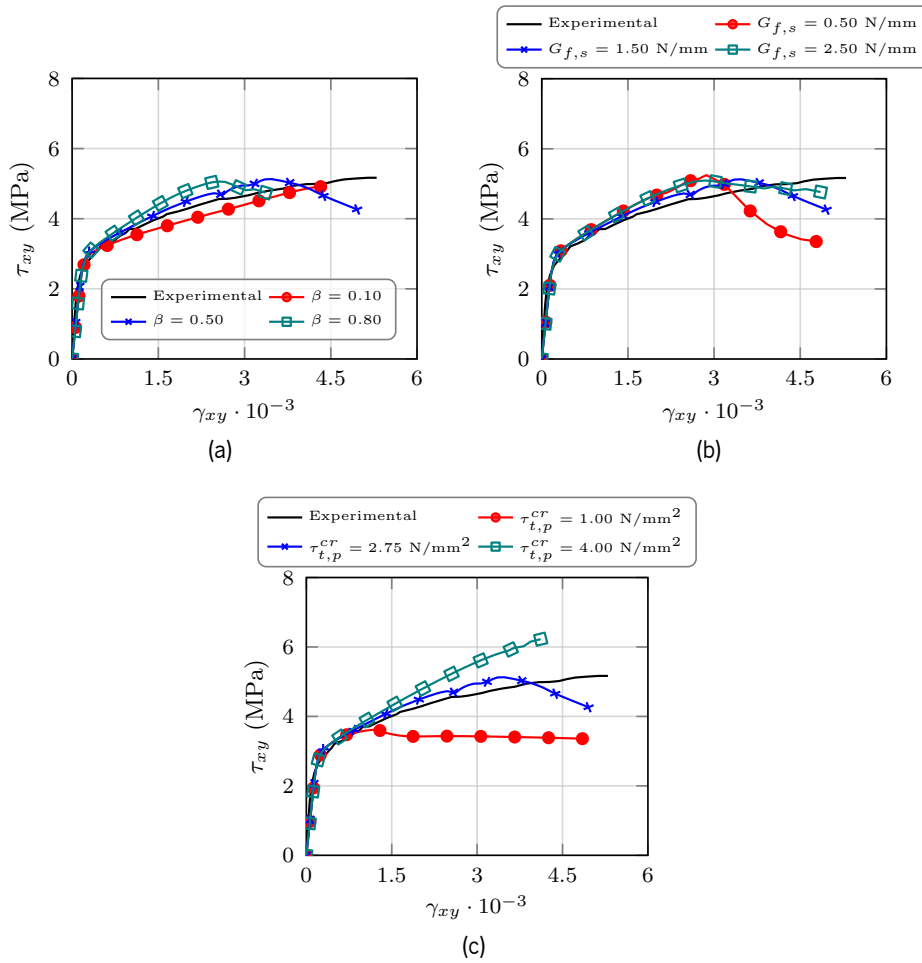


Figure 39: Effect of varying the mode II governing parameters: (a) slope of the initial shear branch ( $\beta$ ), (b) mode II fracture energy and (c) maximum shear strength.

The impact of maximum shear strength is shown in Figure 39c. The results show that the use of higher maximum shear stress values leads to a higher shear stress transferring capacity (teal curve) when compared to lower values (blue and red curves). These results are coherent with the behaviour defined at the material level since the increment in shear strength leads to a direct increment in shear capacity and additionally, to a later transition into the softening stage which also contributes to increased load transferring capacity.

Finally, in terms of predictive performance of the MFSCM it is possible to observe that the parameters that best capture the experimental response are the ones corresponding to the base case scenario, identified in Table 8 with the † symbol ( $\beta = 0.5$ ,  $G_{f,s} = 1.50$  N/mm,  $\tau_{t,p}^{cr} = 2.75$  N/mm<sup>2</sup>).

In Figure 40 a comparison between the experimental (Figure 40a) and numerical crack pattern (Figure 40b) is presented, respectively. These results correspond to the simulation that better approximated the experimental response (blue curve with cross markers). In these results it is possible to observe that the configuration of the major cracks is coherent with the observed pattern in the experimental tests.

Despite the good predictive capacity of the MFSCM approach both in terms of structural response

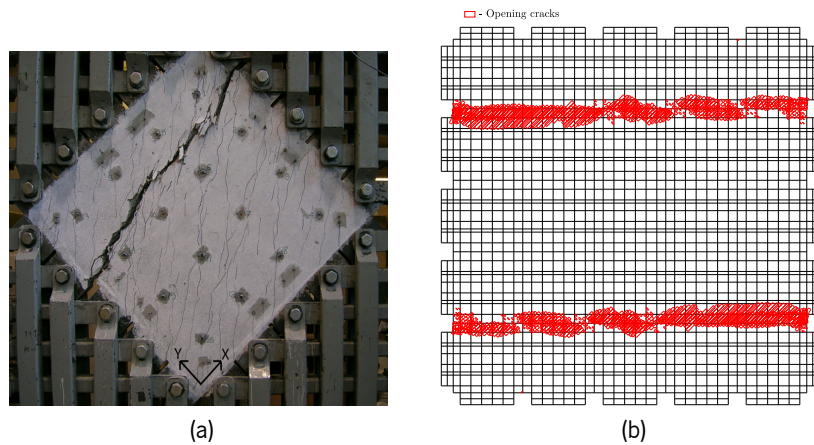


Figure 40: (a) Experimental and (b) numerical crack pattern comparison.

and crack pattern configuration, the considerable impact of the mode II parameters (Figure 39 on the structural response and consequently in the predictive capacity of the model, emphasize the importance of an accurate estimation of such parameters. Hence, the use of models that rely on physical-mechanical parameters can be an alternative to the herein presented approach.

### 3.3.3 FRC railway sleeper

FRC technology is now extensively used in a wide variety of structures. The higher load carrying capacity, formation of diffuse crack patterns with reduced crack widths and greater resilience when compared to conventional steel reinforced concrete, and the possibility to partially or even completely replace shear reinforcement are some of appealing aspects of using such technology. The railway sector is one of the fields that can greatly benefit from using such technology since the structural elements that comprise both ballasted and ballastless tracks are subjected to high impact loads and severe environmental conditions that might reduce its service life if major cracks are formed early on.

In this section, a numerical case study regarding the experimental investigation conducted by Yang et al. [100] is performed and the results analysed. In this experimental research, Yang et al. [100] investigated the potential use of ground granulated blast furnace slag (GGBFS) as a concrete binder and the use of steel fibres to replace conventional reinforcement in monoblock pre-stressed concrete sleepers. A schematic representation of the sleeper investigated by Yang et al. [100] is presented in Figure 41.

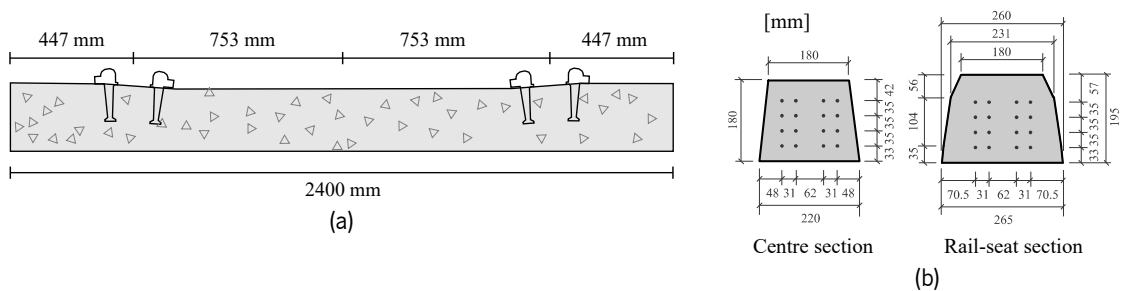


Figure 41: (a) Sleeper geometry and (b) cross-sectional details of the rail-seat/centre sections[100].

Yang et al. [100] conducted several experimental tests, including pullout tests of the rail fastening shoulder, static bending tests at the rail-seat and centre section of the sleeper as well as fatigue tests in order to assess the structural adequacy of the proposed SFRC sleepers. In the present case study both the static bending tests at both rail-seat (Figure 42a) and centre section Figure 42b of the sleeper are simulated.

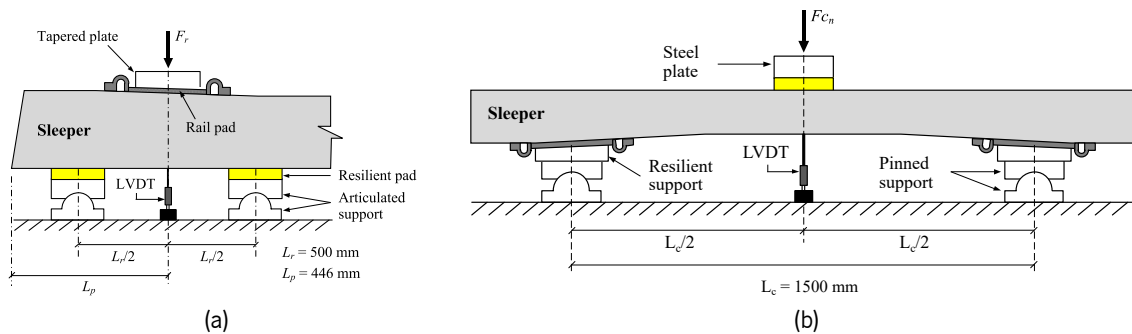


Figure 42: Schematic representation of the static bending tests setup: (a) rail-seat section and (b) centre section [100].

For conducting the numerical simulation, a FE model was developed for each setup configuration, static bending test at centre and rail-seat section. The concrete, loading and support plates were simulated using 8-node plane stress elements with a 2x2 G-L integration scheme. As for the prestressing strands, 3-node embedded cable elements with 2 G-L integration points were used, considering a perfect bond condition with the surrounding matrix. In addition, line interface elements, with a 2 Gauss-Lobatto (G-Lo) integration rule, were introduced between the support plates and the concrete sleeper allowing the relative displacement between these two elements avoiding stress concentration near the support plates during the prestress application. The prestress effect is introduced by means of a thermal load to induce the desired strain on the strands prior to load application. Figures 43a and 43b shows the geometry, FE mesh, loading and support conditions for the FE model for the centre and rail-seat setup configurations, respectively.

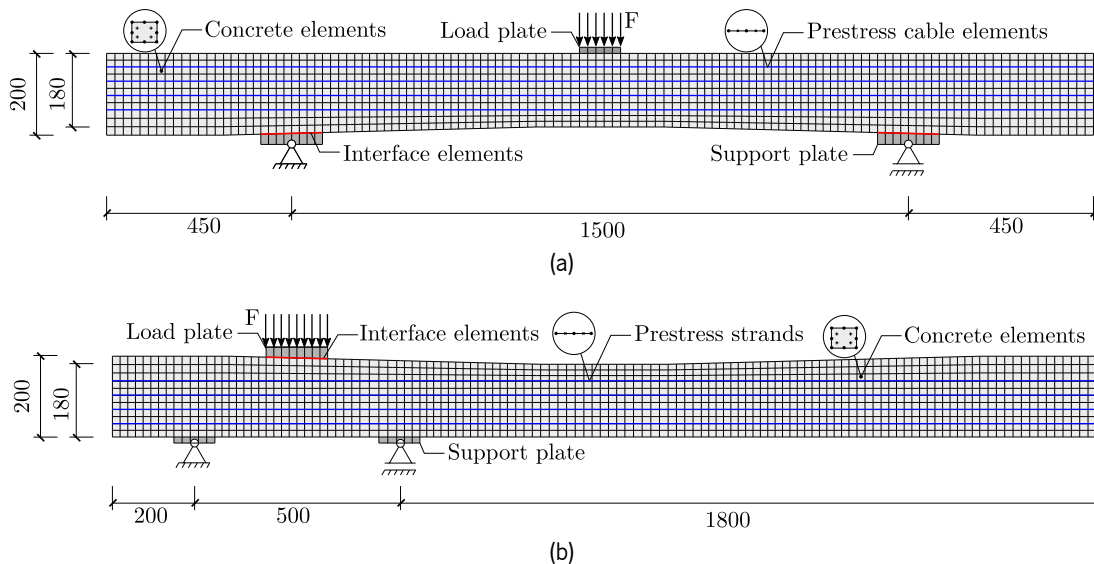


Figure 43: Geometry, loading, support conditions and FE mesh adopted in the simulation: (a) centre section and (b) rail-seat section (dimensions in mm)

For simulating the concrete behaviour a constitutive model capable of simulating the material non-linear behaviour in tension and compression was used due to the fact that in the experimental tests the majority of the specimens failed due to concrete crushing. The tensile behaviour was simulated by using the quadrilinear diagram shown in Figure 30b and the degradation of the shear transferring capacity was considered by using the shear softening diagram depicted in Figure 31. The parameters used to define the aforementioned diagrams are listed in Table 9. The constitutive model used for simulating the prestressing strands is defined by the relationship in Figure 32a and parameters used to define the diagram are presented in Table 10.



Table 9: Parameters used to define the concrete constitutive model.

Property	Value
Poisson's ratio ( $\nu$ )	0.20
Young's modulus (E)	31130 N/mm <sup>2</sup>
Compressive strength ( $f_c$ )	64.2 N/mm <sup>2</sup>
Quadrilinear tension-softening diagram	$f_{ct} = 2.5$ N/mm <sup>2</sup> ; $G_f^I = 3.25$ N/mm; $\xi_1 = 0.019$ ; $\alpha_1 = 0.52$ ; $\xi_2 = 0.130$ ; $\alpha_2 = 0.60$ ; $\xi_3 = 0.300$ ; $\alpha_3 = 0.30$ ;
Shear crack softening diagram	$\beta = 0.7$ ; $\tau_{t,p}^{cr} = 1.2$ N/mm <sup>2</sup> ; $G_f^{II} = 1.25$ N/mm;
Parameter defining the mode I fracture energy available to the new crack	2
Crack band width	$\sqrt{FE}$
Threshold angle	30°
Maximum number of cracks per integration point	2

Table 10: Parameters used to define the steel constitutive model for prestressing strands [100].

$\phi$ (mm)	As (mm <sup>2</sup> )	$\epsilon_{sy}$	$\sigma_{sy}$ (N/mm <sup>2</sup> )	$\epsilon_{sh}$	$\sigma_{sh}$ (N/mm <sup>2</sup> )	$\epsilon_{su}$	$\sigma_{su}$ (N/mm <sup>2</sup> )	p
25	1472.62	2.79e-3	557	2.2e-2	557	0.1	678	1

As mentioned previously, in order to eliminate the stress concentration around the support plates due to the prestress application, an interface element was introduced between the plates and the concrete elements allowing for relative sliding between these elements. Hence, for simulating the behaviour of the interface element a bond stress-slip constitutive law such as the one depicted in Figure 32b was defined by adopting the values presented in Table 11,

Table 11: Values adopted to define the bond-slip behaviour of the interface elements.

$\tau_0$ (N/mm <sup>2</sup> )	$\tau_m$ (N/mm <sup>2</sup> )	$\delta_0$ (mm)	$\delta_m$ (mm)	$\beta_1$	$\beta_2$	$K_n$ (N/mm)
15.50	18.89	0.878	1.439	0.4	0.4	$1.0 \times 10^4$

where  $\tau_0$  and  $\delta_0$  are the stress and slip at the end of the linear branch of the bond stress-slip relationship, respectively.  $\tau_m$  is the peak bond stress,  $\delta_m$  is the strain at the peak bond stress,  $\beta_1$  and  $\beta_2$  are coefficients that define the shape of curve in the pre-peak and post-peak phases, respectively.  $K_n$  is the normal stiffness of the interface element.

Figure 44 shows the comparison between the numerical and experimental results in terms of Force-Deflection at centre (Figure 44a) and rail-seat (Figure 44b) sections, respectively. Regarding the results at centre section (Figure 44a) it is possible to observe that a very good agreement between the numerical and average experimental response is obtained, with the numerical response capturing the degradation of the load carrying capacity both at the initial cracking stages ( $\approx 2$  mm) and at later stages around the peak

load and subsequent drop in load capacity due to concrete crushing. Similarly at the rail-seat section, the experimental response is well captured, both during the elasto-cracked phase ( $\approx 3$  to 5 mm) and at load peak and subsequent drop in load carrying capacity.

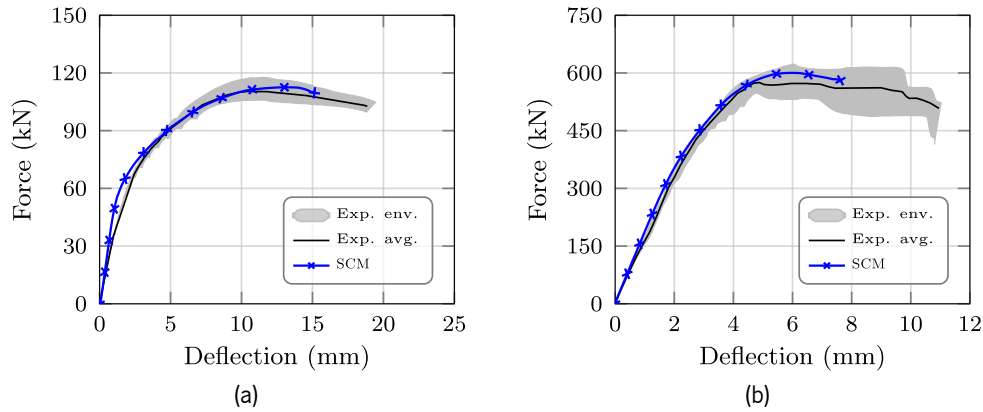


Figure 44: Comparison between numerical and experimental results at (a) centre section and (b) rail-seat section.

In Figure 45 the numerical and experimental crack patterns at failure are presented. It is possible to observe on one hand the formation of flexural cracks around the bottom centre section of the sleeper which is coherent with the observed pattern in the experimental results (Figure 45a), and also the formation of the compressive plastic region at the top region of the sleeper, which can also be observed in the experimental test.

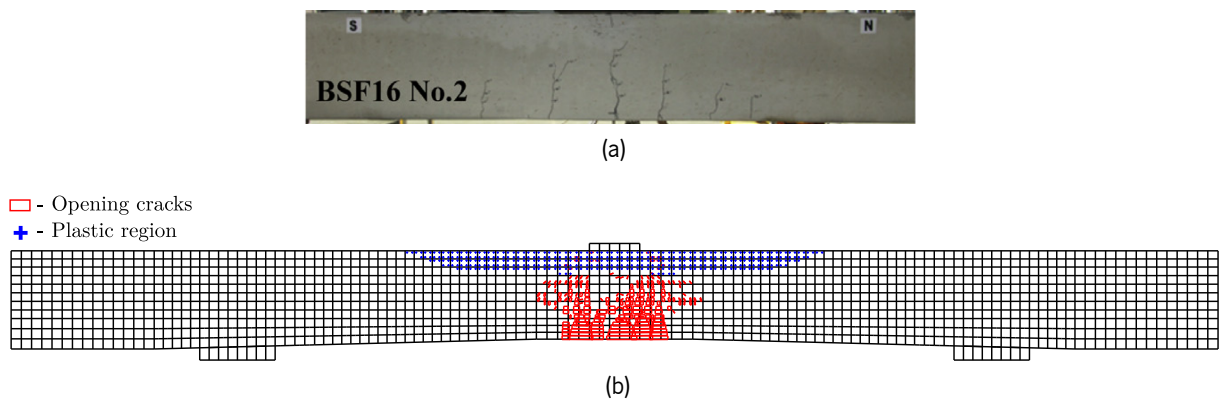


Figure 45: (a) Experimental and (b) numerical crack patterns at failure of the centre section sleeper simulation.

Regarding the crack pattern comparison shown in Figure 46, a good agreement between numerical and experimental results is observed, where the formation of significant flexural cracks propagating along the bottom section of the sleeper and the development of plastic regions both at support and top section of the sleeper as observed in the experimental results (Figure 46a).

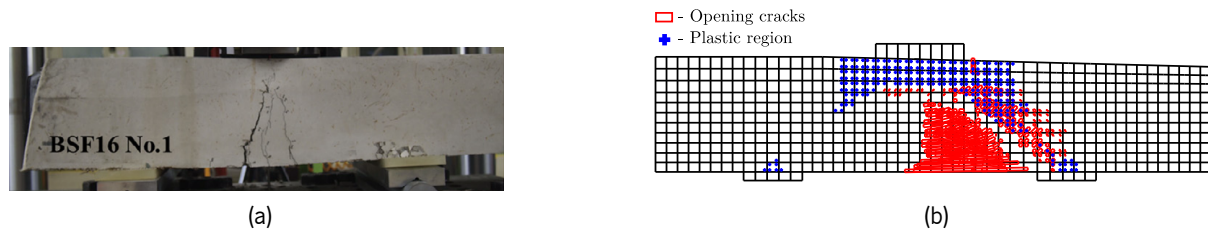


Figure 46: (a) Experimental and (b) numerical crack patterns at failure of the rail-seat section sleeper simulation.

Hence, considering the results shown in Figures 44 to 46 it is possible to conclude that the use of the existing constitutive models available in FEMIX V4.0 to simulate SFRC railway structural elements is adequate, allowing an accurate estimation of the structural behaviour both in terms of structural response and failure mode as long as the choice of the constitutive models and defined parameters are representative of the actual structural behaviour, which is not always possible nor straightforward.

### 3.4 A generalised approach to compute the crack band width

The crack band width (CBW) is a parameter of utmost importance within context of the SCM approach, since it remedies the pathological issue of the dependency of the results on the mesh degree of regularity and refinement. Hence, an accurate estimation of this parameter ensures the correct energy dissipation and remedies the dependency of the results on the discretization of the continuum, or in other words, ensures the objectivity of the results. For regular meshes, the CBW might seem quite easy to compute, however, it is difficult to calculate this parameter in a generalised manner for irregular meshes and arbitrary crack directions.

One of the possible methodologies to estimate the CBW is based on the area or the volume of the elements. Hence, in this methodology the value of the CBW is given by the square root of the area, or the cubic root of the FE volume. This approach is broadly available in commercial software due to its simplicity, however it can lead to less accurate values of this parameter, especially in the case of elongated/distorted elements or even for regular meshes if the crack is not aligned with the element sides. The software FEMIX V4.0 includes the possibility of computing the CBW based on the tributary area/volume of the integration point (IP) or the area/volume of the FE.

Let us consider a single finite element with two cracks in the centre, as depicted in Figure 47. In this simple case, it is evident that an estimation of the CBW based on the square root of the area of the FE would lead to an incorrect estimation of this parameter for crack 2, since the crack is not parallel to the sides of the element, resulting in a lower CBW value. Therefore, another approach can be used, which consists on projected distance between the most farther nodes in the direction orthogonal to the plane of the crack, as defined by  $\ell_{b,2}$  in Figure 47. In this way, the CBW is not only function of the mesh size but also of the crack orientation, resulting in a better estimations of this parameter.

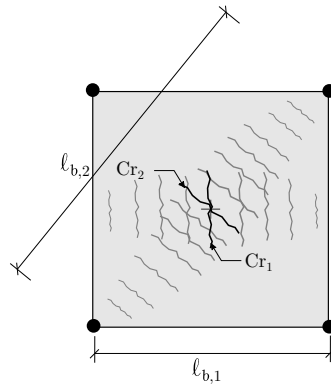


Figure 47: Schematic representation of the projection distance concept of the CBW for an inclined crack.

Oliver and Idelsohn [205] proposed an alternative approach to compute the CBW in an attempt of generalising the computation of this parameter, mitigating the issues that arise from a fixed value approach. In the formulation proposed by Oliver and Idelsohn [205] the crack entity is defined by the concept of ‘singular band’, which is a region where the evolution of the displacement field can be distinct that the one surrounding the limits of the singular band. The concept of singular band and the displacement evolution along the section A-D within this region are represented in Figure 48,

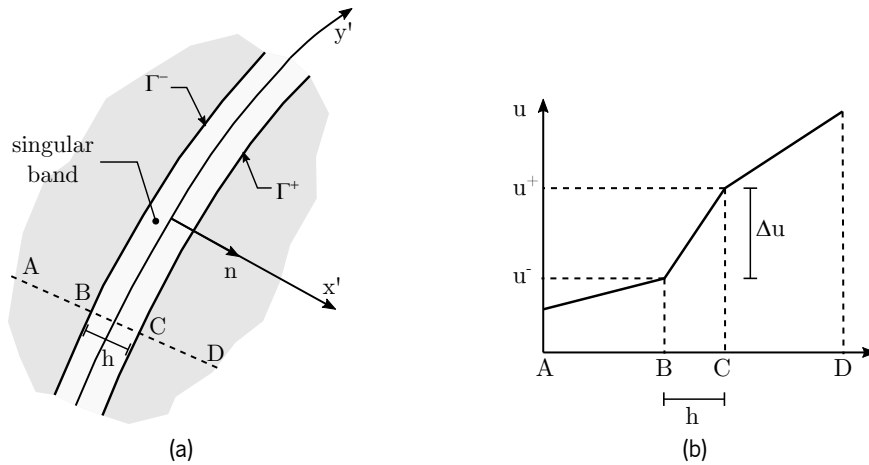


Figure 48: (a) Crack entity represented by the singular band encompassed by two singular lines and (b) displacement field across the singular band (adapted from Oliver and Idelsohn [205]).

where  $x'$  and  $y'$  form the local coordinate system of the singular band,  $\Gamma^-$  and  $\Gamma^+$  represent the left and right region of the band,  $h$  is the width of the singular band,  $u^-$  and  $u^+$  are the displacements at the left and right singular lines and  $\Delta u$  represents the displacement “jump” between singular lines. The displacement variation within the singular band can be defined by Equation (3.1),

$$\Delta u(y') = u^+(y') - u^-(y') \quad (3.1)$$

As the width of the band  $h$  tends to zero, the singular band is modelling a discontinuous displacement field as a limit of a continuous one. In this way, the crack is idealised as the limit of a band of finite elements

where the aforementioned condition is somehow ensured. Hence, the displacements inside the band are governed by the following expression,

$$u(x', y') = u^-(y') + \phi(x', y') \cdot \Delta u \quad (3.2)$$

where  $\phi$  is a function that takes the value of 1 at  $\Gamma^+$  and 0 at  $\Gamma^-$ .

The singular lines represent a continuous line of material where the displacements are continuous but the derivatives are not. In the context of the FEM, the singular lines are represented by the sides of the finite elements, since the discontinuities in the displacement derivatives can only occur between finite elements. Thus, the singular band is defined by a set of finite elements crossed by a crack, as depicted in Figure 49,

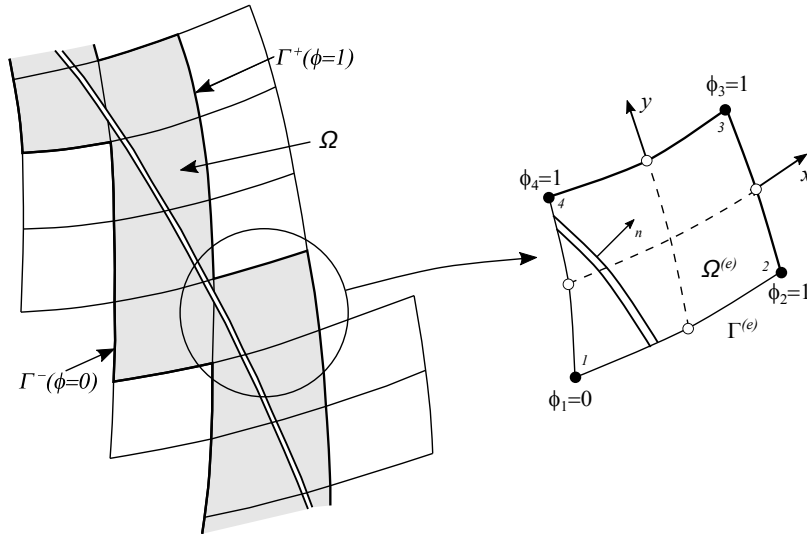


Figure 49: Singular band approximated by finite element discretization (adapted from [205]).

where  $\Gamma^-$  and  $\Gamma^+$  are the singular lines, defined by the sides of the finite elements, and  $\Omega$  is the region defined by the set of finite elements that constitute the singular band.

The behaviour of the singular band is then assigned to the finite elements that comprise this region. If a very refined mesh is assumed, then the set of finite elements will in the limit corresponding to the crack itself and, therefore, lead to a more accurate prediction of the crack behaviour. Oliver and Idelsohn [205] defines the CBW as per Equation (3.3),

$$\ell_b = \frac{1}{\frac{\partial \phi}{\partial x'}} \quad (3.3)$$

where  $x'$  is the normal axis to the crack. The  $\phi$  function has to be continuous and derivable in order to comply with the idealised behaviour of the singular band. Such function can be defined by Equation (3.4),

$$\phi_i(s_1, s_2) = \sum_{i=1}^{N_{nodes}} N_i(s_1, s_2) \cdot \phi_i \quad (3.4)$$

where  $N_{nodes}$  is the number of corner nodes of the finite element,  $N_i(s_1, s_2)$  are the regular FEM shape functions,  $s_1$  and  $s_2$  are the normalised isoparametric coordinates of the finite element, and  $\phi_i$  is the value of the function  $\phi$  at the corner node  $i$ . The value of  $\phi_i$  depends on whether the node  $i$  is located on the right ( $\phi_i = 1$ ) or left ( $\phi_i = 0$ ) region of the crack.

Finally, the CBW can be obtained by means of Equation (3.5),

$$\ell_{b,j} = \left[ \sum_{i=1}^{N_{nodes}} \left( \frac{\partial N_i(s_{1,j}, s_{2,j})}{\partial x_1} \cdot \cos \theta_{cr,j} + \frac{\partial N_i(s_{1,j}, s_{2,j})}{\partial x_2} \cdot \sin \theta_{cr,j} \right) \cdot \phi_i \right]^{-1} \quad (3.5)$$

where  $x_1$  and  $x_2$  are the global coordinate system (GCS) axis and  $j$  is the current gauss point at which  $\ell_b$  is being evaluated.

### 3.4.1 Implementation in FEMIX v4.0

In this section the implementation strategy in FEMIX V4.0 of the approach proposed by Oliver and Idelsohn [205] is presented. For the sake of simplicity a single plane stress situation considering 4-noded elements with a 2x2 G-L integration scheme (Figure 50) is considered as an example.

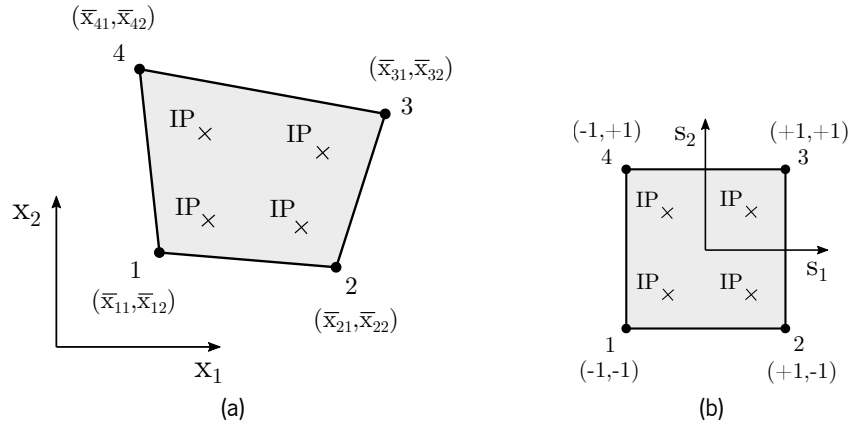


Figure 50: (a) 4-noded element with a 2x2 Gauss-Legendre integration scheme and (b) the same finite element with normalised isoparametric coordinates.

Based on Equation (3.5), the implementation of Oliver's CBW computation approach is straightforward, since the entities involved in the computation of this parameter are already obtained during the FEM calculation steps, except for value of the  $\phi$  function at the element nodes. Hence, the required entities to compute the CBW are:

- The shape functions in the isoparametric coordinate space  $N_i(s_1, s_2)$  given by Equation (3.6)

$$\begin{cases} N_1(s_1, s_2) = (1 - s_1)(1 - s_2) / 4 \\ N_2(s_1, s_2) = (1 + s_1)(1 - s_2) / 4 \\ N_3(s_1, s_2) = (1 + s_1)(1 + s_2) / 4 \\ N_4(s_1, s_2) = (1 - s_1)(1 + s_2) / 4 \end{cases} \quad (3.6)$$

- The derivatives of the shape functions for a 2x2 G-L integration scheme given by Equation (3.7)

$$\frac{\partial \underline{N}}{\partial \underline{s}} = \begin{bmatrix} \frac{\partial N_1}{\partial s_1} & \frac{\partial N_1}{\partial s_2} \\ \frac{\partial N_2}{\partial s_1} & \frac{\partial N_2}{\partial s_2} \\ \frac{\partial N_3}{\partial s_1} & \frac{\partial N_3}{\partial s_2} \\ \frac{\partial N_4}{\partial s_1} & \frac{\partial N_4}{\partial s_2} \end{bmatrix} = \begin{bmatrix} \frac{(-1+s_2)}{4} & \frac{(-1+s_1)}{4} \\ \frac{(+1-s_2)}{4} & \frac{(-1-s_1)}{4} \\ \frac{(+1+s_2)}{4} & \frac{(+1+s_1)}{4} \\ \frac{(-1-s_2)}{4} & \frac{(+1-s_1)}{4} \end{bmatrix} \quad (3.7)$$

- The Jacobian matrix for the transformation between the normalized isoparametric coordinates and the global coordinate system (GCS) coordinates given by Equation (3.8)

$$\underline{J} = \begin{bmatrix} \frac{\partial x_1}{\partial s_1} & \frac{\partial x_1}{\partial s_2} \\ \frac{\partial x_2}{\partial s_1} & \frac{\partial x_2}{\partial s_2} \end{bmatrix} \quad (3.8)$$

where Equation (3.8) is obtained by means of Equation (3.9),

$$\underline{J} = \underline{\bar{x}}^T \frac{\partial \underline{N}}{\partial \underline{s}} \quad (3.9)$$

where  $\underline{\bar{x}}$  is the matrix containing the coordinates in the GCS of the element nodes. If Equation (3.9) is re-written in matrix form Equation (3.10) is obtained.

$$\begin{bmatrix} \frac{\partial x_1}{\partial s_1} & \frac{\partial x_1}{\partial s_2} \\ \frac{\partial x_2}{\partial s_1} & \frac{\partial x_2}{\partial s_2} \end{bmatrix} = \begin{bmatrix} \bar{x}_{11} & \bar{x}_{21} & \bar{x}_{31} & \bar{x}_{41} \\ \bar{x}_{12} & \bar{x}_{22} & \bar{x}_{32} & \bar{x}_{42} \end{bmatrix} \begin{bmatrix} \frac{\partial N_1}{\partial s_1} & \frac{\partial N_1}{\partial s_2} \\ \frac{\partial N_2}{\partial s_1} & \frac{\partial N_2}{\partial s_2} \\ \frac{\partial N_3}{\partial s_1} & \frac{\partial N_3}{\partial s_2} \\ \frac{\partial N_4}{\partial s_1} & \frac{\partial N_4}{\partial s_2} \end{bmatrix} \quad (3.10)$$

With the Jacobian matrix defined by Equation (3.10), the relation between the partial derivatives of the shape functions in the isoparametric space and the partial derivatives of the shape functions in the GCS is given by Equation (3.11),

$$\frac{\partial \underline{N}}{\partial \underline{s}} = \frac{\partial \underline{N}}{\partial \underline{x}} \underline{J} \quad (3.11)$$

Finally, multiplying both left and right hand side of Equation (3.11) by  $J^{-1}$ , the derivatives of the shape functions in the GCS are obtained as per Equation (3.12).

$$\frac{\partial N}{\partial \underline{x}} = \frac{\partial N}{\partial \underline{s}} J^{-1} \quad (3.12)$$

With all the necessary entities defined, the computation of the CBW occurs during the stress updating cycle at a general gauss point  $j$ . Thus, if the criterium for crack initiation is activated, a new crack is formed and the CBW is calculated according to algorithm presented in Figure 51.

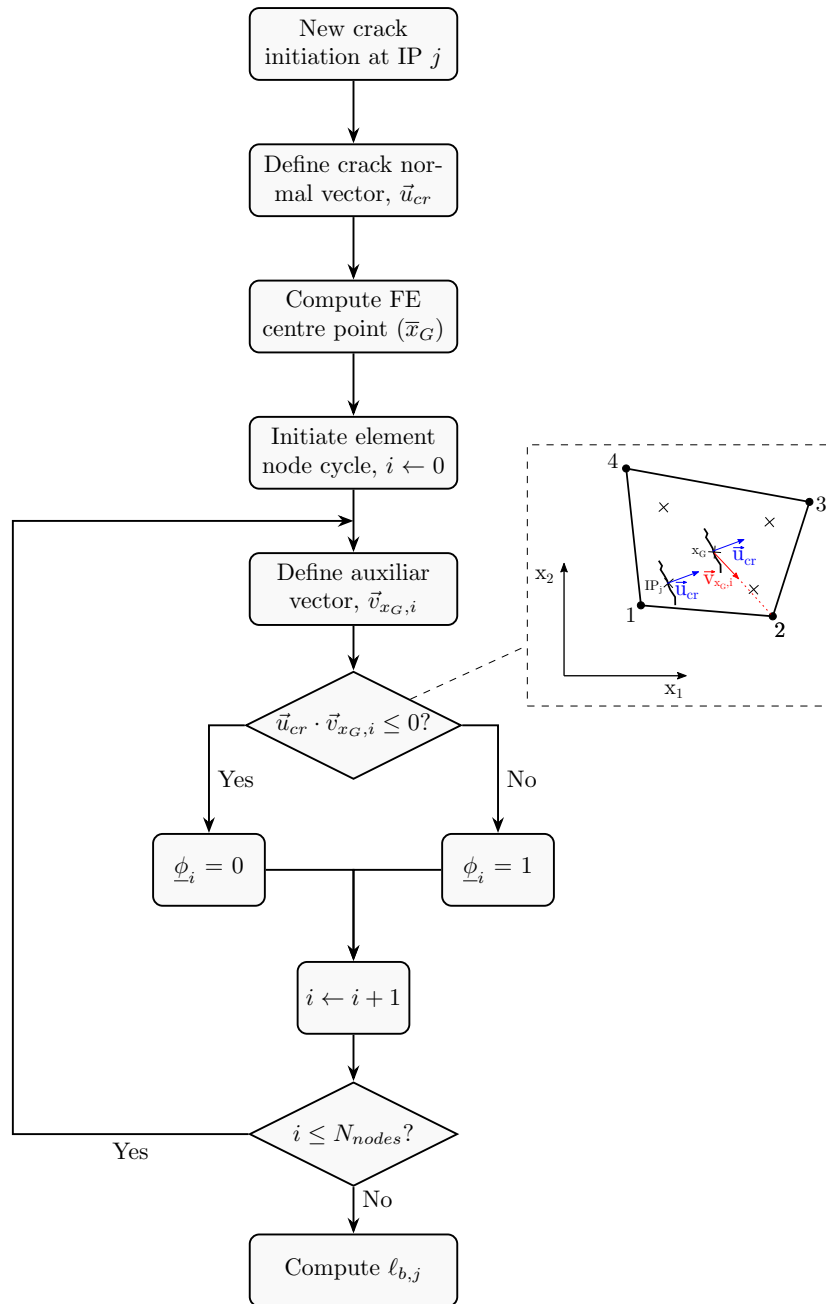


Figure 51: Algorithm to compute the CBW according to Oliver's approach.



### 3.4.2 Issues and modifications to Oliver's approach

Let us consider a two dimensional squared 4-noded element with a  $2 \times 2$  G-L integration scheme and the geometry depicted in Figure 52.

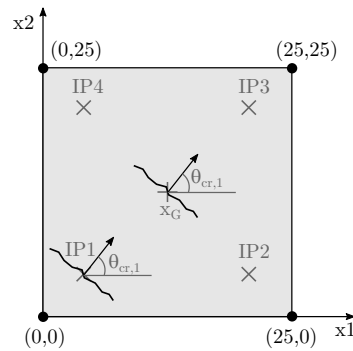


Figure 52: Schematic representation of a 4-noded FE with a  $2 \times 2$  G-L integration scheme.

Now, considering the computation of the CBW for each IP, and for a range of crack orientation angles ( $\theta_{cr,j}$ ), by means of Equation (3.5) and the algorithm presented in Figure 51, the obtained results are presented in Figure 53. It is important to stress that, according to the methodology, albeit the crack is presented in Figure 53. It is important to stress that, according to the methodology, albeit the crack is originated at the IP level, the calculation of the CBW is conducted at the geometric centre of the FE.

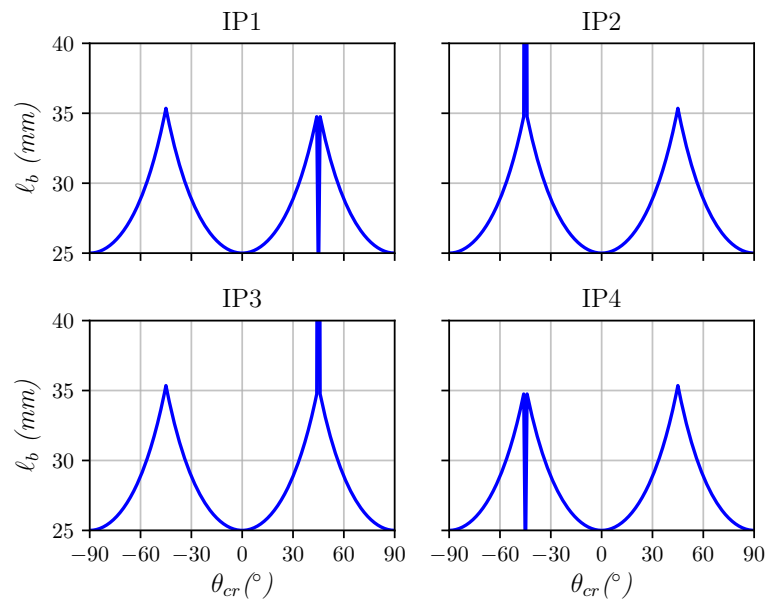


Figure 53: CBW value obtained at each IP considering the value of  $\theta_{cr}$  ranging between  $[-90^\circ, 90^\circ]$

Considering the results presented in Figure 53, it is possible to understand that the obtained values correspond to the distance between the intersection of an imaginary line aligned with the crack normal vector and the element sides, as illustrated in Figure 54. Furthermore, one can also observe that the results exhibit a discontinuity for  $\theta_{cr}$  values around  $45^\circ$  and  $-45^\circ$  when the computation is taken at IP1/IP3 and IP2/4, respectively.

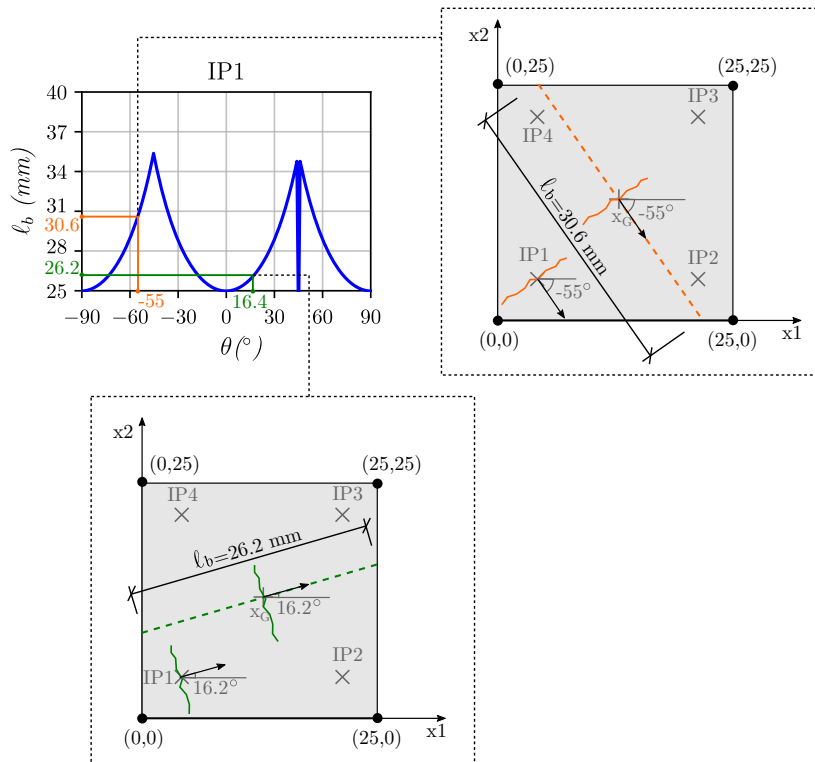


Figure 54: Schematic representation of the geometric meaning of the methodology proposed by [205].

In order to understand the origin of such discontinuities in the results, let us assume a crack situation located at the IP1 with  $\theta_{cr,1} = 45^\circ$ , as represented in Figure 55. With this in consideration, it is possible to observe that at this exact moment, the value of  $\phi_{2,3,4}$  takes the value of 1 and  $\phi_1$  is 0. If these values are plugged into Equation (3.5), the discontinuity observed in Figure 55 is obtained. This is due to the sudden contribution of a new node which seems to unbalance the sum of the partial derivatives of the shape functions. Hence, the aforementioned issue is due to the binary nature of the  $\phi$  function that leads to an abrupt transition when a crack is aligned in such a way that an additional node starts/stops contributing to the CBW computation leading to unreasonable values that are not faithful to the physical meaning of the methodology. Govindjee et al. [206] arrived at the same conclusions while conducting experiments with

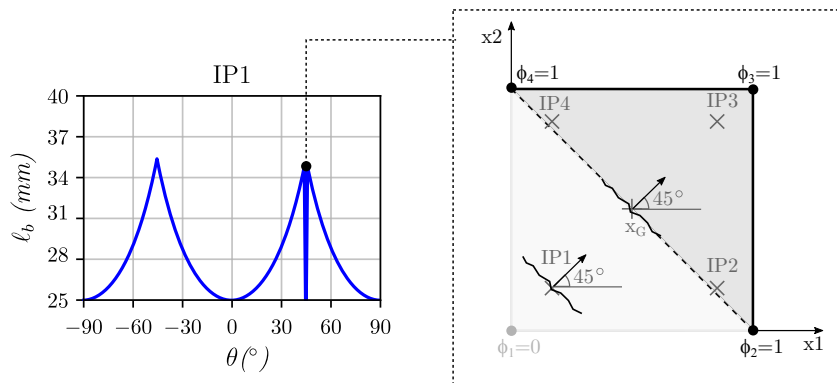


Figure 55: Discontinuity situation of CBW for the IP1 crack scenario.

the CBW in solid element, and proposed a simple “smoothing” function to remedy the binary behaviour of the  $\phi$  function. The alternative approach to compute the  $\phi_i$  values is given by Equation (3.13)

$$\phi_i = \frac{\vec{v}_{xG,i} \cdot \vec{u}_{cr} - \phi_{min}}{\phi_{max} - \phi_{min}} \quad (3.13)$$

with,

$$\phi_{min} = \min (\vec{v}_{xG,i} \cdot \vec{u}_{cr}) \quad (3.14)$$

$$\phi_{max} = \max (\vec{v}_{xG,i} \cdot \vec{u}_{cr}) \quad (3.15)$$

where,  $\phi_{min}$  is the minimum value of the  $\phi$  function,  $\vec{v}_{xG,i}$  is a vector from the centre of the element to the current node  $i$  and  $\vec{u}_{cr}$  is the crack normal vector.

The results presented Figure 53 were plotted against the results obtained by means of the modified version of the methodology and are depicted in Figure 56.

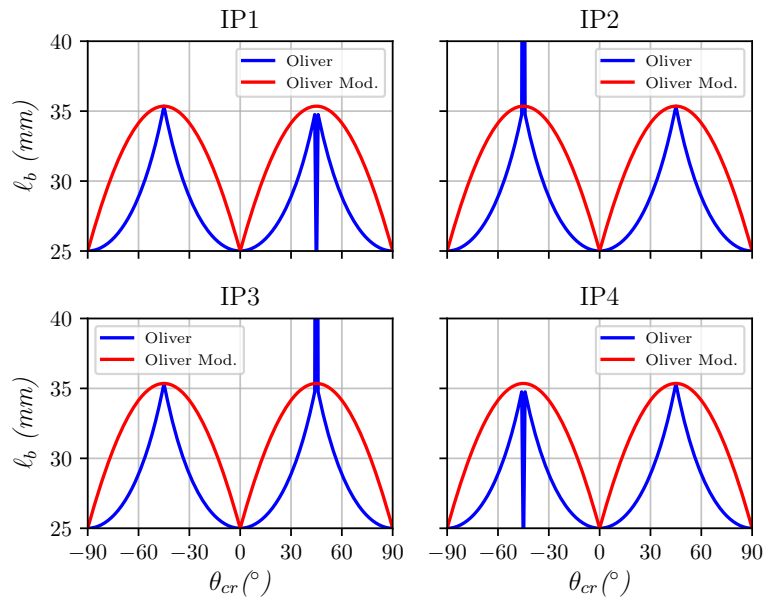


Figure 56: Comparison between the original and modified version of the approach proposed by Oliver and Idelsohn [205].

Considering the results presented in Figure 56, it is possible to observe that the discontinuity issue is solved with the interpolation function given by Equation (3.13), however the CBW values are greater than the original ones. In fact, if the modified version of the Oliver’s methodology is considered, it can be seen that the method “degenerates” to a projection based method (Figure 47), as better depicted in the schematic representation of Figure 57.

The smoothing function proposed by Govindjee et al. [206] (Equation (3.13)) was implemented in the original algorithm presented in Figure 51 resulting in the algorithm presented in Figure 58.

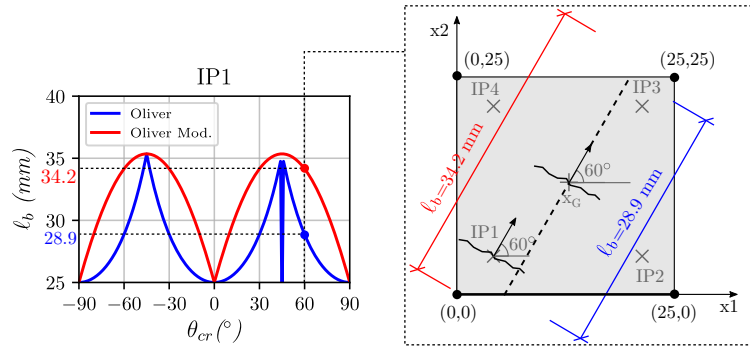


Figure 57: Schematic representation of the obtained CBW values for the original and modified methodology.

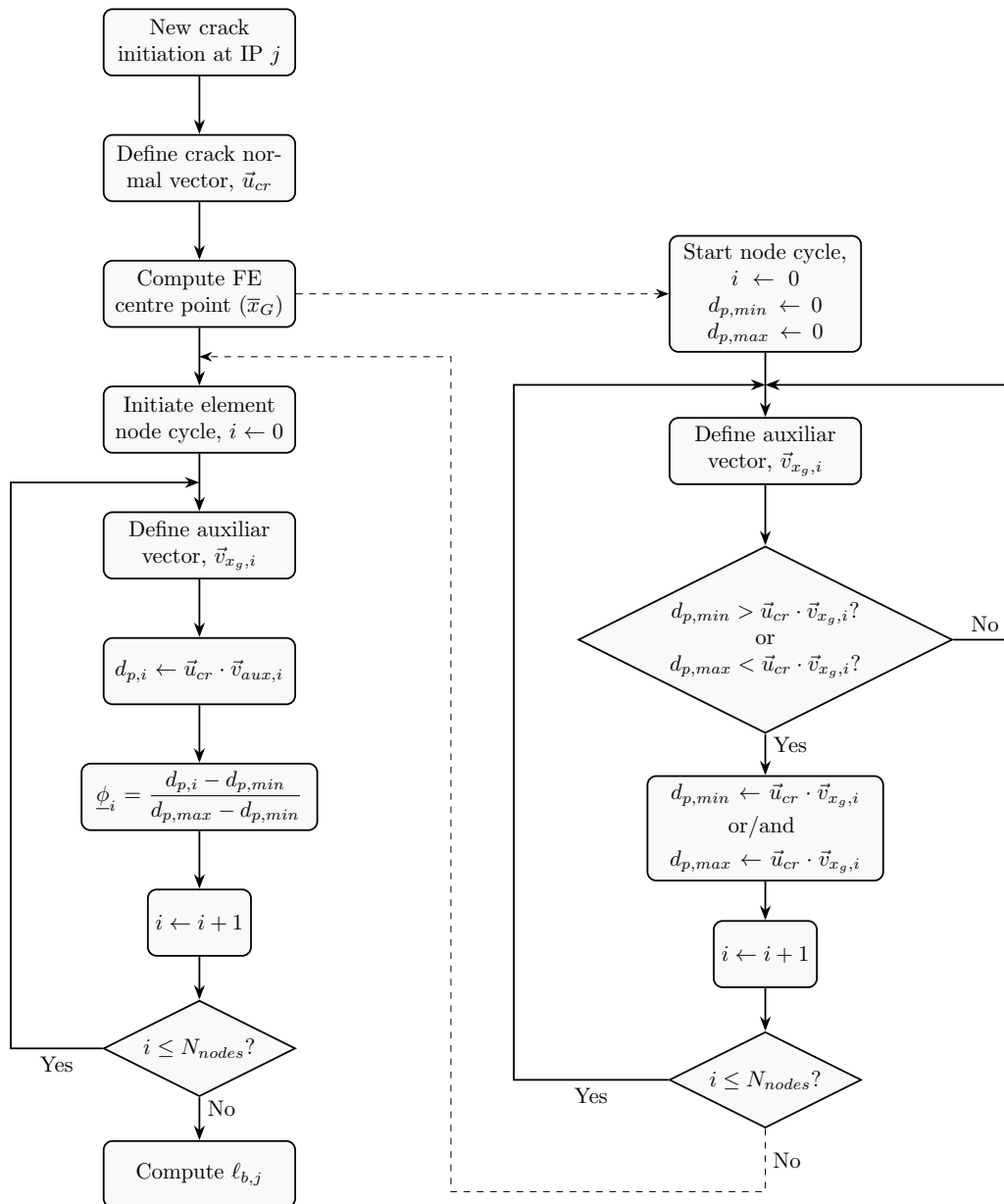


Figure 58: Modified CBW computation algorithm considering the smoothing function proposed by Govindjee et al. [206].

### 3.4.3 Extending Oliver’s method to the integration point level

The previously described methodology estimates the value of the CBW over the dimension of the entire FE. However, the cracks are initiated at the integration points and therefore it makes sense to attempt a computation of the CBW over the IP domain only. Thus, the original methodology rationale is extended to IP level by computing the CBW over the tributary area of the IP. In order to achieve the aforementioned modification, additional steps must be included in the algorithm presented in Figure 58. These additional steps are represented in Figure 59.

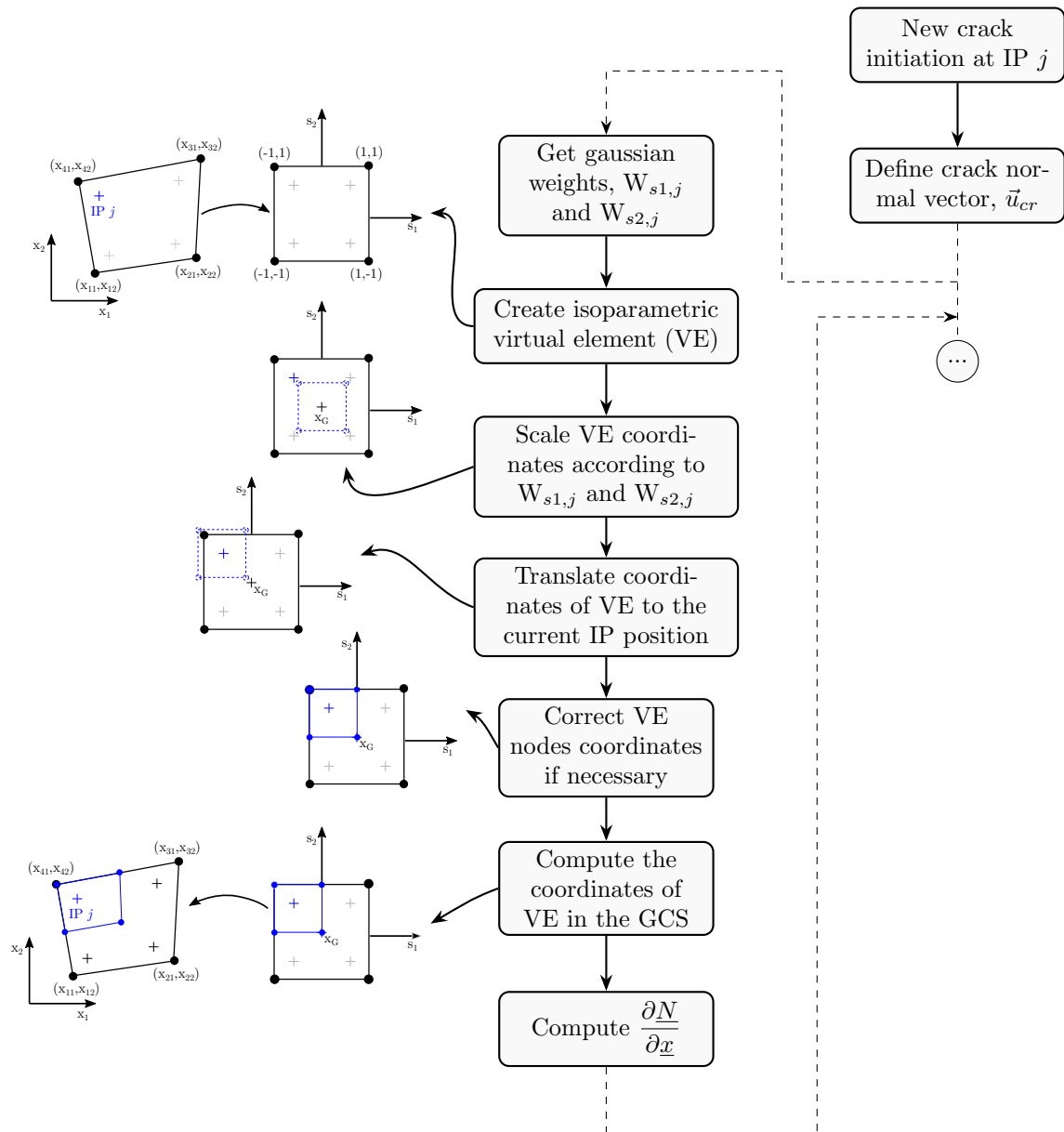


Figure 59: Algorithm of the extended Oliver’s approach to compute the CBW at the IP level with schematic representation of each step for a 4-noded element with a 2x2 G-L integration scheme.

The main difference in the procedure of the algorithm presented Figure 59 resides in the fact that it is necessary to determine the coordinates in the GCS of a virtual FEs that is representative of the tributary

area of the IP. After obtaining this information, the original algorithm presented in Figure 58 is applied (represented by the circle with 3 dots in Figure 59) to the new set of coordinates and the CBW computed accordingly.

Hence, the procedure for obtaining the coordinates of the virtual FE, associated with the tributary area of the IP is as follows:

- Scale the width and height of a virtual isoparametric FE by the weights associated with the current IP ( $j$ ) in the  $s_1$  ( $W_{s1,j}$ ) and  $s_2$  directions ( $W_{s2,j}$ ) as depicted in Figure 60;

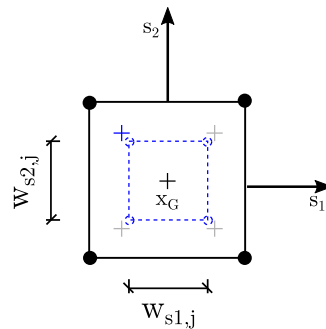


Figure 60: Scaling process of width and height of the isoparametric FE by the corresponding IP's weights.

- Move the scaled virtual FE to the position of the current IP ( $j$ ) by subtracting its coordinates from the coordinates of the scaled FE and check for each node if the boundaries of the original unitary FE are violated, and if so, move the scaled FE to the correct position as shown in Figure 61;

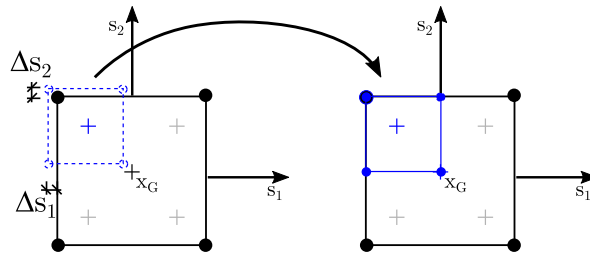


Figure 61: Translation process of the virtual scaled IP to the correct position.

- After obtaining the coordinates of the virtual scaled FE, the coordinates in the GCS are calculated by evaluating the shape functions at each virtual node position and multiplying by the coordinates in GCS of the original FE.
- The CBW is finally computed using the coordinates in the GCS of the previously determined scaled virtual FE by means of the original approach algorithm shown in Figure 59.

### 3.4.4 Appraisal of the implemented CBW calculation approach

In this section, the impact of using the generalised CBW computation approach herein described and implemented is assessed by means of a numerical investigation. For this purpose a numerical study consisting of a T-shaped beam reinforced with glass fibre reinforced polymer (GFRP) bars, as longitudinal

reinforcement. The numerical and experimental responses as well as crack patterns at rupture state are compared considering different mesh sizes and configurations as well as the methodologies to estimate the CBW previously presented.

Figure 62 shows the geometry, finite element mesh, loading and support conditions adopted in this numerical study. To simulate the concrete, 4-node plane stress elements with a 2x2 G-L integration scheme are used. The reinforcement is simulated by means of 2-node embedded cable elements with 2 G-L integration points. These analysis correspond to the simulations of experimental tests carried out by Baghi et al. [207].

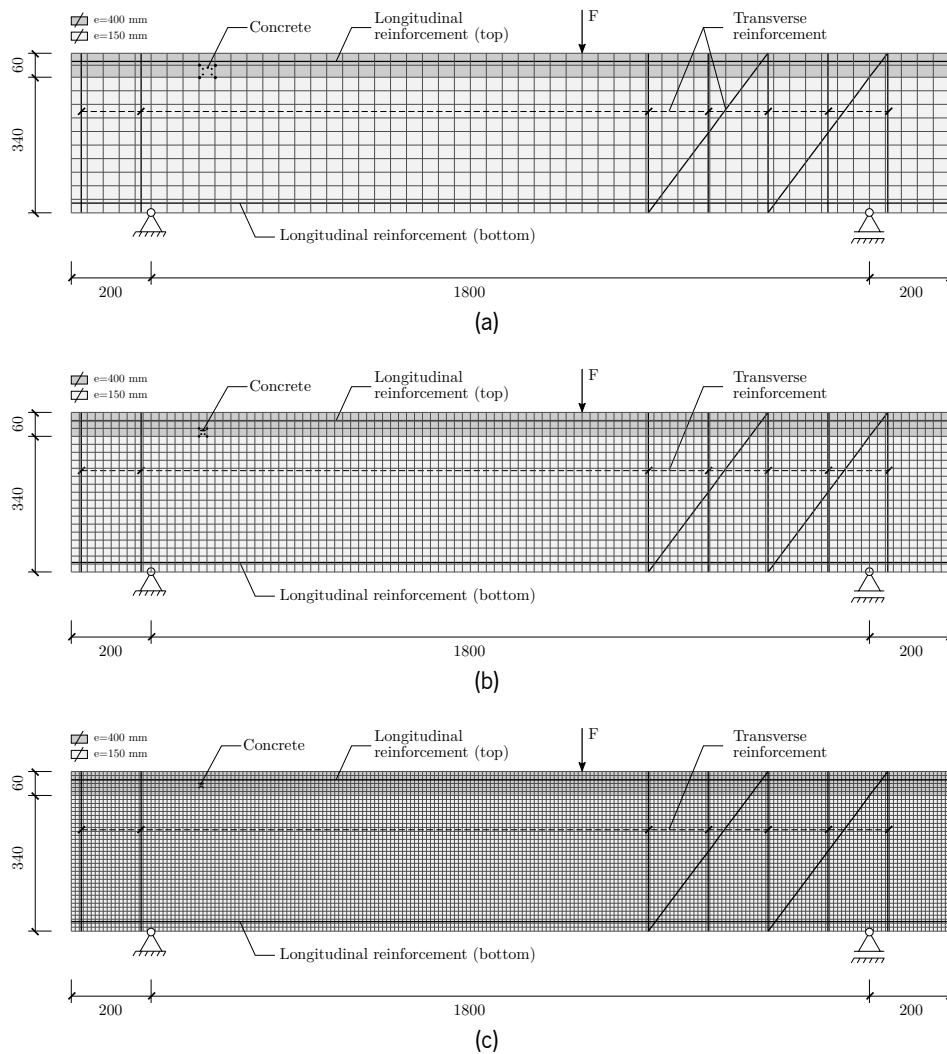


Figure 62: Geometry, loading, support conditions and finite element meshes (a) M40 (40mm), (b) M20 (20mm) and (c) M10(10mm). All dimensions are in millimeters.

### Constitutive laws of the materials

The non-linear behaviour of steel elements was simulated by means of the constitutive relationship presented in Figure 32a. The parameters considered in the definition of the presented constitutive law are summarised in Table 12.

Table 12: Parameters used to define the steel constitutive model for top and transversal reinforcements, and glass fibre reinforced polymer (GFRP) bars for the bottom reinforcement.

Name	$\varepsilon_{sy}$	$\sigma_{sy}$ (N/mm <sup>2</sup> )	$\varepsilon_{sh}$	$\sigma_{sh}$ (N/mm <sup>2</sup> )	$\varepsilon_{su}$	$\sigma_{su}$ (N/mm <sup>2</sup> )	$\rho$
GFRP (Bot.)	$2.38 \times 10^{-3}$	1195	$2.38 \times 10^{-2}$	1*	$2.38 \times 10^{-2}$	0.9*	1
Top. reinf.	$2.60 \times 10^{-3}$	470	$3.00 \times 10^{-2}$	470	$2.20 \times 10^{-1}$	566	1
Transv. reinf.	$2.60 \times 10^{-3}$	470	$3.00 \times 10^{-2}$	470	$2.20 \times 10^{-1}$	566	1

\*Virtual values used to simulate the brittle failure of the GFRP bars.

The material behaviour of the concrete was modelled by means of the trilinear tension-softening relation depicted in Figure 30a. The parameters used to define the referred constitutive model are presented in Section 3.4.4 and listed in Section 3.4.4.

Table 13: Parameters used to define the concrete constitutive model.

Property	Value
Poisson's ratio ( $\nu$ )	0.20
Young's modulus (E)	30650 N/mm <sup>2</sup>
Compressive strength ( $f_c$ )	30.2 N/mm <sup>2</sup>
Trilinear tension-softening diagram	$f_{ct} = 2.2$ N/mm <sup>2</sup> ; $G_f^I = 0.075$ N/mm; $\xi_1 = 0.006$ ; $\alpha_1 = 0.2$ ; $\xi_2 = 0.1$ ; $\alpha_2 = 0.1$ ;
Parameter defining the mode I fracture energy available to the new crack	3
Crack band width	$\sqrt{FE}$ , $\sqrt{IP}$ , $OL_{FE}^1$ , $OL_{IP}^2$
Threshold angle	30°
Maximum number of cracks per integration point	3

<sup>1,2</sup> Crack band width computed according to Figures 58 and 59, respectively.

The force-displacement curves for the meshes M40, M20 and M10 are presented in Figure 63.

Considering the results for the mesh M40 presented in Figure 63a, one can observe that in general the results capture well the initial stage of the response, including the initial stiffness degradation until  $\approx 0.75$  mm for the  $\sqrt{IP}$  and  $OL_{IP}$  and until  $\approx 1.2$  mm for the  $\sqrt{FE}$  and  $OL_{FE}$ , respectively. After this initial stage, the numerical results exhibit a stiffer response, with this discrepancy being higher in the cases where the CBW values are lower, i.e.  $\sqrt{IP}$  and  $OL_{IP}$ .

In Figure 63b the results for the mesh M20, exhibit a similar trend with a more coherent prediction between all curves in the cracked stage of the response.

The results regarding the mesh M10 are presented in Figure 63c. These results are in line with the ones previously referred in terms of overall trend, however, in this case the impact of the low CBW values is quite evident, as one can observe when analysing the curves regarding  $\sqrt{IP}$  and  $OL_{IP}$ . This difference can be explained by the fact that lower CBW values lead to higher load transferring capacity resulting from a more ductile response, while on the other hand, higher CBW values lead to brittle responses.

Regarding the performance of the methodologies, it is possible to observe that in the present case



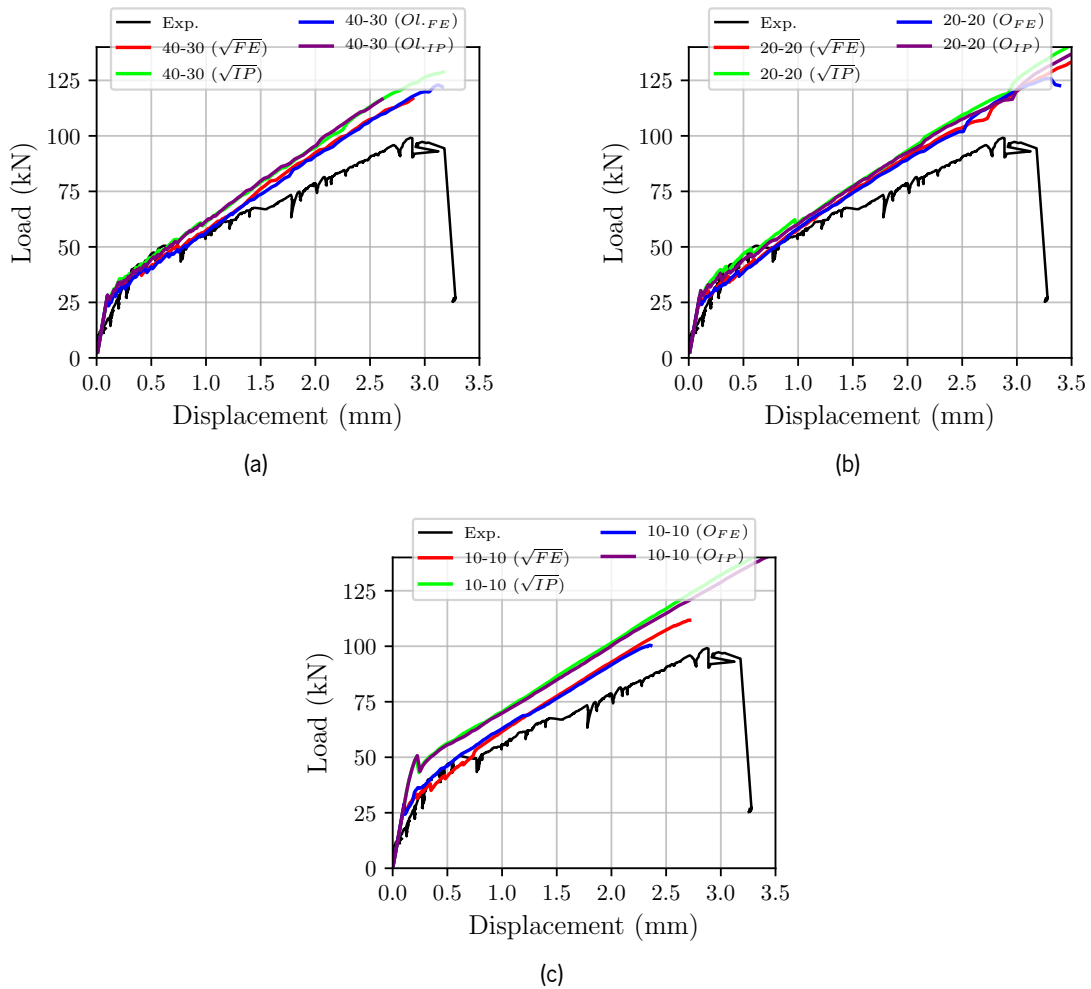


Figure 63: Comparison between the experimental and numerical force-displacement curves obtained for the meshes (a) M40, (b) M20 and (c) M10, and considering different computation methodologies of the CBW.

no significant improvements were obtained in terms of agreement between numerical and experimental results in comparison with the simplistic methodologies to estimate the CBW, such as  $\sqrt{FE}$  and  $\sqrt{IP}$ . This is due to the fact that despite the change in terms of mesh size, the elements aspect ratio remain more or less close to 1, or in other words, the elements are not distorted. Hence, considering the results presented in Figure 63, it is possible to conclude that for meshes formed by approximately squared elements, the use of more sophisticated methodologies to compute the CBW does not lead to better results.

The crack patterns obtained considering the different methodologies for the meshes M40, M20, and M10 are presented in Figures 64 to 66. Regarding the crack patterns depicted in Figure 64 it is possible to see that the methodology that better captured the failure mode was the  $\sqrt{FE}$  (Figure 64b), with a clear formation of a diagonal shear dominant crack. Another relevant observation is related with fact that the methods that produced lower CBW values ( $\sqrt{IP}$  and  $OL_{IP}$ ) tend to originate a greater amount of cracks, with no localization evidence of a dominant crack.

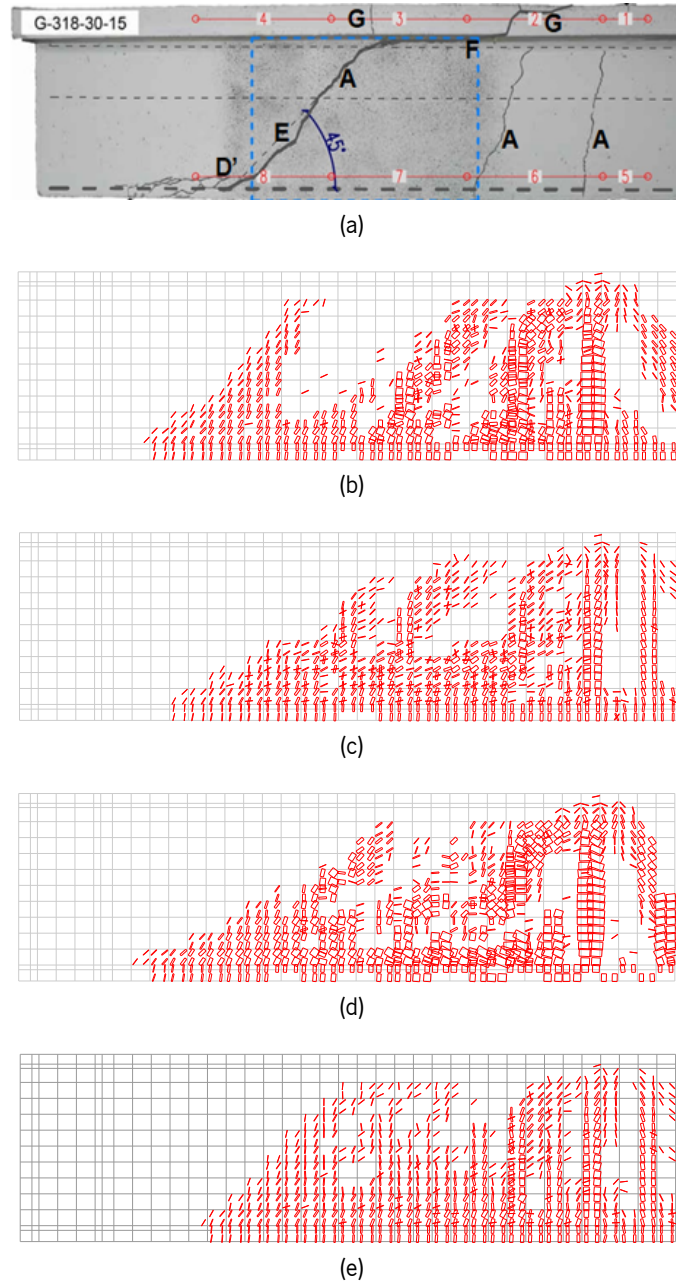


Figure 64: Comparison of the crack patterns, obtained for the mesh M40, considering different CBW computation approaches: (a) experimental pattern, (b)  $\sqrt{FE}$ , (c)  $\sqrt{IP}$ , (d) Oliver FE and (e) Oliver IP.

The patterns for the mesh M20, presented in Figure 65, show a better approximation of the experimental failure mode, with the patterns obtained with the  $\sqrt{FE}$  and  $Ol_{FE}$ , capturing slightly better the diagonal shear crack. Once again one can observe that lower CBW values lead to the proliferation of cracks with lower widths (Figures 65c and 65e), when compared to the methodologies that lead to greater CBW values (Figures 65b and 65c). In fact, Červenka et al. [208] proposes that an upper and lower limit should be imposed to the CBW in order to maintain an acceptable accuracy level. According to these authors, the minimum value should be dependent on the concrete aggregate size, while the maximum on the crack spacing governed by conventional reinforcement.

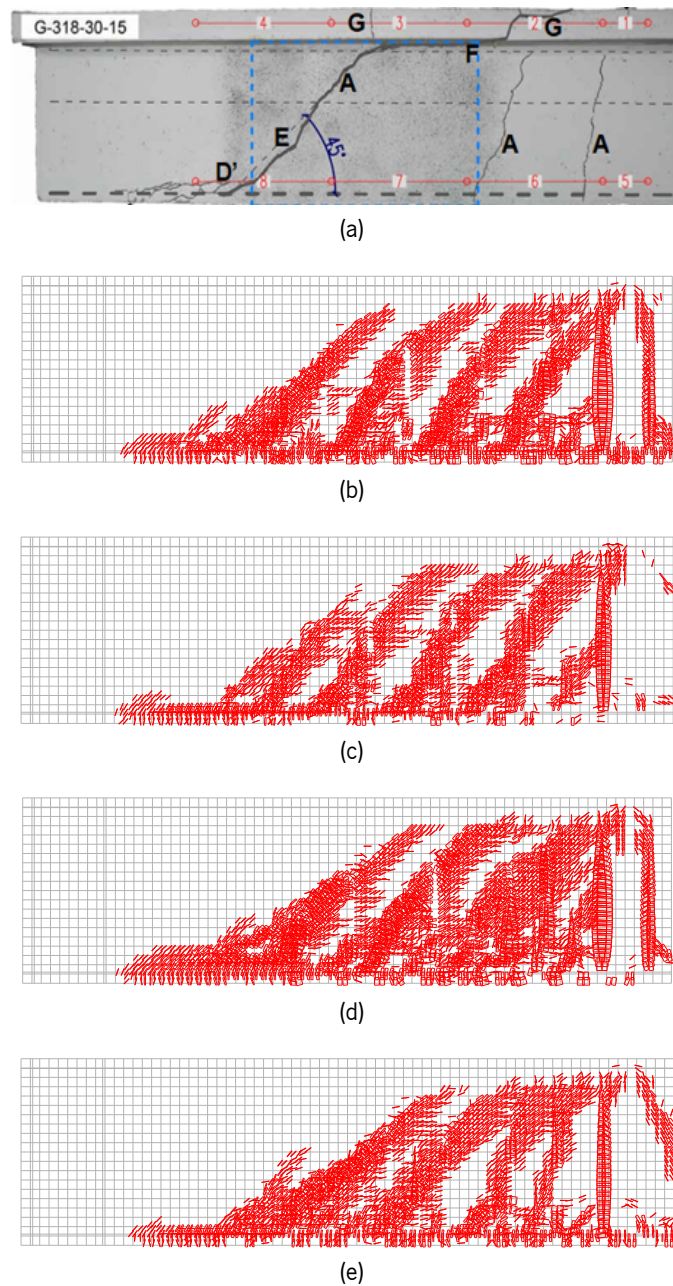


Figure 65: Comparison of the crack patterns, obtained for the mesh M20, considering different CBW computation approaches: (a) experimental pattern, (b)  $\sqrt{FE}$ , (c)  $\sqrt{IP}$ , (d) Oliver FE and (e) Oliver IP.

Finally, the crack patterns obtained for the M10 mesh are depicted in Figure 66 and the results show that in general a better approximation of the failure mode is obtained with this finer mesh, when compared to the results obtained with meshes M40 and M20, respectively. In this case the  $Ol_{FE}$  (Figure 66d) show a slightly better estimation of the failure mode. Once again, the formation of a greater number of cracks is also visible in the cases where lower estimatives of the CBW where obtained (Figures 66c and 66e). In addition, the crack patterns of Figures 66d and 66e seem to have better overall alignment when compared to the ones of Figures 66b and 66c as it is possible to observe in the diagonal crack bands of these patterns.

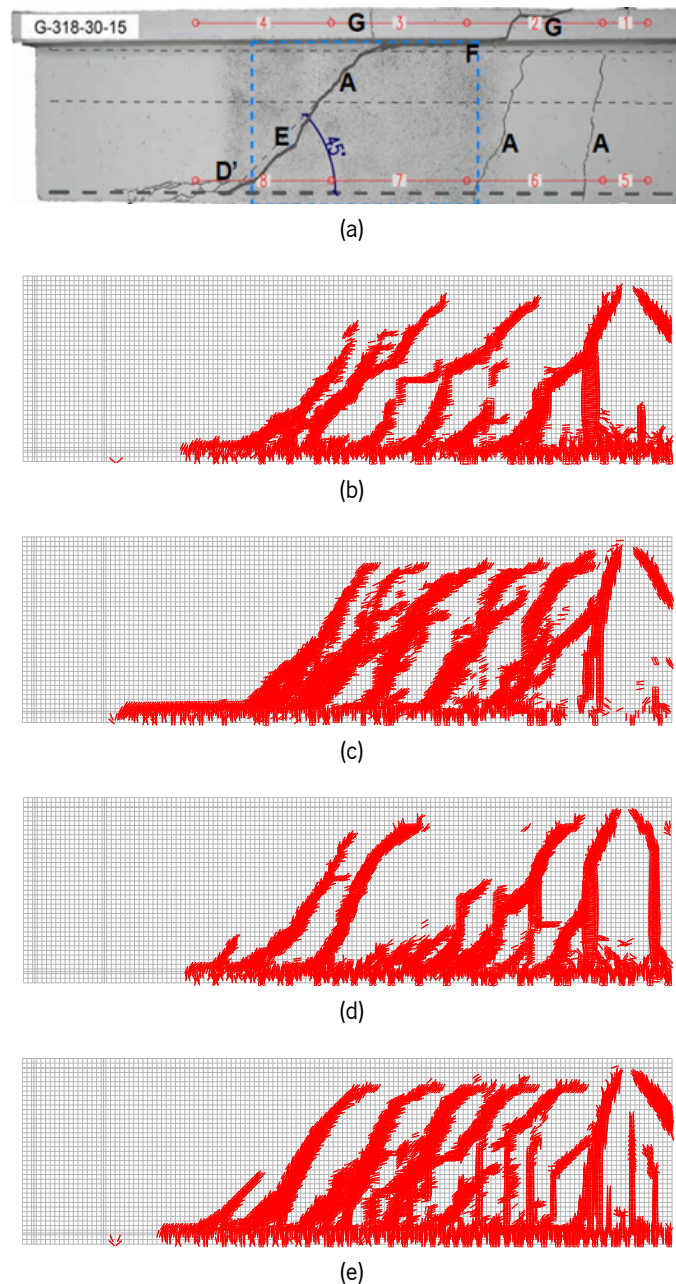


Figure 66: Comparison of the crack patterns, for the mesh M10, considering different CBW computation approaches: (a) experimental pattern, (b)  $\sqrt{FE}$ , (c)  $\sqrt{IP}$ , (d) Oliver FE and (e) Oliver IP.

The results presented in Figures 63a to 63c were obtained considering the regular meshes depicted in Figures 62a to 62c. However, albeit the meshes present different refinement levels, the aspect ratio of the finite elements is 1 except for the mesh M40 where the ratio reaches  $\approx 1.18$ . Thus, in order to further explore the potential of Oliver's approach, two more mesh configurations are investigated. These mesh configurations are depicted in Figure 67.

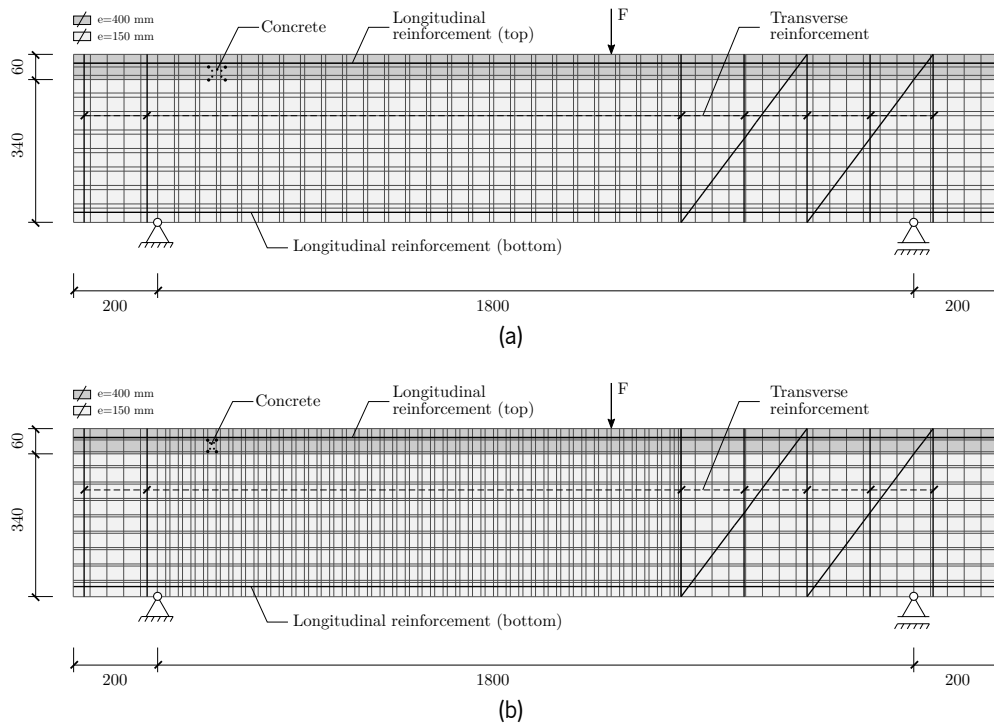


Figure 67: Schematic representation of the mosaic meshes configuration: (a) mesh MO1 and mesh (b) MO2. All dimensions are in millimeters.

The meshes depicted in Figure 67, herein designated mosaic meshes, are composed by finite elements with different aspect ratios (width/height) which will reveal the impact of using the simplistic methodologies of  $\sqrt{FE}$  and  $\sqrt{IP}$  that one knows are less suitable for not so regular meshes. Hence, the comparison between the numerical and experimental force-displacement curves for both meshes and considering different CBW computation methods is presented in Figure 68.

Regarding the mesh MO1, the results presented in Figure 68a show an overall very good agreement with the experimental curve. In an initial stage the numerical response is stiffer than the experimental one, regardless of the CBW computation approach, however the elasto-cracked phase is in general well captured. The cracked stage of the response is also well approximated by all curves, however the  $\sqrt{IP}$  method, deviates from the remaining curves, and even a snap-back instability is observed ( $\approx 1.8$  mm). Once again, the approaches that lead to lower values of the CBW originate a higher load carrying capacity (green and violet curves in Figure 68a). The response obtained by means of the  $Ol_{FE}$  method, lead a better estimation of the experimental response when compared with the remaining approaches.

In what concerns the results for the MO2 mesh (Figure 68b), the conclusions are quite similar to the

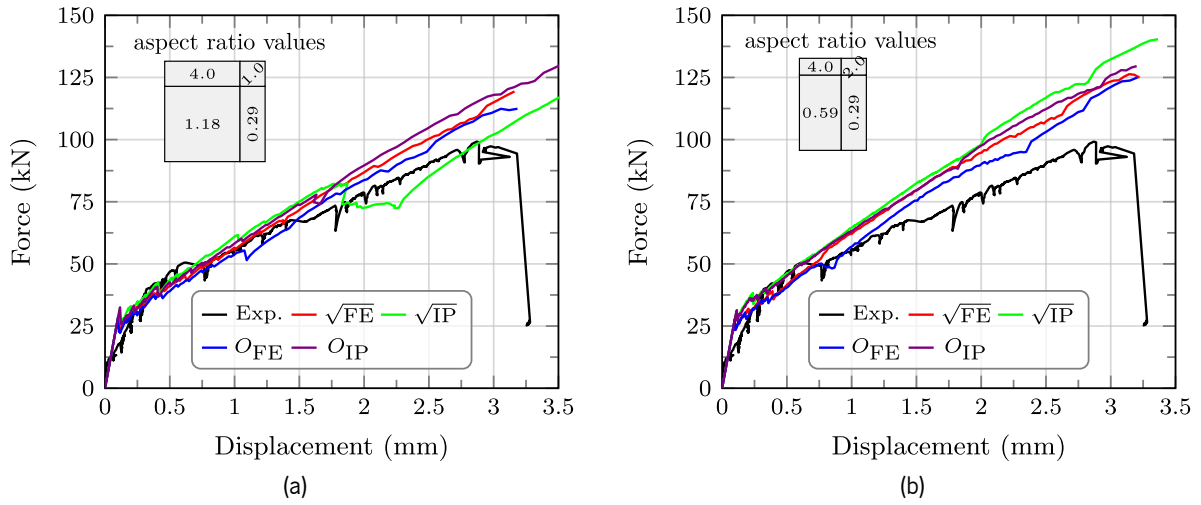
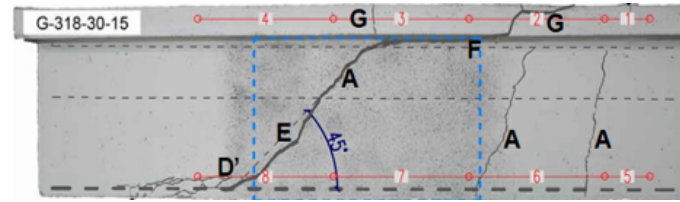


Figure 68: Comparison between experimental and numerical force-displacement curves for the meshes (a) MO1 and (b) MO2 considering different CBW computation approaches.

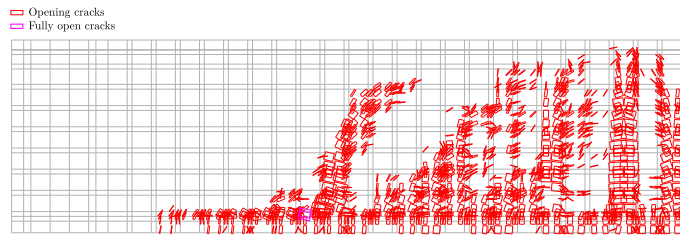
ones already drawn for the results of Figure 68a, however in this case, the elasto-cracked stage of the response seems to be slightly stiffer than the experimental curve which can be attributed to the fact that the CBW is lower for the case of MO2 leading to an increase in load carrying capacity. The  $OL_{FE}$  method provides once again the better approximation to the experimental results.

The crack patterns regarding the mosaic meshes MO1 and MO2 are depicted in Figures 69 and 70, respectively. In what concerns the mesh MO1, the crack pattern that better captures the failure mode is the one represented in Figure 69d, which clearly shows the localization of a diagonal shear crack band. Once again for the  $\sqrt{IP}$  and  $OL_{IP}$  a greater amount of cracks is obtained with no clear localization of a dominant crack which is aligned with the already documented conclusions in previous results. Regarding the mesh MO2, the conclusions are similar to the ones already drawn for the MO1 mesh, in this case the best approximation is also the  $OL_{FE}$  approach with an even more realistic crack pattern than the one obtained for mesh MO1.

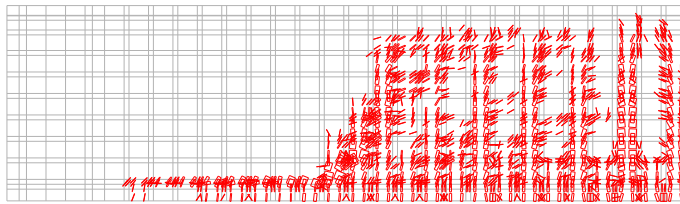
An interesting difference worth stressing in these crack patterns, which is related with the uniformity of the crack widths. If one takes a closer look into Figures 70b and 70d, more precisely to the vertical crack band close to the right edge, it is possible to observe that the vertical cracks presented in Figure 70b exhibit distinct crack widths in subsequent elements with different aspect ratios (squared and elongated elements), which is not observed in Figure 70d. This is due to the fact that in elements with a higher aspect ratio, or in other words, elongated elements, the use of a CBW equal to  $\sqrt{FE}$  will lead to an underestimation of the CBW, which consequently results in a lower crack width when compared to an element that has an aspect ratio closer to 1. On the other hand, the  $OL_{FE}$  approach captures the correct CBW, which results in a much more uniform crack band. This is also verified in patterns of Figures 70c and 70e. To further highlight this aspect the crack patterns shown in Figures 70b and 70d are presented in a coloured fashion according to the crack width value of the cracks in Figures 71a and 71b.



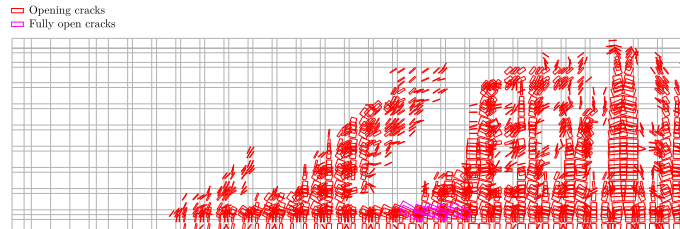
(a)



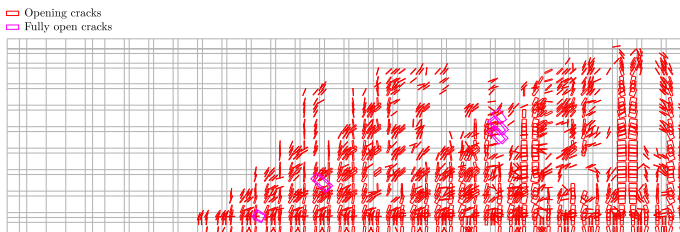
(b)



(c)

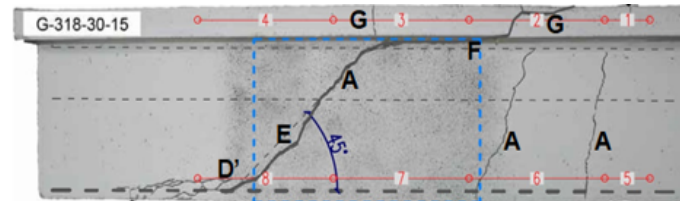


(d)

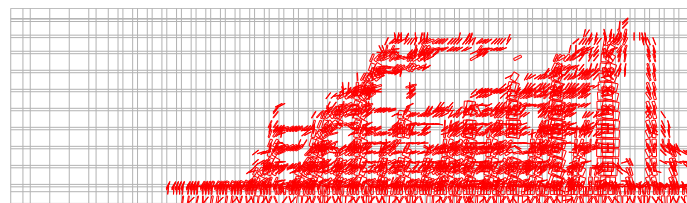


(e)

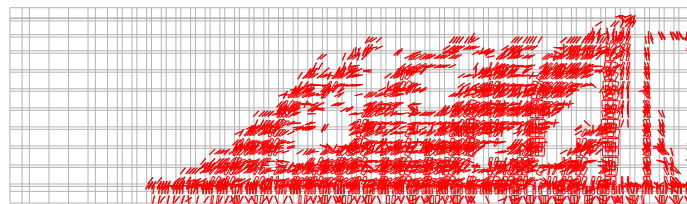
Figure 69: Comparison between (a) the experimental failure mode and the crack patterns obtained for the mesh MO1, considering the (b)  $\sqrt{FE}$ , (c)  $\sqrt{IP}$ , (d)  $OL_{FE}$  and (e)  $OL_{IP}$  methodologies to estimate the CBW.



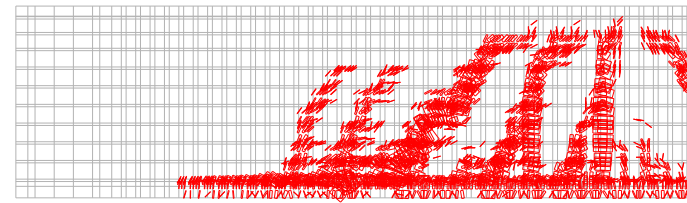
(a)



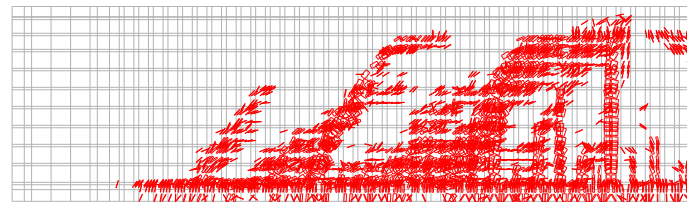
(b)



(c)



(d)



(e)

Figure 70: Comparison between (a) the experimental failure mode and the crack patterns obtained for the mesh MO2, considering the (b)  $\sqrt{F_E}$ , (c)  $\sqrt{I_P}$ , (d)  $OL_{FE}$  and (e)  $OL_{IP}$  methodologies to estimate the CBW



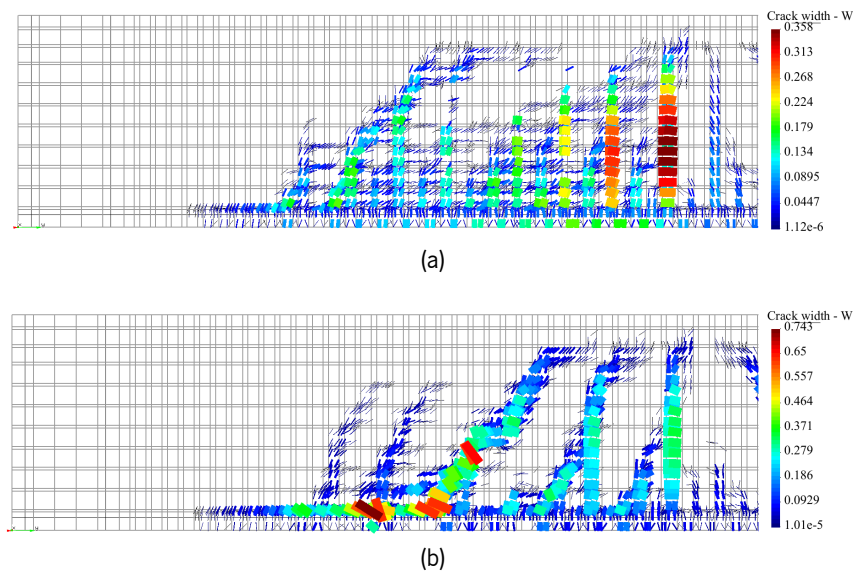


Figure 71: Comparison between the crack patterns according to the crack width value obtained for the mesh MO2, considering the (a)  $\sqrt{FE}$  and (b)  $Ol.FE$  methodologies.

### 3.5 Summary and Conclusions

In this chapter, an overview on the simulation of FRC elements using the MFSCM approach available in the FEMIX V4.0 computer code is provided. Firstly, several numerical simulations are conducted and the importance of the parameters that govern mode I and mode II is analysed by means of a parametric study. The mode I parameters are investigated by means of a 3PNBBT case study where the influence of tensile strength ( $f_{ct}$ ), fracture energy ( $G_{fI}$ ) and shape of the tensile-softening constitutive relationship is analysed. Subsequently the simulation of FRC panels subject to shear loading is analysed. In this case different parameters are used to define the shear-softening diagram and its influence on the structural response are analysed and compared to available experimental results. In addition, the good predictive performance of the previously used constitutive models is demonstrated by means of a prestressed FRC railway sleeper. Furthermore, a generalised approach to compute the CBW parameter is described and implemented in the FEMIX V4.0 computer code. The most common approaches to compute the CBW are described and the influence of this parameter on the results is investigated by means of a numerical case study considering different mesh configurations and sizes.

Considering the results of the numerical simulations presented in Section 3.3 and 3.4.4 the following conclusions can be drawn:

- The mode I parameters have a significant impact in the structural response and the estimation of such parameters by means of IA leads to very good results. Consequently, the development of a reliable, robust and automatic approach to conduct IA is of utmost importance for improving the reliability of the simulations of FRC elements.
- The good predictive performance of the available constitutive models in FEMIX V4.0 is demonstrated by the results shown in the prestressed FRC railway sleeper case study. In this case, the

inelastic behaviour of concrete was simulated by means of the plastic damage multidirectional smeared crack model available in FEMIX V4.0 and the model was able to accurately capture the structural response both at centre section and rail-seat section and the obtained crack patterns were coherent with the observed experimental ones.

- The methodology proposed by Oliver and Idelsohn [205] does not produce significant differences in the results both in terms of force-displacement curves or crack patterns when regular mesh configurations (aspect ratio  $\approx 1$ ) are used.
- The study regarding the “mosaic” type meshes, comprising two different variants of FE aspect ratios, revealed that the herein implemented methodology, designated in the results as  $Ol_{FE}$  better captured the experimental response, when compared to the remaining methodologies.
- The crack patterns obtained for the analysed mosaic type meshes (MO1 and MO2) and the methodologies  $Ol_{IP}$  and  $Ol_{FE}$ , revealed to be more coherent in terms of crack width uniformity for cracks originated in adjacent elements with distinct aspect ratios, and therefore, produced more realistic crack patterns, indicating that when irregular/distorted meshes are used, the methodologies herein implemented can lead to a better results.

# 4 A New Inverse Analysis Approach To Derive The Fracture Mode I Parameters of FRC

## 4.1 Introduction

*This Chapter describes the development of a new inverse analysis (IA) approach to derive the fracture mode I parameters of fibre reinforced concrete (FRC) by using the experimental data obtained from three-point notched beam bending tests (3PNBBT) and round panel tests supported on three points (RPT-3PS). The proposed approach is based on a global fitting strategy, in which the numerical response is simulated by means of analytical models, and fitted to the experimental results by modifying the variables that govern the tensile behaviour of FRC. The procedure relies on a bounded multi-variable nonlinear least squares fitting algorithm, coupled with an automatic updating module of the input parameters based on the force deviation error between numerical and experimental results. The performance and predictive potential of the proposed approach are assessed by means of experimental results from 3PNBBT and RPT-3PS retrieved from the literature. Also, the robustness of the implemented methodology is investigated by evaluating the impact of the initial guess of the input variables in the derived fracture parameters. Finally, the developed tool is applied within the context of the analysis of a real-scale FRC beam, where the mode I fracture parameters were derived using the newly proposed methodology. The novelties of the herein developed IA approach can be summarised in the following key aspects:*

- Possibility to fix or include the tensile strength and Young's modulus in the IA procedure;*
- Different data point sampling density can be used, giving the user the flexibility to refine the modelled curve in critical regions without compromising computational efficiency;*
- The automatic variable updating procedure based on the force deviation between the numerical and experimental response makes the IA process less sensible to the provided initial input of the user;*
- Possibility of implementing additional analytical models to simulate different experimental setups.*

*Published in: [10.1016/j.engfracmech.2021.107613](https://doi.org/10.1016/j.engfracmech.2021.107613)*

## 4.2 Proposed inverse analysis approach

### 4.2.1 General overview of the developed tool

For deriving the fracture mode I parameters by means of IA two main strategies are usually followed. The first strategy consists in determining the  $\sigma_n^{cr} - w_n^{cr}$  relationship in a point-by-point manner, where the minimisation of the discrepancy observed between the experimental and numerical data points leads to the definition of a new point in the stress crack width relationship. The main advantage of this approach relies in the fact that the  $\sigma_n^{cr} - w_n^{cr}$  is determined without an initial assumption about its shape. On the other hand, the determination of each new point depends on the previous one, which might lead to the accumulation of errors [209].

The second strategy is based on a global optimisation procedure where the  $\sigma_n^{cr} - w_n^{cr}$  relationship is defined a-priori, and its governing parameters are modified in consequence of the optimisation procedure. This approach allows the user to choose between different types of  $\sigma_n^{cr} - w_n^{cr}$  relationships, i.e. nonlinear continuous functions or multi-linear diagrams. The main disadvantage of this approach is the tendency to produce spurious solutions due to the existence of local minima in the objective function.

The developed IA tool, henceforth designated COFIT (the name attributed to the corresponding developed software), is based on the second strategy, and is comprised by two main modules (Global fitting module and Parameter updating module) as depicted in Figures 72 and 73. The first module, related to the global fitting procedure, consists in a nonlinear least-squares fitting (NLSQ) algorithm that minimises the error function given by Equation (4.1),

$$\min \sum_{i=1}^n \left( F_{Exp}^i - F_{Num}^i \right)^2 \quad (4.1)$$

where  $n$  is the number of numerical data points. The experimental data (deflection, crack mouth opening displacement (CMOD) or crack tip opening displacement (CTOD)) is discretised for evaluation of the deviation between experimental and numerical values. Hence,  $F_{Exp}^i$  is the interpolated experimental data point (because the discretisation level aimed by the user can lead to values not registered experimentally) and  $F_{Num}^i$  is the predicted numerical data point by the model.

For this purpose, a library designated by MPFit [210] implemented in the C language is used to conduct the NLSQ fitting. This library is an implementation of the least square fitting library MINPACK-1 [211], which is based on the Levenberg-Marquardt algorithm (LMA) [212, 213].

The LMA is a broadly used NLSQ fitting technique that combines two minimisation methods, namely, the Gauss-Newton and gradient descent methods. In the gradient descent method the sum of the residuals is minimised by updating the variables in the direction of the steepest-descent of the error function, whereas in the Newton-Gauss method, the sum of the residuals is reduced by assuming that the minimised function is locally quadratic and by determining the minimum value of the quadratic function. The LMA combines the two aforementioned methods by relying on the gradient descent method when the

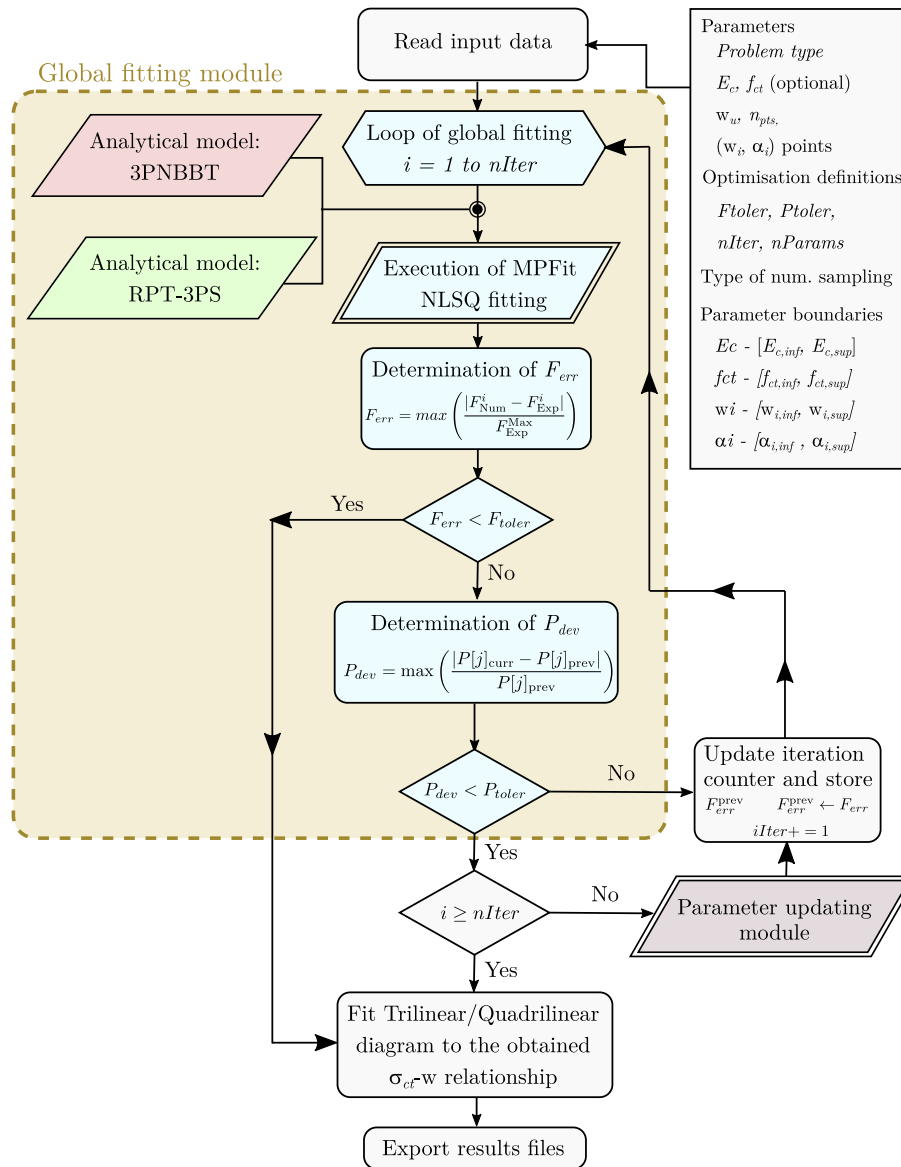


Figure 72: Global overview of the proposed IA algorithm.

parameters are far from the minimum (significant reduction of the sum of the residuals between iterations), and the Newton-Gauss when the solution is close to the optimal value (slow reduction of the sum of the residuals). For a detailed description of the theoretical aspects of the LMA and its implementation in MINPACK-1 and MPFit the reader is referred to Markwardt [210] and Moré [211].

Also, MPFit allows the definition of a lower and upper boundary for each fitting variable, which constitutes an important feature, since the restricted variation range of the variables reduces the probability of obtaining spurious solutions. Nonetheless, it is possible that in some occasions the obtained solution corresponds to a local minimum of the objective function, specially if the initial guess of the variables is very far from the desired solution. Hence, in order to tackle this issue, an automatic updating strategy for the optimised variables was coupled to the global fitting procedure.

The parameter updating algorithm (see Figure 73) is the second module of COFIT, which consists in

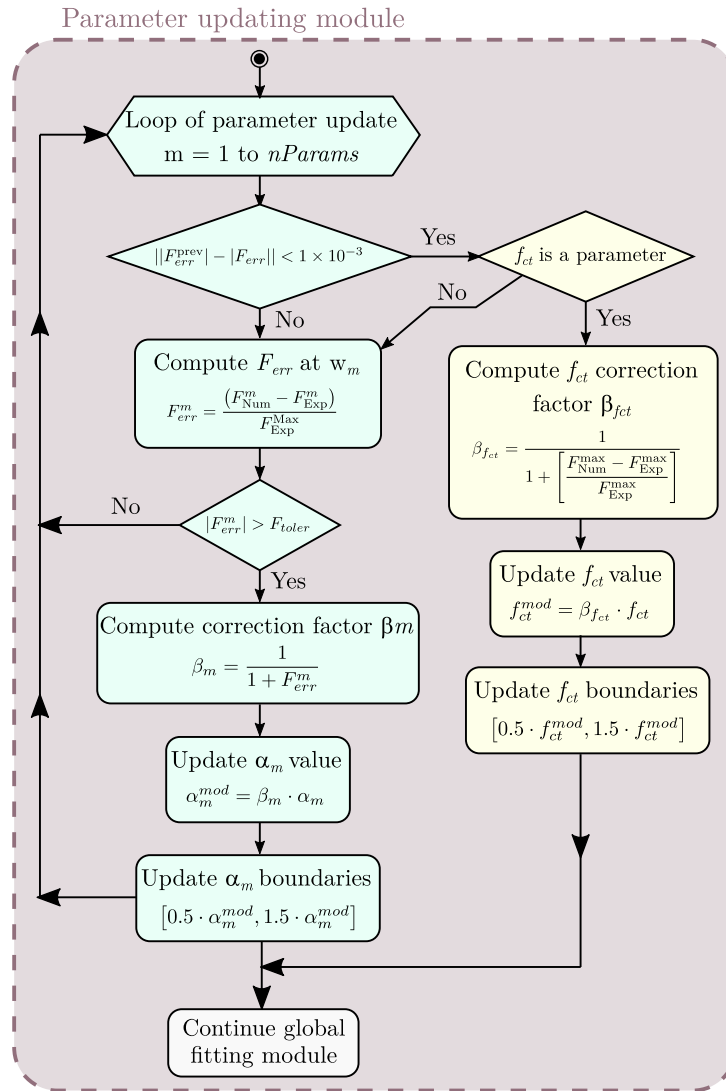


Figure 73: Algorithm of the parameter updating module.

modifying the optimised variables and boundaries, related to the  $\sigma_n^{cr} - w_n^{cr}$  relationship, in an automatic fashion, based on the deviation error between the numerical and experimental curve corresponding to the region of each  $w_i$  value. After the variable modification, the fitting algorithm is triggered once again, leading to a new set of optimal parameters. The main purpose of this algorithm is to ensure that a global solution for the set of input parameters is obtained, even if the initial guess is far from the optimum solution, and in this way reducing the sensibility of COFIT to the initial input provided by the user.

The governing variables of COFIT are, the concrete tensile strength ( $f_{ct}$ ), Young's modulus ( $E_c$ ), the coordinates ( $w_i, f_{ct} \cdot \alpha_i$ ) and ultimate crack width ( $w_u$ ), which define the material tensile behaviour (see Figure 77). The  $f_{ct}$  and  $E_c$  that define the pre-peak tensile response Figure 77a, can be fixed (optionally), excluding them from the optimisation process. In this case, the variables defining the  $\sigma_n^{cr} - w_n^{cr}$  relationship will be the ones to be obtained. This constitutes a major advantage since  $f_{ct}$  and  $E_c$  have a great impact in the results and gives the user the possibility to fix these values according to his experience or

obtaining them from independent tests. In addition to the material parameters, the user also must specify the type of problem to be analysed (3PNBBT or RPT-3PS), and provide additional parameters regarding the optimisation procedure, namely, the force deviation tolerance ( $F_{toler}$ ), parameter variation tolerance ( $P_{toler}$ ), number of global fitting iterations ( $nIter$ ), number of optimisation parameters ( $nParams$ ) and type of numerical sampling procedure (uniform or uneven) that will reflect the discretisation scheme of the numerical curve. For each material parameter ( $E_c$ ,  $f_{ct}$  and  $w_i$ ,  $f_{ct} \cdot \alpha_i$ ) the user must provide an initial guess and the corresponding lower and upper limit.

Hence, the IA strategy implemented in COFIT can be summarised in the following steps:

1. The input parameters and experimental data are read from the input data file. The parameters that define the material behaviour are stored in the fitting variables vector  $\underline{P} = [E_c; f_{ct}; w_i; \alpha_i; \dots; w_n; \alpha_n]$  and the corresponding limits in the matrix  $\underline{L}$  with two columns defining the lower and upper limits, respectively. During this initial stage, the experimental curve is pre-processed, eliminating parasitic snap-backs, in order to ensure a monotonic increase in the measured displacement;
2. Depending on the problem type chosen by the user (3PNBBT or RPT-3PS), the corresponding analytical model is used to compute the numerical response. Hence, the vector of parameters  $\underline{P}$  and matrix  $\underline{L}$  are provided to the global fitting algorithm (MPFit) and the sum of the square of the residuals between experimental and numerical curve (computed using the selected analytical model) is minimised. In order to ensure consistency between experimental and numerical data points, the experimental force values ( $F_{Exp}^i$ ) are interpolated so that numerical ( $F_{Num}^i$ ) and experimental values correspond to the same abscissa ( $w_{ctod}/w_{ctod}/\delta$ ). The parameters of vector  $\underline{P}$  that lead to the lowest residuals are the output of this procedure;
3. After obtaining the optimised parameters  $\underline{P}$ , the force deviation error is computed for each numerical data point by means of Equation (4.2), and the maximum value stored. If the maximum error ( $F_{err}$ ) is lower than a given tolerance ( $F_{toler}$ , provided by the user), the optimisation process is completed and the output is written;

$$F_{err} = \max \left( \frac{|F_{Num}^i - F_{Exp}^i|}{F_{Exp}^{Max}} \right) \quad (4.2)$$

4. If  $F_{err} > F_{toler}$ , the force tolerance criterium was violated and the parameter deviation is computed for each parameter of vector  $\underline{P}$  (from  $j$  to  $nParams$ ) and the maximum value stored in the variable  $P_{dev}$  as given by Equation (4.3),

$$P_{dev} = \max \left( \frac{|P[j]_{curr} - P[j]_{prev}|}{P[j]_{prev}} \right) \quad (4.3)$$

where  $P[j]_{curr}$  and  $P[j]_{prev}$  is the  $j^{th}$  component of the vector  $\underline{P}$  of the fitting parameters of the current and previous fitting cycle, respectively. If the maximum parameter variation violates the

user defined tolerance ( $P_{toler}$ ), the fitting procedure is repeated using the optimised variables from the current iteration. The process continues until  $P_{dev} < P_{toler}$ ;

- When the parameter tolerance is fulfilled, it means that the force criterium was not met (since it is evaluated after the force tolerance check), which indicates that the parameters are not varying in consecutive fitting cycles. Hence, when this situation occurs, an automatic variable updating procedure is triggered. This process consists of multiplying the  $\alpha_m$  parameters by a corrective factor ( $\beta_m$ ) that is computed according to Equation (4.4),

$$\beta_m = \frac{1}{1 + \left( \frac{F_{Num}^m - F_{Exp}^m}{F_{Exp}^{Max}} \right)} \quad (4.4)$$

where  $F_{Num}^m$  and  $F_{Exp}^m$  are the numerical and experimental force values corresponding to the  $w_{cmod,m}$  value matching  $w_m$ , as shown in Figure 74.

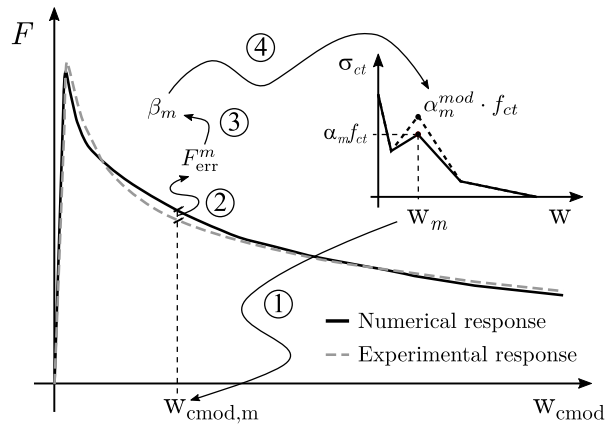


Figure 74:  $w_m$  mapping between the  $\sigma_{ct} - w_{cmod,m}$  relationship and global response.

Furthermore, the boundaries of the modified parameters are also updated according to the following rule:  $[0.5 \cdot \alpha_m^{mod}, 1.5 \cdot \alpha_m^{mod}]$  where  $\alpha_m^{mod}$  is the  $\alpha_m$  parameter multiplied by the corresponding corrective factor  $\beta_m$ . In addition, if  $f_{ct}$  is an optimisation parameter, and the error ( $F_{err}$ ) obtained in consecutive fitting iterations does not vary, the updating strategy employed to the  $\alpha_i$  parameters is applied to  $f_{ct}$ .

- Finally, the entire fitting process is repeated considering the previously modified  $\alpha_m$  (or  $f_{ct}$ ) values and lower and upper boundaries. The iteration cycle continues until the maximum number of optimisation iterations ( $nIter$ ), specified by the user, is reached or the force tolerance is met. If the algorithm is unable to achieve the force deviation tolerance, the best approximation of the experimental response, and the corresponding optimised parameters,  $\underline{P}$ , are exported.

The number of data points discretising the numerical curve has a major impact in the computation time of the fitting process. It would be impracticable to use the same number of points as the experimental



curve since, generally, thousands of readings are acquired during experimental tests and it would be a too high computing time process. Nonetheless, it is important to define a sufficient amount of points so that a satisfactory resolution of the experimental curve is obtained, and an adequate fitting is achieved.

COFIT has two possibilities for dealing with this aspect. The first possibility consists of providing the total number of data points into which the numerical curve will be discretised. In this case, the abscissa of the curve will be sampled in an uniform fashion (Figure 75a). However, this approach might prove to be inadequate in situations where just after the peak load and abrupt force decay occurs, followed by a smooth variation of the load. In fact, when the experimental curve has a very sinuous shape, a considerable amount of points is necessary in order to capture the main regions of the response with sufficient resolution, resulting in higher computational cost. Thus, in order to tackle this issue and keep the number of data points at an acceptable level, the user has the possibility to discretise the numerical curve in an uneven way, meaning that a different amount of points can be assigned to different areas of the curve. In Figure 75, a schematic representation of a possible numerical sampling strategy is presented, where 3 ranges of discretisation were adopted for the uneven discretisation approach.

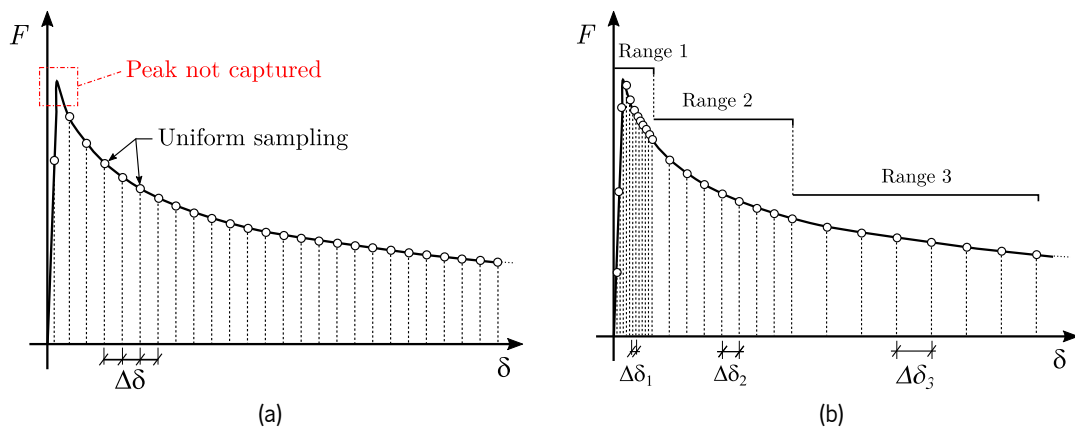


Figure 75: Numerical sampling approaches implemented in COFIT: (a) uniform sampling approach and (b) custom method with specification of different sampling in different regions of the response.

After the IA process is completed, another fitting is conducted, but this time to the optimised  $\sigma_n^{cr} - w_n^{cr}$  relationship. For this purpose, the user has the possibility to choose between a trilinear or quadrilinear tensile softening diagram in order to be used with the in-house developed finite element method (FEM) software FEMIX V4.0 [200], which will be used later in the simulation of the behaviour of real scale FRC structures.

#### 4.2.2 Strategy for simulating the response of 3PNBBT and RPT-3PS

The simulation of the response of 3PNBBT and RPT-3PS test setups in COFIT is accomplished by means of the analytical models proposed by Salehian et al. [194], which makes use of a numerical model proposed

by Barros and Figueiras [195] for deriving the moment-curvature response of the cross section of steel-fibre reinforced concrete (SFRC). In this model the cross-section is discretised in a given number of layers and different material properties and constitutive models can be assigned to each layer. In the present work, a simplified version is adopted by considering only one material model, constant layer width and thickness and only rectangular cross-sections.

This simple yet powerful model (Figure 76) is used to derive the moment-rotation curve, which combined with the concept of nonlinear hinge, is capable of computing the force-deflection response of beams subjected to bending. To this end, the rotation at the extremities of the nonlinear hinge is gradually incremented and the contribution of each layer is computed based on the strain distribution originated by the imposed rotation.

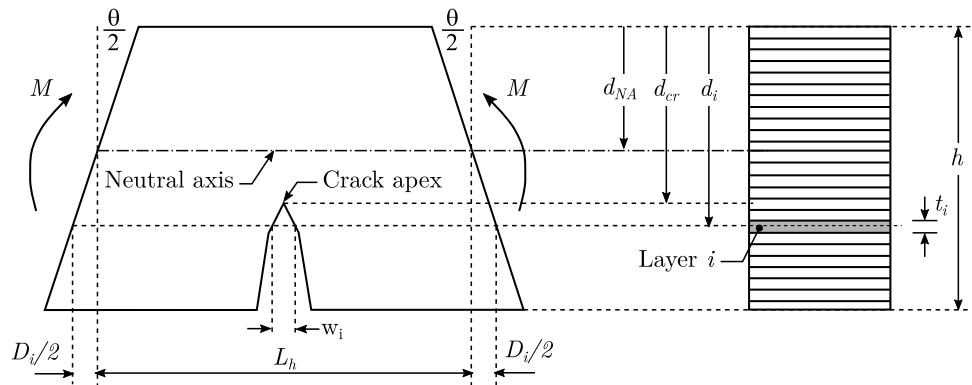


Figure 76: Schematic representation of the nonlinear hinge model subjected to bending: hinge deformed configuration and layered cross sectional model on the left and right, respectively (adapted from [194]).

To simulate the nonlinear behaviour of concrete, the constitutive models depicted in Figure 77 are adopted.

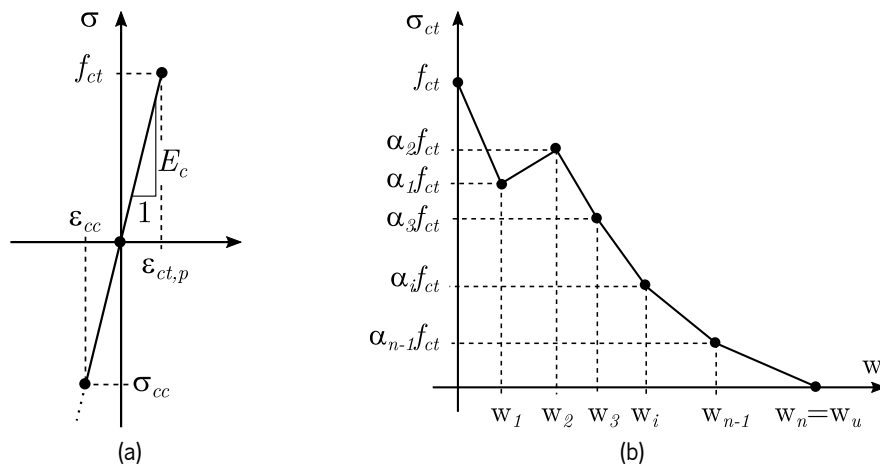


Figure 77: Tensile constitutive model of FRC in tension: (a) pre-peak stress-strain, and (b) post-peak multi-linear stress-crack width diagram [194].

The compressive and tensile pre-peak behaviour is given by Equations (4.5) and (4.6),

$$\sigma_{cc}(\varepsilon_{cc}) = E_c \cdot \varepsilon_{cc} \quad \varepsilon_{cc} \leq 0 \quad (4.5)$$

$$\sigma_{ct}(\varepsilon_{ct}) = E_c \cdot \varepsilon_{ct} \quad (0 \leq \varepsilon_{ct} \leq \varepsilon_{ct,p}) \quad (4.6)$$

where  $\varepsilon_{cc}$  is the compressive strain,  $\varepsilon_{ct}$  is the tensile strain and  $\varepsilon_{ct,p}$  is the tensile strain corresponding to the tensile strength.

The post-peak response of FRC is defined by means of a multi-linear stress-crack width relationship given by Equation (4.7),

$$\sigma_{ct}(w) = \left[ \alpha_m + (\alpha_{m+1} - \alpha_m) \cdot \frac{w - w_m}{w_{m+1} - w_m} \right] \cdot f_{ct} \quad (w_m < w \leq w_{m+1}) \quad (4.7)$$

where  $m$  is a post-peak branch counter, ranging between 1 and  $n_{branches}$ . In this equation  $\alpha$  is a stress multiplication factor that relates  $f_{ct}$  with  $\sigma_{ct,m}$ ,  $\alpha_m = \sigma_{ct,m}/f_{ct}$ , and  $w_0 = 0$ ,  $w_n = w_u$ ,  $\alpha_0 = 1$  and  $\alpha_n = 0$ . In the current version of COFIT, only FRC of tensile strain softening or pseudo-hardening behaviour can be simulated, since it is assumed that the tensile deformation is localised in the opening of a critical crack.

In the algorithm proposed by Salehian et al. [194] for determining the moment-rotation curve, the neutral axis (NA) depth is sought using a brute-force approach, where subsequent increments of NA positions are considered until the force equilibrium is reached. In COFIT, the Brent's root finding algorithm [214] is used to seek the NA position, which drastically reduces the computational time of this operation. In addition, the same root-finding algorithm is used to determine the crack width when the tensile strength is violated in a given layer.

The numerical response of 3PNBBT is simulated by means of a nonlinear hinge model combined with the aforementioned moment-rotation algorithm, in which the prismatic beam is assumed composed by two regions, the nonlinear hinge, subjected to an equivalent uniform bending moment ( $M_u$ ) and the remaining areas where the behaviour is linear elastic (Figure 78). The nonlinear behaviour occurs within the region of the nonlinear hinge, whose length,  $L_h$ , is considered to be equal to the height of the cross-section over the notch, as recommended by Model Code 2010 (MC2010) [203].

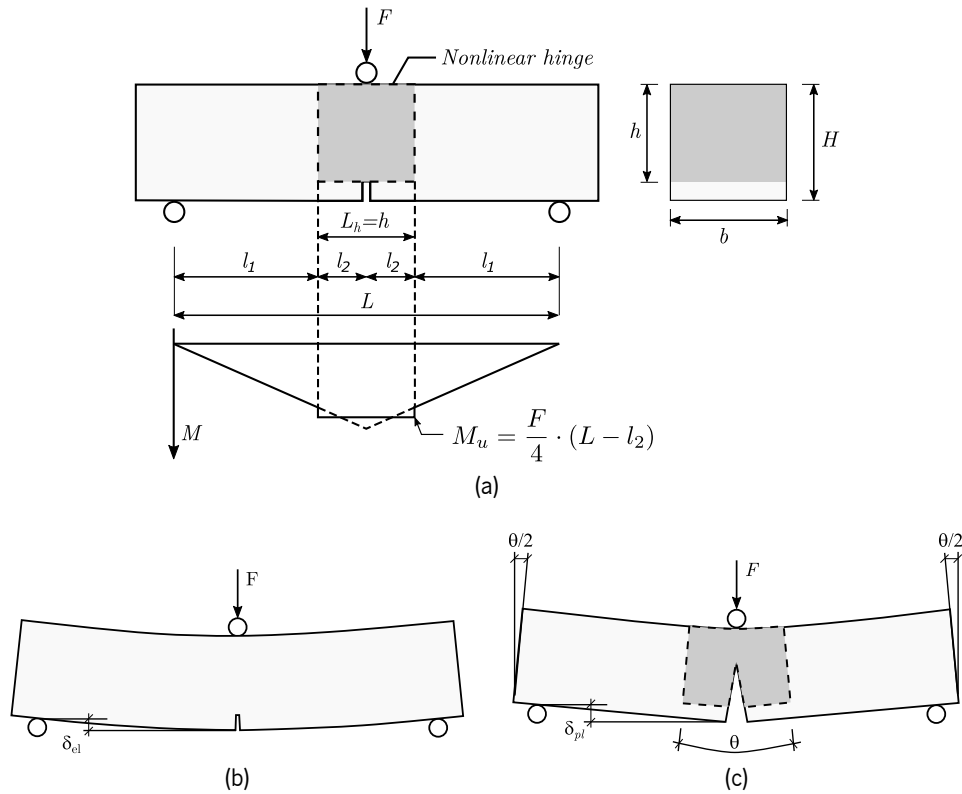


Figure 78: Idealization of nonlinear mechanisms in a 3PNBBT for the prediction of its deflection: (a) elastic and (b) plastic components of the beam deflection.

The force-deflection is obtained by superimposing the elastic and plastic deflection of the prismatic specimen:

$$\delta_v = \delta_{el} + \delta_{pl} \quad (4.8)$$

$$\delta_{el} = \frac{F}{2E_c I_2} \cdot \left[ \frac{l_2^3}{3} + l_2^2 \cdot l_1 + l_2 \cdot l_1^2 + \frac{I_2}{I_1} \cdot \frac{l_1^3}{3} \right] \quad (4.9)$$

$$\delta_{pl} = \frac{\theta L}{4} \quad (4.10)$$

where  $l_1$  and  $l_2$  are the lengths of the linear and nonlinear regions of the beam,  $\theta$  is the rotation of the nonlinear hinge,  $I_1$  and  $I_2$  are the second moment of inertia of the section of each beam region:

$$I_1 = bH^3/12 \quad (4.11)$$

$$I_2 = bh^3/12 \quad (4.12)$$

Besides the force-deflection curve, COFIT also has the possibility to conduct IA based on the crack mouth opening displacement ( $w_{cmo}$ ) or crack tip opening displacement ( $w_{ctod}$ ). The CMOD value is obtained by assuming that the tip lies in the NA, while the CTOD value is interpolated, as depicted in Figure 79 and given by Equation (4.13).

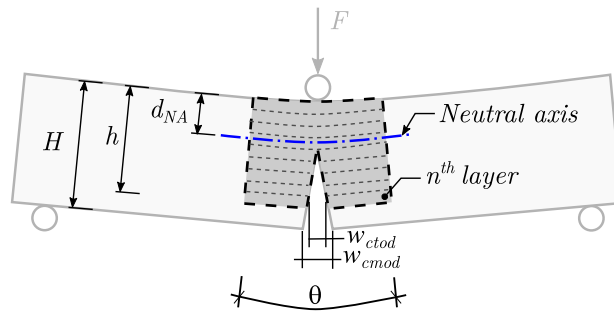


Figure 79: Schematic representation of the CTOD and CMOD entities.

$$w_{cmod} = w_{ctod} \cdot \frac{(H - d_{NA})}{(h - d_{NA})} \quad (4.13)$$

For obtaining the numerical response of RPT-3PS setup, the model described in Salehian et al. [194] is also adopted. The RPT-3PS is a statically determined test in which the rupture mechanism is typically formed by three rigid plates. Radial cracks usually occur at  $120^\circ$  apart, in which the rotation axis of two adjacent plates intercept in a point located within an imaginary line with the direction of the crack dividing the two plates. However, this is not always the case, and sometimes the cracks are deviated, at an angle  $\beta$ , from the middle line between two supports. This results in a different location of the interception point of the rotation axis of two contiguous plates, which leads to the formation of two imaginary pivot points. Figure 80 presents the geometric entities and parameters involved in the formulation of the analytical approach for the rotational crack analysis.

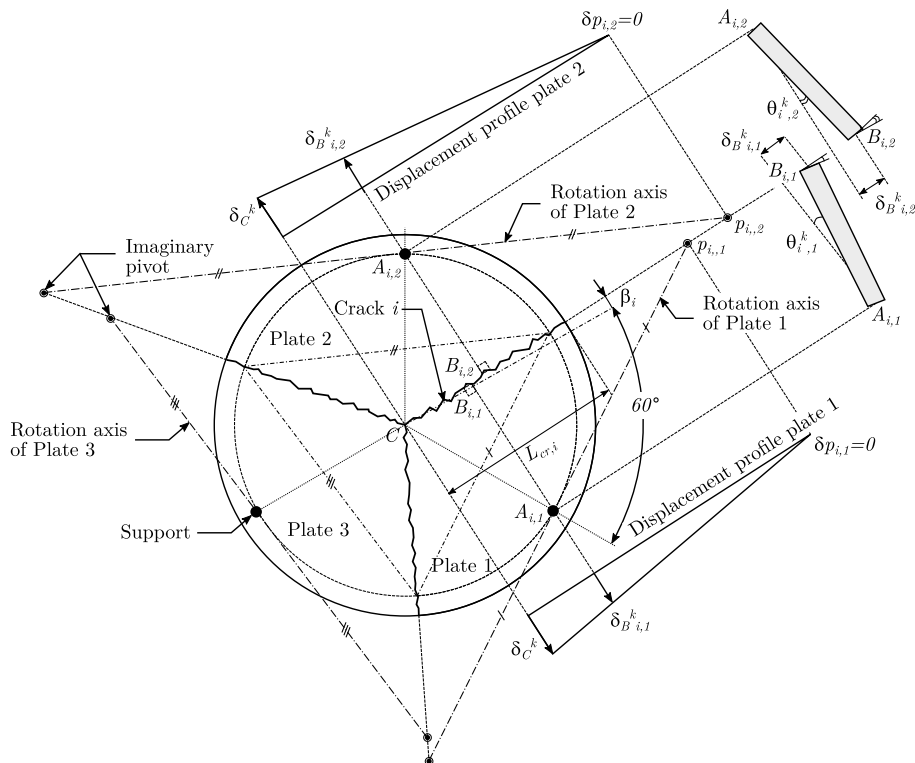


Figure 80: Analysis of the crack rotation kinematic mechanism [194].

Considering a crack  $i$ , with a deviation angle  $\beta$  relatively to the median line between two supports (Figure 80), the rotation axis of adjacent plates is defined by tracing an imaginary line, tangent to the support point and parallel to the line that unites the intersection points of the two consecutive cracks (rotation axis of plates 1/2 in Figure 80), and the perimeter support line. The intersection points of the rotation axis of each plate with an imaginary line aligned in the crack direction, form the imaginary pivot points  $p_{i,1}$  and  $p_{i,2}$ . Each plate develops a vertical displacement profile that is 0 at the corresponding pivot point and maximum in the centre of the panel. With this information it is possible to establish a relation between the vertical displacement of each plate and the corresponding panel rotation.

The force-deflection curve of the panel is obtained by increasing in a stepwise manner the central displacement of the panel. Thus, for a certain increment of displacement,  $\delta_c^k$ , and for each radial crack, the vertical displacements in the points  $B_{i,1}$  and  $B_{i,2}$  are obtained. Subsequently, the rotation of each plate is calculated and the overall rotation for the step  $k$  and crack  $i$  is computed. The bending moment ( $M_i^k$ ) per metre is obtained by means of the flexural model and multiplied by the crack length ( $L_{cr,i}$ ). The process is repeated for every crack and  $F^k$  is finally computed.

## **4.3 Assessment and validation of the developed approach**

### **4.3.1 Introduction**

In this section the predictive performance and robustness of COFIT is assessed. For this purpose, COFIT is used to derive the fracture mode I parameters from experimental results of 3PNBBT and RPT-3PS published in the literature, as well as from experimental results of 3PNBBT of SFRC notched specimens, tested in the context of a blind simulation competition organised by *fib* WG 2.4.1[134]. The IA simulations were conducted in a desktop PC with an average system configuration (3.6GHz octa-core CPU with 32GB of RAM), and the runtime for each case is presented.

### **4.3.2 Three-point notched beam bending tests (3PNBBT)**

For the application of COFIT to 3PNBBT, the experimental results obtained by Zamanzadeh et al. [215], Soltanzadeh [216] and Soltanzadeh et al. [217] are used.

Soltanzadeh [216] conducted 3PNBBT to analyse the flexural behaviour of High Performance Fibre Reinforced Concrete (HPFRC). The test was carried out on prismatic beams of same dimensions and notch geometry of those in Soltanzadeh [216] and the results were obtained in terms of force-deflection. Also, Soltanzadeh et al. [217] analysed different methods for characterising and simulating the post-cracking behaviour of steel-fibre reinforced self-compacting concrete (SFRSCC) and, part of the study was related to the characterisation of the post-cracking behaviour of SFRSCC specimens by means of 3PNBBT. The test was carried out on prismatic beams with 150x150 mm<sup>2</sup> cross section with a total length of 600 mm,

500 mm span and a notch depth of 25 mm at midspan, however, in Soltanzadeh et al. [217] the results were obtained in terms of force-CMOD.

The results obtained from the inverse analysis of the experimental results collected by Soltanzadeh [216] and Soltanzadeh et al. [217] are presented in Figure 81, and for each case, the global response and the obtained  $\sigma_n^{cr} - w_n^{cr}$  relationship are presented.

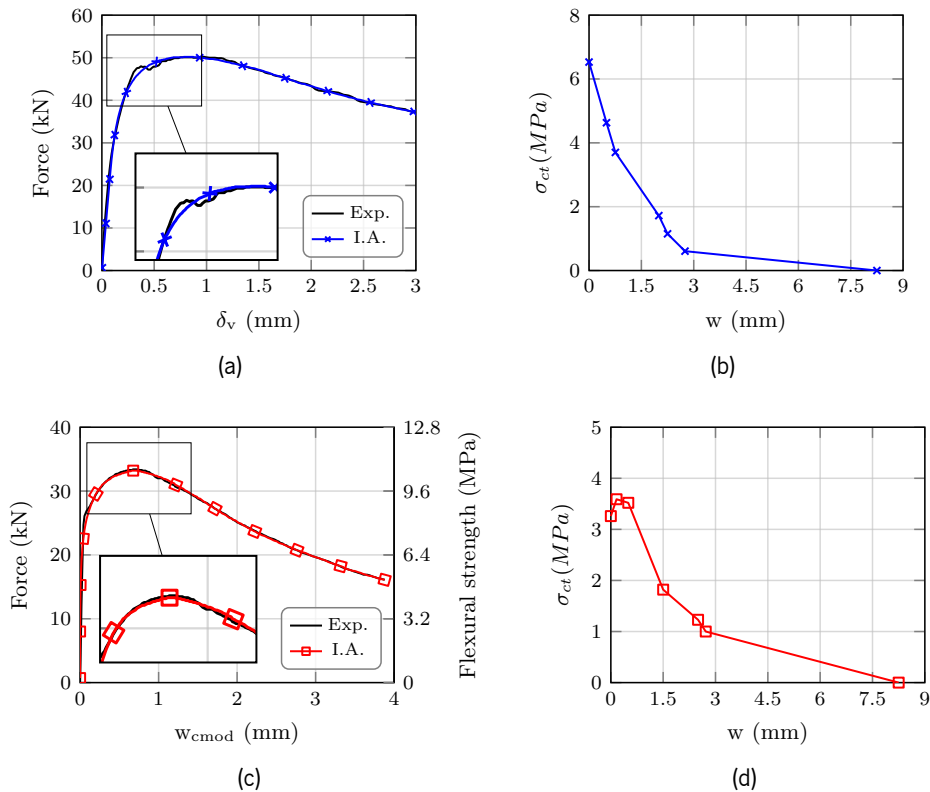


Figure 81: Results of the inverse analysis: (a) experimental results of 3PNBBT in terms of force-deflection [216] and (b) in terms of force-CMOD [217], (c) and (d) obtained  $\sigma_n^{cr} - w_n^{cr}$  for the results shown in (a) and (b), respectively.

The results of Figure 81 show that a very good agreement between the numerical and experimental responses is obtained for both force-deflection (Figure 81a) and force-CMOD situations (Figure 81c). Furthermore, a good prediction of the peak load is also achieved (Figures 81a and 81c).

Regarding the  $\sigma_n^{cr} - w_n^{cr}$  relationships and concerning the results shown in Figure 81b, the tensile strength seems higher than the expected one, since according to the MC2010 recommendations and considering the compressive strength obtained experimentally ( $\approx 60$  MPa), the tensile strength would be 4.1-4.4 MPa. However, this tensile strength is in agreement with the one obtained from the values of the splitting tensile tests published in Soltanzadeh [216] on samples of the same material.

Concerning the results of Figure 81d, one can also note that the configuration of the multi-linear diagram has allowed to capture perfectly the full response recorded experimentally. In addition, the value of tensile strength obtained for this case is also aligned with the results published in Soltanzadeh et al.

[217], since the average flexural tensile strength at the limit of proportionality (maximum load achieved at a CMOD of 0.05 mm) was 8.30 MPa.

Zamanzadeh et al. [215] evaluated the structural performance in bending and shear of recycled steel-fibre reinforced concrete (RSFRC) beams. For this purpose, recycled steel fibres (RSF) from waste rubber tires were used in an experimental program involving prismatic specimens with 45, 60 and 90 kg/m<sup>3</sup> of recycled steel fibres. Hence, 3PNBBT were carried out in RSFRC specimens and in industrial steel-fibre reinforced concrete (ISFRC) specimens for comparison purposes. The experimental results obtained by Zamanzadeh et al. [215] are used in the context of the present work to conduct IA using COFIT (Figure 82).

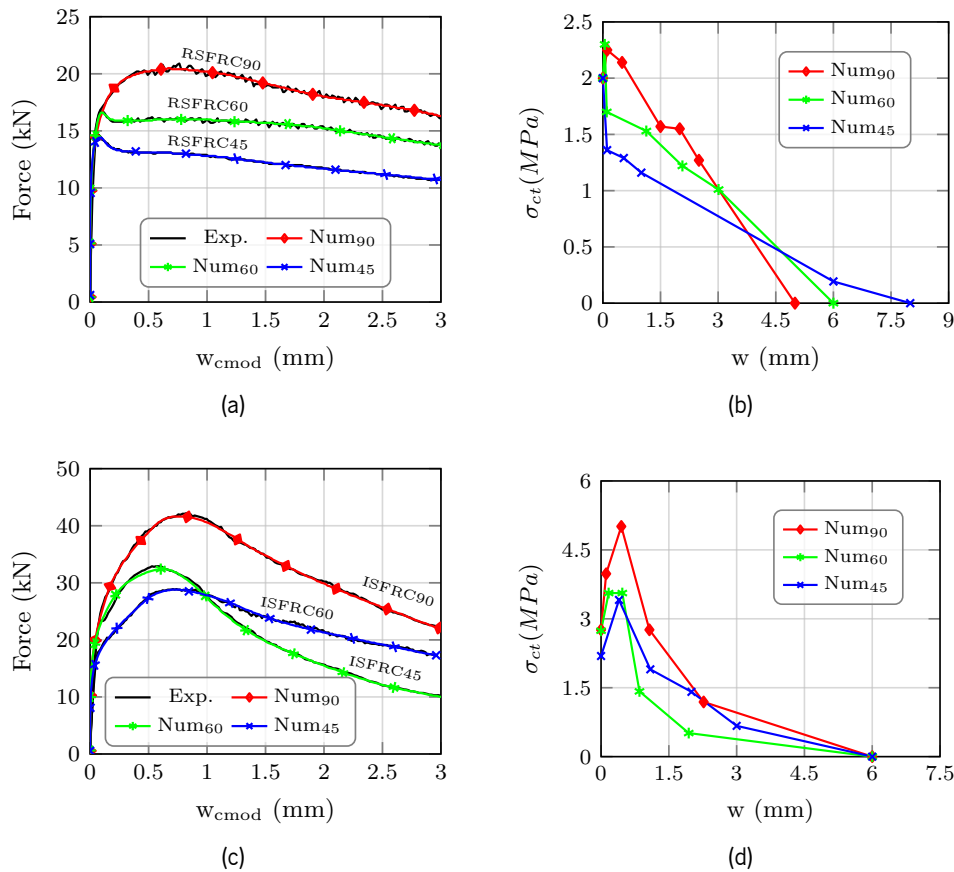


Figure 82: Results of the inverse analysis: (a)/(c) comparison between experimental and numerical responses for RSFRC/ISFRC specimens and (b)/(d) the corresponding  $\sigma_n^{cr} - w_n^{cr}$  relationship.

Considering the results presented in Figure 82, and regarding the numerical and experimental global responses (Figures 82a and 82c), it is possible to state that a very good agreement is obtained in all regions of the experimental responses (pre-peak and post-peak), for both RSFRC and ISFRC specimens. In addition, and regarding the  $\sigma_n^{cr} - w_n^{cr}$  relationship, the results are coherent with the global response, showing that the developed approach is capable of capturing both softening and pseudo-hardening behaviours.



Using finite element analysis (FEA) to estimate the fracture mode I parameters by IA is a well-established approach in the literature. In the present work, the conventional IA by employing FEM is compared to the herein developed tool, using experimental results from 3PNBBT of 10 SFRC notched specimens. These results were provided by *fib* W.G. 2.4.1 [134] within the context of a blind simulation competition of two SFRC real-scale beams.

Hence, the FEM simulation was conducted in FEMIX V4.0 computer program [200], using a multi-directional fixed smeared crack approach. For simulating the material nonlinear behaviour in fracture mode I, a quadrilinear tensile softening relationship was used (Figure 83b). Regarding the characteristics of the finite element (FE) model, the prismatic specimens with 550x150x150 mm were simulated by means of 4 node plane stress FEs, considering a 2x2 Gauss-Legendre (G-L) integration scheme, except for the FE located in the symmetry axis, above the notch, to which were assigned a 2x1 G-L integration rule, and a crack band width ( $\ell_b$ ) equal to the square root of the area of the FE, which in this case corresponds to 5 mm. This layout of integration points forces the propagation of the crack to develop along the symmetry axis. A linear elastic behaviour was assigned to all elements except the three columns of elements exactly above the notch. The FE mesh, loading conditions and support conditions are depicted in Figure 83.

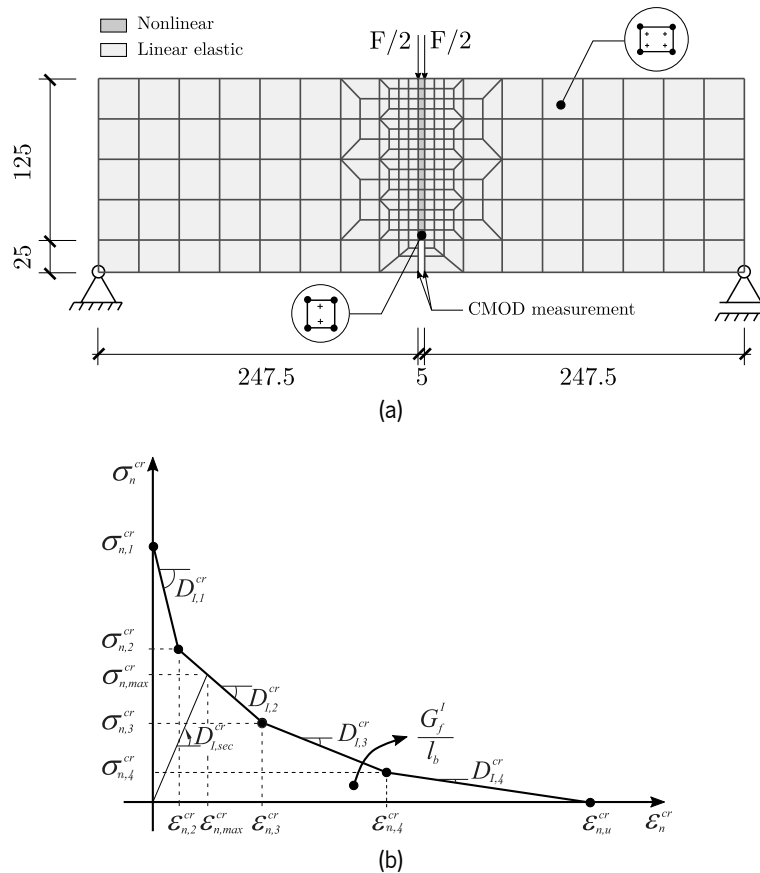


Figure 83: (a) FE mesh, loading and support conditions adopted in the simulation and (b) quadrilinear diagram used to simulate the material nonlinear behaviour of FRC ( $\sigma_{n,1}^{cr} = f_{ct}$ ,  $\sigma_{n,2}^{cr} = \alpha_1 \cdot \sigma_{n,1}^{cr}$ ,  $\sigma_{n,3}^{cr} = \alpha_2 \cdot \sigma_{n,1}^{cr}$ ,  $\sigma_{n,4}^{cr} = \alpha_3 \cdot \sigma_{n,1}^{cr}$ ,  $\varepsilon_{n,2}^{cr} = \xi_1 \cdot \varepsilon_{n,u}^{cr}$ ,  $\varepsilon_{n,3}^{cr} = \xi_2 \cdot \varepsilon_{n,u}^{cr}$ ,  $\varepsilon_{n,4}^{cr} = \xi_3 \cdot \varepsilon_{n,u}^{cr}$ ).

The IA was conducted iteratively by modifying the parameters of the quadrilinear tensile softening law (Figure 83b) until the numerical response matched the experimental one.

For the IA using COFIT, the numerical response was simulated by means of the approach described in Section 4.2.2, considering a force- $w_{cmod}$  response. In addition, the  $\sigma_n^{cr} - w_n^{cr}$  relationship was defined by 3 intermediate points (5 points in total with 4 branches) in order to establish a coherent comparison between the two approaches. The experimental response used in the IA corresponds to the average force-CMOD curve of the 10 SFRC specimens, and the results using both approaches are presented in Figure 84.

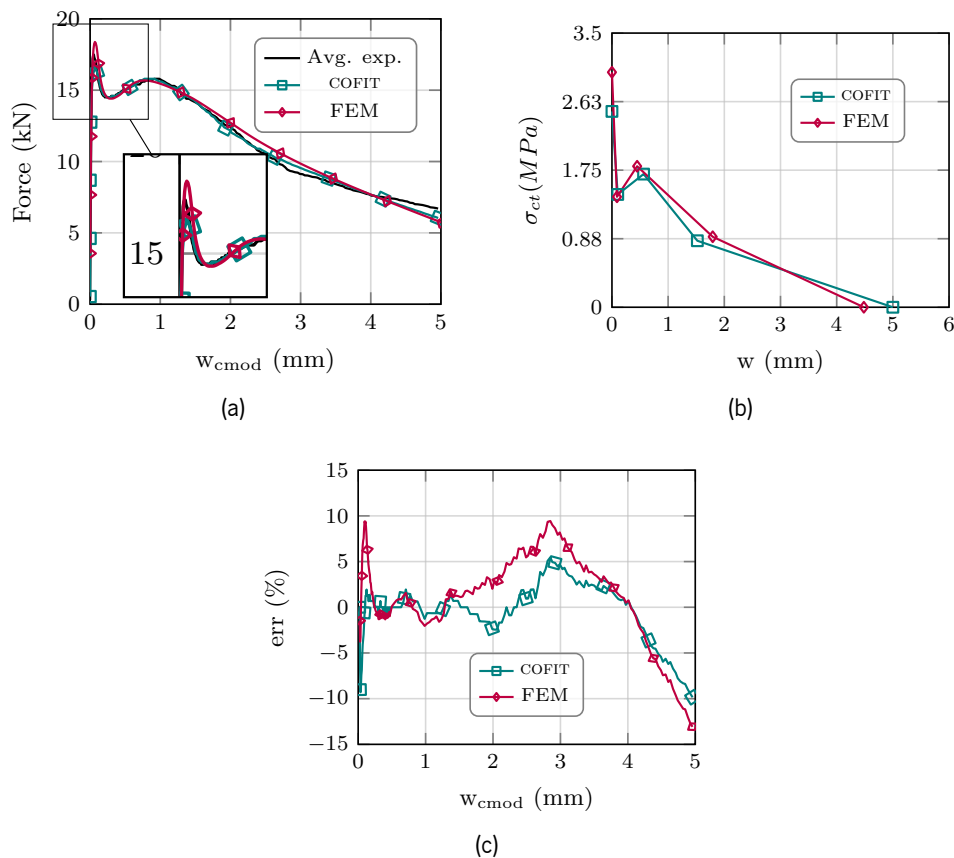


Figure 84: Results of the IA using FEM and COFIT approaches: (a) comparison in terms of force-CMOD, (b) comparison in terms of the tensile stress vs crack width.

In Figure 84a it is possible to observe that both approaches provide similar results in terms of force-CMOD response and  $\sigma_n^{cr} - w_n^{cr}$  relationship. The two approaches exhibit the same level of error in terms of peak prediction ( $\approx \pm 10\%$ ) except that COFIT provided a slightly better approximation in the post-peak response when compared to the conventional FEM approach (Figure 84c). However, despite providing similar results, COFIT IA execution is significantly faster, taking only 58.81s (Table 14) to derive the optimum parameters, and benefits from a simplified approach since no FEM modelling is required.

In Table 14 the runtime of each IA process for the 3PNBBT cases is presented. For each case, the total number of points defining the  $\sigma_n^{cr} - w_n^{cr}$  relationship as well as the number of sampling points used

to discretise the numerical curve are provided.

Table 14: Time elapsed during the IA process for 3PNBBT cases using COFIT.

Case	$\sigma_n^{cr} - w_n^{cr}$ Points	Sampling Points	Time elapsed (s)
Figure 81a	7	175	66.69
Figure 81c	7	200	58.79
Figure 82a(90)	7	200	116.42
Figure 82a(60)	7	200	76.35
Figure 82a(45)	6	250	112.60
Figure 82c(90)	6	200	76.74
Figure 82c(60)	6	200	63.92
Figure 82c(45)	6	200	73.94
Figure 84a	7	200	58.81

The results listed in Table 14 show that the fastest IA using COFIT required 58.79s and the slowest analysis needed 112.60s to complete. The average runtime of all the 3PNBBT was 78.25s, considering 200 sampling points (see Figure 75) and 12 optimisation parameters, which is usually sufficient to capture the critical regions of the experimental response. In what concerns the comparison of runtimes between the conventional FEM approach and COFIT, and despite the difficulty in quantifying the runtime of IA using FEM (since it heavily depends on user experience), it is reasonable to state that COFIT performs significantly faster (58.81s in this case) than the FEM-based approach.

### 4.3.3 Round panel tests (RPT-3PS)

For the case of RPT-3PS, the experimental results presented in the works of Montaignac et al. [186] and Frazão et al. [218] were used to derive the  $\sigma_n^{cr} - w_n^{cr}$  relationship by IA. The numerical responses were obtained by means of the RPT-3PS analytical model described in Section 4.2.2 in combination with the IA algorithm presented in Figure 72.

Montaignac et al. [186] conducted an experimental program for characterising the tensile behaviour of SFRC beams and panels by means of direct tensile test (DTT), 3PNBBT and RPT-3PS. For this purpose, specimens with different fibre geometry and volume ratios were fabricated, using steel fibres with 35 and 60 mm. The panels have a radius of 800 mm, radius to support of 375 mm, and a thickness of 80 mm. Two designations are adopted herein, namely, FRC35 and FRC60, corresponding to the fibre lengths of 35 and 60 mm, respectively. The results of the IA are presented in Figure 85 in terms of global response and  $\sigma_n^{cr} - w_n^{cr}$  relationship. In this case, the average results of the DTT of samples with the same material are also compared to the obtained post-cracking relationships.

In this case, two panels of each mixture type (35 mm and 60 mm fibres) were analysed. Regarding the force-central deflection curves presented in Figures 85a and 85c, the results show a very good agreement between the numerical prediction and experimental response, both in the pre-peak and post-peak phases, and for both mixture types (FRC35 and FRC60). In terms of the obtained  $\sigma_n^{cr} - w_n^{cr}$  relationship, and

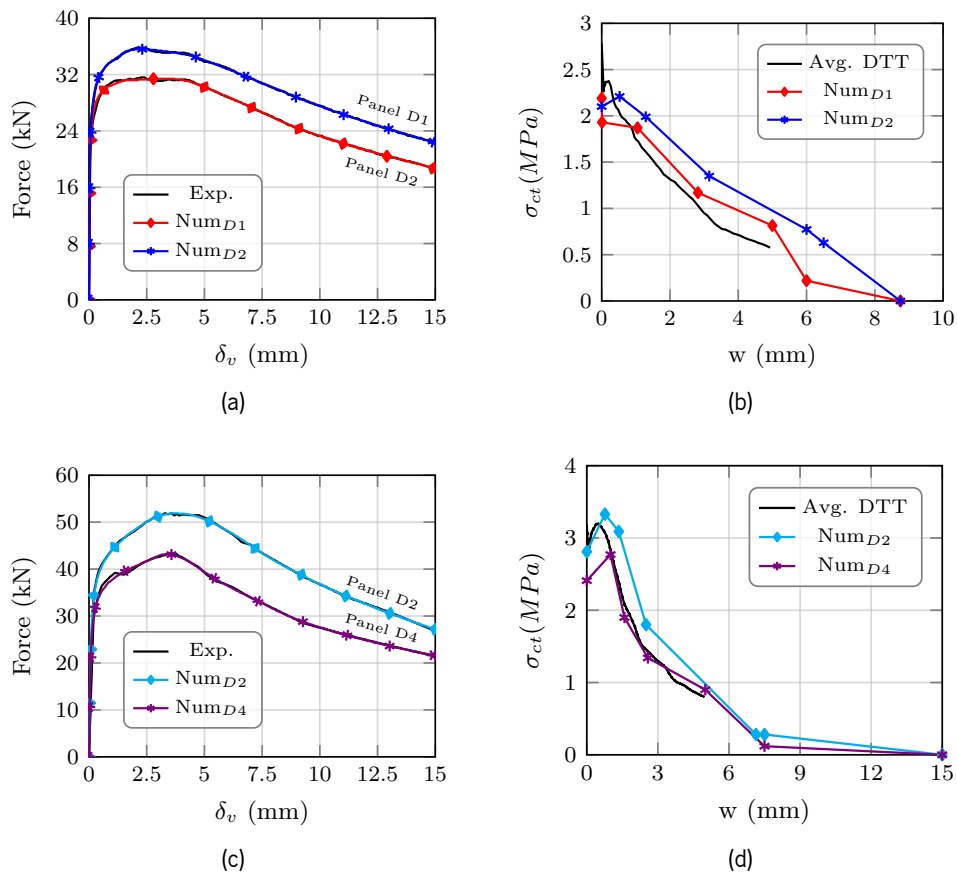


Figure 85: Results of the inverse analysis for the RPT-3PS of the experimental results obtained by Montaignac et al. [186]: (a)/(c) numerical and experimental force-central deflection curves and (b)/(d) the obtained  $\sigma_n^{cr} - w_n^{cr}$  relationships.

in case of the relationships presented in Figure 85b, it is possible to observe that the numerical results capture with reasonable accuracy the experimental relationship, with a slight underestimation of the tensile strength and a slight overestimation of the curve, nonetheless the results are quite good and coherent with the DTT. Regarding the post-cracking relationships obtained for the FRC60 panels (Figure 85d), the results show very good agreement between the numerical and experimental post-cracking tensile curves, since the overall shape of the  $\sigma_n^{cr} - w_n^{cr}$  relationship is very well captured as well as the tensile strength.

Frazão et al. [218] evaluated the long-term effects of chloride attack on the post-cracking behaviour of RSFRC by means of splitting tensile tests and RPT-3PS. For this purpose panels with 600 mm diameter and 60 mm thickness reinforced with 20 mm recycled steel fibres were tested. In this case, two responses were analysed and the results are presented in Figure 86. Once again the IA results are presented in terms of approximation between numerical and experimental response and the obtained  $\sigma_n^{cr} - w_n^{cr}$  relationship.

Also in this case, the results presented in Figures 86a and 86b show an excellent agreement between the experimental and the fitted numerical response, in terms of overall and peak load prediction.

The results in terms of runtimes are listed in Table 15, as well as, the total number of points defining the  $\sigma_n^{cr} - w_n^{cr}$  relationship, the number of sampling points used to discretise the numerical curve.

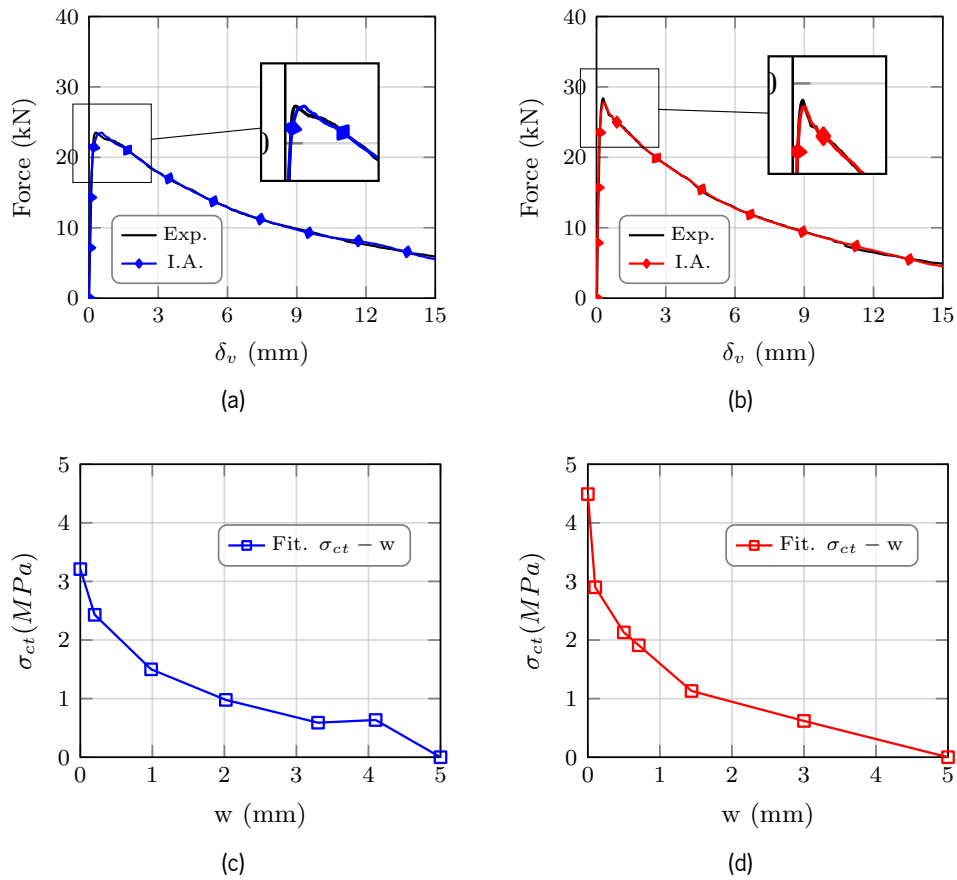


Figure 86: Results of the inverse analysis for the RPT-3PS of the experimental results obtained by Frazão et al. [218]: (a)/(b) Force-central deflection curve fitting and (c)/(d) the obtained  $\sigma_n^{cr} - w_n^{cr}$  relationship.

Table 15: Time elapsed during the IA process for RPT-3PS cases using COFIT.

Case	$\sigma_n^{cr} - w_n^{cr}$ Points	Sampling Points	Time elapsed (s)
Figure 85a(D1)	7	300	379.22
Figure 85a(D2)	7	300	186.17
Figure 85c(D2)	7	300	232.19
Figure 85c(D4)	7	300	379.61
Figure 86a	7	150	107.76
Figure 86b	7	200	189.73

In this case, the results listed in Table 15 show that IA of RPT-3PS take longer to compute, when compared to the 3PNBBT, requiring a minimum of 107.76 s and a maximum of 379.61 s to complete the IA, with an average runtime of 245.78 s, considering 300 sampling points and 12 optimisation parameters. This is justified by fact that the RPT-3PS problem involves the calculation of several cracks per panel, which increases the computational cost. Nonetheless, the presented runtimes are quite satisfactory.

#### 4.3.4 Impact of the initial guess for the stress-crack width relationship

The main disadvantage of using a global fitting approach for IA is that spurious solutions might be found if the variables are not bounded or if the initial guess is too far from a realistic solution. One of the advantages of COFIT is the fact that the parameters and respective boundaries are automatically updated based on the force deviation error. Hence, in order to assess the robustness of the algorithm and evaluate the impact of the initial guess on the results, the experimental data presented in Figure 81c was reanalysed considering distinct initial guesses for the  $\sigma_n^{cr} - w_n^{cr}$  relationship as shown in Figure 87a. The results in terms of global response and optimised  $\sigma_n^{cr} - w_n^{cr}$  relationship are presented in Figures 87b and 87c.

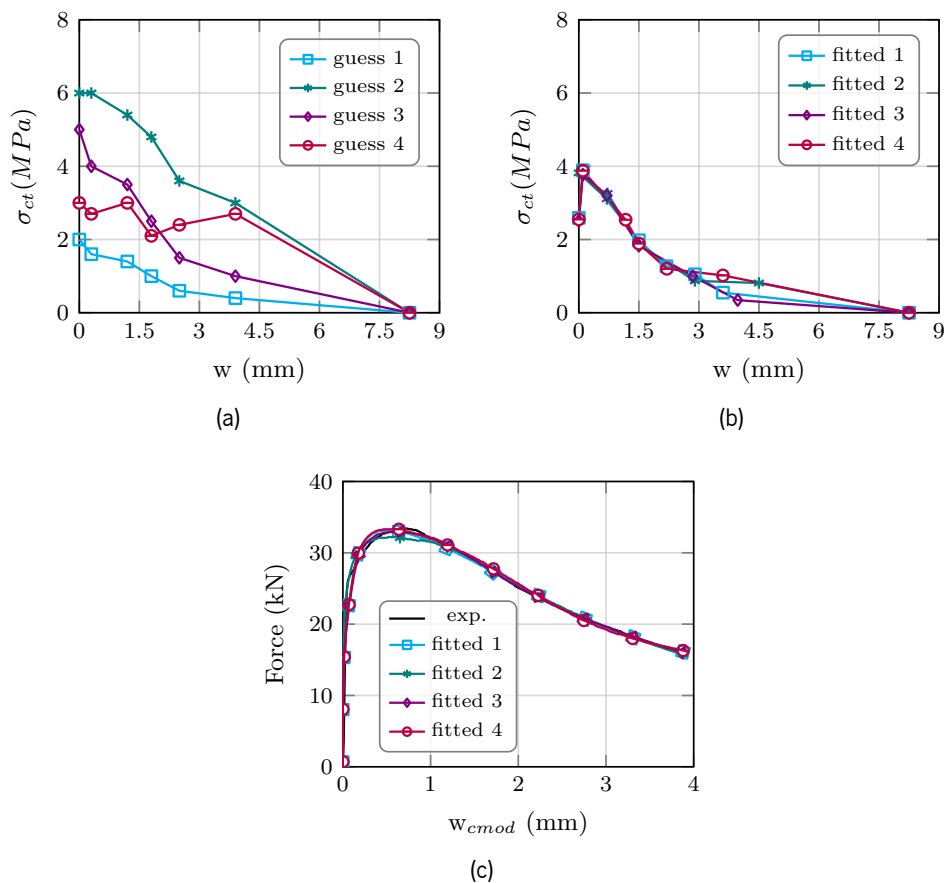


Figure 87: Impact of the initial  $\sigma_n^{cr} - w_n^{cr}$  relationship: (a) initial guesses for the post-peak multi-linear diagram, (b) optimised relationships and (c) results in terms of global fitted response.

The results presented in Figure 87 show that despite the differences in the provided  $\sigma_n^{cr} - w_n^{cr}$  relationships (Figure 87a) the algorithm converges to similar results both in terms of the final shape and values of the post-cracking diagram and global response (Figures 87b and 87c). In Figure 87b it is possible to observe some differences between the curves after  $w$  has reached 4 mm. This is due to the fact that the experimental response was only measured until 4 mm and consequently the points in the  $\sigma_n^{cr} - w_n^{cr}$  located beyond this value can not be fitted properly, hence the observed disparity.

This results demonstrate the robustness of the developed algorithm and its independence regarding the user input, granting that the obtained results are not severely affected by the user experience.

## 4.4 Application of the proposed IA approach to the analysis of a real-scale FRC beam

### 4.4.1 Introduction

In this section the numerical simulation of a three-point beam bending test of a real scale FRC beam reinforced with steel fibres and steel reinforcement is carried out. The experimental tests of two real-scale FRC beams were conducted at the School of Engineering of the University of Minho within the context of a blind simulation competition organised by *fib* WG 2.4.1 [134]. The simulation was conducted in the FEMIX V4.0 [200] computer program, using a multi-directional fixed smeared crack approach. FEMIX V4.0 includes several types of FEs and static or dynamic analysis can be carried out, considering linear or nonlinear material behaviour. In addition, different types of FEs can be included in the same analysis. A more detailed description of the main features included in the FEMIX V4.0 program can be found in Barros [219].

### 4.4.2 Geometry and experimental setup

Figures 88a and 88b show a schematic representation of the cross section and elevation view of the beam. As shown in the Figure 88, the beam has a T-shaped cross section, reinforced with flexural reinforcement in the flange and web. Steel stirrups were disposed in the beam's flange and also in its web in the longest shear span (3 m) as depicted in Figure 88b. Such shear reinforcement combined with eccentric loading, aims to favour the occurrence of shear failure in the shortest span without stirrups.

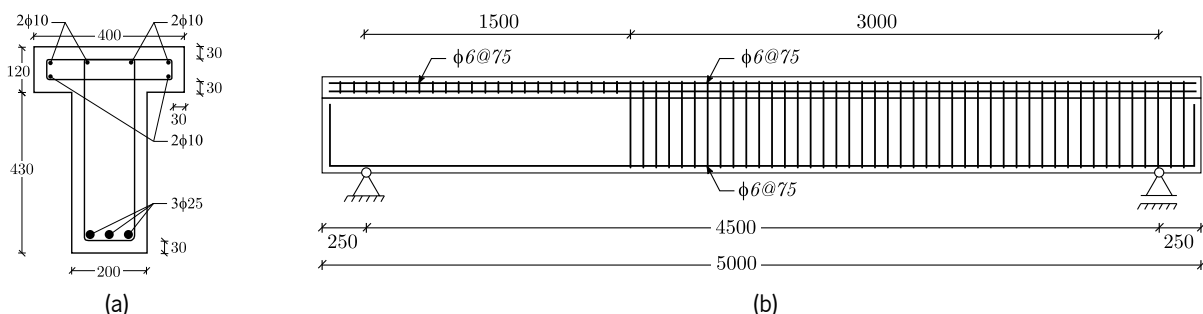


Figure 88: Geometry of the beam: (a) cross section and (b) lateral view (dimensions in mm).

Thus, the test consisted in subjecting the beams to eccentric loading under displacement control of  $50 \mu\text{m/s}$  until failure, using the linear voltage differential transducers (LVDTs) placed accordingly to the sketch of Figure 89 to measure deflection and concrete strain at the level of the bottom reinforcement.

For supporting the LVDTs, a Japanese yoke system was used so that parasitic values of deflection were avoided.

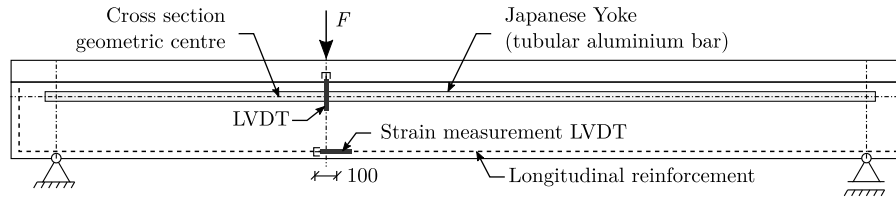


Figure 89: Experimental setup and location of LVDTs for measuring the deflection and concrete strain at the longitudinal reinforcement level.

### 4.4.3 Assessment of the Mode I fracture parameters

It is well known that estimating the fracture mode I parameters from the average experimental curve of 3PNBBT often leads to an overestimation of the tensile capacity of FRC. This is due to the fact that the models used to conduct IA assume that the fracture surface occurs throughout the notched plane, whereas in reality several sinuous cracks are formed during the propagation of the macro-crack, dissipating additional energy. Hence, when the total energy is assumed to be dissipated in a smooth fracture surface, an overestimation of the post-cracking tensile capacity is obtained. This effect is even more prominent for higher fibre volumes, since more micro and meso-cracks are formed during the propagation of the macro-crack. Also, the geometry of the specimens induce a beneficial effect in terms of fibre orientation, due to the wall-effect originated by the relation between fibre length and cross-section dimensions.

Hence, in order to minimise the overestimation of the tensile capacity, COFIT was used to conduct IA but using the 5% fractile experimental curve instead of the average response. Furthermore, the number of intermediate points comprising the  $\sigma_n^{cr} - w_n^{cr}$  relationship was set to 3 so that the optimised parameters could be used directly in the definition of the quadrilinear diagram used in the FEM simulations.

The results obtained by COFIT in terms of global response and  $\sigma_n^{cr} - w_n^{cr}$  relationship are presented in Figure 90.

### 4.4.4 Beam FE mesh, loading and support conditions

Figure 91 shows the geometry, finite element mesh, loading and support conditions adopted in this numerical study. Conventional steel reinforcement is placed at the top and bottom of the beam as well as transversal reinforcement in the larger span (Figure 91). The concrete was simulated by means of 4-node plane stress elements with a 2x2 G-L integration scheme, and the conventional reinforcement using 2-node cable elements with 2 G-L integration points. In order to account for the bond behaviour between the bottom reinforcement and the surrounding concrete elements, line interface finite elements with a 2 Gauss-Lobatto (G-Lo) integration rule were introduced between the concrete FEs and the embedded cable elements.



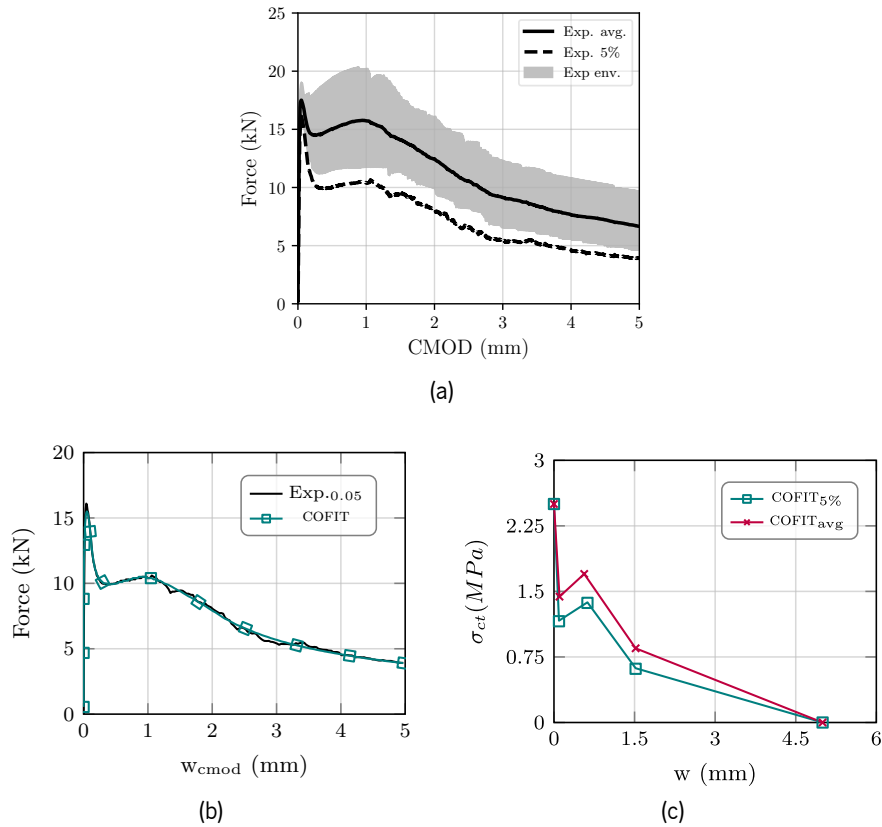


Figure 90: (a) Experimental envelope, average and 5% fractile force-CMOD curves, (b) results of the IA for 5% fractile curve and (c)  $\sigma_n^{cr}$  -  $w_n^{cr}$  relationship derived by cofit.

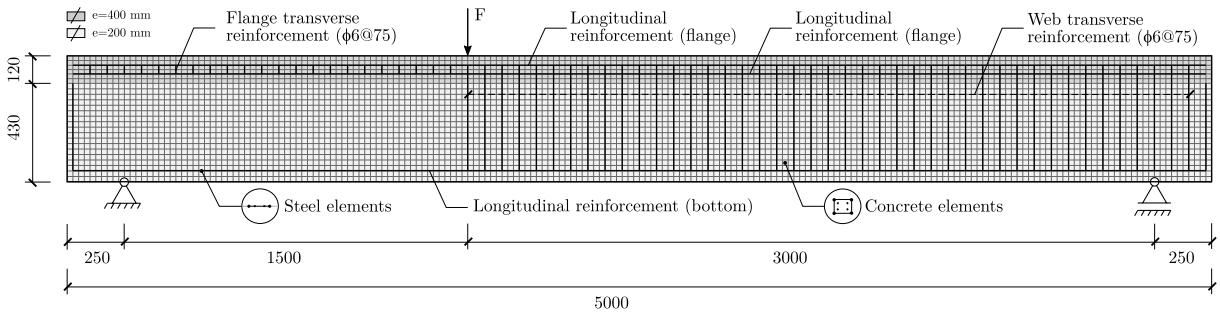


Figure 91: Geometry, loading, support conditions and finite element mesh adopted in the simulation (FE of  $\approx 25 \times 25$  mm). Dimensions in mm.

#### 4.4.5 Constitutive laws to simulate the nonlinear behaviour of the materials

The material nonlinear behaviour of the conventional reinforcement was simulated by means of the constitutive relationship presented in Figure 92. The curve is formed by the points PT1, PT2, and PT3 and the parameter  $p$ , which defines the shape of the last branch. The parameters adopted to define the steel constitutive law are summarised in Table 16.

The behaviour of SFRC in fracture mode I was modelled by means of the quadrilinear diagram already

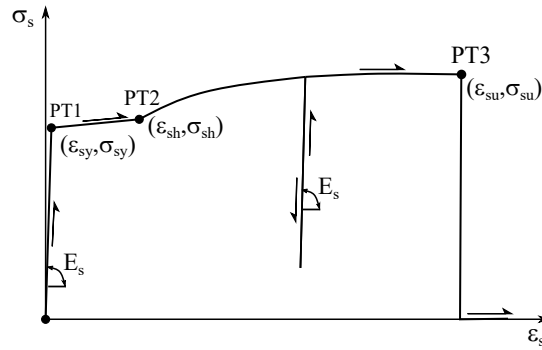


Figure 92: Constitutive model used to simulate the nonlinear material behaviour of the conventional steel reinforcement [220].

Table 16: Parameters used to define the steel constitutive model for top, transversal reinforcements, and bottom reinforcement.

Name	$\phi$ (mm)	$A_s$ (mm <sup>2</sup> )	$\epsilon_{sy}$	$\sigma_{sy}$ (N/mm <sup>2</sup> )	$\epsilon_{sh}$	$\sigma_{sh}$ (N/mm <sup>2</sup> )	$\epsilon_{su}$	$\sigma_{su}$ (N/mm <sup>2</sup> )	$\rho$
Bot.	25	1472.62	$2.79 \times 10^{-3}$	557	$2.2 \times 10^{-2}$	557	0.1	678	1
Top.(Web)	10	314.16	$2.69 \times 10^{-3}$	557	$2.2 \times 10^{-2}$	538	$9 \times 10^{-2}$	678	1
Top.(Flg.)	10	157.08	$2.69 \times 10^{-3}$	557	$2.2 \times 10^{-2}$	538	$9 \times 10^{-2}$	678	1
Stir.(Flg.)	6	113.10	$2.64 \times 10^{-3}$	557	$2.2 \times 10^{-2}$	527	$7.5 \times 10^{-2}$	678	1
Stir.(Web)	6	56.55	$2.64 \times 10^{-3}$	557	$2.2 \times 10^{-2}$	527	$7.5 \times 10^{-2}$	678	1

shown in Figure 83b using the parameters obtained by COFIT. In addition, to simulate the degradation of crack shear transferring capacity, a linear shear softening diagram was used (Figure 93). The parameters adopted for defining the diagrams of Figures 83b and 93 are listed in Table 17.

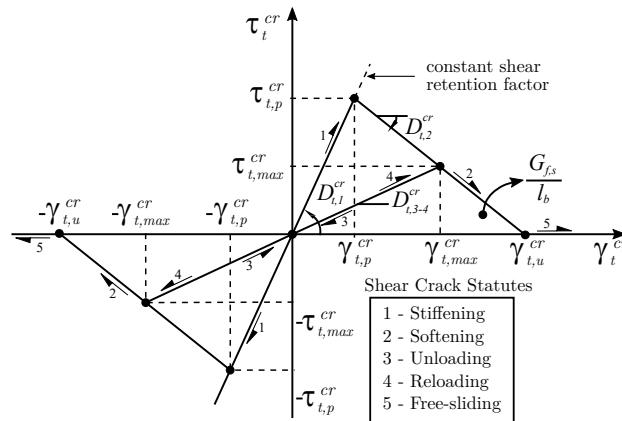


Figure 93: Shear softening diagram used to simulate the decrease of shear transferring capacity [141].

For simulating the sliding component of the constitutive law of the interface finite elements placed between the concrete and bottom reinforcement, the bond stress-slip law depicted in Figure 95a was used. The  $\tau_0$  and  $\delta_0$  are the stress and slip at the end of the linear branch of the bond stress-slip relationship, respectively, and  $\beta_1$  and  $\beta_2$  are coefficients that define the shape of the bond stress-slip relationship, respectively. The bond strength,  $\tau_m$  and its corresponding slip,  $\delta_m$  are determined from Equations (4.14) and (4.15). In these equations,  $c_s$  is the concrete cover thickness in mm,  $\phi$  is the diameter of the rebar

Table 17: Parameters used to define the concrete constitutive model.

Property	Value
Poisson's ratio ( $\nu$ )	0.20
Young's modulus (E)	31130 N/mm <sup>2</sup>
Compressive strength ( $f_c$ )	64.2 N/mm <sup>2</sup>
Quadrilinear tension-softening diagram	$f_{ct} = 2.5$ N/mm <sup>2</sup> ; $G_f^I = 3.25$ N/mm; $\xi_1 = 0.019$ ; $\alpha_1 = 0.52$ ; $\xi_2 = 0.13$ ; $\alpha_2 = 0.60$ $\xi_3 = 0.30$ ; $\alpha_3 = 0.30$ ;
Shear crack softening diagram	$\beta = 0.7$ ; $\tau_{t,p}^{cr} = 1.2$ N/mm <sup>2</sup> ; $G_f^{II} = 1.25$ N/mm;
Parameter defining the mode I fracture energy available to the new crack	2
Crack band width	$\sqrt{FE}$
Threshold angle	30°
Maximum number of cracks per integration point	2

in mm,  $f_{cm}$  is the average concrete compressive strength in MPa and  $c_0$  is the clear distance between ribs in the rebar, which in this case was adopted as 15 mm in accordance with DIN488 [221].  $K_n$  is the normal stiffness of the interface element.

$$\tau_m = \left[ 1.77 + 0.49 \cdot \left( \frac{c_s}{\phi} \right) \right] \cdot \sqrt{f_{cm}} \quad (4.14)$$

$$\delta_m = c_0 (0.0035 \cdot c_0 + 0.006) \quad (4.15)$$

The bond parameters that define the bond-slip relationship were obtained based on the recommendations of Model Code 2010 [203], considering confined and unconfined regions of the reinforcement as depicted in Figure 94. The obtained bond-slip relationship considering confined and unconfined conditions, as well as the parameters used in the model are presented in Figure 95 and Table 18, respectively.

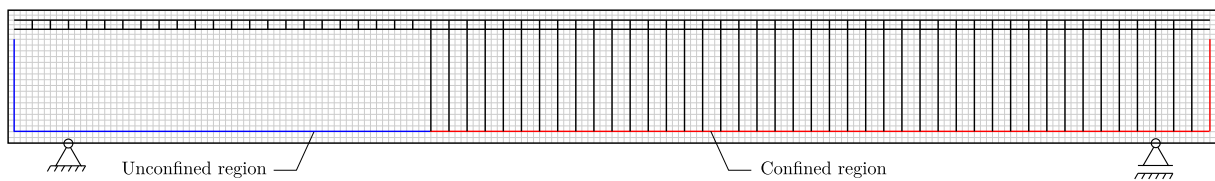


Figure 94: Representation of the regions assigned with confined and unconfined bond-slip properties.

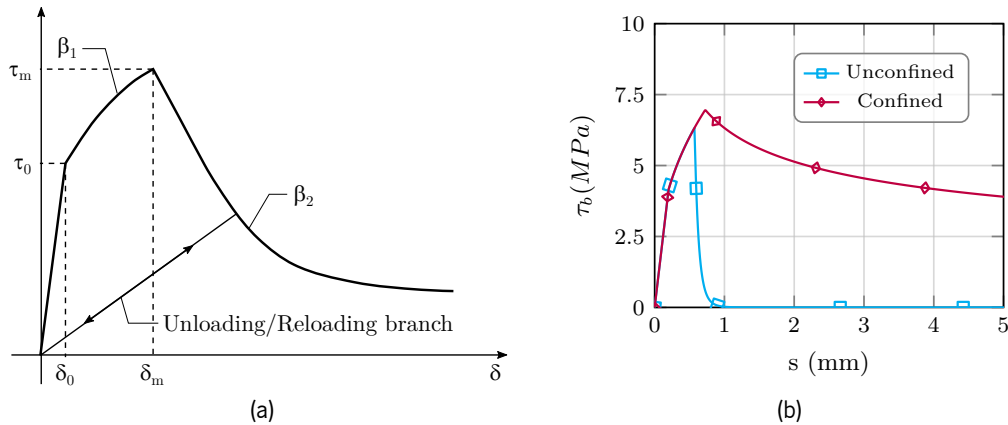


Figure 95: (a) Bond shear stress-slip relationship and (b) bond-slip relationship for the confined and unconfined regions considering bad bond conditions.

Table 18: Parameters of the bond-slip confined and unconfined relationship.

Property	Confined	Unconfined
$\tau_0$ (N/mm <sup>2</sup> )	4.16	4.16
$\tau_m$ (N/mm <sup>2</sup> )	6.96	6.33
$\delta_0$ (mm)	0.2	0.2
$\delta_m$ (mm)	0.725	0.571
$\beta_1$	0.4	0.4
$\beta_2$	0.3	10.0
$K_n$ (N/mm)	1.0e+4	1.0e+4

#### 4.4.6 Results and discussion

Considering the information presented in the previous sections, the simulated structural response of the beam is compared to the experimental force-deflection curve and crack pattern, and presented in Figures 96a and 96b, respectively.

Regarding the results presented in Figure 96, particularly the force-deflection curve (Figure 96a), one can observe that, in general, the experimental response is well captured. The linear elastic phase of the beam is accurately predicted, however, the elasto-cracked phase of the response is slightly overestimated, despite exhibiting similar stiffness to the experimental response. The peak load was also predicted with a satisfactory error ( $\approx 4.2\%$ ), and the failure crack pattern (Figure 96b) reasonably captured the shear failure mode, exhibiting the formation of a major shear crack as also observed in the experimental tests. Considering these results, it is possible to conclude that COFIT provided a good estimation of the fracture mode I parameters, as these highly influence the elasto-cracked phase. It is also observed that an estimation of these parameters by means of the average experimental curve of the 3PNBBT, would lead to

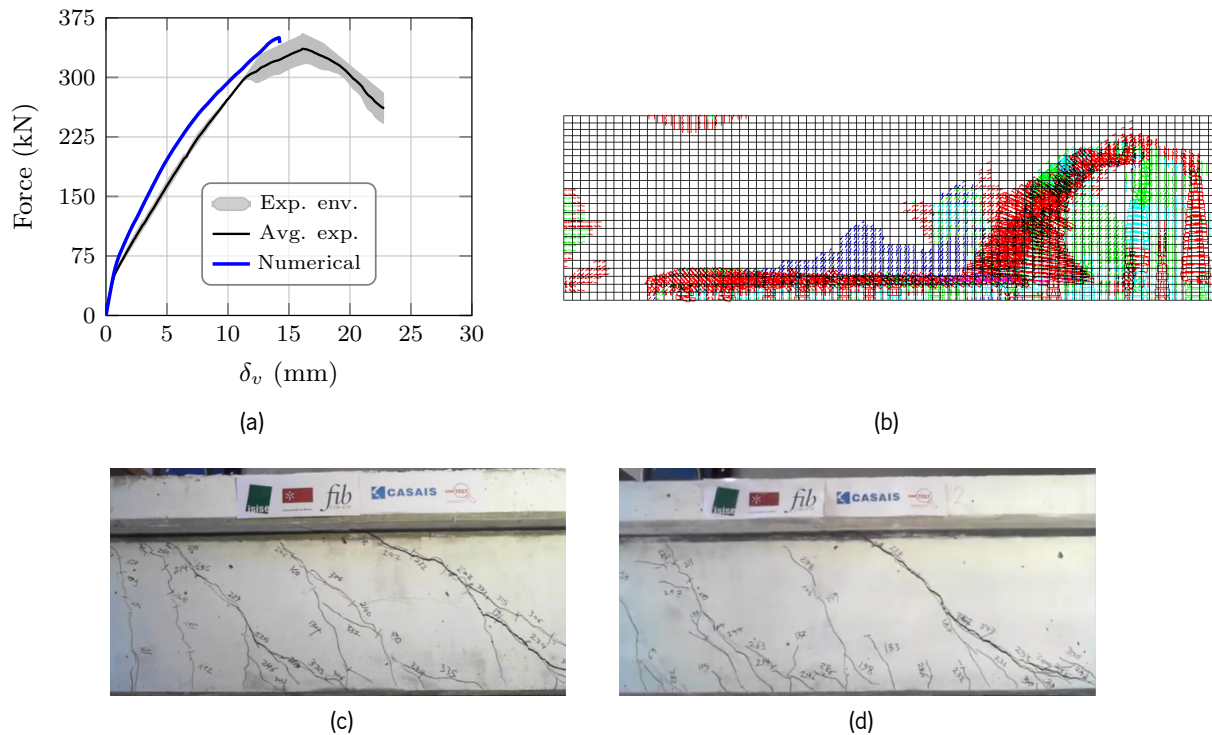


Figure 96: (a) Comparison between numerical and experimental results in terms of force-deflection curve, (b) crack pattern (magenta: fully open cracks; red: opening cracks; green: closing cracks; blue: closed cracks; cyan: reopening cracks;) and (c)/(d) experimental crack pattern at failure.

an overestimation of the load carrying capacity, as expected. The 5% fractile experimental curve seems to provide good numerical predictions.

## 4.5 Summary and Conclusions

In this chapter a new IA approach for deriving the fracture mode I parameters of FRC from 3PNBBT and RPT-3PS is proposed. The described methodology relies on a global NLSQ fitting procedure coupled with an automatic parameter updating algorithm based on the force deviation error between numerical and experimental curves. The proposed approach relies on well-established analytical models to simulate the numerical response of the experimental tests. Furthermore, the NLSQ fitting algorithm allows the specification of lower and upper limit to the optimising variables reducing the probability of obtaining spurious solutions. In addition, the developed approach allows the user to simulate the numerical response in terms of force-CMOD, force-CTOD or force-deflection. Furthermore, the numerical curve can be discretised in an uneven manner, allowing the user to prescribe more or less data points in different regions of interest of the response.

The performance and validity of the developed approach was investigated by means of experimental results of 3PNBBT and RPT-3PS collected from the literature, and 3PNBBT results obtained within the context of a blind simulation competition organised by *fib* WG 2.4.1 [134]. Additionally, the sensibility of

the tool to the initial guess provided by the user was also investigated. Finally, the approach was applied to a case study consisting of a real-scale beam reinforced with steel fibres and conventional reinforcement. The fracture mode I parameters were derived using the herein presented methodology and the obtained results discussed.

Hence, considering the results presented in this chapter, the following conclusions can be drawn:

- The developed IA approach revealed a very good performance in terms of numerical and experimental prediction and the values obtained for the multi-linear softening diagrams were consistent with the material characteristics;
- The developed tool was able to capture different tensile behaviours (softening and hardening) validating its applicability potential. In addition, the runtimes varied from 1 to 2 minutes approximately, for the case of 3PNBBT and from 4 to 6 minutes in then case of RPT-3PS, which is significantly faster when compared to the conventional FEM approach;
- The results of the impact of the initial variable guess of the multi-linear post-peak diagram demonstrated the robustness of the developed algorithm since the obtained output was not significantly affected by the initial values provided by the user demonstrating the effectiveness of the automatic variable updating procedure;
- The proposed IA methodology revealed to be more accurate, in terms of prediction of the experimental response of 3PNBBT specimens, and simpler when compared to conventional manual FEM IA since no FEM model is required and the fracture parameters are estimated automatically;
- The estimation of the mode I parameters should not be based on the average experimental response of 3PNBBT but instead, i.e., on a 5% fractile, in order to avoid the overestimation of the tensile capacity of FRC.

# 5 Two-Dimensional Integrated Mixed-Mode Smearred Crack Model

## 5.1 Introduction

*This Chapter describes the development of a two-dimensional mixed-mode fracture smeared crack model (MMFSCM) for fibre reinforced concrete (FRC) by combining the fibre and aggregate interlock resisting mechanisms. The proposed model predicts the normal and shear stresses in function of the crack opening and crack sliding displacements. For this purpose, two well established aggregate interlock models and three fibre pull-out models reported in the literature are used, and their predictive performance is assessed in the context of the present study. In order to understand the impact of the variables involved in the model, a parametric study is conducted targeting different maximum aggregate diameters, concrete compressive strengths and fibre volume ratios. Finally, the predictive performance of the model is assessed by comparing the numerical predictions with experimental results collected from the literature. The results show that the model is capable of predicting the shear peak-stress with good accuracy, however the post-peak response is generally overestimated. A modification to the aggregate interlock models is proposed in order to adapt the original formulations for FRC. The results of the modified version show an overall much better agreement between the numerical and experimental results.*

Published in: [10.1016/j.cemconcomp.2020.103618](https://doi.org/10.1016/j.cemconcomp.2020.103618)

## 5.2 General overview

The benefits of using fibres as reinforcement is well recognised within the academic community. In the last decades, many authors studied the influence of fibres in both tensile and shear capacity of FRC at material [17, 222, 223] and structural level [224–229]. In terms of tensile performance, fibres greatly enhance the post-cracking behaviour of FRC, allowing a higher energy absorption capacity due to the residual tensile strength provided by the fibres [17, 230]. In addition, the shear performance is also highly influenced, since the presence of fibres greatly reduce the crack width and spacing, favouring the

shear stress transferring mechanisms [204, 231].

The crack arrest mechanisms provided by the fibres bridging the cracks are of key importance on the post-cracking tensile capacity of FRC [230], which is highly affected by the pull-out behaviour of the individual fibres. During the last decades, several authors contributed to the development of fibre pull-out models to account the fibre contribution for the post-cracking tensile capacity of FRC [222, 232–234].

On the other hand, the aggregate interlock consists in the shear transferring mechanism between two faces of an existing crack in a concrete element. In conventional concrete, the matrix resistance is lower than the aggregates, leading to the propagation of cracks around the aggregates, and progressing through the matrix, forming a rough crack surface. The aggregates protruding from the crack plane in contact with the matrix on the opposing crack face originate contact stresses when a sliding displacement occurs [235, 236]. In case of high strength concrete, the cracks might propagate through the aggregates, since the difference between paste and aggregate strength is not so pronounced as in conventional concrete. A smoother crack surface is formed and, consequently, the contribution of the aggregate interlock mechanism for the crack shear stress transfer capacity is lower.

Since the 80s several authors conducted experimental investigations on the effect of the aggregate interlock mechanism in the shear behaviour of concrete [231, 237–242]. Push-off tests [235, 243, 244], JSCE shear tests [245] and FIP shear tests [241] are the most common experimental approaches to assess the aggregate interlock in plain, reinforced and fibre reinforced concrete. In consequence of these research activities, empirical models were developed from regression curves adjusted to experimental results [246, 247]. However, the empirical nature of these models and their dependency on the experimental conditions and calibration parameters restrict their application scope. Therefore, some authors attempted a more physical approach to model the aggregate interlock mechanism, such as the Two-phase model developed by Walraven [235], and the Contact Density Model introduced by Li et al. [248].

Despite the abundance of experimental research on the behaviour of FRC structures, a consensual modelling approach that accurately predicts the shear and tensile behaviour in a physical-mechanical manner is still lacking in the literature. In an attempt for minimizing this gap, Soetens and Matthys [245] conducted direct shear tests on a large set of samples, evaluating the shear-frictional behaviour of concrete elements with and without fibre usage. In addition, Soetens and Matthys [245] also proposed a model to predict the direct shear behaviour of FRC that accounts for the fibre pull-out contribution, the aggregate interlock and the effect of confinement stresses in the shear strength capacity by introducing a friction coefficient. Kaufmann et al. [249] also investigated the shear transfer mechanism of FRC by considering the fibre contribution and aggregate interlock contribution. However, only one pull-out constitutive law is considered in this research, and no comprehensive study was conducted on the influence of the parameters of the model in its predictive performance.

In this Chapter, a constitutive model for FRC that relates the cracking kinematics (crack opening and sliding displacement) with the normal and shear stresses that arise from the combination of the fibre and aggregate interlock resisting mechanisms is presented. For this purpose, three fibre pull-out constitutive laws [222, 232, 250] and two aggregate interlock models [246–248] reported in the literature are reviewed



and assessed, namely the rough crack model (RCM) by Bažant and Gambarova [246] and the contact density model (CDM) by Li et al. [248]. Furthermore, an extensive parametric study is conducted in order to assess the role of the main variables involved in the model formulation. The model predictive performance is assessed by comparing the numerical results using different fibre pull-out models with experimental results available in the literature [231, 241, 245]. Finally, a modification to the RCM and CDM is proposed in order to enhance the post-peak predictive performance of the model.

## 5.3 Constitutive model description

### 5.3.1 Introduction

The herein proposed constitutive model accounts for the tensile contribution provided by the fibres including the effect of fibre orientation, the normal and shear stresses that arise from the aggregate interlock mechanism and the coupling of these mechanisms in terms of cracking process. For this purpose, the most well known fibre pull-out models and two well established aggregate interlock models are presented. Furthermore, the contribution of the matrix in mode I fracture is also included in order to simulate the full tensile behaviour of FRC.

The idealisation of the crack kinematics and displacement entities are depicted in Figure 97, where  $n$  and  $t$  axis are orthogonal and tangential to the crack plane, respectively.

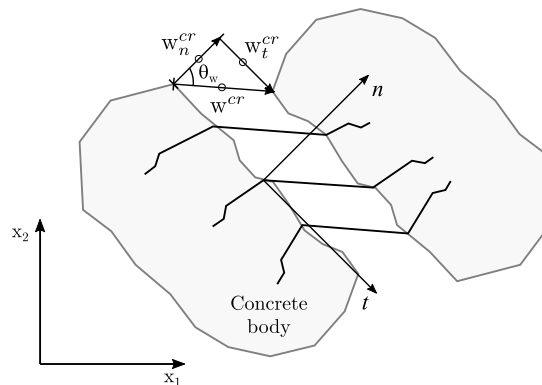


Figure 97: Schematic representation of a crack opening ( $w_n^{cr}$ ) and sliding ( $w_t^{cr}$ ), crack displacement ( $w^{cr}$ ), and fibre embedment length ( $l_{bf}$ ).

According to this figure,  $w_n^{cr}$  and  $w_t^{cr}$  are the crack opening and sliding displacements, while  $w^{cr}$  is the crack displacement given by Equation (5.1).

$$w^{cr} = \sqrt{(w_n^{cr})^2 + (w_t^{cr})^2} \quad (5.1)$$

### 5.3.2 Fibre resisting mechanisms

Fibres bridging a crack introduce several resisting mechanisms when they are being pulled-out by limiting the crack displacement. The adhesion and friction to the surrounding matrix and the snubbing effect at the fibre exit point (when fibre is inclined towards the crack displacement) are common resisting mechanism of fibres, while micro-mechanical anchorages are further ones in deformed type fibres, mainly those of high stiffness [230, 251]. Considering this advantage, many authors conducted experimental investigations involving FRC, and demonstrated the beneficial effect of using fibre reinforcement to improve the flexural capacity, toughness, shear strength and ductility of concrete elements [224–226, 228].

One of the key aspects affecting the tensile behaviour of FRC is the pull-out behaviour of the individual fibres. Several researchers have contributed to the development of fibre pull-out constitutive models to simulate the beneficial contribution of the fibres in the tensile capacity of FRC. In this document, three fibre pull-out models reported in the literature, such as the Pfy's Engagement Model [232], the unified engagement model (UVEM) [222] and the simplified diverse embedment model (SDEM) [250] are concisely described, and their performance is assessed in Section 5.4.

#### 5.3.2.1 Pfy's Engagement Model

The Pfy's Engagement Model [232] is based on the following assumptions:

- i) fibres are assumed to be uniformly distributed and randomly oriented;
- ii) flexural stiffness of the fibres is neglected and, therefore, the fibre and loading have the same direction;
- iii) matrix deformation is disregarded;
- iv) the bond stress along the embedded length of the fibres is assumed to be constant (see Equation (5.5));

The model does not account for fibre fracture, which is a fibre failure mode that should be avoided so that the favourable fibre reinforcement effect in FRC is not jeopardized. This can be, in general, assured by increasing the number of fibres per unit concrete volume, decrease the fibre length,  $l_f$ , and/or the fibre tensile strength, when the concrete strength is increased. After integrating the contribution of all fibres bridging the crack, the tensile stress sustained by the fibres and transferred to the matrix is given by Equation (5.2),

$$\sigma_{cf}^{cr}(w) = \begin{cases} \left( 2 \cdot \sqrt{\frac{w^{cr}}{w_{c0}^{cr}}} - \frac{w^{cr}}{w_{c0}^{cr}} \right) \cdot \sigma_{cf0}^{cr} & , 0 \leq w^{cr} \leq w_{c0}^{cr} \\ \left( 1 - \frac{2w^{cr}}{l_f} \right)^2 \cdot \sigma_{cf0}^{cr} & , w_{c0}^{cr} < w^{cr} \leq \frac{l_f}{2} \end{cases} \quad (5.2)$$

where  $\sigma_{cf0}^{cr}$  is the fibre effectiveness given by Equation (5.3),  $w_{c0}^{cr}$  is the crack opening at which the fibre

with the longest embedment length starts to pull-out (Equation (5.4)).

$$\sigma_{cf0}^{cr} = \eta_{\theta f} \cdot \frac{V_f \cdot \tau_{bf} \cdot l_f}{d_f} \quad (5.3)$$

$$w_{c0}^{cr} = \frac{\tau_{bf} \cdot l_f^2}{d_f \cdot E_f} \quad (5.4)$$

$$\tau_{bf} = 2 \cdot f_{ct} \quad (5.5)$$

where  $d_f$  is the fibre diameter (the model was developed for circular type cross section fibres),  $\eta_{\theta f}$  is the fibre orientation factor (see Equation (5.6)),  $V_f$  is the fibre content ratio in volume,  $\tau_{bf}$  (Equation (5.5)) is the fibre average bond stress,  $E_f$  is the modulus of elasticity of the fibres and  $f_c$  is the concrete compressive strength.

The fibre orientation factor for a bidimensional stress-strain problem (2D) is computed by means of Equation (5.6), where the range of possible fibre orientation angles,  $\theta_f$ , is restricted since some fibres are not immediately activated due to their unfavourable orientations relatively to the loading direction. Figure 98 shows the orientation interval of the considered active and inactive fibres for the indicated loading direction, where  $\theta_w$  is the pull-out loading direction angle that is given by Equation (5.7).

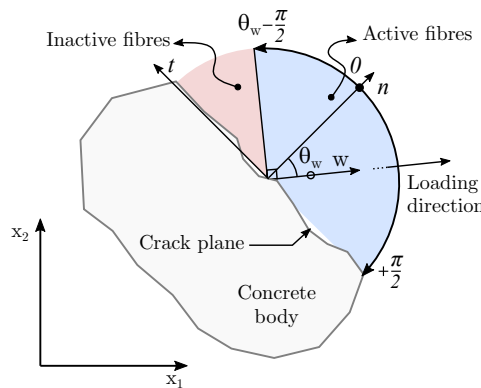


Figure 98: Concept of intervals of active and inactive fibres regarding the loading direction.

$$\eta_{\theta f} = \frac{1}{\pi} \cdot \int_{\theta_w - \pi/2}^{\pi/2} \cos \theta_f \cdot d\theta_f = \frac{1 + \cos \theta_w}{\pi} \quad (5.6)$$

$$\theta_w = \left| \arctan \left( \frac{w_t^{cr}}{w_n^{cr}} \right) \right| \quad (5.7)$$

### 5.3.2.2 Unified Variable Engagement Model (UVEM)

The UVEM [222] is based on the variable engagement model I (VEMI) [233] and variable engagement model II (VEMII) [252] which were developed to simulate the behaviour of FRC under fracture mode I and

II, respectively. In the UVEM, the concepts of the previous models are combined, allowing the simulation of the behaviour of FRC under mixed mode fracture situations which is the case of the herein proposed constitutive model.

The formulation of the UVEM is founded on the following assumptions:

- i) the fibre-matrix overall response is obtained by adding the matrix and fibre component contribution;
- ii) the fibres are assumed to have uniform distribution and equal orientation probability;
- iii) the pull-out is assumed to occur from the shorter embedded side of the fibre, while the longer side stays perfectly bonded to the surrounding matrix (no sliding);
- iv) elastic strains of the fibres are disregarded;
- v) the energy consumed in the fibre bending is also disregarded. In the UVEM, a uniform bond stress model is adopted since, according to Htut and Foster [222] the additional complexity in using a lumped model approach as in VEMIII did not justify accuracy gains;

In the UVEM the orientation between the fibre direction and the orthogonal to the crack plane is defined by the angle  $\theta_f$ , taken as positive in the clockwise direction and negative otherwise (Figure 99). In addition, a fibre bending angle  $\gamma$  and pull-out loading direction  $\phi$  are also defined as depicted in Figure 99. In this

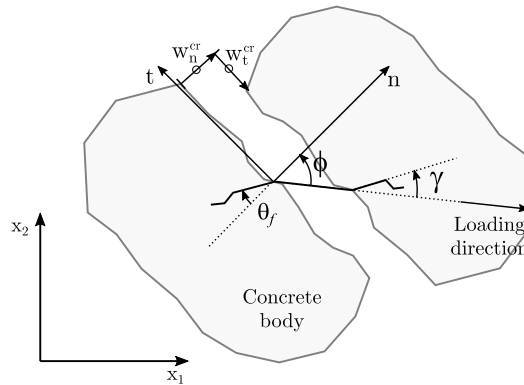


Figure 99: Fibre orientation and bending angle definition according to Htut and Foster [222].

model the tensile contribution of the fibres is obtained by means of Equation (5.8),

$$\sigma_{cf}^{cr} = \eta_{f,uvem} \cdot l_f / d_f \cdot V_f \cdot \tau_{b,avg} \quad (5.8)$$

where  $\eta_{f,uvem}$  is the fibre orientation factor, and  $\tau_{b,avg}$  is the average bond stress of all engaged fibres which is given by Equation (5.9),

$$\tau_{b,avg} = \tau_{b,0} + 0.0625 \cdot \gamma_{crit}^3 \quad (5.9)$$

in which  $\tau_{b,0}$  is the bond stress when the fibre is aligned with the pull-out loading direction ( $\gamma = 0$ ),  $\gamma_{crit}$  is a critical fibre bending angle, given by Equation (5.10), that represents the angle up to which fibres

contribute to the stress transferring mechanism,

$$\gamma_{crit} = \frac{2 \cdot \gamma_{max}}{\pi} \cdot \tan^{-1} \sqrt[3]{\frac{3.5 \cdot w^{cr}}{d_f}} \quad (5.10)$$

$$\gamma_{max} = |\phi| - \frac{\pi}{2}, \quad \pi/2 \leq \gamma_{max} \leq \pi \quad (5.11)$$

$$\eta_{f,uvem} = \left( \frac{a+b}{\pi} \right) \cdot p \cdot k_{avg} \quad (5.12)$$

$$a = \min [\gamma_{crit}, \pi/2 - |\phi|] \quad (5.13)$$

$$b = \gamma_{crit} \quad (5.14)$$

$$p = \left( 1 - \frac{2 \cdot w^{cr}}{l_f} \right) \quad (5.15)$$

$$k_{avg} = \frac{1}{2} - \frac{w^{cr}}{l_f} \quad (5.16)$$

where  $\gamma_{max}$  is the maximum fibre bending angle and is given by Equation (5.11).

### 5.3.2.3 Simplified Diverse Embedment Model (SDEM)

The SDEM proposed by Lee et al. [250] is a simplified version of the diverse embedment model (DEM) [253]. The DEM accounts for the behaviour of a fibre embedded on both sides of the matrix, fibre orientation and random distribution of embedment lengths. However, DEM relies on a double integration scheme in order to obtain the average tensile stress provided by the fibres, which confers extra complexity and computing time that can be considerable when the model is aimed to be integrated in a finite element method (FEM)-based computer program for the material nonlinear analysis of FRC structures. Hence, the SDEM eliminates the need for a double integration scheme by introducing the following simplifications:

- i) the pull-out behaviour is assumed to be a rigid-body translation;
- ii) the crack width is equal to the slip of the shorter embedded side of the fibre;

The fibre tensile stress is obtained by adding the frictional and mechanical anchorage components of the fibres given by Equation (5.17).

$$\sigma_{cf}^{cr}(w^{cr}) = \sigma_{cf,st}^{cr} + \sigma_{cf,eh}^{cr} \quad (5.17)$$

The frictional component is obtained by means of Equation (5.18),

$$\sigma_{cf,st}^{cr}(w^{cr}) = \eta_{\theta f} \cdot V_f \cdot K_{st} \cdot \tau_{st,max} \cdot \frac{l_f}{d_f} \cdot \left( 1 - \frac{2 \cdot w^{cr}}{l_f} \right)^2 \quad (5.18)$$

where  $\eta_{\theta f}$  is the fibre orientation factor (Equation (5.6)),  $\tau_{f,max}$  is the maximum frictional bond stress (equal to  $0.396 \cdot \sqrt{f_c}$  [18]), and  $K_{st}$  is a coefficient given by Equation (5.19),

$$K_{st}(w^{cr}) = \begin{cases} \frac{\beta_f}{3} \cdot \frac{w^{cr}}{s_f} & , w^{cr} < s_f \\ 1 - \sqrt{\frac{s_f}{w^{cr}}} + \frac{\beta_f}{3} \cdot \sqrt{\frac{s_f}{w^{cr}}} & , w^{cr} \geq s_f \end{cases} \quad (5.19)$$

in which  $\beta_f$  is the coefficient that compensates for the slip of the longer embedded side of the fibre, equal to 0.67 according to Lee et al. [250], while  $s_f$  is the slip at maximum frictional bond stress, which is an input parameter.

The mechanical anchorage effect is considered by means of the relation between the force at the anchorage and its slip. The force-slip relationship used in SDEM is the same as the one used in the DEM model, which is based on the works of Sujivorakul et al. [254]. After simplification, the tensile stress conferred by the anchorage of the fibres is given by Equation (5.20),

$$\sigma_{cf,eh}^{cr}(w^{cr}) = \eta_{\theta f} \cdot V_f \cdot K_{eh} \cdot \tau_{eh,max} \cdot \frac{2 \cdot (l_i - 2 \cdot w^{cr})}{d_f} \quad (5.20)$$

where  $K_{eh}$  is a fibre state coefficient (pre-peak, post-peak or full hook deterioration) given by Equation (5.21),  $\tau_{eh,max}$  is an input parameter and corresponds to the maximum bond strength provided by the mechanical anchorage (equal to  $0.429 \cdot \sqrt{f_c}$  [18]), and  $l_i$  is the internal fibre length (length of the fibre without the hooks),

$$K_{eh}(w^{cr}) = \begin{cases} \beta_{eh} \cdot \left[ \frac{2}{3} \cdot \frac{w^{cr}}{s_{eh}} - \frac{1}{5} \cdot \left( \frac{w^{cr}}{s_{eh}} \right) \right] & , w^{cr} < s_{eh} \\ 1 + \left( \frac{7 \cdot \beta_{eh}}{15} - 1 \right) \cdot \sqrt{\frac{s_{eh}}{w^{cr}}} - \frac{2 \cdot \left( \sqrt{w^{cr}} - \sqrt{s_{eh}} \right)^2}{l_f - l_i} & , s_{eh} \leq w^{cr} \leq \frac{l_f - l_i}{2} \\ \left( \frac{l_i - 2 \cdot w^{cr}}{2 \cdot l_i - l_f} \right)^2 \cdot K_{eh,i} & , \frac{l_f - l_i}{2} < w^{cr} < \frac{l_i}{2} \end{cases} \quad (5.21)$$

in which  $K_{eh,i}$  is  $K_{eh}$  evaluated at  $w_n = (l_f - l_i) / 2$  (see Equation (5.22)),  $\beta_{eh}$  is a coefficient that accounts for the fibres that do not attain the maximum anchorage force, being considered equal to 0.76 [250], and  $s_{eh}$  is the anchorage slip at maximum bond stress of an aligned fibre, which is also an input parameter.

$$K_{eh,i} = K_{eh}(w^{cr} = (l_f - l_i)/2) \quad (5.22)$$

### 5.3.3 Models for simulating the aggregate interlock resisting mechanism

The aggregate interlock resisting mechanism is integrated in the MMFSCM by means of two acknowledged aggregate interlock models, namely, the RCM proposed by Bažant and Gambarova [246] and later enhanced by Gambarova and Karakoç [247], and the CDM introduced by Li et al. [248].

#### 5.3.3.1 Rough Crack Model (RCM)

For the development of the RCM, Bažant and Gambarova [246] idealised the crack morphology as a series of saw shaped asperities, as depicted in Figure 100, and the model was based on empirical relations and experimental results obtained by Paulay and Loeber [255]. Later on, Gambarova and Karakoç [247] improved the original model by considering the experimental tests results obtained by Daschner and Kupfer [238] and by incorporating the effect of aggregate size. The normal and shear stresses are obtained by Equations (5.23) and (5.24),

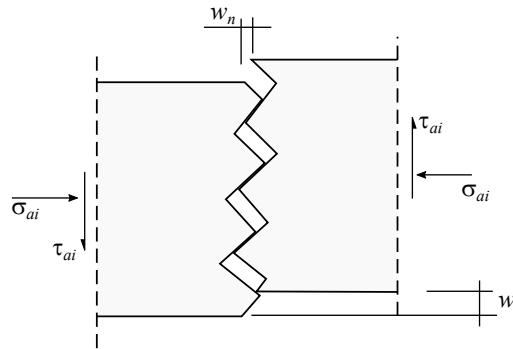


Figure 100: Crack morphology according to the RCM [246].

$$\sigma_{n,ai}^{cr}(w_n^{cr}, w_t^{cr}) = -0.62 \cdot \frac{w_t^{cr}}{\sqrt[4]{w_n^{cr2} + w_t^{cr2}}} \cdot \tau_{t,ai}^{cr}(w_n^{cr}, w_t^{cr}) \quad (5.23)$$

$$\tau_{t,ai}^{cr}(w_n^{cr}, w_t^{cr}) = \tau_0 \cdot \left(1 - \sqrt{\frac{2 \cdot w_n^{cr}}{D_{max}}}\right) \cdot \frac{w_t^{cr}}{w_n^{cr}} \cdot \frac{\frac{2.45}{\tau_0} + 2.44 \cdot \left(1 - \frac{4}{\tau_0}\right) \cdot \left|\frac{w_t^{cr}}{w_n^{cr}}\right|^3}{1 + 2.44 \cdot \left(1 - \frac{4}{\tau_0}\right) \cdot \left(\frac{w_t^{cr}}{w_n^{cr}}\right)^4} \quad (5.24)$$

where  $\sigma_{n,ai}^{cr}$  and  $\tau_{t,ai}^{cr}$  are the normal compressive stress (assumed positive in the present work) and shear stress at the crack generated by the aggregate interlock effect,  $D_{max}$  is the maximum size of the aggregates, and  $\tau_0$  (Equation (5.25)) is the crack shear strength as the crack opening approaches the null value ( $w_n^{cr} \rightarrow 0$ ),

$$\tau_0 = [0.25 - 0.30] \cdot f_c \quad (5.25)$$

#### 5.3.3.2 Contact Density Model (CDM)

In the CDM, the crack surface is idealised as a series of infinitesimal potential contact planes (see Figure 101a), with different orientation angles defined by a contact density function independent of the

aggregate distribution and dimension. In Figure 101b a schematic representation of the main entities of the model is presented, namely, the normal contact stress direction ( $\theta$ ), resultant contact stress angle ( $\theta_s$ ) and the normal and sliding displacement in the contact plane ( $w_{n\theta}$  and  $w_{t\theta}$ , respectively).

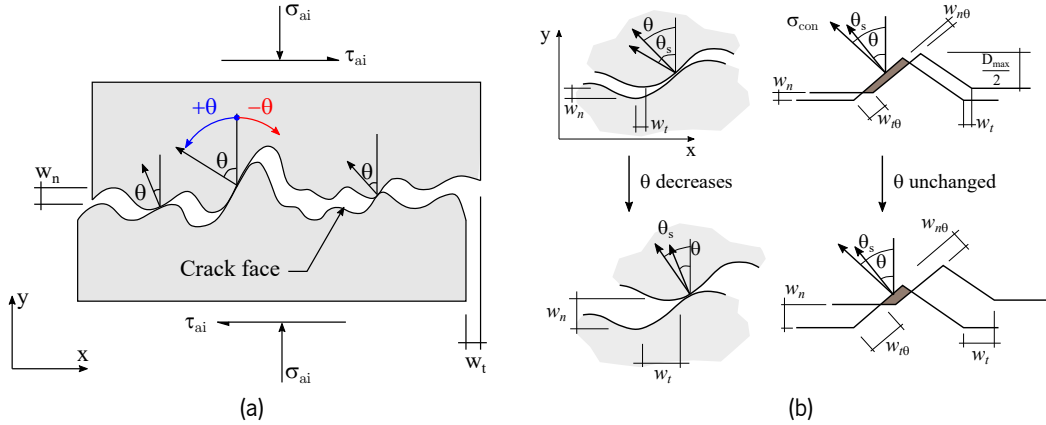


Figure 101: Crack contact idealisation: (a) direction of contact stress in the crack face and (b) local normal and tangential displacement in the contact plane according to Li et al. [248].

The resultant contact angle  $\theta_s$  deviates from the normal contact stress direction  $\theta$  due to existence of frictional shear stresses, and the occurrence of plastic deformations in the contact plane. However, according to Maekawa et al. [256], the influence of the plastic deformation compensates the effect of the frictional shear stresses and, therefore, these two effects cancel each other. Hence, the resultant contact angle ( $\theta_s$ ) can be assumed to be equal to the normal contact angle ( $\theta_s = \theta$ ).

The model is based on the physical-mechanical behaviour of the contact between infinitesimal planes, in which the contact stress developed between two potential contacting planes is governed by a rigid-plastic or elasto-plastic relationship. Thus, due to the nonlinear relationship of the contact stress, the model is able to capture the path-dependent behaviour of the aggregate interlock. Nonetheless, the simplified form of this model is more often used and is also applied in the context of the present work. Hence, considering a monotonic loading path, the occurrence of contact between infinitesimal planes, and assuming a rigid-plastic model for the contact stress, the Equations (5.26) and (5.27) are obtained,

$$\sigma_{n,ai}^{cr}(w_n^{cr}, w_t^{cr}) = k(w_n^{cr}) \cdot \left( \frac{\pi}{2} - \tan^{-1} \frac{w_n^{cr}}{w_t^{cr}} - \frac{w_n^{cr} \cdot w_t^{cr}}{w_n^{cr2} + w_t^{cr2}} \right) \quad (5.26)$$

$$\tau_{t,ai}^{cr}(w_n^{cr}, w_t^{cr}) = k(w_n^{cr}) \cdot \frac{w_t^{cr2}}{w_n^{cr2} + w_t^{cr2}} \quad (5.27)$$

where,

$$k(w_n^{cr}) = \left( 1 - \frac{2 \cdot w_n^{cr}}{D_{max}} \right) \cdot 3.83 \cdot f_c^{1/3} \quad (5.28)$$



### 5.3.4 Coupling the fibre and aggregate interlock resisting mechanisms

The tensile capacity of the matrix (Equation (5.29)) [233] is also accounted for in the normal component of the stress,

$$\sigma_{n,c}^{cr} (w_n^{cr}) = f_{ct} \cdot e^{-cw_n^{cr}} \quad (5.29)$$

where  $f_{ct}$  is the tensile strength of the matrix and  $c$  is a material dependent coefficient (15 for concrete and 30 for mortar).

The total capacity of FRC is obtained by adding the normal and shear stresses originated by the aggregate interlock, the normal and tangential components of the tensile stress provided by the fibres, and the matrix contribution as depicted in Figure 102. Hence, the total normal and shear stresses are given by Equations (5.30) and (5.31).

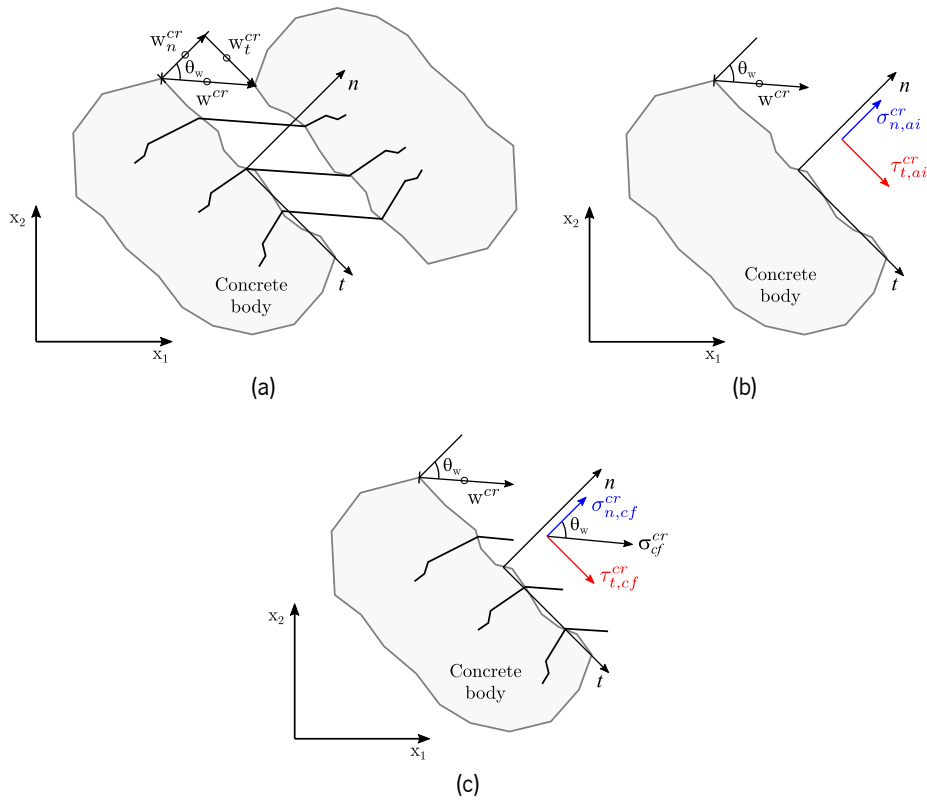


Figure 102: Concept of mixed-mode fracture smeared crack model: (a) crack opening and sliding displacement representation, (b) aggregate interlock contribution and (c) equivalent fibre pullout contribution.

$$\sigma_n^{cr} = \sigma_{n,c}^{cr} + \sigma_{n,cf}^{cr} + \sigma_{n,ai}^{cr} = \sigma_{n,c}^{cr} + \sigma_{cf}^{cr} \cdot \cos \theta_w + \sigma_{n,ai}^{cr} \quad (5.30)$$

$$\tau_t^{cr} = \sigma_{t,cf}^{cr} + \tau_{t,ai}^{cr} = \sigma_{cf}^{cr} \cdot \sin \theta_w + \tau_{t,ai}^{cr} \quad (5.31)$$

where  $\sigma_n^{cr}$  is the stress in the crack normal direction,  $\sigma_{n,c}^{cr}$ ,  $\sigma_{n,ai}^{cr}$  and  $\sigma_{n,cf}^{cr}$  are the fibre pullout, aggregate interlock and matrix stresses in the normal direction, respectively,  $\tau_t^{cr}$ ,  $\tau_{t,cf}^{cr}$  and  $\tau_{t,ai}^{cr}$  are the total crack shear stress and the components of the fibre pullout and aggregate interlock, respectively, and  $\theta_w$  is the

pullout loading direction angle. Due to the small dimension of the material's constituents, it is assumed that the concrete matrix does not contribute to the crack shear stress transference.

### **5.3.5 Parametric study**

In this section the results of a parametric study targeting the most influential variables of the model is conducted. For this purpose, the Pfyl's Engagement Model [232] is used in combination with the RCM and CDM aggregate interlock models.

Prior to the parametric study, a sensitivity analysis was conducted in order to identify the variables that have greater influence in the model output.

#### **5.3.5.1 Sensitivity Analysis**

sensitivity analysis (SA) techniques allow the study of how the uncertainty in the output of a model can be apportioned to the different sources of uncertainty in the model input factors [257]. SA analysis is a very useful tool in the development of numerical simulation models and can be mainly classified in two main categories, local SA approach and global SA approach.

The local approach can be defined by a one-at-a-time (OAT) measure approach, which consists in varying a single input parameter while keeping the remaining factors constant. The main disadvantage of this approach is the inability to capture interaction effects between input parameters. Further, this sort of techniques present limitations such as assumptions on the model linearity and normality. This kind of methodologies are commonly used in solving large environmental systems such as climate modelling, oceanography among others [258].

Global SA techniques on the other hand, consider the whole variance range of the input [259] and attempt to quantify the variance effect of the input variables to the variance of the model output. These methods present appealing features such as model independence, ability to capture the influence of the full range of variation of the inputs, capturing of interaction effects among input factors. On the other hand, the main disadvantage of this sort of methodologies is related with the high computational cost, reason why many researchers attempted to optimize computational efficiency in the numerical computation of such approaches [260].

There are several objectives underlying a sensibility analysis, namely the identification and prioritization of the most influential inputs, identification of non-relevant parameters, mapping of the output behaviour and calibration of model input parameters [260]. In the present case the main objective is the identification of the parameters with the most impact in the model output.

In the present case, given the low number of input factors (Table 19) and the low computational cost of the model evaluation, Sobol' method [261] is used to determine the first-order ( $S_i$ ) and total effect indices ( $S_{T_i}$ ). The first-order indices represent the contribution of each input to the variance of the output result, whereas the total effect indices account for the total contribution of one factor to the output variance,

including not only the first-order effect but also the higher order effects due to interactions between that input and the remaining ones [260].

The SA was conducted in python by means of the library “SALib - Sensitivity Analysis Library in Python” and by employing the Sobol’ method. The total number of model executions to estimate the full set of the variance-based indices ( $S_i, S_{T_i} = 1, 2, \dots, D$ ) is given by  $N \cdot (2 \cdot D + 2)$  in which  $N$  is the number of samples for each variable and  $D$  is the number of input factors, which resulted in 32000 model evaluations ( $N = 2000$ ). For a detailed description of the mathematical formulation of the model and the sampling method used see [259, 261, 262]. The input factors considered in the SA analysis are presented in Table 19.

Table 19: Input factors, description and range of variation considered in the SA.

Input	Description	Unit	Interval
$w_n^{cr}$	Crack normal displacement	mm	[0 to 1] - [1 to 7]
$w_t^{cr}$	Crack tangential displacement	mm	[0 to 1] - [1 to 7]
$f_c$	Concrete compressive strength	MPa	[25 to 60]
$l_f$	Fibre length	mm	[20 to 80]
$l_f / d_f$	Ratio between fibre length and diameter	-	[45 to 80]
$D_{max}$	Maximum aggregate diameter	mm	[4 to 32]
$V_f$	Fibre ratio in volume	%	[0.25 to 2]

Due to the abrupt changes in both normal and shear stress for small crack openings, two sensitivity analysis were conducted. One considering crack opening ( $w_n^{cr}$ ) and sliding ( $w_t^{cr}$ ) ranging between 0 and 1mm and another one for crack opening and sliding varying between 1 and 7 mm, as presented in Table 19.

The results presented in Figure 103 represent the first-order and total-effect indices considering the RCM and CDM aggregate interlock model and for the two ranges of crack widths.

Considering the results for the small crack interval (Figure 103a to Figure 103d), it is possible to say that in general the inputs  $w_n^{cr}$ ,  $w_t^{cr}$ ,  $f_c$  and  $V_f$  are the most relevant ones. For the case of the RCM and what concerns the normal stress (Figure 103a),  $w_t^{cr}$ ,  $w_n^{cr}$  and  $V_f$  are the inputs with the most impact in the results, with decreasing impact in that order.  $f_c$  revealed to have little impact.

In case of the shear stress results (Figure 103b),  $w_t^{cr}$ ,  $w_n^{cr}$  and  $f_c$  were the most influential variables considering the substantially higher first-order and total effect indices when compared with the remaining inputs.  $V_f$  and  $D_{max}$  had a slight impact in the model outcome. In case of the CDM model (Figures 103c and 103d) the results show similar trend, however the  $f_c$  and  $V_f$  show lower impact in the results when compared with the RCM.

Regarding the higher crack opening range ([1 to 7] mm) it is possible to observe that for both aggregate interlock models and both normal and shear stress results,  $w_n^{cr}$ ,  $w_t^{cr}$ ,  $f_c$  and  $D_{max}$  are the most influential variables, since the first-order and total effect indices are substantially higher when compared with the remaining inputs, except for the  $f_c$  which shown little influence in case of the CDM model.

In case of the RCM model (Figures 103e and 103f), the results show that in terms of normal stress,  $w_n^{cr}$ ,  $w_t^{cr}$ ,  $D_{max}$  and  $f_c$  are the most influential parameters with decreasing impact in that order. Considering the shear stress results, the variable with the most significant impact is  $w_n^{cr}$  followed by  $D_{max}$  while  $f_c$  and  $w_t^{cr}$  show similar impact.

Regarding the CDM model (Figures 103g and 103h), the inputs revealing the most impact in terms of normal stress are  $w_n^{cr}$ ,  $w_t^{cr}$ ,  $D_{max}$ , respectively. In terms of shear stress,  $w_n^{cr}$ ,  $D_{max}$ ,  $w_t^{cr}$  and  $f_c$  show greater impact, with decreasing relevance in that order.

It is noticeable that the total effect sensitivity indices ( $S_{T_i}$ ) are greater than the first-order indices ( $S_i$ ) indicating the existence of interaction between input variables. Nonetheless, in the present case the interest relies in identifying the most contributing parameters to the model output variance, therefore the interaction effect indices was not investigated. In conclusion, the considered range of variation of the input variables fibre length ( $l_f$ ) and fibre aspect ratio ( $l_f / d_f$ ) revealed to have little to no impact in the variance of the model output and therefore fixed values will be assumed in the parametric study.

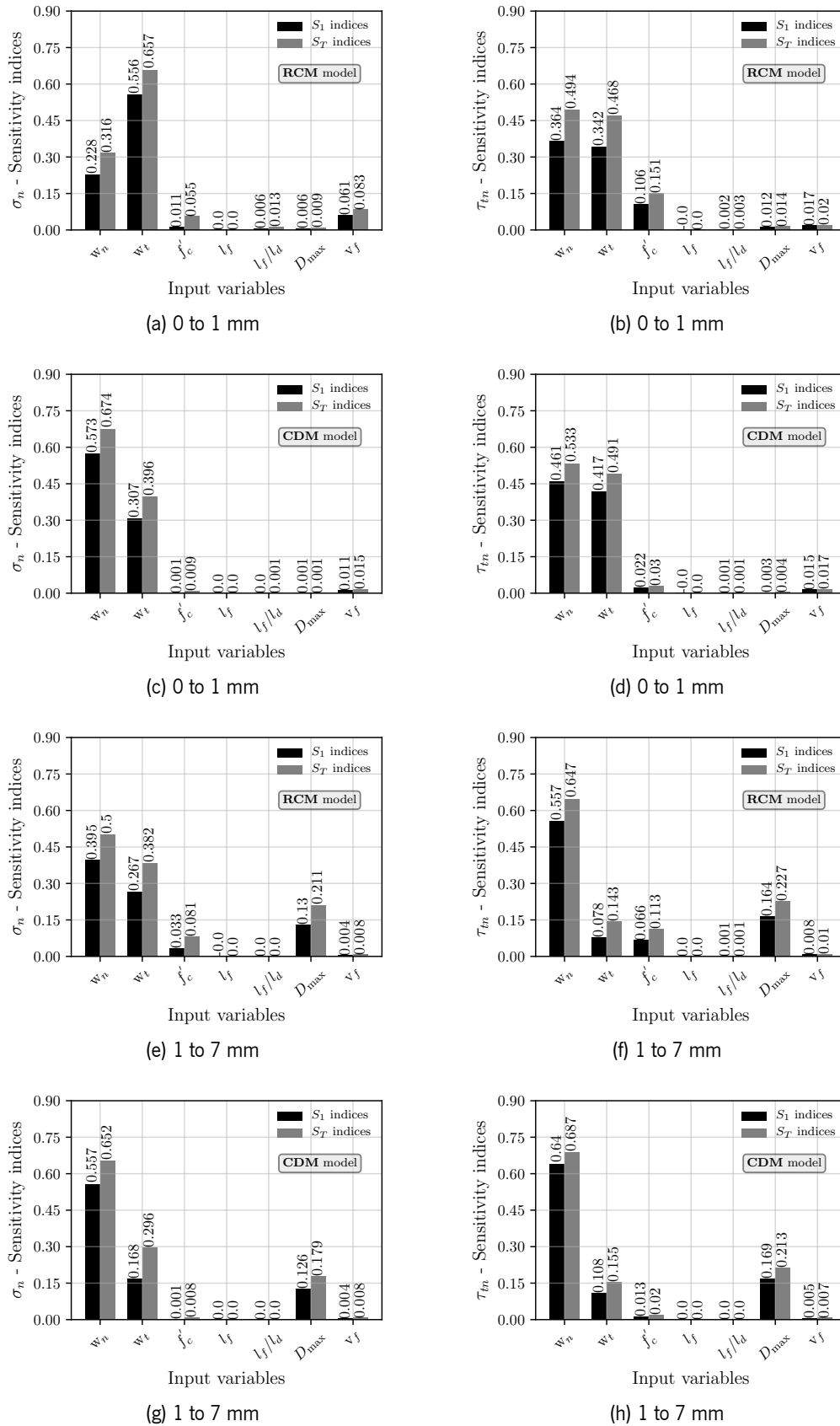


Figure 103: First order and total sensitivity indices for the input parameters considering the RCM (a,b,e,f) and CDM (c,d,g,h) aggregate interlock models.

### 5.3.5.2 Results of the parametric study

Considering the results of the sensitivity analysis, a parametric study was conducted considering the variables that revealed to have the greater variance in the model output. The investigated variables are presented in Table 20.

Table 20: List of the selected variables for the parametric study.

Input	Description	Unit	Range
$w_n^{cr}$	Crack opening	mm	[0 to 6]
$w_t^{cr}$	Crack sliding	mm	[0 to 6]
$f_c$	Concrete compressive strength	MPa	[25 to 60]
$D_{max}$	Maximum aggregate diameter	mm	[4 to 32]
$V_f$	Fibre ratio in volume	%	[0.5 to 2]

In Figures 104a and 104b a comparison between the RCM and CDM aggregate interlock models is presented. The two aforementioned models show very similar behaviour trends, both in case of normal and shear stresses, albeit the CDM shows substantially higher normal and shear stress values.

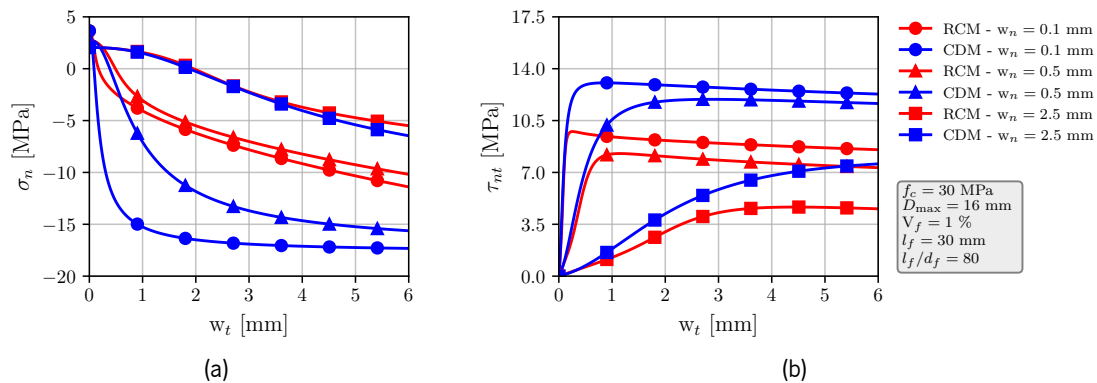


Figure 104: Comparison of results in terms of (a) normal and (b) shear stresses, obtained with the RCM and CDM aggregate interlock models for different crack opening widths.

The results of the parametric test, considering the RCM and CDM aggregate models, are presented in Figures 105 and 106, respectively. Three crack opening values are analysed ( $w_n^{cr} = 0.1, 0.5, 2.5$  mm) for both models.

In Figures 105a and 105b, the  $f_c$  was varied within the range presented in Table 20 for each value of  $w_n^{cr}$  and by fixing the remaining variables to the values presented in the figure. In terms of normal stress (Figure 105a), higher  $f_c$  values lead to higher tensile and compressive stresses for all crack opening values considered. The results seem to be physically coherent since on one hand, higher  $f_c$  values lead to higher tensile resistance of the matrix and on the other hand, lower values of  $w_n^{cr}$  lead to higher stresses of compressive nature due to the aggregate interlock effect. In case of shear stress transfer (Figure 105b), it is possible to observe that greater  $f_c$  values lead to higher shear peak stresses regardless of the crack opening

value. The results regarding the influence of the maximum aggregate dimension  $D_{max}$  are presented in Figures 105c and 105d. In terms of normal stresses, it is possible to observe that greater values of  $D_{max}$  originate higher stresses of compressive nature regardless of the crack opening value considered. In terms of shear stresses (Figure 105d), the results show the same trend since higher aggregate dimensions lead to higher peak shear stress values for all the considered values of  $w_n^{cr}$ . Figures 105e and 105f show the influence of the fibre volume in the normal and shear stress for the different crack opening values considered. Regarding the normal stresses, the maximum fibre volume considered (2%) leads to higher tensile stress capacity, regardless of the crack opening value. The same trend is verified for the case of the shear stresses, revealing that higher fibres volumes lead to higher shear stress transfer capacity.

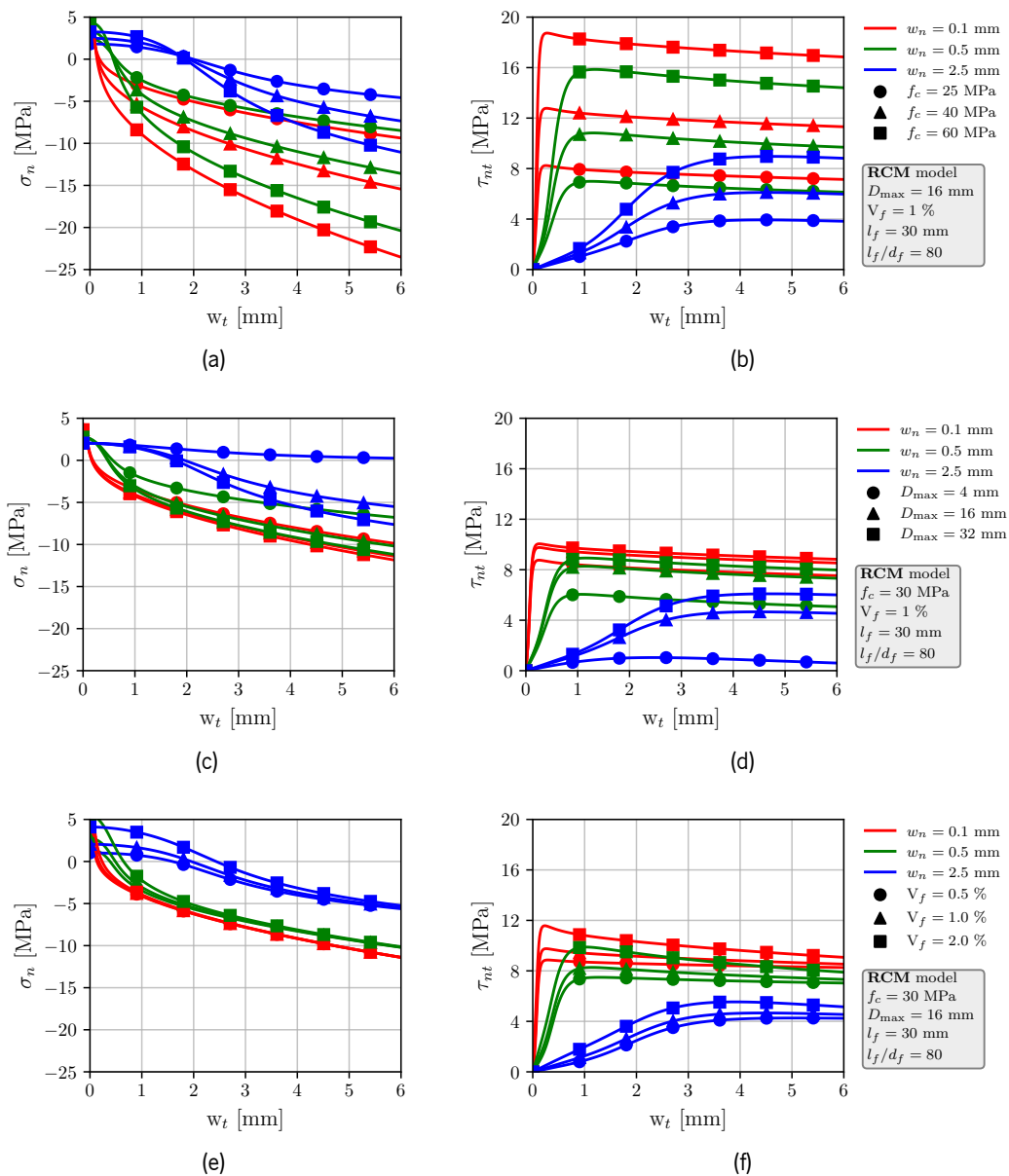


Figure 105: Results of the parametric study considering the RCM aggregate interlock model.

In Figure 106 the same investigation is conducted but now using the CDM. Generally, the results are similar to the ones obtained considering the RCM aggregate interlock model for all the variables ( $f_c$ ,  $D_{max}$  and  $V_f$ ). In fact, the most significant difference resides in the maximum values attained for both normal and shear stresses as already seen in Figures 104b, 105 and 106. Furthermore, in case of CDM, the compressive strength ( $f_c$ ) seems to have less impact in the variation of both normal and shear stress (Figures 106a and 106b) when compared with the results obtained considering the RCM aggregate interlock model.

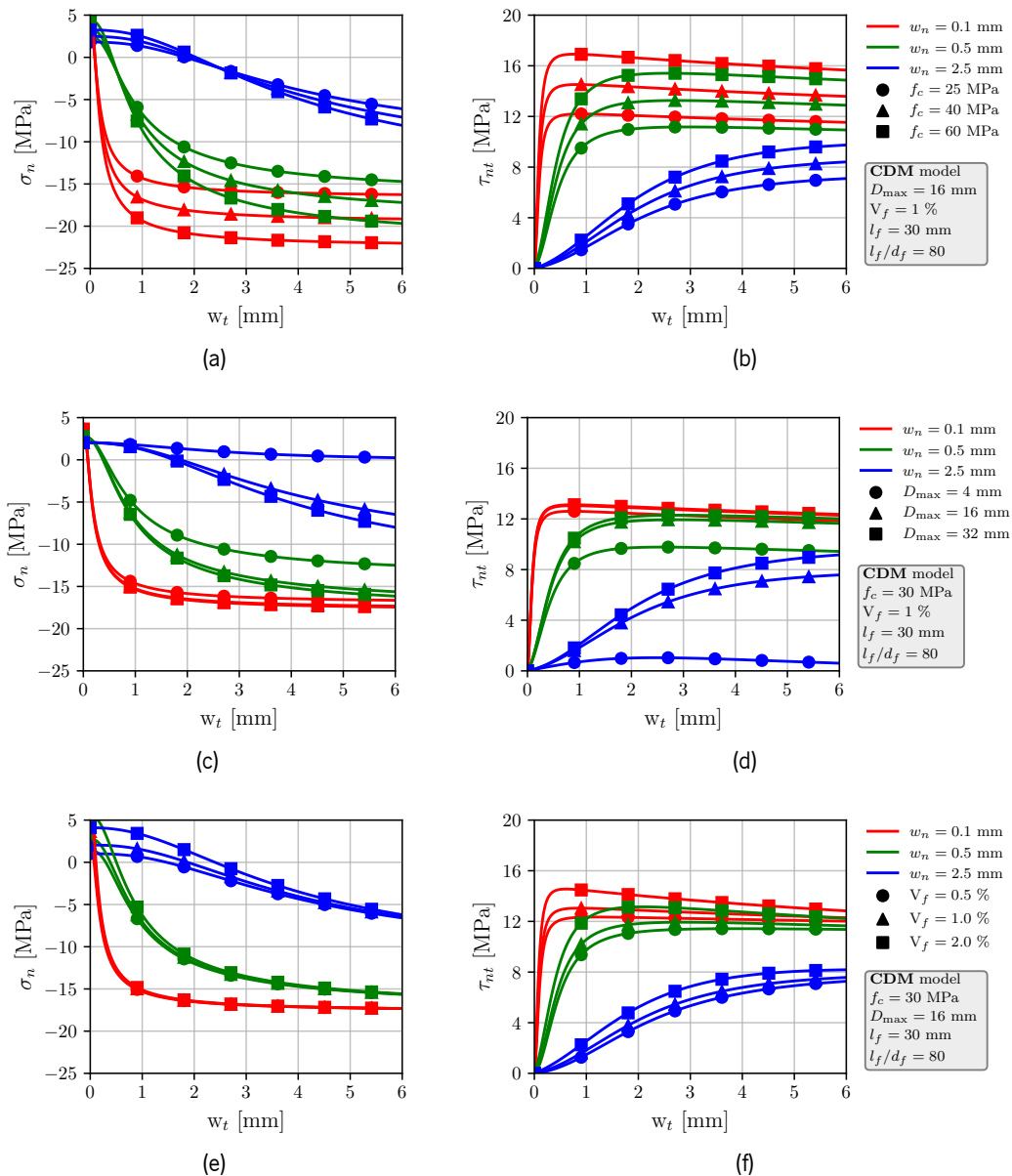


Figure 106: Results of the parametric study considering the CDM aggregate interlock model.

To further understand the contribution of aggregate and fibre resisting mechanisms to the stress transferring capacity, the corresponding parcel of each component is plotted against the total normal and



shear stresses. A crack opening ( $w_n^{cr}$ ) of 0.5 mm is considered and both aggregate interlock models are analysed. The results are presented in Figures 107 and 108.

In terms of normal stresses (Figures 107c and 108c) the results show that the fibre contribution decreases as the sliding movement increases, whereas on the other hand the aggregate interlock parcel increases with the sliding displacement. This was expected since the increasing sliding movement leads to a reduction of the normal component of the tension stress sustained by the fibres and on the other hand the growing contact between the crack faces generates stresses of compressive nature due to the aggregate interlock. This is verified for both aggregate interlock models.

In case of shear stresses (Figure 107b) the increase of tangential displacement leads to a rapid increase in shear stress due to the relatively small crack opening width ( $w_n = 0.5$  mm), being the maximum value reached for a tangential displacement of 1mm for the case of the RCM and 2 mm for the case of the CDM. In both cases, the influence of the aggregate interlock effect is substantially higher when compared to the fibre contribution, especially for the CDM. For the present scenario the aggregate interlock contribution is 3 times higher than the fibre contribution when the RCM is considered and around 5 times greater when the CDM is used.

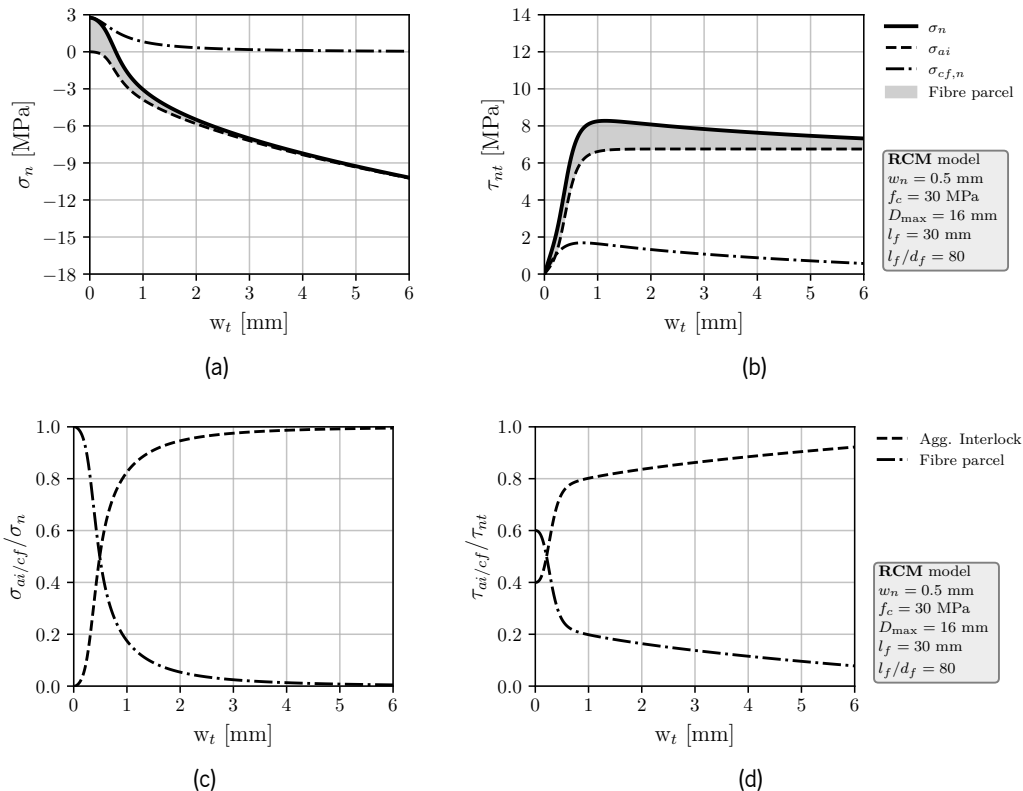


Figure 107: Aggregate interlock and fibre contribution in terms of (a) normal and (b) shear stresses considering the RCM and (c), (d) relative contribution of fibres and aggregate interlock.

In terms of normal stress contribution (Figures 109a, 109c and 109e) the use of bigger aggregates translates into higher contribution of the aggregate interlock effect, since larger aggregates results in higher

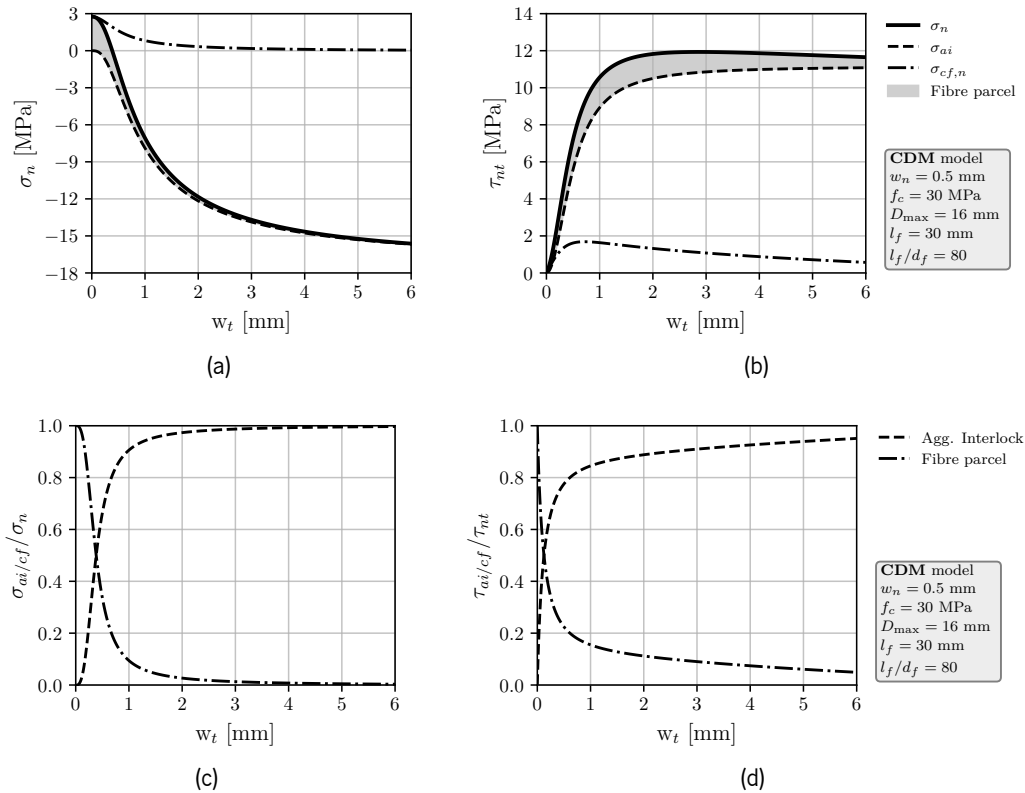


Figure 108: Aggregate interlock and fibre contribution in terms of (a) normal and (b) shear stresses considering the CDM and (c), (d) relative contribution of fibre and aggregate interlock.

compressive stresses (as shown in Figures 105c and 106c). Furthermore, the use of smaller aggregates such as 4 mm restricts the range of crack opening values  $w_n^{cr}$  in which the aggregate interlock contributes, since as shown in Figure 109a, the aggregate interlock contribution is null within the interval [2, 6] mm regardless of the slipping displacement value. The same conclusions can be drawn for the case of CDM aggregate interlock model (Figure 110).

The shear stress contribution results show the same tendency as the normal stress ones, however it can be observed that fibre contribution is less significant, especially when the CDM is used (Figures 110d and 110f).

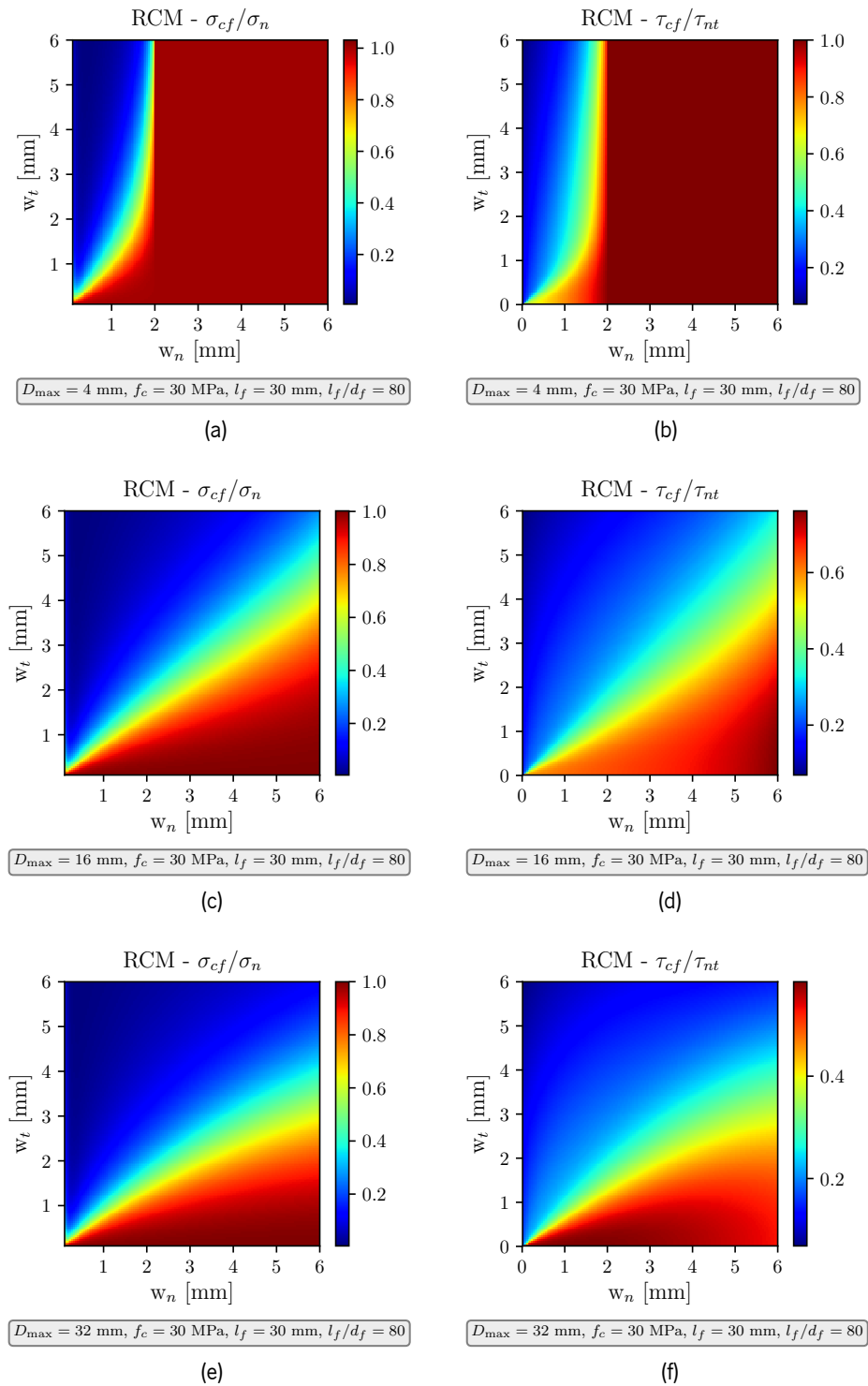


Figure 109: Fibre/total stress ratio in terms of normal and shear stresses considering the RCM. A ratio of 1 means only fibre contribution.

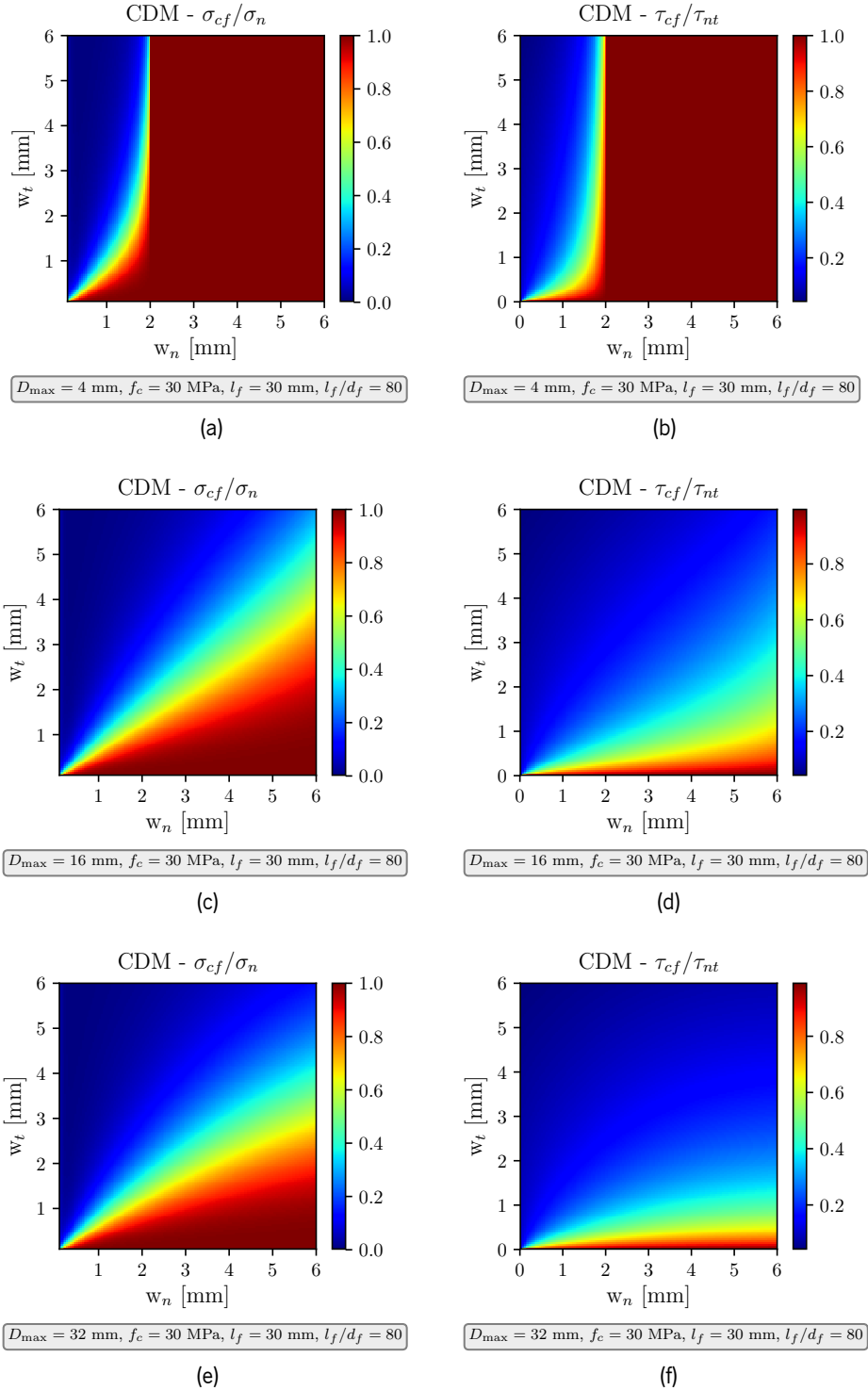


Figure 110: Fibre/total stress ratio in terms of normal and shear stresses considering the CDM. A ratio of 1 means only fibre contribution.

## 5.4 Assessment of the predictive performance of the model

The predictive performance of the model is evaluated by comparing reported experimental results [231, 241, 245] with the numerical predictions obtained with the proposed model. Firstly, the influence of the aggregate interlock model is evaluated by plotting the results obtained using the RCM/CDM, combined with the Pfyl's model [232], against the experimental results. Subsequently, the performance of the different pull-out models is analysed by adopting the RCM aggregate interlock model.

Khanlou et al. [241] analysed the shear performance of steel-fibre reinforced concrete (SFRC) specimens by means of the FIP standard shear test as illustrated in Figure 111.

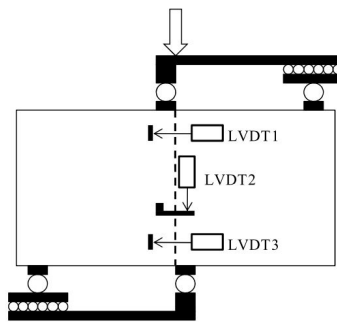


Figure 111: Schematic representation of the experimental setup used by Khanlou et al. [241].

The tests involved two reference concrete mixes, 35 and 60 MPa compressive strength class, reinforced with end-hooked fibres of different volume fibre dosages (0.25%, 0.51%, 0.76% and 1.0%). The specimens have 250x250x540 mm dimensions, and notches were introduced along the lateral faces resulting in a net shear plane of 220x220 mm. The experimental results obtained for the C35 concrete strength class (with experimental compressive strength of  $f_c \approx 45$  MPa) considering two fibre dosages (0.51% and 1.00%) are plotted against the numerical results in Figure 112. The results show an overall reasonable correlation, especially for the cases when lower fibre content is used. Generally, the RCM model gives a more approximate post-peak behaviour, which is not so well captured in the cases where higher fibre contents are used (Figures 112c and 112d).

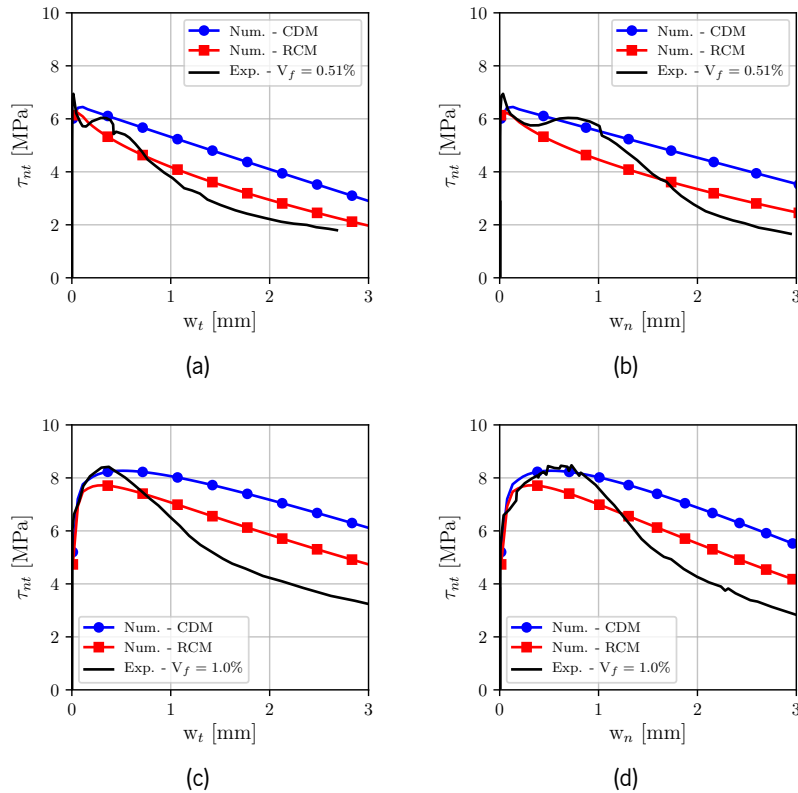


Figure 112: Experimental and numerical results comparison for two fibre dosages [241].  $f_c = 45$  MPa,  $l_f = 60$  mm,  $l_f/d_f = 80$ ,  $D_{max} = 13$  mm.

Regarding the fibre pull-out models, the experimental results are plotted against the numerical results in Figure 113. When low fibre volume ratios are considered, such as 0.51%, the results between the different pull-out models show similar trends (Figures 113a and 113b), which is expected since the response is mainly dominated by the aggregate interlock component. However, when higher fibre volume ratios are used (Figures 113c and 113d) a higher influence of the fibre contribution is obtained. In this case, one can observe that the Pfyf's model better captures the pre-peak and peak response, whereas the remaining models underestimate the experimental results. All models show similar trends in what concerns the post-peak response, exhibiting an overestimation of the post-peak behaviour.

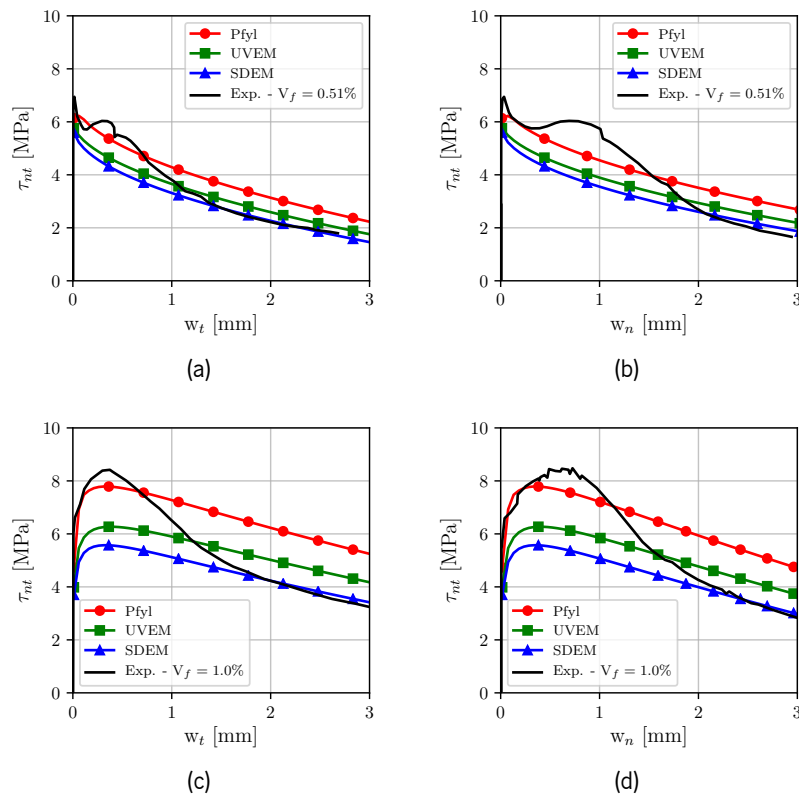


Figure 113: Experimental and numerical results comparison considering different fibre pull-out models and the RCM.  $f_c = 45$  MPa,  $l_f = 60$  mm,  $l_f/d_f = 80$ ,  $D_{max} = 13$  mm.

Soltanzadeh et al. [231] characterized the shear behaviour of FRC specimens ( $f_c \approx 60$  MPa,  $D_{max} = 12.5$  mm and  $V_f = 1.125\%$ ) by using a double shear specimen (DSS), which consists of rectangular specimens of  $150 \times 146$  mm<sup>2</sup> cross-section and 47 mm thickness. Notches in the top, bottom, front and rear faces of the specimen were executed resulting in a shear plane area of  $20 \times 100$  mm<sup>2</sup>. The specimen was supported on two rigid edges 61 mm apart, and was loaded in two loading points excluding any confining pressure as depicted in Figure 114.

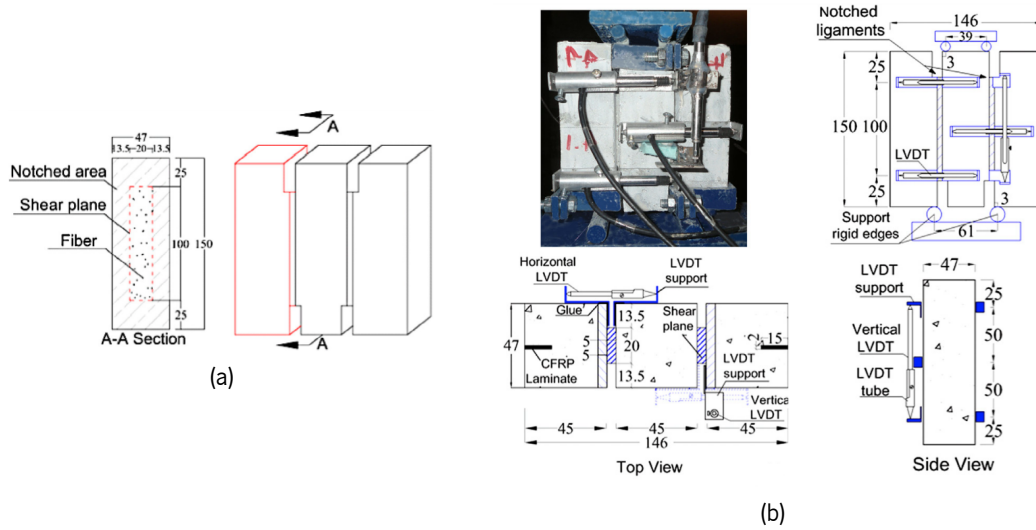


Figure 114: Geometry and loading configuration of the specimen [231].

The results regarding the comparison between the two aggregate interlock models in combination with the Pfyl's model are presented in Figure 115. The model shows an overall acceptable correlation between the numerical and experimental results. Once again, the RCM seems to better capture the peak stress, as well as the post-peak behaviour. In addition, the average experimental response is always overestimated by the RCM, while the CDM underestimates the pre-peak and some part of the post-peak response. In terms of shear - crack width response portrayed in Figure 115b, it is possible to observe that both models estimate the response within the experimental envelope. Nonetheless, the RCM showed better overall performance.

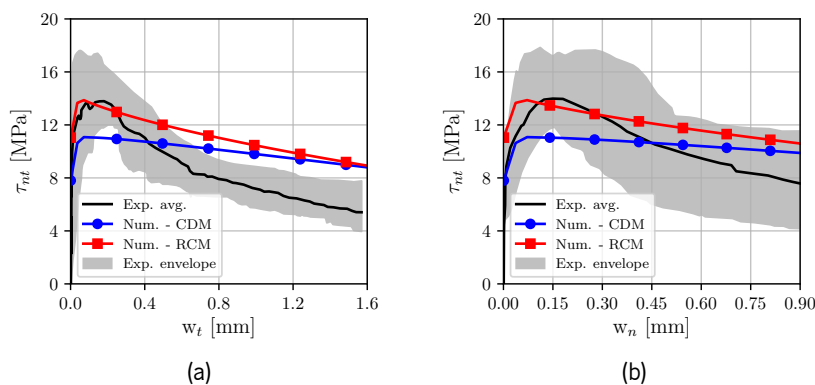


Figure 115: Comparison between experimental and numerical results: (a) shear stress - sliding displacement and (b) shear stress - opening displacement.  $l_f = 30$  mm,  $l_f/d_f = 80$ ,  $V_f = 1.125\%$

Considering the use of different fibre pull-out models in combination with the RCM, the corresponding results are as presented in Figure 116. These results show that the Pfyl's model captures well the pre-peak response, while the remaining models seem to underestimate the response. In terms of post-peak behaviour, all models show a similar trend by overestimating the overall response.



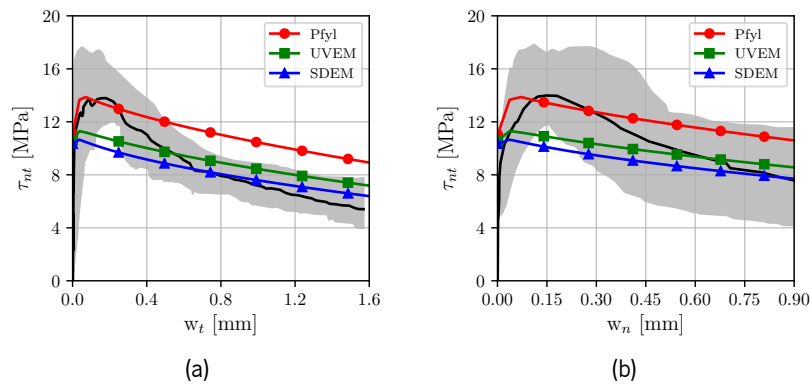


Figure 116: Comparison between experimental and numerical results considering different fibre pull-out models in combination with the RCM.  $l_f = 30$  mm,  $l_f/d_f = 80$ ,  $V_f = 1.125\%$

Soetens and Matthys [245] conducted direct shear tests by means of an adapted version of the test developed by the Japanese Society of Civil Engineers (JSCE) JSCE-SF6. These authors carried out a series of tests with traditional concrete (TC) and self-compacting concrete (SCC), long (60 mm) and short (30 mm) hooked-end steel fibres with C50/60 concrete grade specimens in order to investigate the influence of volume fibre dosage (0.25%, 0.50%, 0.75%), fibre type and concrete type on the shear behaviour of SFRC. The specimens consist in standard prisms with 150x150x600 mm and a predefined crack plane is induced by introducing 30 mm deep and 4 mm wide notches resulting a final shear plane of 90x150 mm.

In Figure 117 the predictions obtained by the herein proposed constitutive model are compared with the SCC and TC experimental results. Regardless the type of aggregate interlock model, the developed approach predicts quite well the experimental results up to peak shear stress, but in the post-peak stage, apart the specimens TC-40S, an overestimation of the shear stress capacity is estimated by the both models, mainly when using the CDM. This overestimation is caused by the aggregate interlock models, since it was already verified that above approximately 1 mm sliding displacement, the fibre reinforcement mechanisms have relatively small influence on the shear stress transference through the crack.

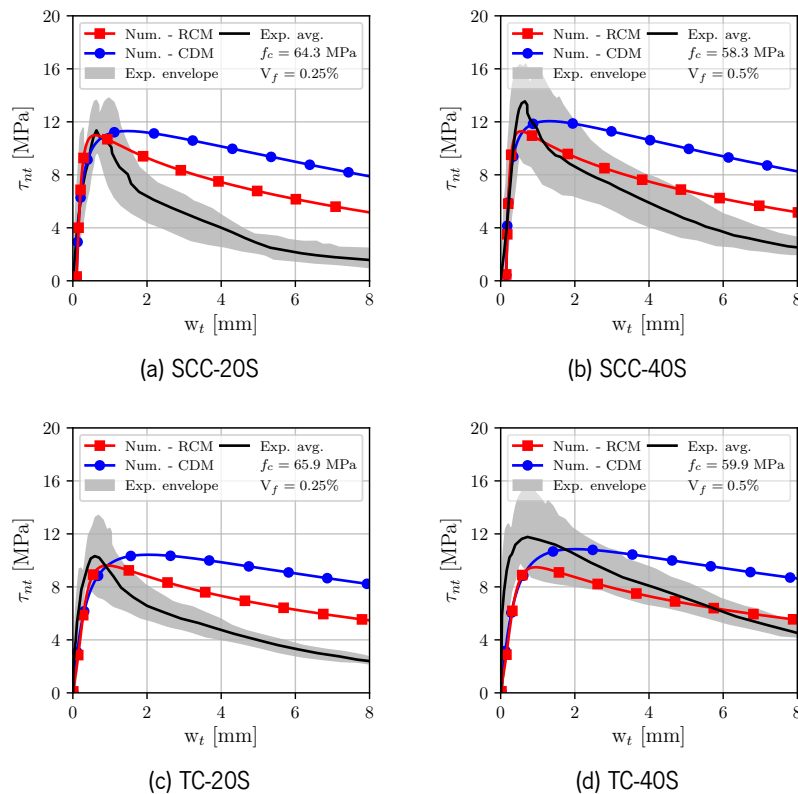


Figure 117: Comparison of the experimental and numerical results:  $l_f = 30$  mm,  $l_f/d_f = 80$ ,  $D_{max} = 7$  mm.

Once again the use of different pull-out models is compared against the experimental results in Figure 118, which show the same trend as the results presented previously (Figures 113 and 116). For this type of tests, the fibre pull-out model has a relatively small influence on the predictive performance of the developed approach due to the low content of fibres adopted in these experimental programs and the predominant influence of the aggregate interlock component on the crack shear stress transfer capacity.

## 5.5 Modification of the aggregate interlock resisting mechanism

Considering the results presented in Figures 112, 115 and 117, one can observe that, generally, the peak stress is well captured whereas the post-peak behaviour is always overestimated regardless of the aggregate interlock model used. This is justified by the fact that both aggregate interlock models were developed for conventional reinforced concrete, where the level of crack width and sliding for the mobilization of cracking resisting mechanisms is much smaller than in case of FRC. The crack stress transfer for crack opening levels occurring in FRC must be adapted for not estimating unrealistic high values.

Thus, in order to enhance the post-peak predictive performance of the model, the RCM and CDM were modified by increasing the degradation rate of the aggregate interlock effect with the increase of the

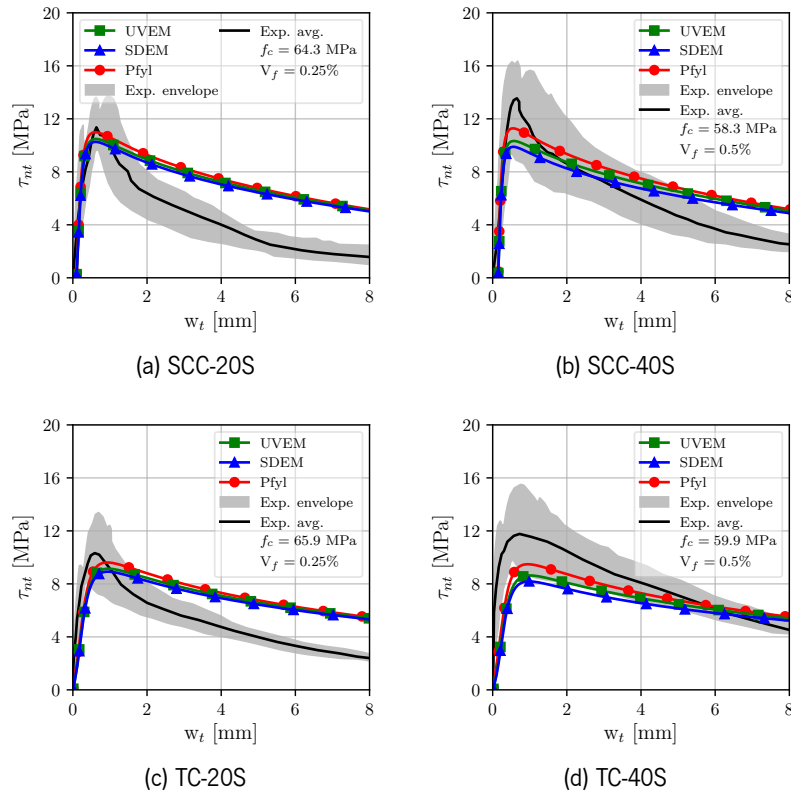


Figure 118: Comparison of the numerical predictions obtained using different fibre pull-out models.

crack opening. This is achieved by multiplying the original equations (Equations (5.24), (5.26) and (5.27)) by an inverted special sigmoid function, known as Gompertz function, given by Equation (5.32),

$$S(w_n^{cr}, D_{max}) = 1 - a \cdot e^{-b \cdot e^{-c \cdot \left(\frac{w_n^{cr}}{D_{max}}\right)}} \quad (5.32)$$

where  $a$  is a coefficient that represents the horizontal asymptote of the function,  $b$  induces a translation in the abscissa axis direction (representing the  $w_n$ ) and  $c$  sets the growth rate of the function in the ordinate axis (representing the  $S$  function). The influence of the coefficients  $b$  and  $c$  is illustrated in Figure 119.

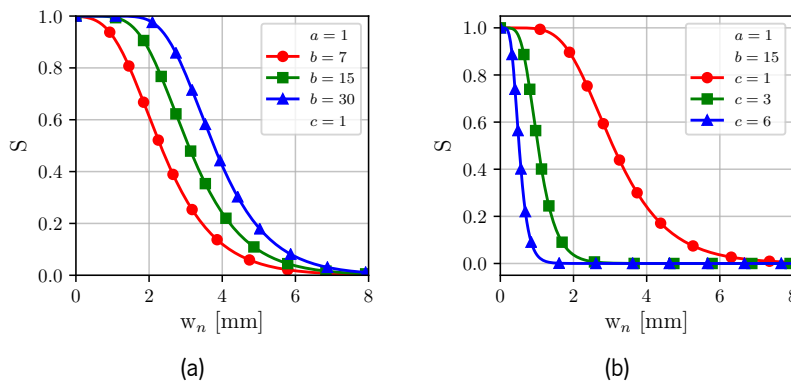


Figure 119: Effect of varying the coefficients (a)  $b$  and (b)  $c$  in Equation (5.32).

To determine the optimum values for the coefficients  $b$  and  $c$ , the experimental results presented in Figures 113a, 113c, 115a, 117a, 117b and 117c were fitted as much as possible for each aggregate interlock model, and the obtained results are presented in Table 21.

Table 21: Average values of the coefficients  $b$  and  $c$  of Equation (5.32).

Model	$b_{avg}$	$c_{avg}$
RCM	7.04	12.60
CDM	6.48	15.19

The results of the simulations of the experimental tests obtained considering the modified version of the aggregate interlock models are presented in Figures 120 and 121. Generally, the results show a much better agreement between numerical and experimental results (apart from Figure 121d) in terms of post-peak behaviour, especially in the case of the results obtained by Soetens and Matthys [245]. Furthermore, with this modification the RCM and CDM exhibit similar predictions in the post-peak phase.

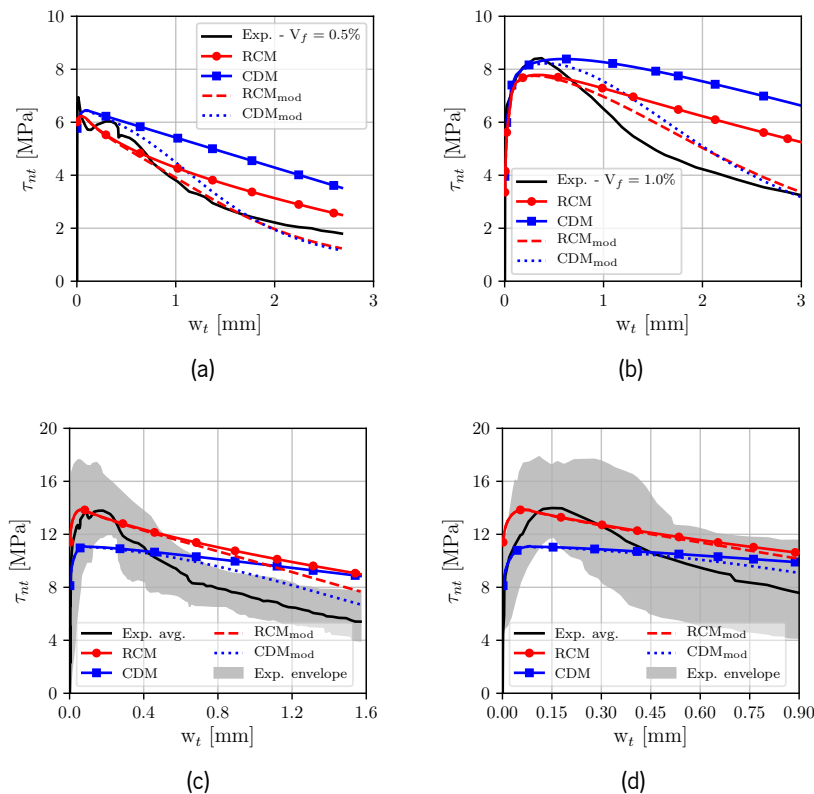


Figure 120: Comparison of the results given by the original and modified RCM/CDM and the experimental results obtained by (a), (b) Khanlou et al. [241] and (c), (d) Soltanzadeh et al. [231].

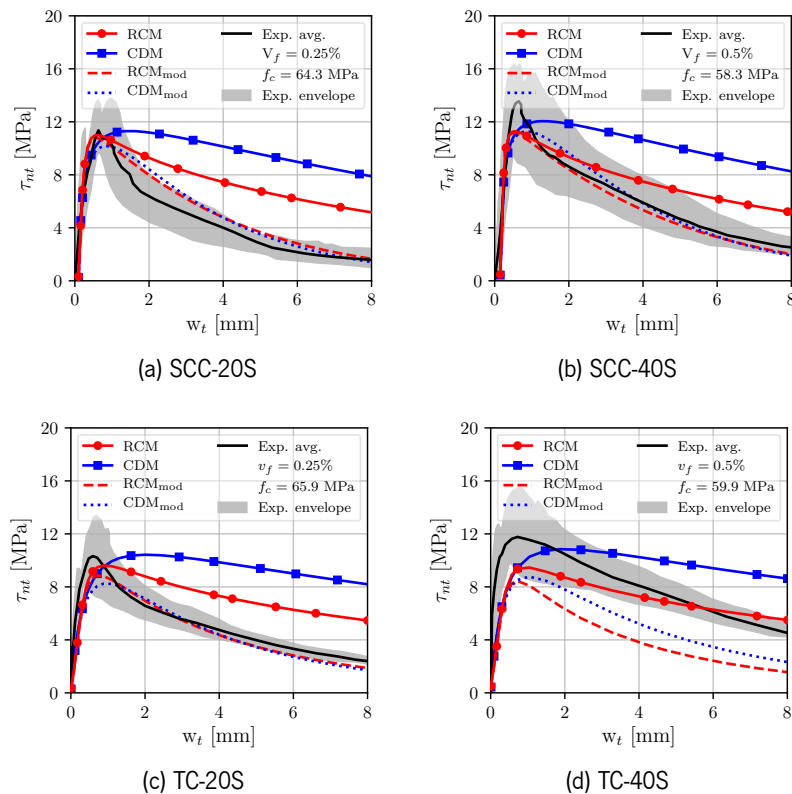


Figure 121: Comparison of the results given by the original and modified RCM/CDM and the experimental results obtained by Soetens and Matthys [245].

## 5.6 Summary and Conclusions

In this chapter a new constitutive model that predicts the behaviour of FRC in mixed-mode fracture is proposed. The model accounts for the fibre and aggregate interlock resisting mechanisms, as well as the interaction between these effects. Furthermore, a parametric study is conducted with the purpose of assessing the impact of the main parameters of the model. The numerical predictions of the constitutive model using different fibre pull-out laws are compared against experimental results reported in the literature. Finally, a modification to the aggregate interlock models is proposed in order to enhance the post-peak predicting performance of the model.

Considering the results presented in this paper, the following conclusions can be drawn,

- The parametric study shows that higher fibre volume ratios allow for greater normal and shear stresses to develop. In addition, the concrete compressive strength greatly impacts the maximum normal and shear stress values in both the RCM and CDM aggregate interlock models. Aggregate size governs the contribution of the aggregate interlock component, especially when greater crack sliding values are considered.

- The results presented in the experimental validation show that the RCM gives a better overall agreement with the experimental results comparatively to the CDM. Furthermore, the comparison between fibre pull-out models show that the Pfyl's simple model captures both peak and post-peak response with higher accuracy when compared to the other models. In addition, Pfyl's model has the advantage of requiring less input parameters when compared the SDEM.
- The model seems to capture reasonably the peak stresses, however, the post-peak response is overestimated in all the experimental tests simulated. This is justified by the fact that both the RCM and CDM were developed for conventional reinforced concrete, where the level of crack width and sliding for the mobilization of cracking resisting mechanisms is much smaller than in case of FRC.
- Both the RCM and CDM where adapted in order to better represent the aggregate interlock mechanisms in FRC, since their original version was founded in experimental results from conventional concrete. By applying a special sigmoid type function to the original formulation of the RCM and CDM, a much better predictive performance was obtained.

# 6 Implementation of the Two-Dimensional Mixed-Mode Smearred Crack Model

## 6.1 Introduction

*In this Chapter the implementation in the FEMIX V4.0 computer code of the two dimensional mixed-mode fracture model presented in Chapter 5 is detailed. In addition, the predictive performance of the model is assessed by simulating three numerical case studies consisting of a three-point notched beam bending tests (3PNBBT) for assessing the structural behaviour in mode I, a shear panel test to appraise the predictive performance of the model in mode II, and finally a prismatic beam subjected to a mixed-mode loading condition. In an attempt to further enhance the predictive performance of the fibre pullout models, modifications to the original formulations are proposed and appraised. Also, a multi-linear branch model is proposed to facilitate the use of the inverse analysis (IA) tool developed in Chapter 4 for defining the mode I behaviour. The numerical simulations demonstrated the good accuracy of the model in predicting the experimental responses, both in mode I and mode II, capturing not only the peak loads but also the evolution trend of the post-peak responses in the analysed scenarios. The modifications proposed to the fibre pullout models resulted in an enhanced predictive performance of the mixed-mode fracture smearred crack model (MMFSCM). The multi-linear branch model exhibited excellent performance, capturing the experimental response with very good accuracy in all 3PNBBT simulations.*

*The key novelties of the herein presented work can be summarised in the following points:*

- The aggregate interlock and fibre pullout models that comprise the MMFSCM model rely on actual physical parameters (i.e. geometric properties of the fibres, aggregate diameter, concrete compressive strength), which simplifies the simulation process;*
- The results at the crack level can be obtained by resisting mechanism that grants the possibility to further analyse the contribution of each parcel to the overall structural behaviour;*
- The mode I can be defined by a multi-linear branch stress - crack width relationship that can be derived by IA when experimental results are available, granting more flexibility in the simulations;*

- Possibility to include additional aggregate interlock or fibre pullout models due to the modular implementation strategy adopted in the FEMIX V4.0 computer code.

Submitted for publication in: [Engineering Fracture Mechanics](#)

---

## 6.2 Two dimensional mixed-mode fracture smeared crack model

### 6.2.1 Introduction

The fracture behaviour of fibre reinforced concrete (FRC) elements involves complex phenomena as different resisting mechanisms are mobilized during the fracture process, such as the fibre pullout and aggregate interlock resisting mechanisms. The fibres bridging the cracks contribute to the crack arrest process leading to smaller crack widths, higher load-carrying capacity, ductility and energy absorption capability of FRC structures [230]. In addition, the use of fibre reinforcement originates a higher degree of interlock between the aggregates that in turn generate greater shear stress transferring capacity as the sliding motion increases, and forces the aggregates to collide against each other [249, 263].

Hence, the presence of fibres in FRC enhances the shear stress transferring capacity and strength as already documented in several studies [231, 234, 242, 245, 249, 263]. Despite the variety of techniques and approaches proposed throughout the last decades, a unified consensual approach to accurately simulate the behaviour of FRC elements does not yet exist.

In this section the implementation of the two dimensional mixed-mode fracture smeared crack model (MMFSCM) in a finite element method (FEM)-based computer software, designated FEMIX V4.0, is detailed. For this purpose, a brief description of the model and the constitutive equations are presented, followed by the main computational aspects of its implementation in FEMIX V4.0 computer code. In addition, the model implementation is validated by means of numerical examples.

### 6.2.2 General description of the model

As referred in Chapter 5, the MMFSCM is based on the combination of the aggregate interlock and fibre pullout resisting mechanisms and their interdependency in order to simulate both mode I and mode II fracture of FRC elements.

For this purpose, two well-established models are used to simulate the aggregate interlock component, namely, the rough crack model (RCM) proposed by Bažant and Gambarova [246] and later enhanced by Gambarova and Karakoç [247], and the contact density model (CDM) developed by Li et al. [248]. As for the fibre pullout behaviour, three models are considered, namely, the Pfyl's fibre engagement model [232], the unified engagement model (UVEM) proposed by Ng et al. [264] and the simplified diverse embedment model (SDEM) developed by Lee et al. [250]. Finally, the matrix contribution is also



accounted for in mode I by means of an exponential relationship that simulates the softening nature of the fracture propagation in this type of materials.

The idealised crack kinematics and contribution of each referred resisting mechanism are depicted in Figure 102 (Chapter 5). The constitutive equations of the MMFSCM are defined by combining the aggregate interlock, fibre pullout and matrix contributions in the normal (n) and tangential (t) direction as depicted in Figure 102. The analytical formulation of the model is given by Equations (5.30) and (5.31) already presented in Chapter 5.

### 6.2.3 Model implementation in FEMIX V4.0

The MMFSCM approach relies on the strain decomposition of the incremental strain vector by splitting the strains of the cracked and uncracked concrete Sena-Cruz [220]. Hence, the incremental strain vector according to this formulation is given by Equation (6.1),

$$\Delta \underline{\varepsilon} = \Delta \underline{\varepsilon}^{cr} + \Delta \underline{\varepsilon}^{co} \quad (6.1)$$

where  $\underline{\varepsilon}^{cr}$  and  $\underline{\varepsilon}^{co}$  are the crack incremental strain vector and uncracked incremental strain vector, respectively.

The crack normal and tangential strains are defined by  $\varepsilon_n^{cr}$  and  $\gamma_t^{cr}$ , respectively, and the increment of strains at the crack local coordinate system (LCS) is given by Equation (6.2).

$$\Delta \underline{\varepsilon}_\ell^{cr} = \begin{bmatrix} \Delta \varepsilon_n^{cr} & \Delta \gamma_t^{cr} \end{bmatrix}^T \quad (6.2)$$

On the other hand, the strains in the global coordinate system (GCS) are comprised of three components as defined by Equation (6.3).

$$\Delta \underline{\varepsilon}^{cr} = \begin{bmatrix} \Delta \varepsilon_1^{cr} & \Delta \varepsilon_2^{cr} & \Delta \gamma_{12}^{cr} \end{bmatrix}^T \quad (6.3)$$

The increment of crack strain components in the LCS and GCS are related from the transformation matrix according to Equation (6.4),

$$\Delta \underline{\varepsilon}^{cr} = [\underline{T}^{cr}]^T \Delta \underline{\varepsilon}_\ell^{cr} \quad (6.4)$$

that depends on the angle  $\theta_{cr}$  between the x axis and the orthogonal to the plane of the crack.

The increment of stress components at a given crack can be defined as given by Equation (6.5),

$$\Delta \underline{\sigma}_\ell^{cr} = \begin{bmatrix} \Delta \sigma_n^{cr} & \Delta \tau_t^{cr} \end{bmatrix}^T \quad (6.5)$$

that are in equilibrium with the increment of the stress components in the GCS,  $\Delta \underline{\sigma}_\ell^{cr}$ , through Equation (6.6),

$$\Delta \underline{\sigma}_\ell^{cr} = \underline{T}^{cr} \Delta \underline{\sigma} \quad (6.6)$$

The concrete between cracks is assumed to be undamaged and therefore to behave elastically in the present phase of the model development. Thus, the constitutive relationship between the increment of strains and stresses in the undamaged concrete is given by Equation (6.7),

$$\Delta \underline{\sigma} = \underline{D}^{co} \Delta \underline{\varepsilon}^{co} \quad (6.7)$$

where  $\underline{D}^{co}$  is the elasticity matrix.

The present model is formulated in terms of normal ( $w_n^{cr}$ ) and tangential ( $w_t^{cr}$ ) displacements at the crack level and, consequently, it is necessary to convert the strains into displacements. This is achieved by means of the crack band width (CBW) parameter, which represents the length of the material band in which the crack displacements of the smeared cracks are related to the crack strains (Equation (6.8)),

$$\Delta \underline{w}_\ell^{cr} = [\underline{\ell}_b^{cr}]^{-1} \Delta \underline{\varepsilon}_\ell^{cr} \quad (6.8)$$

where  $\underline{\ell}_b^{cr}$  is a matrix containing the inverse of the CBW parameter:

$$\underline{\ell}_b^{cr} = \begin{bmatrix} \frac{1}{\ell_b} & 0 \\ 0 & \frac{1}{\ell_b} \end{bmatrix} \quad (6.9)$$

therefore it is assumed the same CBW for crack opening and crack sliding, which is arguable, but without reliable data from comprehensive research in this topic, it was decided to adopt this assumption in the present phase of the model development. The crack constitutive law at the incremental level of displacements and stresses is:

$$\Delta \underline{\sigma}_\ell^{cr} = \underline{D}^{cr} \Delta \underline{w}_\ell^{cr} \quad (6.10)$$

with,

$$\underline{D}^{cr} = \begin{bmatrix} D_{11}^{cr} & D_{12}^{cr} \\ D_{21}^{cr} & D_{22}^{cr} \end{bmatrix} \quad (6.11)$$

where  $D_{11}^{cr}$ ,  $D_{12}^{cr}$ ,  $D_{21}^{cr}$  and  $D_{22}^{cr}$  are the terms of the crack constitutive matrix, whose values can be positive or negative, depending on the hardening or softening nature of the FRC.

These coefficients are obtained by computing the Jacobian matrix of the  $D_{\max}$  matrix:

$$\underline{D}^{cr} = \begin{bmatrix} \frac{\partial \Delta \sigma_n^{cr}}{\partial \Delta w_n^{cr}} & \frac{\partial \Delta \sigma_n^{cr}}{\partial \Delta w_t^{cr}} \\ \frac{\partial \Delta \tau_t^{cr}}{\partial \Delta w_n^{cr}} & \frac{\partial \Delta \tau_t^{cr}}{\partial \Delta w_t^{cr}} \end{bmatrix} \quad (6.12)$$

The elements that compose the  $D_{\max}$  are obtained according to the procedure described in Annex II.

When a strain increment ( $\Delta \underline{\varepsilon}_m$ ) occurs at a given cracked integration point, the stress state has to be updated accordingly ( $\underline{\sigma}_m$ ). Thus, the total stresses can be obtained from:

$$\underline{\sigma}_{\ell,m}^{cr} = \underline{T}_m^{cr} \underline{\sigma}_m \quad (6.13)$$

$$\underline{\sigma}_{\ell,m-1}^{cr} + \Delta \underline{\sigma}_{\ell,m}^{cr} = \underline{T}_m^{cr} (\underline{\sigma}_{m-1} + \Delta \underline{\sigma}_m) \quad (6.14)$$

Substituting Equations (6.4), (6.7) and (6.8) in Equation (6.14) it is obtained:

$$\underline{\sigma}_{\ell,m-1}^{cr} + \Delta \underline{\sigma}_{\ell,m}^{cr} (\Delta \underline{w}_{\ell,m}^{cr}) + \underline{T}_m^{cr} \underline{D}^{co} [\underline{T}_m^{cr}]^T \underline{\ell}_b^{cr} \Delta \underline{w}_{\ell,m}^{cr} - \underline{T}_m^{cr} \underline{\sigma}_{m-1} - \underline{T}_m^{cr} \underline{D}^{co} \Delta \underline{\varepsilon}_m = \underline{0} \quad (6.15)$$

where the vector of incremental crack stress ( $\Delta \underline{\sigma}_{\ell,m}^{cr}$ ) depends on the vector of the incremental crack displacements ( $\Delta \underline{w}_{\ell,m}^{cr}$ ), which are the unknown variables to be determined. After obtaining  $\Delta \underline{w}_{\ell,m}^{cr}$ , the vector of incremental crack strains ( $\Delta \underline{\varepsilon}_{\ell,m}^{cr}$ ) are obtained by means of Equation (6.8).

The Newton-Raphson method is employed to solve the system of nonlinear equations given by Equation (6.15):

$$\underline{f} (\Delta \underline{w}_{\ell,m}^{cr}) = \underline{\sigma}_{\ell,m-1}^{cr} + \underline{D}^{cr} \Delta \underline{w}_{\ell,m}^{cr} + \underline{T}_m^{cr} \underline{D}^{co} [\underline{T}_m^{cr}]^T \underline{\ell}_b^{cr} \Delta \underline{w}_{\ell,m}^{cr} - \underline{T}_m^{cr} \underline{\sigma}_{m-1} - \underline{T}_m^{cr} \underline{D}^{co} \Delta \underline{\varepsilon}_m \quad (6.16)$$

Considering that:

$$\underline{\sigma}_{\ell,m-1}^{cr} = \begin{bmatrix} \sigma_{n,m-1}^{cr} \\ \tau_{t,m-1}^{cr} \end{bmatrix} \quad (6.17)$$

$$\Delta \underline{\sigma}_{\ell,m}^{cr} = \begin{bmatrix} D_{11}^{cr} \Delta w_{n,m}^{cr} + D_{12}^{cr} \Delta w_{t,m}^{cr} \\ D_{21}^{cr} \Delta w_{n,m}^{cr} + D_{22}^{cr} \Delta w_{t,m}^{cr} \end{bmatrix} \quad (6.18)$$

$$\underline{T}_m^{cr} \underline{\sigma}_{m-1} = \begin{bmatrix} A_1 \\ A_2 \end{bmatrix} \quad (6.19)$$

$$\underline{T}_m^{cr} \underline{D}^{co} \Delta \underline{\varepsilon}_m = \begin{bmatrix} B_1 \\ B_2 \end{bmatrix} \quad (6.20)$$

$$\underline{T}_m^{cr} \underline{D}^{co} [\underline{T}_m^{cr}]^T \underline{\ell}_b^{cr} = \begin{bmatrix} C_{11} & C_{12} \\ C_{21} & C_{22} \end{bmatrix} \quad (6.21)$$

where A, B, C are constants, Equation (6.16) can get the following configuration:

$$\begin{aligned}
 \begin{bmatrix} \hat{f}_1 \\ \hat{f}_2 \end{bmatrix} &= \begin{bmatrix} \sigma_{n,m-1}^{cr} \\ \tau_{t,m-1}^{cr} \end{bmatrix} + \begin{bmatrix} D_{11}^{cr} \Delta w_{n,m}^{cr} + D_{12}^{cr} \Delta w_{t,m}^{cr} \\ D_{21}^{cr} \Delta w_{n,m}^{cr} + D_{22}^{cr} \Delta w_{t,m}^{cr} \end{bmatrix} \\
 &+ \begin{bmatrix} C_{11} & C_{12} \\ C_{21} & C_{22} \end{bmatrix} \begin{bmatrix} \Delta w_{n,m}^{cr} \\ \Delta w_{t,m}^{cr} \end{bmatrix} - \begin{bmatrix} A_1 \\ A_2 \end{bmatrix} - \begin{bmatrix} B_1 \\ B_2 \end{bmatrix}
 \end{aligned} \tag{6.22}$$

whose unknowns can be obtained from:

$$\frac{\partial f}{\partial \Delta w_{\ell,m}^{cr}} = \begin{bmatrix} \frac{\partial \hat{f}_1}{\partial \Delta w_{n,m}^{cr}} & \frac{\partial \hat{f}_1}{\partial \Delta w_{t,m}^{cr}} \\ \frac{\partial \hat{f}_2}{\partial \Delta w_{n,m}^{cr}} & \frac{\partial \hat{f}_2}{\partial \Delta w_{t,m}^{cr}} \end{bmatrix} \tag{6.23}$$

where,

$$\frac{\partial \hat{f}_1}{\partial \Delta w_{n,m}^{cr}} = D_{11} + \frac{\partial D_{11}}{\partial \Delta w_{n,m}^{cr}} \cdot \Delta w_{n,m}^{cr} + \frac{\partial D_{12}}{\partial \Delta w_{n,m}^{cr}} \cdot \Delta w_{t,m}^{cr} + C_{11} \tag{6.24}$$

$$\frac{\partial \hat{f}_1}{\partial \Delta w_{t,m}^{cr}} = \frac{\partial D_{11}}{\partial \Delta w_{t,m}^{cr}} \cdot \Delta w_{n,m}^{cr} + D_{12} + \frac{\partial D_{12}}{\partial \Delta w_{t,m}^{cr}} \cdot \Delta w_{t,m}^{cr} + C_{12} \tag{6.25}$$

$$\frac{\partial \hat{f}_2}{\partial \Delta w_{n,m}^{cr}} = D_{21} + \frac{\partial D_{21}}{\partial \Delta w_{n,m}^{cr}} \cdot \Delta w_{n,m}^{cr} + \frac{\partial D_{22}}{\partial \Delta w_{n,m}^{cr}} \cdot \Delta w_{t,m}^{cr} + C_{21} \tag{6.26}$$

$$\frac{\partial \hat{f}_2}{\partial \Delta w_{t,m}^{cr}} = \frac{\partial D_{21}}{\partial \Delta w_{t,m}^{cr}} \cdot \Delta w_{n,m}^{cr} + D_{22} + \frac{\partial D_{22}}{\partial \Delta w_{t,m}^{cr}} \cdot \Delta w_{t,m}^{cr} + C_{22} \tag{6.27}$$

which can be rearranged into Equation (6.28),

$$\frac{\partial f}{\partial \Delta w_{\ell,m}^{cr}} = \underline{D}^{cr} + \hat{\underline{D}}^{cr} \Delta \hat{w}_{\ell,m}^{cr} + \underline{T}_m^{cr} \underline{D}^{co} [\underline{T}_m^{cr}]^T \underline{\ell}_b^{cr} \tag{6.28}$$

where  $\underline{\hat{D}}^{cr}$  and  $\Delta\underline{\hat{w}}_{l,m}^{cr}$  are given by Equations (6.29) and (6.30),

$$\underline{\hat{D}}^{cr} = \begin{bmatrix} \frac{\partial D_{11}}{\partial \Delta w_{n,m}^{cr}} & \frac{\partial D_{12}}{\partial \Delta w_{n,m}^{cr}} & \frac{\partial D_{11}}{\partial \Delta w_{t,m}^{cr}} & \frac{\partial D_{12}}{\partial \Delta w_{t,m}^{cr}} \\ \frac{\partial D_{21}}{\partial \Delta w_{n,m}^{cr}} & \frac{\partial D_{22}}{\partial \Delta w_{n,m}^{cr}} & \frac{\partial D_{21}}{\partial \Delta w_{t,m}^{cr}} & \frac{\partial D_{22}}{\partial \Delta w_{t,m}^{cr}} \end{bmatrix} \quad (6.29)$$

$$\Delta\underline{\hat{w}}_{l,m}^{cr} = \begin{bmatrix} \Delta w_{n,m}^{cr} & 0 \\ \Delta w_{t,m}^{cr} & 0 \\ 0 & \Delta w_{n,m}^{cr} \\ 0 & \Delta w_{t,m}^{cr} \end{bmatrix} \quad (6.30)$$

The  $\underline{\hat{D}}^{cr}$  matrix is obtained by computing the derivatives of each  $\underline{D}^{cr}$  element with respect to each component of the incremental crack displacement vector ( $\Delta\underline{w}_l^{cr}$ ). However, due to the complexity of the expressions that constitute the  $D_{\max}$ , computing the second derivative of such expressions analytically would be impractical and error prone. Therefore, the elements of  $\underline{\hat{D}}^{cr}$  are obtained in a numeric fashion by means of a finite differences procedure included in the GNU scientific library (GSL).

#### Crack status management

During the loading process a crack can undergo different statuses either due to the formation of new cracks in the same integration point (IP) of the existing crack, or in the neighbourhood IPs, or due to stress redistribution in consequence of damage evolution or alteration of the loading conditions.

The crack status of each crack is stored as an historical variable so that it can be used throughout the nonlinear analysis to correctly accomplish the assumptions adopted for the crack constitutive law for representing the cracking process.

In the MMFSCM, a crack can be assigned 6 distinct crack statuses in mode I following the approach proposed by Sena-Cruz [220], namely, 1. *initiation*, 2. *opening*, 3. *closing*, 4. *reopening*, 5. *closed* and 6. *fully open*. On the other hand, 5 crack status are adopted for mode II, 1. *stiffening*, 2. *softening*, 3. *unloading*, 4. *reloading*, 5. *free-sliding*. In addition, it is considered that the fracture mode I governs the crack state, which means that a crack only exists until a *closed* status is assigned regardless of the status in fracture mode II.

In Figure 122 a schematic representation of the crack normal and shear stress surfaces and the correspondent possible crack status for each fracture mode is presented.

Regarding fracture mode I, a new crack is assigned the *initiation* status as the principal stress ( $\sigma_I$ ) attains  $f_{ct}$  at less than an adopted tolerance, and the angle formed by this new crack and the already existing cracks in the IP exceeds the adopted threshold angle.

As  $w_n^{cr}$  increases the crack is assigned an *opening* status, provided that  $w_n^{cr}$  is lower than the ultimate crack opening displacement ( $w_{ult,I}^{cr}$ ).

When  $w_n^{cr}$  exceeds  $w_{ult,I}^{cr}$  the crack is attributed a *fully open* status. If however  $w_n^{cr}$  decreases, but is still positive, a *closing* status is considered and the crack stress state is updated according to a secant

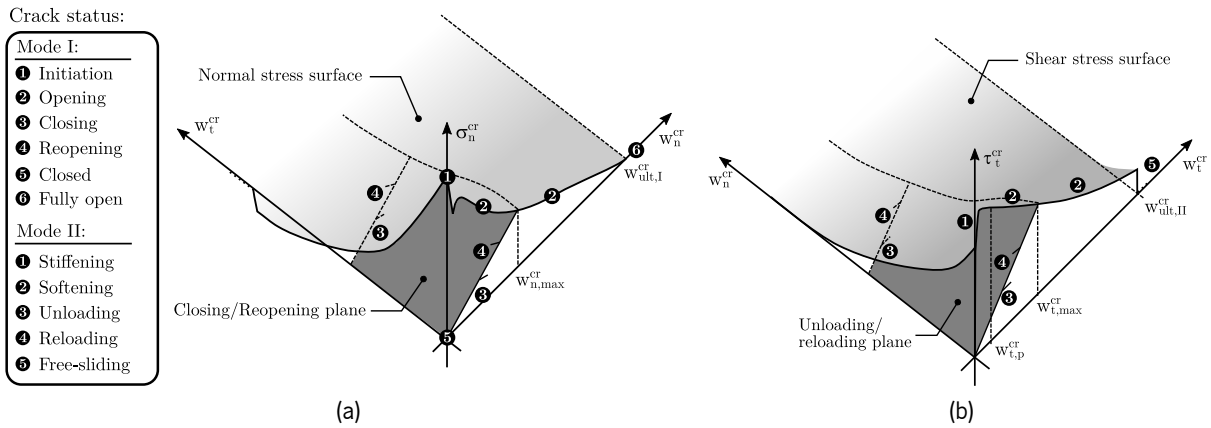


Figure 122: Schematic representation of possible crack status a crack can assume in (a) mode I and (b) mode II.

approach based on the maximum crack opening displacement ( $w_{n,max}^{cr}$ ) as shown in Figure 122a.

On the other hand, if a *closing* crack undergoes a positive  $w_n^{cr}$  increment, the status is changed to *reopening* provided that the  $w_n^{cr}$  is lower than  $w_{n,max}^{cr}$ , otherwise an *opening* status is assigned again. If  $w_n^{cr}$  exceeds  $w_{ult,I}^{cr}$  or decreases to 0, a *fully-open* or *closed* status is considered, respectively.

Regarding mode II, a *stiffening* status is assigned to a new crack until the sliding peak displacement ( $w_{t,p}^{cr} = D_{max}/100$ ) is attained. During this stage, the crack status will remain in *stiffening* status regardless of the type of increment of  $w_t^{cr}$ .

The mode II crack status is changed to *softening* when  $w_t^{cr}$  is larger than  $w_{t,p}^{cr}$ , but lower than the ultimate crack sliding displacement ( $w_{ult,II}^{cr}$ ).

The *unloading* status is assigned to a crack when occurring a negative increment of  $w_t^{cr}$ , and similarly to mode I, the stress state is updated based on a secant trajectory as shown in Figure 122b. An *unloading* crack will be set to a *reloading* state if a positive  $w_t^{cr}$  increment is observed, provided that  $w_t^{cr}$  does not exceeds  $w_{t,max}^{cr}$ . If  $w_t^{cr}$  or  $w_t^{cr}$  exceeds  $w_{ult,II}^{cr}$ , the crack is considered to be in a *free-sliding* state.

Since the MMFSCM is formulated based on the fibre pullout and aggregate interlock resisting mechanisms, the concept of fracture energy of the FRC is not explicitly used and, consequently, it is not used to determine  $w_{ult,I}^{cr}$  and  $w_{ult,II}^{cr}$ .

Hence, for fracture mode I the value of  $w_{ult,I}^{cr}$  is assumed to be equal to the ultimate fibre pullout value, which is typically considered equal to  $l_f/4$  [265, 266], whilst for mode II  $w_{ult,II}^{cr}$  is assumed equal to  $D_{max}/2$ , which corresponds to the  $w_n^{cr}$  value to which the aggregate interlock component is null.

### 6.2.4 Model validation

To validate the implementation of the MMFSCM, a single finite element (FE) simulation is carried out and the numerical results are compared against the analytical results obtained using Equations (5.30) and (5.31). The model consists of a four nodes FE with a single IP, subjected to a horizontal load as shown in Figure 123.

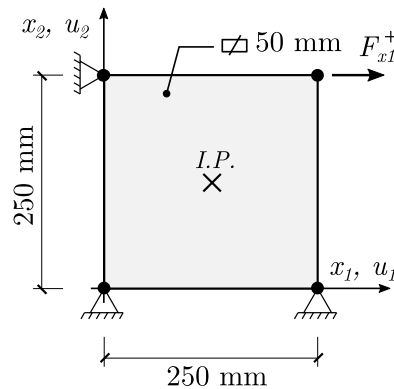


Figure 123: Mesh geometry, loading and support conditions of the single element simulation.

The results are obtained using the contribution of the matrix, aggregate interlock and fibre pullout models using the expressions presented in I. Each combination of aggregate interlock and fibre pullout models is designated according to the following rule, “X.Y-Z”, where “X” is the nature of the results “A” for analytical and “N” for numerical results, “Y” and “Z” are the type character of the aggregate interlock and fibre pullout models, respectively. For instance, the analytical results obtained using the RCM and Pfyl’s pullout model is designated “A.R-P”.

The values adopted for the properties that define the constitutive models are listed in Table 22.

The results in terms of stresses at the integration point level are presented in Figure 124 and show that the results obtained from the numerical analysis using FEMIX V4.0 are in perfect agreement with the analytical ones obtained from the analytical expressions for each aggregate interlock/fibre pullout model combination (expressions presented in Annex I), validating the implementation in the FEMIX V4.0 computer software.

Table 22: Parameters used to define the MMFSCM model in the single FE simulations.

Property	Value
<b>Generic properties</b>	
Poisson's ratio ( $\nu$ )	0.2
Young's modulus ( $E_c$ )	33000 N/mm <sup>2</sup>
Tensile strength ( $f_{ct}$ )	2.0 N/mm <sup>2</sup>
Crack band width	$\sqrt{A_{FE}}$ *
Threshold angle	30°
Maximum number of cracks per integration point	2
<b>RCM/CDM</b>	
Compressive strength ( $f_c$ )	30 N/mm <sup>2</sup>
Maximum aggregate diameter ( $D_{max}$ )	5.0 mm
<b>Fibre pullout common properties</b>	
Fibre diameter ( $d_f$ )	0.55 mm
Fibre length ( $l_f$ )	33.0 mm
Fibre volume fraction ( $V_f$ )	0.75%
<b>Pfyl's model</b>	
Fibre Young's modulus ( $E_f$ )	200000 N/mm <sup>2</sup>
<b>SDEM</b>	
Maximum frictional bond stress ( $\tau_{st,max}$ ) <sup>†</sup>	2.17 N/mm <sup>2</sup>
Maximum bond stress of the mechanical anchorage ( $\tau_{eh,max}$ ) <sup>†</sup>	2.35 N/mm <sup>2</sup>
Slip at maximum frictional bond stress ( $s_{st}$ ) <sup>‡</sup>	0.01 mm
Slip of the anchorage at maximum bond stress ( $s_{eh}$ ) <sup>‡</sup>	0.1 mm
Length of the hooked-end part of the fibre ( $l_{eh}$ )	4.0 mm
<b>UVEM</b>	
Bond stress at fibre aligned with pullout direction ( $\tau_{b,0}$ ) <sup>§</sup>	4.4 N/mm <sup>2</sup>

\* Square root of the area of the finite element; †Computed according to Voo and Foster [233] and Seong-Cheol Lee, and Frank J. Vecchio [267]; ‡Calculated according to Naaman and Najm [18]; §According to Htut and Foster [222];



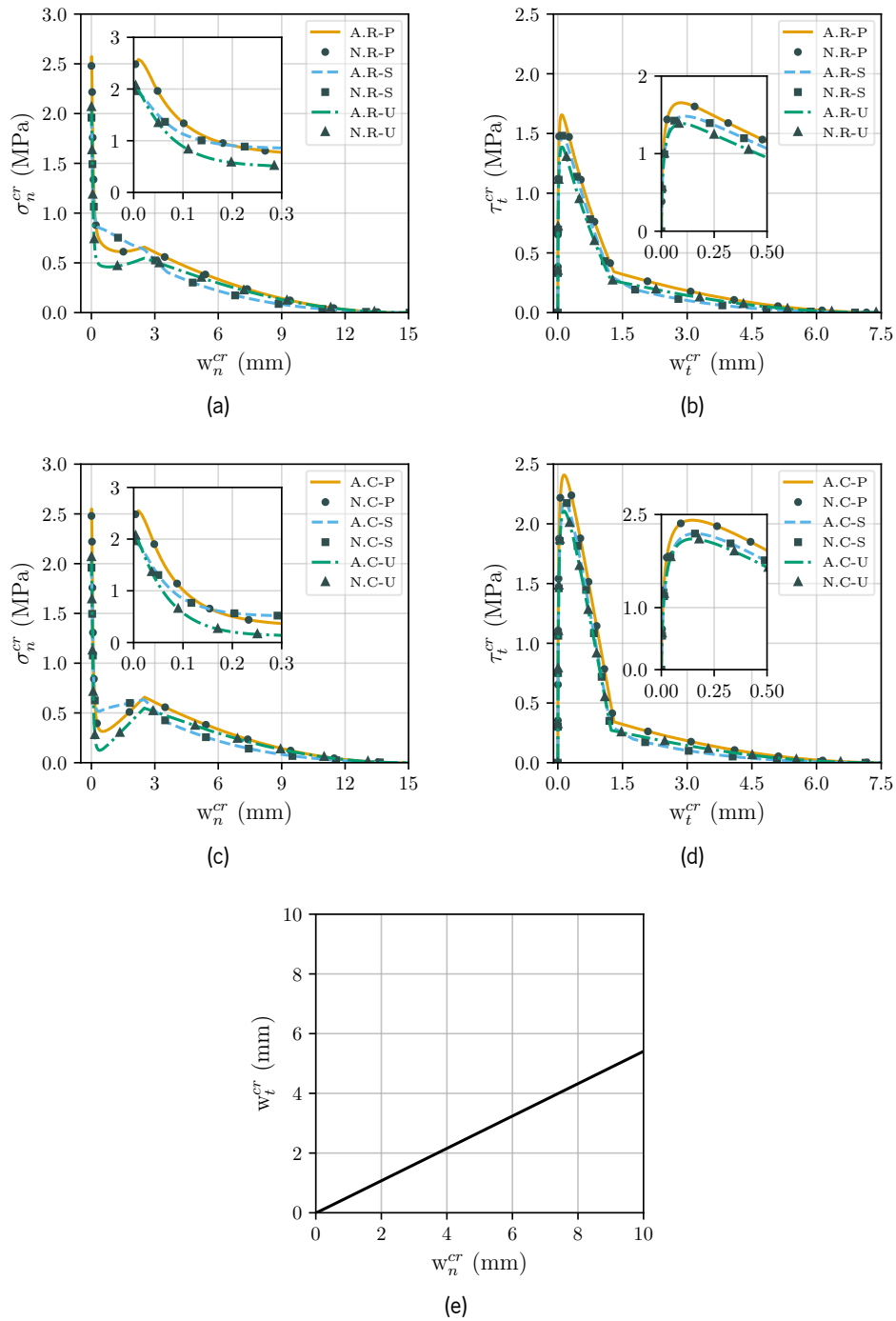


Figure 124: Results of the single element simulation: (a)  $\sigma_n^{cr} - w_n^{cr}$  considering the RCM, (b)  $\tau_t^{cr} - w_t^{cr}$  considering the RCM, (c)  $\sigma_n^{cr} - w_n^{cr}$  considering the CDM, (d)  $\tau_t^{cr} - w_t^{cr}$  considering the CDM, (e)  $w_n^{cr} - w_t^{cr}$  relation in the LCS.

Regarding the normal stress results (Figures 124a and 124c), it is possible to observe that the Pfyl's (P) model exhibits a higher contribution at the onset of the crack formation (up to 0.2 mm) followed by the SDEM (S) and UVEM (U), respectively. In the range of 0.2 to 3 mm SDEM presents a higher stress transferring capacity whereas for higher  $w_n^{cr}$  values, the UVEM exhibits a higher contribution, with the Pfyl

and SDEM providing the highest and lowest load carrying capacity, respectively. In terms of shear stress behaviour, the CDM has a much more prominent contribution ( $\approx 40\%$  higher) when compared to the RCM as shown in Figures 124b and 124d. Also, the CDM exhibits higher compressive stresses in mode I when compared to the RCM, although not as significant as the difference observed in terms of shear stresses.

These results are coherent with the loading path shown in Figure 124e where a 2:1 linear  $w_n^{cr}/w_t^{cr}$  ratio is observed, and consequently the collision of aggregates is expected to generate compressive stresses. For model validation purposes this loading path trend is acceptable, however, the authors are aware that the evolution trend of the  $w_n^{cr}/w_t^{cr}$  in FRC elements subjected to shear is typically a non-linear relation, where the  $w_n^{cr}/w_t^{cr}$  ratio is higher at earlier stages than for the later phase where  $w_t^{cr}$  is more significant than  $w_n^{cr}$  as documented by several authors [231, 245].

One of the advantages of the herein presented model is the possibility to break down the results by resisting mechanism i.e. matrix/aggregate interlock/fibre pullout. Hence, in order to further understand the impact and contribution of each resisting mechanism, the individual component results in the model combination N.R-S are shown in Figure 125.

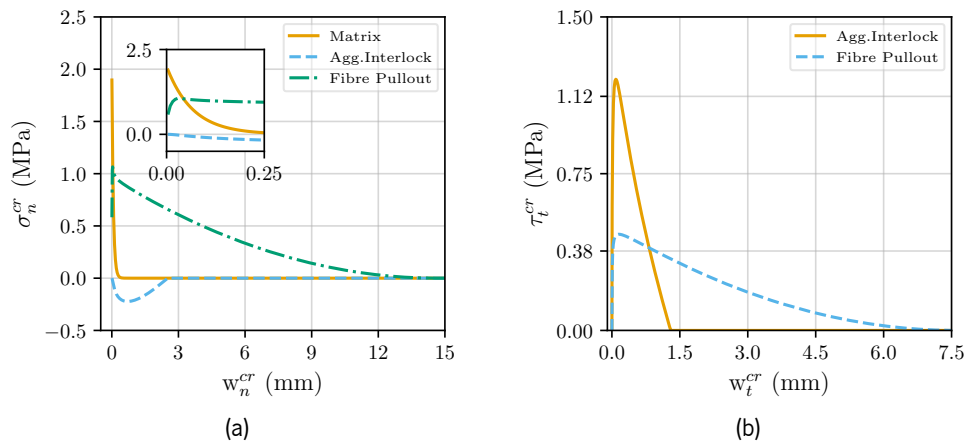


Figure 125: Results break down by resisting mechanism i.e. matrix, aggregate interlock and fibre pullout contribution in the N.R-S case: (a)  $\sigma_n^{cr}$  -  $w_n^{cr}$  relation at the crack LCS, (b)  $\tau_t^{cr}$  -  $w_t^{cr}$  relation at the crack LCS.

Considering the results of Figure 125, in particular Figure 125a, it is possible to observe the contribution of each resisting mechanism is in accordance with the expected behaviour, with the matrix rapidly exhausting its capacity, while the fibres contribute in a more consistent manner as the crack opening increases. It is also noteworthy the compression stresses induced by the aggregate interlock mechanism. This behaviour was expected since the loading path has a 2:1 opening-sliding ratio as shown in Figure 124e and therefore the collision between aggregates generates the referred compressive stresses. On the other hand, in the results of Figure 125b it is possible to observe that the aggregate interlock resisting mechanism has a much more prominent effect contribution, up to  $\approx 1$  mm of  $w_t^{cr}$ , when compared to the fibre pullout parcel, that is responsible for up to 30% of the total stress carrying capacity for the presented  $w_n^{cr}$ - $w_t^{cr}$  (Figure 124e) loading path.

## 6.3 Assessment of the model's predictive performance

### 6.3.1 Introduction

In this section the predictive performance of the MMFSCM is assessed by means of two numerical simulations. The first simulation is a 3PNBBT typically used to obtain the mode I fracture parameters of FRC by IA. The numerical results are compared to a series of experimental tests gathered from the literature [134] and provided by the civil engineering company CiviTest. The second case study covers a direct shear test conducted by Susetyo et al. [204] and consists of an in-plane shear test of steel-fibre reinforced concrete (SFRC) panels with different fibre volumes. The numerical predictions are compared against the experimental results and the predictive capability of the model is appraised.

### 6.3.2 Three-point notch beam bending tests (3PNBBT)

The 3PNBBT simulations are carried out in this section. Firstly, the experimental results obtained within the scope of a blind simulation competition organised by the *fib Working Group (WG) 2.4.1 - Modelling of Fibre Reinforced Concrete Structures* [134] are considered, and subsequently additional experimental series are used to further appraise the performance of the MMFSCM.

The 3PNBBT experimental tests were conducted according to the recommendations of Model Code 2010 [203]. Prismatic specimens of 550x150x150 mm dimensions were simulated by means of 4 node plane stress FEs, considering a 2x2 Gauss-Legendre (G-L) except for the elements directly above the notch which were assigned a 2x1 G-L scheme for limiting the propagation of cracks along the symmetry axis of the specimen, which is close to the experimental evidence.

A material nonlinear behaviour was assigned to the elements above the notch, whilst the remaining elements were considered linear elastic behaviour. The numerical simulations were performed by using the Newton-Raphson method and by controlling the relative displacement between the nodes at the notch extremity.

The FE mesh, loading and support conditions are depicted in Figure 126 and the values used to define the properties of the MMFSCM are listed in Table 23. The SFRC material properties listed in the table were provided by the organising committee of the blind simulation competition [134].

In this case, three simulations were conducted by adopting each fibre pullout model available (Pfyl, UVEM and SDEM). Since fracture mode I is the dominant behaviour in this kind of test, the impact of the aggregate model is negligible and therefore only the RCM model is used. The comparison between the numerical and experimental results using the fibre pullout models available in the MMFSCM is shown in Figure 127a.

According to the results shown in Figure 127a, the SDEM fibre pullout model provides the best approximation to the experimental response, capturing the peak load with very good accuracy ( $\approx +3.7\%$ ) and better estimating the post-peak response when compared to the Pfyl and UVEM models. In general, the Pfyl's model overestimates the response both in terms of peak force ( $\approx +20\%$ ) and post-peak stage,

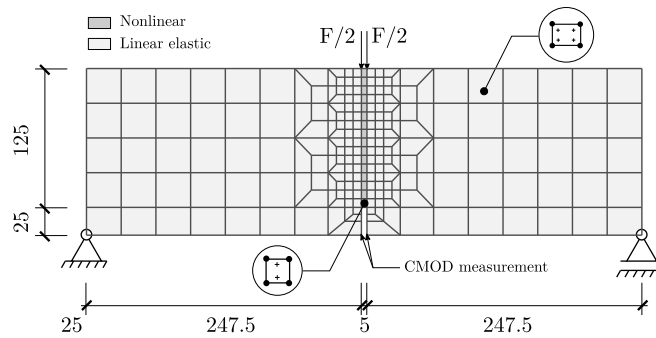


Figure 126: Geometry, mesh, loading and support conditions of the 3PNBBT numerical model (all dimensions in mm).

Table 23: Parameters used to define the MMFSCM model in the 3PNBBT simulations.

Property	Value
<b>Generic properties</b>	
Poisson's ratio ( $\nu$ )	0.2
Young's modulus ( $E_c$ )	32900 N/mm <sup>2</sup>
Tensile strength ( $f_{ct}$ )	3.0 N/mm <sup>2</sup>
Crack band width	$\sqrt{A_{FE}}$
Threshold angle	30°
Maximum number of cracks per integration point	2
<b>RCM/CDM</b>	
Compressive strength ( $f_c$ )	64.2 N/mm <sup>2</sup>
Maximum aggregate diameter ( $D_{max}$ )	14.0 mm
<b>Fibre pullout common properties</b>	
Fibre diameter ( $d_f$ )	0.55 mm
Fibre length ( $l_f$ )	33.0 mm
Fibre volume fraction ( $V_f$ )	0.75%
<b>Pfyl's model</b>	
Fibre Young's modulus ( $E_f$ )	200000 N/mm <sup>2</sup>
<b>SDEM</b>	
Maximum frictional bond stress ( $\tau_{st,max}$ )	3.17 N/mm <sup>2</sup>
Maximum bond stress at anchorage ( $\tau_{eh,max}$ )	3.44 N/mm <sup>2</sup>
Slip at maximum frictional bond stress ( $s_{st}$ )	0.01 mm
Slip of the anchorage at maximum bond stress ( $s_{eh}$ )	0.1 mm
Length of the hooked-end part of the fibre ( $l_{eh}$ )	4.5 mm
<b>UVEM</b>	
Bond stress at fibre aligned with pullout direction ( $\tau_{b,0}$ )	6.6 N/mm <sup>2</sup>

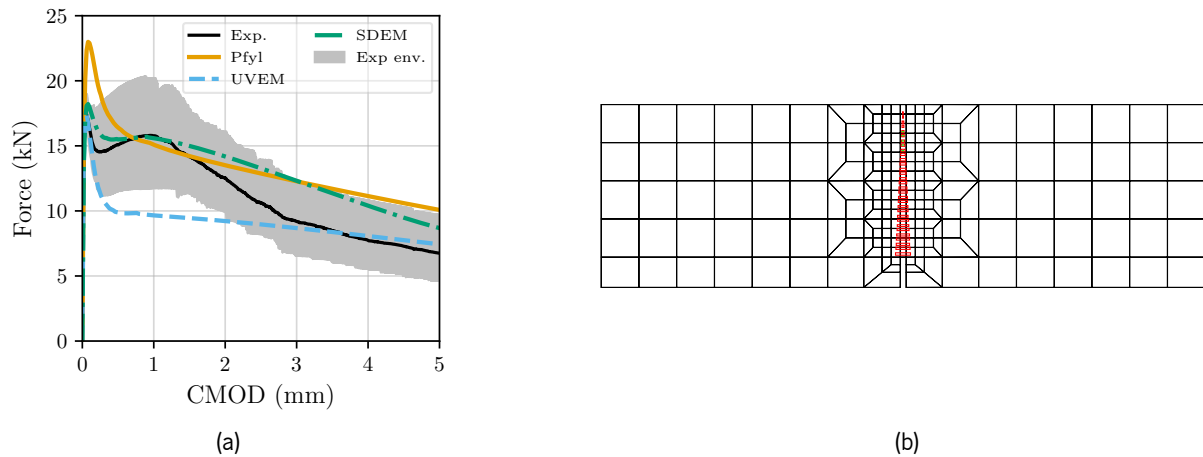


Figure 127: Results of the 3PNBBT simulations: (a) Force-CMOD curve and (b) crack pattern at CMOD=5mm obtained using the Pfyl model (red: opening cracks; green: closing cracks;).

specially for higher values of CMOD. On the other hand, the UVEM model underestimates the load carrying capacity, mainly at the initial stage of the post-peak response, despite capturing the peak load with good accuracy ( $\approx -3.4\%$ ). The crack pattern presented in Figure 127b is coherent with the failure mode of the specimens, exhibiting the progression of a major vertical crack along the notched plane.

To further understand the structural responses presented in 127a, the contribution of the resisting mechanisms at the crack level that develop on the first FE above the notch as depicted in Figure 128, namely those provided by the matrix, fibre pullout and aggregate interlock, at the integration point level.

Considering the results presented in Figure 128 the following conclusions can be drawn: firstly the results at the crack level are coherent with the observed structural response since the Pfyl's pullout model exhibits a higher stress transferring capacity when compared to the SDEM and UVEM, which consequently originates the overestimation in the structural response (Figure 127). Secondly, the Pfyl's model exhibits a pseudo-hardening behaviour just after the crack initiation as can be observed in Figure 128a, which leads to an increase of the load carrying capacity of the specimen in that phase. This is due to the fact that the model assumes that the fibres are almost immediately activated at the crack onset, reaching the peak contribution at around 0.15 mm, resulting in the referred pseudo-hardening behaviour, which is not coherent with the experimental behaviour.

Regarding the SDEM model (Figure 128c), which is the one that produces the best prediction of the experimental response (see Figure 127a), it is possible to observe that the peak load and the drop in the load after the peak is reasonably well captured. However, just after the peak contribution of the fibre pullout resisting mechanisms, the stress transference decay is relatively smooth, preventing the model from capturing the load carrying decrease registered experimentally in this stage.

Finally the UVEM model (Figure 128b) captures very well the peak load, however the overall post-peak response is underestimated (Figure 127a), also exhibiting an almost linear post-peak trend evolution similar to the SDEM model. This behaviour is also consistent with the results at the crack level presented in Figure 128b, since this model provides the lowest fibre pullout contribution when compared to the Pfyl

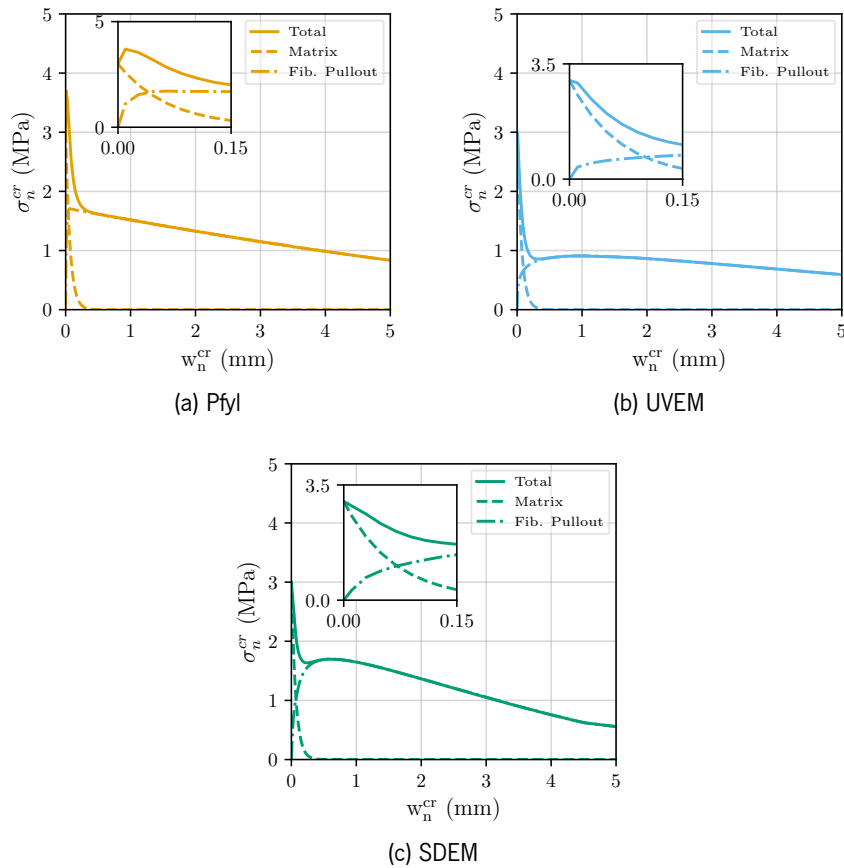


Figure 128: Results in the integration point of the first element above the notch: (a) using Pfyl's, (b) UVEM and (c) SDEM model, respectively.

and SDEM models, resulting in the overall underestimation of the response. The almost bilinear configuration relationship at crack level (Figure 128b) is reflected in the post-peak bilinear response estimated for the specimen's behaviour (Figure 127a), with a too abrupt load decay just after crack initiation and too smooth stress decrease in the phase governed by the fibre pullout resisting mechanisms.

Hence, considering the results shown in Figure 127 and Figure 128, and the conclusions presented above, a set of modifications are proposed in Section 6.3.2.1 to each fibre pullout model in order to mitigate the deficiencies that originated the deviations from the experimental results presented previously.

### 6.3.2.1 Modifications proposed to the Pfyl, SDEM and UVEM models

**Pfyl's model** The Pfyl's fibre pullout model is defined by two branches (see 2), the first governing the initial engagement of the fibres until the maximum value is attained, which follows a nonlinear trend (Figure 129). The second branch dictates how the pullout trend unfolds until the fibres are completely pulled out of the matrix.

In the results presented in Figure 128a, it is possible to observe that the fibres are immediately engaged and consequently initiate the crack arrest for a too small crack opening value, leading to an

unrealistic pseudo-hardening behaviour. Hence, to mitigate this effect and reduce the exaggerated initial contribution of the fibre resisting mechanisms, a modification to this model is proposed consisting in adopting a linear branch up to the maximum stress value instead of a nonlinear branch, as depicted in the schematic representation presented in Figure 129.

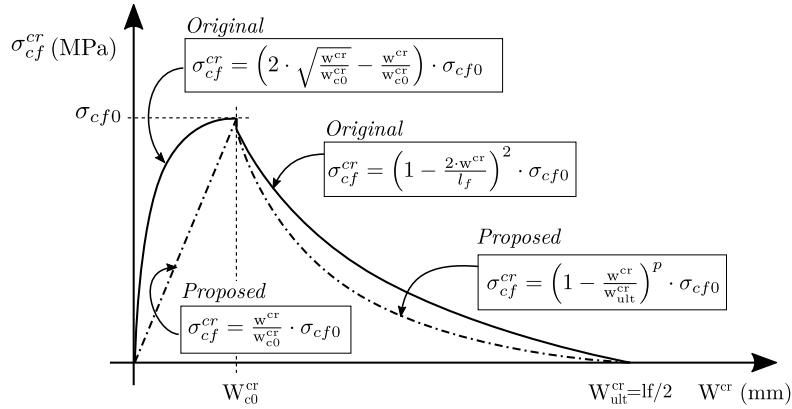


Figure 129: Schematic representation of the proposed modification to the Pfyl's fibre pullout model.

The original formulation adopted a quadratic variation of the post-peak branch until reaching the ultimate fibre pullout value ( $l_f/2$ ), governing the degradation rate of the post-peak fibre pullout contribution. Hence, in order to introduce an additional degree of flexibility to the model, the quadratic exponent is now transformed into a parameter ( $p$ ), allowing the adaptation to different post-peak trends. Also, the model was modified to accommodate different ultimate fibre pullout values ( $w_{ult}^{cr}$ ) since it usually varies between  $[l_f/2 - l_f/4]$ . Considering this modification, if a lower value of  $w_{ult}^{cr}$  is adopted, the post-peak degradation of the pullout resisting mechanism is increased. Hence, the modified Pfyl's model is now governed by the following equation:

$$\sigma_{cf}(w) = \begin{cases} \frac{w^{cr}}{w_{c0}^{cr}} \cdot \sigma_{cf0} & , 0 \leq w^{cr} \leq w_{c0}^{cr} \\ \left(1 - \frac{w^{cr}}{w_{ult}^{cr}}\right)^p \cdot \sigma_{cf0} & , w_{c0}^{cr} < w^{cr} \leq w_{ult}^{cr} \end{cases} \quad (6.31)$$

To assess the impact of these modifications, and using the material properties indicated in Table 23, the original formulation of the Pfyl's model and the modified version, considering different values for the post-peak degradation parameter,  $p$ , and ultimate fibre pullout,  $w_{ult}^{cr}$ , are plotted against each other and shown in Figure 130.

As shown in the results of Figure 130, the modified version of the model (Pfyl Mod.) results in a much more gradual activation of the fibre pullout mechanism when compared to the original formulation (Pfyl). Also, the adoption of lower ultimate fibre pullout values (Pfyl Mod. ( $l_f/4$ )) and by adopting a  $p$  value greater than 2 (Pfyl Mod. ( $p=3$ )), a much higher degradation rate of the post-peak behaviour is obtained which significantly affects the load carrying capacity at a structural level.

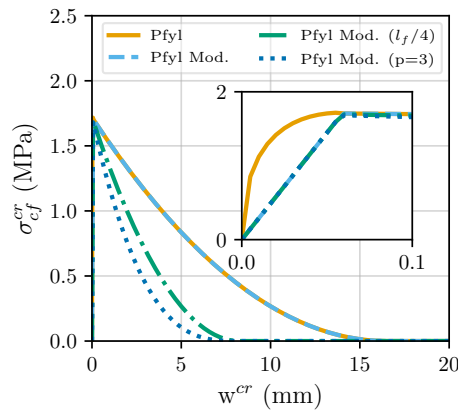


Figure 130: Comparison between the original formulation of the Pfyl's model and the modified version proposed in the present work. Pfyl - original formulation; Pfyl Mod. - linear pre-peak phase; Pfyl Mod. ( $l_f/4$ ) - linear pre-peak phase and  $w_{ult}^{cr} = l_f/4$ ; Pfyl Mod. ( $p=3$ ) - linear pre-peak phase,  $w_{ult}^{cr} = l_f/4$  and  $p = 3$ .

New simulations of the 3PNBBT tests were carried out considering the modified version for the pfyl's model, by adopting different ultimate fibre pullout values ( $w_{ult}^{cr} = l_f/4$ ). The results considering the original formulation and the modified version in terms of Force-crack mouth opening displacement (CMOD) are shown in Figure 131.

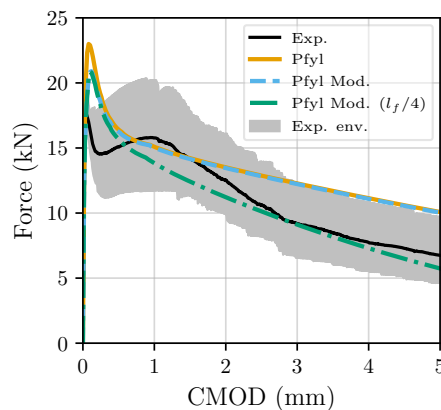


Figure 131: Assessment of the effect of the modified version of the Pfyl's model on the structural behaviour of the 3PNBBT FEM simulation.

As shown in the results (Figure 131), the numerical prediction obtained using the modified Pfyl's model shows a lower peak load estimation, in consequence of the modification of the shape of the first branch of the pullout model (see Figure 129). In addition, the modification regarding the ultimate fibre pullout value, results in a better approximation of the post-peak behaviour despite not capturing the slight increase in load capacity (0.5 - 1.5 mm) after the peak load drop. Nonetheless, the results fall within the experimental envelope, providing a better prediction of the experimental response when compared to the original version of the model.



**UVEM model** In the results of Figure 127a the UVEM model provided an underestimation of the experimental response, despite capturing with very good accuracy the peak load. Hence, the original UVEM expressions presented in Table 3 are modified in an attempt to improve its predictive performance.

The parameter that governs the evolution trend of the pullout model is  $\eta_{f,UVEM}$  given by:

$$\eta_{f,uvem} = \frac{1}{2} \cdot \left( \frac{a+b}{\pi} \right) \cdot \left( 1 - \frac{2 \cdot w^{cr}}{l_f} \right)^2 \quad (6.32)$$

$$a = \min [\gamma_{crit}, \pi/2 - |\phi|] \quad (6.33)$$

$$b = \gamma_{crit} \quad (6.34)$$

where the meaning of the presented symbols is detailed in Table 3.

Equation (6.32) is derived considering  $l_f/2$  as the ultimate fibre pullout value, which results in a very soft decay in the post-peak region of the pullout constitutive model and consequently the slow-decaying structural response observed in the results of Figure 127a. To mitigate this effect, Equation (6.32) was modified to include different ultimate fibre pullout values and is now given by:

$$\eta_{f,uvem} = \frac{1}{2} \cdot \left( \frac{a+b}{\pi} \right) \cdot \left( 1 - \frac{w^{cr}}{w_{ult}^{cr}} \right)^2 \quad (6.35)$$

In the original formulation the bond stress parameter,  $\tau_{b0}$ , varied between 1 and 3 times the  $f_{ct}$  value depending on the fibre geometry and ultimate tensile strength. Hence, in order to assess the impact of the modified model (Equation (6.35)) and the effect of different bond strength values, the model is plotted (Figure 132) using the parameters defined in Table 23 as baseline and different values for the ultimate fibre pullout parameter and bond strength.

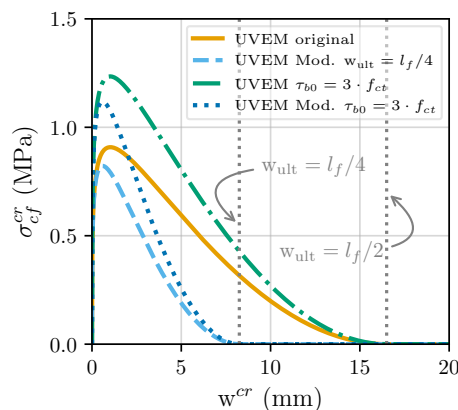


Figure 132: Comparison between the original UVEM model and the modified version including the  $w_{ult}$  parameter and different  $\tau_{b0}$  values.

As shown in the results of Figure 132, decreasing  $w_{ult}^{cr}$  to  $l_f/4$  results in a much faster degradation of the post-peak pullout response when compared to the original formulation, which considered a  $w_{ult}^{cr} =$

$l_f/2$ . Regarding the bond strength, it is possible to observe that the stress transferring capacity increases with  $\tau_{b0}$ .

Considering the aforementioned modification to the model and the results presented in Figure 132, the modified UVEM model was reimplemented in FEMIX V4.0 and the 3PNBBT simulation carried out again considering  $\tau_{b0} = 3 \cdot f_{ct}$  and  $w_{ult}^{cr} = l_f/4$ . This modification has increased the load carrying capacity in the initial phase of the cracking propagation, and a higher load decay in the remaining stages (Figure 133) leading to a better approximation of the experimental response.

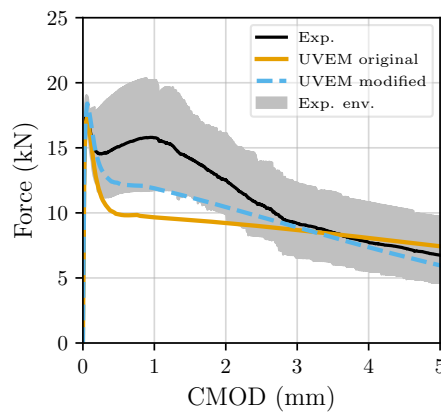


Figure 133: Comparison between the original and modified UVEM model in the results of the 3PNBBT FEM simulation.

The results presented in Figure 133 show that the prediction of the experimental response using the UVEM model falls within the experimental envelope, providing a much better agreement between the experimental and numerical results.

**SDEM model** The SDEM model provided the best estimation of the average experimental response, as shown in the results of Figure 127a, capturing the peak load with very good accuracy ( $\approx 3.5\%$ ) and providing a reasonable estimation of the trend of the post-peak response, including the slight increase in load carrying capacity after the peak load drop. However, the overall trend of the late post-peak phase (1.0 - 5.0 mm) exhibits a linear trend, which is not aligned with the experimental results. Hence, modifications to the expressions presented in Table 4 are proposed in order to enhance the predictive performance of the SDEM model.

This fibre pullout model is composed by the contribution of the following two resisting mechanisms: 1) the bond of the straight smooth portion of the fibres; 2) the mechanical anchorage of the hooked-end component of the fibres when being pulled out of the matrix. Using the properties indicated in Table 23, the tensile stress capacity of the FRC provided by the referred components is plotted in Figure 134.

As can be observed in the results of Figure 134, the hook provides a significant contribution to the overall tensile capacity, however, after reaching its peak capacity its contribution is rapidly exhausted, while the smooth portion of the fibres provides a much softer decay until the ultimate fibre pullout ( $w_{ult}^{cr}$ ) value is attained.

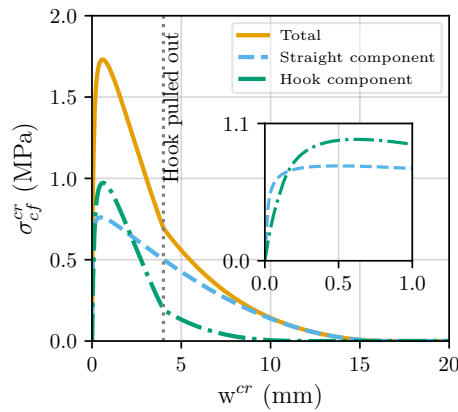


Figure 134: Plot by resisting component (straight portion and hooked-end part of the fibre) of the SDEM model using the properties indicated in Table 23

The post-peak contribution of the smooth portion of the fibre is governed by Equation (6.36), where the meaning of the symbols is detailed in Table 4.

$$\sigma_{cf,st}(w^{cr}) = \eta_{\theta f} \cdot v_f \cdot K_{st} \cdot \tau_{st,max} \cdot \frac{l_f}{d_f} \cdot \left(1 - \frac{2 \cdot w^{cr}}{l_f}\right)^2 \quad (6.36)$$

According to Equation (6.36), the ultimate pullout value is attained when  $w^{cr} = l_f/2$ , which leads to the soft decay in the pullout resisting mechanism, resulting in a higher load transferring capacity at the structural level. Hence, in order to mitigate this effect, the model was modified by including the  $w_{ult}^{cr}$  as a parameter. The contribution of the smooth portion of the fibre is now given by the following equation:

$$\sigma_{cf,st}(w^{cr}) = \eta_{\theta f} \cdot v_f \cdot K_{st} \cdot \tau_{st,max} \cdot \frac{l_f}{d_f} \cdot \left(1 - \frac{w^{cr}}{w_{ult}^{cr}}\right)^2 \quad (6.37)$$

Regarding the hooked-end contribution, and according to the plot shown in Figure 134, this mechanism is comprised by two phases, the first when the hooked-end part is being pulled out of the matrix, and a much softer region after the hook is completely pulled out. This branch is governed by the parameter  $K_{eh}$ , in particular the last equation which in the original formulation is given by Equation (6.38).

$$K_{eh}(w^{cr}) = \left(\frac{l_i - 2 \cdot w^{cr}}{2 \cdot l_i - l_f}\right)^2 \cdot K_{eh,i} \quad , l_{eh} < w^{cr} < \frac{l_i}{2} \quad (6.38)$$

$$K_{eh,i} = K_{eh}(w^{cr} = l_{eh}) \quad (6.39)$$

$$l_i = l_f - 2 \cdot l_{eh} \quad (6.40)$$

Equation (6.38) was modified to account for the ultimate fibre pullout value provided by the user, and is now given by Equation (6.41),

$$K_{eh}(w^{cr}) = \left( \frac{w^{cr} - w_{ult}^{cr}}{l_{eh} - w_{ult}^{cr}} \right)^2 \cdot K_{eh,i} \quad , l_{eh} < w^{cr} < w_{ult}^{cr} \quad (6.41)$$

The original and modified SDEM model are plotted against each other in Figure 135 in order to understand the impact of the aforementioned modifications.

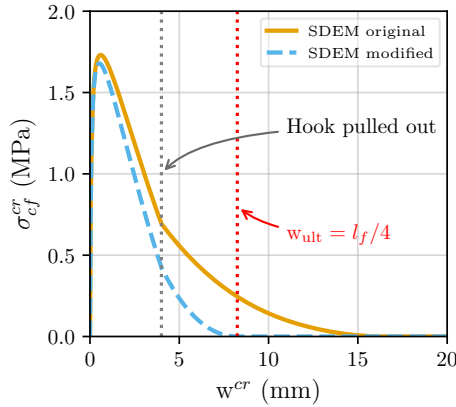


Figure 135: Comparison between the original and modified version of the SDEM model using the properties indicated in Table 23.

As can be observed in the results of Figure 135, the incorporation and adoption of a lower ultimate fibre pullout value ( $w_{ult} = l_f/4$ ) results, as expected, in a greater degradation of the post-peak region of the pullout process, which will result in a significant reduction of the load carrying capacity at the structural level.

The modified model was implemented in FEMIX V4.0, and the 3PNBBT simulation was once again conducted in order to assess the predictive performance of the modified SDEM model. The results of the 3PNBBT simulation considering the original and modified models are presented in Figure 136. The results

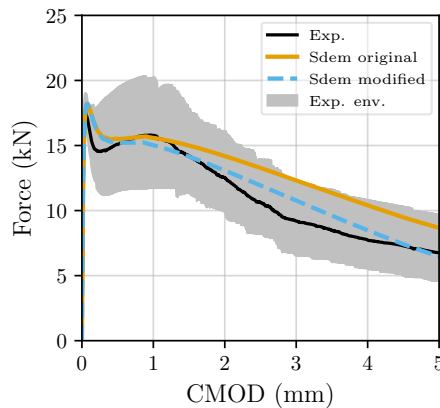


Figure 136: Comparison between the original and modified SDEM model in the results of the 3PNBBT FEM simulation.

presented in Figure 136 show a much better agreement between the experimental and numerical results obtained using the modified version of the SDEM model when compared to the original formulation.

### 6.3.2.2 Additional 3PNBBT simulations

Considering the modifications to the fibre pullout models proposed in Section 6.3.2.1, two additional set of simulations were conducted to analyse the validity of such modifications and the improvement in the predictive capacity of the MMFSCM.

The material properties used to define the constitutive models in each 3PNBBT simulation are listed in Table 24.

Table 24: Parameters used to define the MMFSCM model in the additional series of the 3PNBBT simulation.

Property	Value		
	S1	S2	S3
<b>Generic properties</b>			
Poisson's ratio ( $\nu$ )		0.2	
Young's modulus ( $E_c$ ) (MPa)	32900	29430	29400
Tensile strength ( $f_{ct}$ ) (MPa)	3.0	3.99	3.89
Crack band width (mm)		$\sqrt{A_{FE}}$	
Threshold angle ( $^\circ$ )		$30^\circ$	
Max. cracks per IP		2	
<b>RCM/CDM</b>			
Compressive strength ( $f_c$ ) (MPa)	64.2	55.7	54.7
Max. aggregate diameter ( $D_{max}$ ) (mm)	14.0	12.7	12.7
<b>Fibre pullout common properties</b>			
Fibre diameter ( $d_f$ ) (mm)	0.55	0.75	0.75
Fibre length ( $l_f$ ) (mm)	33	60	60
Fibre volume fraction ( $V_f$ ) (%)	0.75%	1.0%	0.75%
<b>Pfyl's model</b>			
Fibre Young's modulus ( $E_f$ ) (MPa)		200000	
<b>SDEM</b>			
Max. frictional bond ( $\tau_{st,max}$ ) (MPa)	3.17	3.67	3.58
Max. anchorage bond ( $\tau_{eh,max}$ ) (MPa)	3.44	3.99	3.89
Slip at max. frictional bond ( $s_{st}$ ) (mm)		0.01	
Slip at max. anchorage bond ( $s_{eh}$ ) (mm)		0.1	
Hook length ( $l_{eh}$ ) (mm)		4.5	
<b>UVEM</b>			
Bond strength ( $\tau_{b,0}$ ) (MPa)	6.56	11.97	11.67

The results of the numerical simulations are presented in Figure 137.

Regarding the results presented in Figure 137a, it is possible to observe that in general a better agreement between the numerical and experimental results is obtained using the modified pullout models when compared to the results initially presented in Figure 127a. Nonetheless, the Pfyl's model still provides

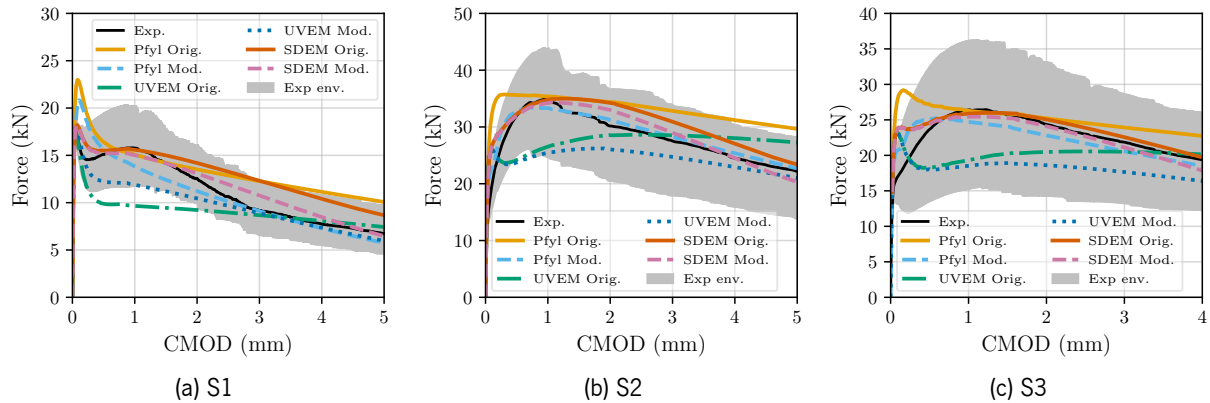


Figure 137: Numerical results for the 3PNBBT series considering the modified fibre pullout models (properties listed in Table 24).

a worse estimation of the peak force compared to the UVEM and SDEM models. In terms of post-peak response, the SDEM seems to provide the better estimation of the evolution trend of the experimental results, while the UVEM exhibits a more prominent drop in the response when compared to the Pfy1 and SDEM models. This is explained by the fact that the UVEM provides a lower fibre pullout contribution when compared to the remaining models (see Figure 128). Nonetheless, all modified models predict the response within the experimental envelope.

Regarding the additional set of results shown in Figures 137b and 137c, one can observe that the modified versions of the Pfy1's and SDEM models provide better estimates of the experimental response when compared to the UVEM, capturing with good accuracy the average experimental response both in terms of peak load and post-peak trend evolution, validating the modifications introduced in Section 6.3.2.1. Despite providing less accurate predictions when compared to the SDEM and Pfy1, the UVEM model still falls within the experimental envelope.

Hence, considering the above presented results, it is possible to conclude that there is a clear improvement in the numerical predictions when the modified pullout models are considered, demonstrating the adequacy of the MMFSCM for simulating FRC elements in mode I.

### 6.3.2.3 Implementation of a multi-linear constitutive model for Mode I

Despite the modifications to the pullout models introduced and described in Section 6.3.2.1, the results still exhibit slight deviations from the average experimental response, especially when the UVEM model is used. This is due to the fact that the pullout constitutive models are based on semi-empirical formulations which are then calibrated according to given set of experimental results. However, this calibration might prove inadequate for some situations, and consequently lead to less acceptable numerical predictions.

Hence, in order to improve the MMFSCM predictive performance, a new constitutive model for simulating the fracture mode I behaviour is proposed in addition to the already introduced pullout models. The constitutive model proposed in this section is based on a multi-linear branch configuration defined by

a maximum of 5 sets of  $(w^{cr}, \sigma^{cr})$  points, besides the point at crack initiation and the point at ultimate crack width. The use of such a diagram has been shown to be very effective in capturing the behaviour of SFRC exhibiting different response trends [137], and therefore the herein proposed model configuration is sufficient to capture a wide range of response types and shapes.

The model comprises the matrix and fibre pullout contributions, and consequently fully governs the fracture mode I and a schematic representation is presented in Figure 138.

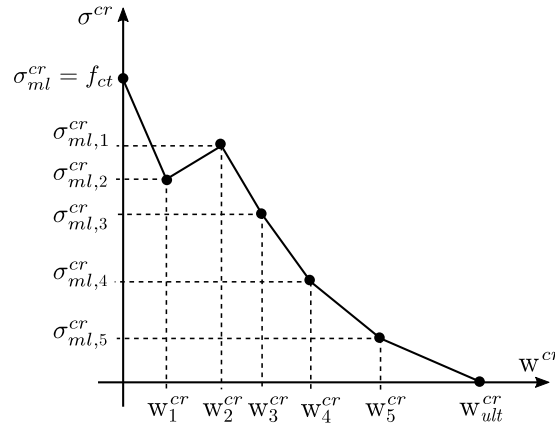


Figure 138: Multi-linear mode I constitutive model implemented in the MMFSCM.

The stress-width relationship of the multi-linear branch model is given by the following equation:

$$\sigma_{ml}^{cr} = \sigma_i^{cr} + (\sigma_{i+1}^{cr} - \sigma_i^{cr}) \cdot \frac{w^{cr} - w_i^{cr}}{w_{i+1}^{cr} - w_i^{cr}} \quad \text{for, } w_i^{cr} < w^{cr} \leq w_{i+1}^{cr} \quad (6.42)$$

where  $\sigma_i^{cr}$  and  $\sigma_{i+1}^{cr}$  and  $w_i^{cr}$  and  $w_{i+1}^{cr}$ , are the stress and crack width values of the  $i^{th}$  and  $i^{th} + 1$  points that define a generic branch formed by points  $i$  and  $i+1$ , respectively.

The advantage of the multi-linear branch constitutive model relies on the fact that the MMFSCM can now be calibrated using an inverse analysis tool to derive the mode I constitutive law and directly define the herein presented model. Hence, to assess the performance of the proposed multi-linear branch model, the 3PNBBT simulations presented in Section 6.3.2.2 were performed once again but now including the multi-linear model. In the present case, an inverse analysis tool developed by the authors and designated COFIT [137] is used to derive the  $\sigma^{cr} - w^{cr}$  diagram from the experimental results and define the multi-linear branch model configuration. The  $\sigma^{cr} - w^{cr}$  relationships obtained from the 3PNBBT experimental results and the results from the 3PNBBT simulations are presented in Figure 139.

As can be observed in the results shown in Figure 139, the multilinear branch constitutive model provides excellent predictions of the experimental response in all analysed cases, both in terms of peak load prediction and overall trend evolution of the response.

Hence, the multi-linear branch constitutive model approach to simulate the mode I is significantly better alternative to the experimentally calibrated fibre pullout models, when experimental results for conducting inverse analysis are available. Nonetheless, the Pfyl, SDEM and UVEM fibre pullout models are still a reasonable alternative when scarce information is available and inverse analysis is not possible.

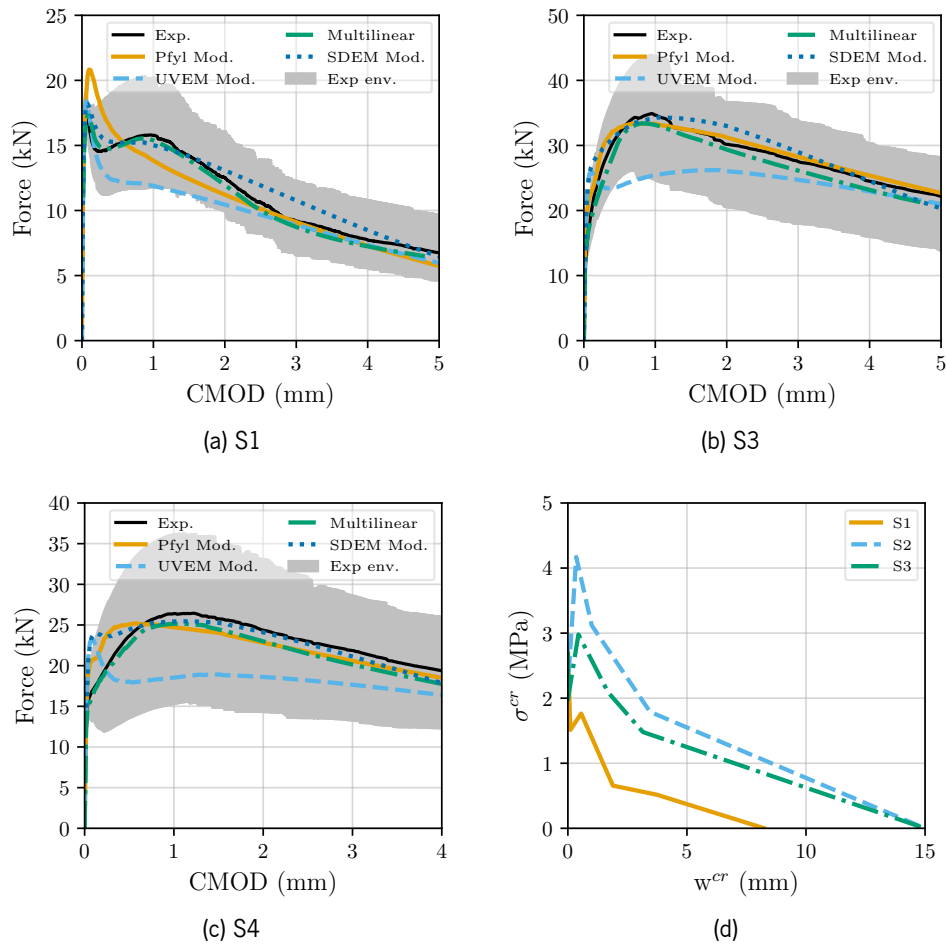


Figure 139: Assessment of the multi-linear branch model performance in the 3PNBBT simulations.

### 6.3.3 Shear panel tests

In this section the MMFSCM model is used to simulate the SFRC panels analysed by Susetyo et al. [204], which aimed to analyse the influence of concrete grade, fibre length ( $l_f$ ), fibre diameter ( $d_f$ ) and fibre volume ratio ( $V_f$ ) on the shear capacity of SFRC elements. The experimental test consists in subjecting a specimen to an in-plane pure-shear monotonic loading condition by means of vertical and horizontal actuators connected to steel keys embedded in the concrete elements, as depicted in Figure 140a. The specimens are 890 x 890 mm by 70 mm thick and were reinforced with conventional steel in one direction ( $\rho = 3.31\%$ ), as depicted in Figure 140b.

The numerical simulations were conducted in FEMIX V4.0 using a single 4 nodes plane stress element with a 2x2 G-L integration scheme to simulate the SFRC concrete panels, and 2-noded embedded cable elements with 2 G-L integration points to model the conventional steel reinforcement. The panel is supported in the vertical and horizontal directions in the lower left corner node and in the vertical direction in the lower right corner one. Vertical and horizontal loads are applied to the top nodes and lower right corner node in opposite directions to simulate the pure-shear loading condition of the experimental test.



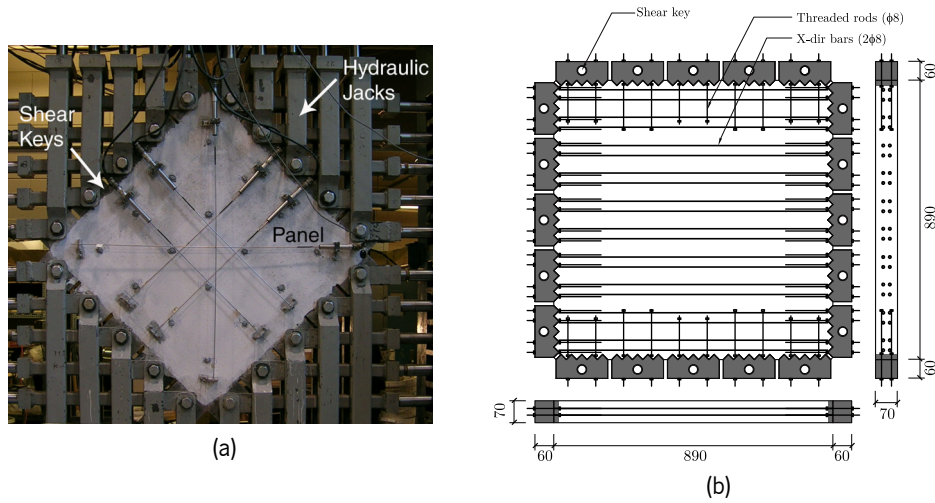


Figure 140: (a) Experimental test setup and (b) schematic representation of the shear FRC panels tested by Susetyo et al. [204]. Dimensions in mm.

Figure 141 shows the geometry, FE mesh, loading and support conditions adopted in the simulations.

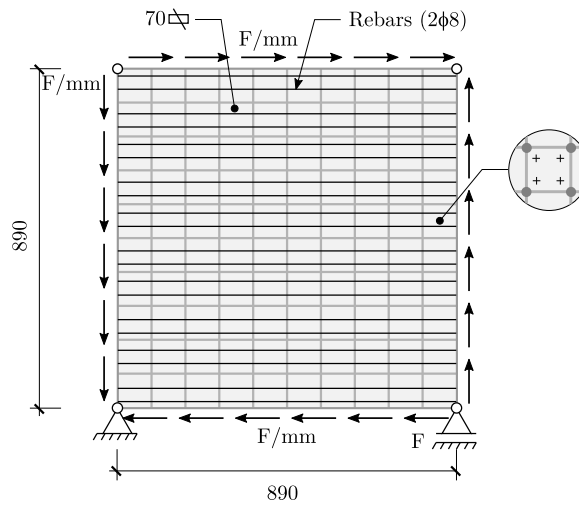


Figure 141: Geometry, FE mesh, loading and support conditions of the numerical model. Dimensions in mm.

For simulating the material nonlinear behaviour of SFRC, the MMFSCM constitutive model was used, considering different combinations of aggregate interlock and the modified fibre pullout models. The material properties used to define each model are listed in Table 25.

The constitutive model used for simulating the conventional steel reinforcement is defined by the relationship depicted in Figure 142. The diagram is defined by the points PT1, PT2 and PT3 and the parameter  $p$ , which governs the shape of the third branch and the parameters used to define this constitutive model are listed in Table 26.

The results of the carried out simulations are shown in Figure 143 where a comparison between numerical and experimental results for each SFRC panel type is presented.

Table 25: Parameters used to define the MMFSCM model in the shear panel test simulations [204].

Property	Value			
	C1F1V1	C1F1V2	C1F2V3	C1F3V3
<b>Generic properties</b>				
Poisson's ratio ( $\nu$ )			0.2	
Young's modulus ( $E_c$ )	30695	31243	32930	29042
Tensile strength ( $f_{ct}$ ) <sup>*</sup>	2.59	2.67	2.88	3.36
Crack band width (mm)			$\sqrt{(A_{IP})}^\dagger$	
Threshold angle(°)			30°	
Max. number of cracks / integration point			2	
<b>RCM/CDM</b>				
Compressive strength ( $f_c$ )	51.4	53.4	59.7	45.5
Max. aggregate diameter ( $D_{max}$ )(mm)			10.0	
<b>Fibre pullout common properties</b>				
Fibre diameter ( $d_f$ )	0.62	0.62	0.38	0.55
Fibre length ( $l_f$ )	50.0	50.0	30.0	35.0
Fibre volume fraction ( $V_f$ )	0.5%	1.0%	1.5%	1.5%
<b>Pfyl's model</b>				
Fibre Young's modulus ( $E_f$ )			200000	
<b>SDEM</b>				
Maximum frictional bond stress ( $\tau_{st,max}$ ) <sup>‡</sup>	2.84	2.89	3.06	3.56
Maximum anchorage bond stress ( $\tau_{eh,max}$ ) <sup>‡</sup>	3.08	3.13	3.31	3.86
Slip at maximum frictional bond stress ( $s_{st}$ ) <sup>§</sup>			0.01	
Anchorage slip at maximum bond stress ( $s_{eh}$ ) <sup>§</sup>			0.1	
Hooked-end length( $l_{eh}$ )			4.0	
<b>UVEM</b>				
Bond aligned with pullout direction ( $\tau_{b,0}$ ) <sup>**</sup>	5.71	5.88	6.34	7.39

<sup>\*</sup>  $f_{ct}$  values retrieved from the uniaxial tensile tests conducted by Susetyo et al. [204]; <sup>†</sup>Square root of the tributary area of the integration point; <sup>‡</sup>Values defined according to Voo and Foster [233] and Seong-Cheol Lee, and Frank J. Vecchio [267]; <sup>§</sup>According to Naaman and Najm [18]; According to Htut and Foster [222];

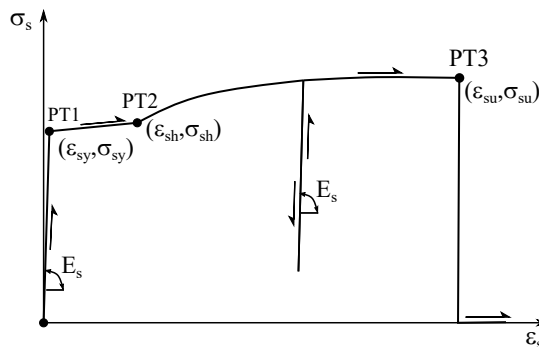
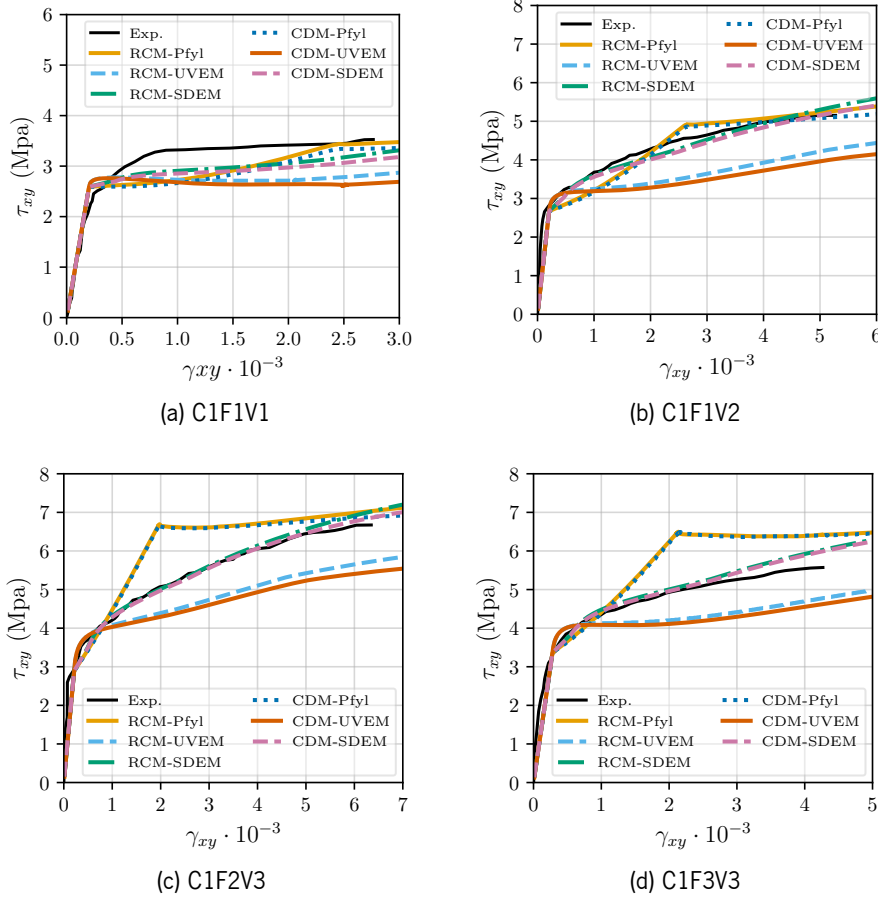


Figure 142: Constitutive model used to simulate the nonlinear material behaviour of the conventional steel reinforcement [220].

Table 26: Parameters used to define the steel reinforcement constitutive model.

$\phi$ (mm)	$A_s$ (mm <sup>2</sup> )	$\varepsilon_{sy}$	$\sigma_{sy}$ (N/mm <sup>2</sup> )	$\varepsilon_{sh}$	$\sigma_{sh}$ (N/mm <sup>2</sup> )	$\varepsilon_{su}$	$\sigma_{su}$ (N/mm <sup>2</sup> )	$\rho$
8	50.27	2.457e-3	552	1.0e-2	552	0.1	647	1


 Figure 143: Comparison between the experimental and numerical results of the SFRC panels, in terms of  $\tau_{xy} - \gamma_{xy}$ .

Regarding the results shown in Figure 143a it is possible to observe that the response is underestimated regardless of the combination of aggregate interlock and fibre pullout model used. Nonetheless, the Pfyl and SDEM models provide slightly better approximations of the response when compared to the UVEM model.

In Figures 143b to 143d the results follow similar trends where the SDEM model provides very good estimates of the experimental response, with the Pfyl's and UVEM models overestimating and underestimating the response, respectively, especially in case of C1F2V3 and C1F3V3.

In order to further understand the contribution of each resisting mechanism in the results of Figure 143, another set of simulations was conducted considering exclusively the contribution of the aggregate interlock resisting mechanism. The results are compared against the model combination that provided the best prediction of the experimental response for each panel analysed. The results obtained

from the aforementioned simulations are presented in Figure 144.

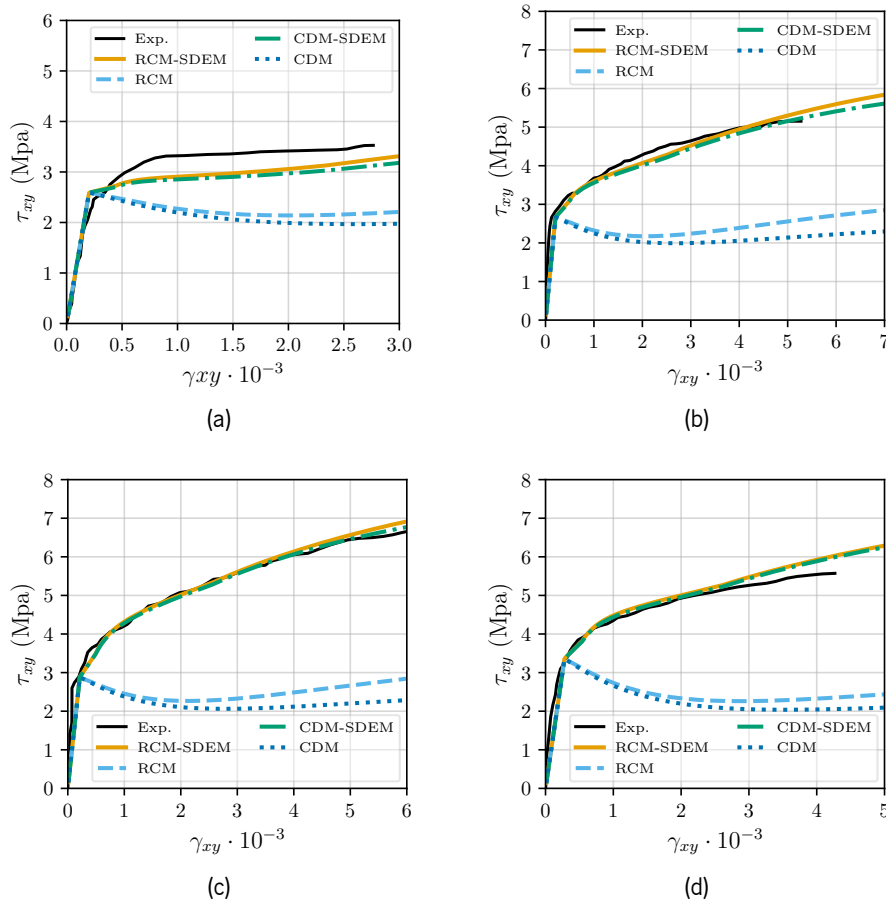


Figure 144: Comparison between experimental and numerical results considering only the contribution of the aggregate interlock resisting mechanism.

As shown in the results presented in Figure 144, the fibre pullout resisting mechanism has a very relevant contribution to the response, accounting up to approximately 50% of the shear stress transferring capacity of the FRC specimens, and even greater when higher fibre volume ratios (1.0% / 1.5%) are used (Figures 144c and 144d).

The important contribution of the fibre resisting mechanism to the shear stress transferring capacity also explains the odd shape of the numerical responses observed in the results of Figure 143 when using the Pfyl's model. To confirm this observation, the contribution of the fibre pullout resisting mechanism, for the Pfyl, UVM and SDEM models, for a given crack at an IP in case of panel C1F3V3 is shown in Figure 145. According to the results shown in Figure 145 it is possible to observe that in fact the Pfyl's model originates a higher contribution when compared to the SDEM and UVM models originating the shape of the structural response of the panel observed in Figure 143d.

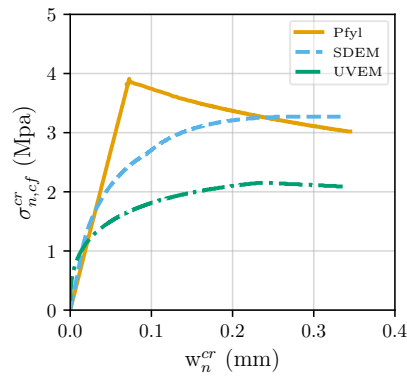


Figure 145: Comparison between the fibre pullout contribution at a given crack of the panel C1F3V3.

### 6.3.4 Mixed-mode test

In this section the predictive performance of the MMFSCM in mixed-mode fracture is assessed. For this purpose the well-known experimental test conducted by Arrea and Ingraffea [268] is simulated. Hence, two numerical simulations are conducted using the two aggregate interlock models available in the MMFSCM namely, the RCM and CDM, in order to understand the impact of each model in the results.

The beam with 1322x306x156 mm was modelled using 8 node plane stress FEs, considering a 3x3 G-L integration scheme. A material nonlinear behaviour was assigned to the elements inside the refined area, whilst the remaining elements were considered linear elastic behaviour. The numerical simulations were performed using the Newton-Raphson method by controlling the relative vertical displacement between the nodes at the notch extremity. The adopted FE mesh, loading and support conditions of the simulated beam are presented in Figure 146. For simulating the nonlinear material behaviour the MMFSCM model it was adopted the values listed in Table 27.

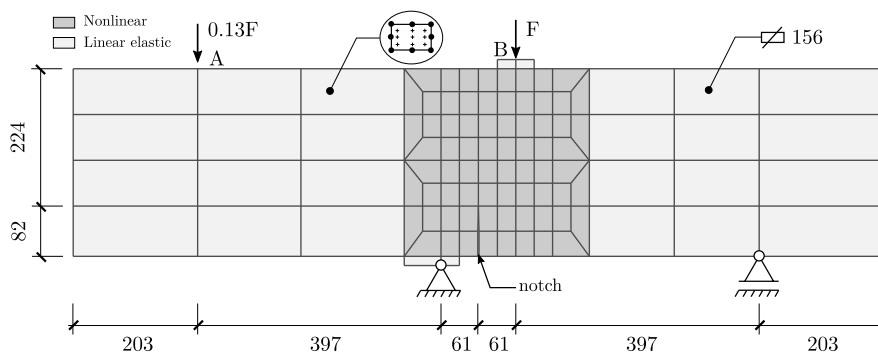


Figure 146: Geometry, mesh, support and loading conditions of the mixed-mode test conducted by Arrea and Ingraffea [268] (all dimensions in mm).

Figures 147a and 147b show the results obtained in terms of Force (at point B) vs crack mouth sliding displacement (CMSD), given by the difference of vertical displacement between the pair nodes located at each side of the notch, and the crack pattern obtained at the last converged combination for the simulation considering the CDM aggregate interlock model, respectively. Regarding the results of Figure 147a it is possible to observe that until the peak force is attained the results are the same regardless of the aggregate

Table 27: Parameters used to define the MMFSCM model in the mixed-mode test conducted by [268].

Property	Value
<b>Generic properties</b>	
Poisson's ratio ( $\nu$ )	0.18
Young's modulus ( $E_c$ )	24800
Tensile strength ( $f_{ct}$ )	2.8
Crack band width (mm)	$\sqrt{(A_{FE})}^*$
Threshold angle( $^\circ$ )	$60^\circ$
Max. number of cracks / integration point	2
<b>RCM/CDM</b>	
Compressive strength ( $f_c$ )	48.7
Max. aggregate diameter ( $D_{max}$ )(mm)	10.0

\* Square root of the are of the finite element;

interlock model. The peak force is estimated with good accuracy, and very similar results are obtained for both the RCM and CDM in the post-peak phase of the response. This behaviour is coherent with the results previously shown for the shear panel simulations (Figure 144) where a small difference between the RCM and CDM was observed. The model provides and overestimation of the post-peak phase of the experimental response, attributed to a smoother decay in the post-peak phase when compared to the experimental results, nonetheless, the results are within reasonable estimations. The numerical crack pattern shown in Figure 147b is consistent with the expected failure mode of the beam.

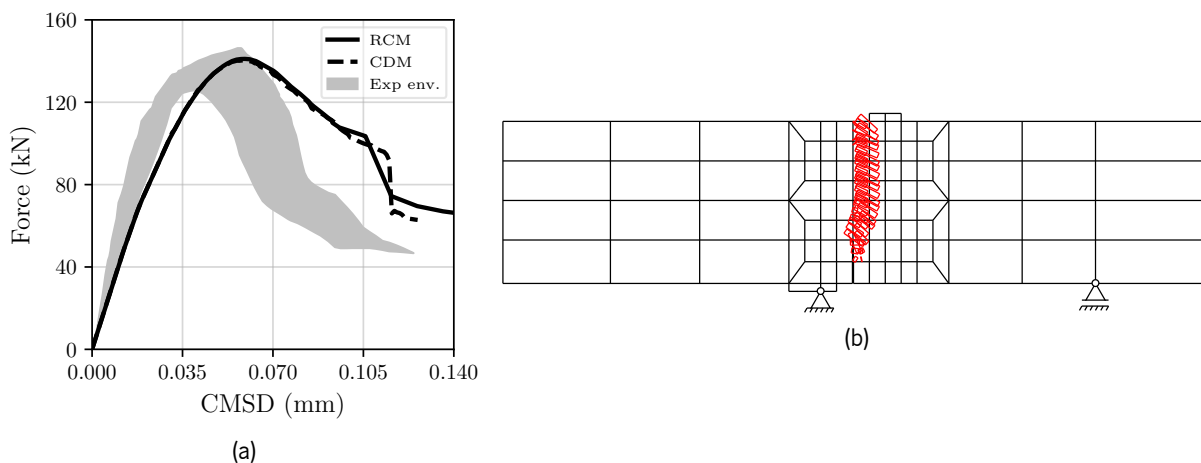


Figure 147: (a) Force (B) - crack mouth sliding displacement (CMSD) and (b) crack pattern obtained using the RCM model.

## 6.4 Summary and Conclusions

In this chapter, the implementation of a two dimensional mixed-mode fracture smeared crack model (MMFSCM) in a FEM-based software designated FEMIX V4.0 is detailed. The constitutive model is based on well established aggregate interlock models, namely the RCM and CDM, and fibre pullout models such as the Pfyf's, the UVEM and SDEM. The implementation of the MMFSCM is validated through a simple example based on a single FE simulation by comparing the numerical records with the analytical results obtained through the mathematical expressions.

In order to assess the predictive performance of the implemented constitutive model, two numerical case studies were carried out. The first case consisted in the numerical simulation of a three-point notched beam bending test (3PNBBT) and aimed at analysing the predictive performance of the MMFSCM in fracture mode I, and the adequacy of the fibre pullout models for simulating the fibre pullout resisting mechanism. The performance of the model was assessed by comparing the numerical and experimental results found in the literature and also experimental results provided by the Portuguese civil engineering company CiviTest. Furthermore, modifications to the original formulation of the pullout models were introduced in order to enhance the overall predictive performance of the model. Also, a multi-linear branch constitutive model for simulating the fracture mode I was implemented in order to mitigate the lower degree of flexibility of the fibre pullout models, allowing the possibility to use inverse analysis tools to directly derive the mode I fracture relationship.

The second case was related to the simulation of SFRC concrete panels subjected to in-plane shear loading conditions. The predictive performance of the MMFSCM was once again analysed, including the contribution of each resisting mechanism to the overall structural response. For this purpose the experimental results of 4 SFRC panels manufactured with different fibre volume ratios and fibre geometry were analysed. The good performance of the model is also demonstrated by means of a popular mixed-mode test simulation.

Based on the obtained results, the following conclusions can be drawn:

- Regarding the 3PNBBT test, the original formulations of the pullout models provided reasonable estimations of the experimental peak load, however the post-peak trend of the responses exhibited a lower degradation rate than the observed experimental results, leading to overestimations of this phase of the response.
- To mitigate this effect, the original formulations of the pullout models were modified to account for an ultimate pullout value of  $l_f/4$  instead of  $l_f/2$  and the modified version provided better predictions of the experimental responses in all analysed cases.
- To further improve the MMFSCM model predictive performance in mode I, a multi-linear branch constitutive model was implemented. The multi-linear model provided excellent predictions of the experimental results for all 3PNBBT series, after deriving the  $\sigma^{cr} - w^{cr}$  relationship using an inverse analysis tool.

- The multi-linear branch model was able to perfectly capture the experimental results regardless of the response evolution trend.
- Regarding the SFRC panels, The SDEM model in combination with the RCM and CDM models, provided very accurate predictions of the experimental responses of the SFRC panels. Regarding the PfyI and UVEM models, an overestimation and underestimation of the responses was observed, respectively.
- The importance of the fibre pullout resisting mechanism was shown to contribute up to  $\approx 50\%$  of the shear transferring capacity of the SFRC panel specimens.
- The MMFSCM is able to simulate FRC elements in both fracture mode I, mode II and in mixed-mode fracture and its adequacy for estimating the flexural and shear capacity of FRC was demonstrated in the present work.



# 7 Conclusions

## 7.1 General conclusions

The research work presented in this Thesis aimed at on one hand enhance the existing models and methodologies to simulate and analyse fibre reinforced concrete (FRC) elements and on the other hand to propose and implement a new integrated mixed-mode constitutive model in finite element method (FEM)-based software designated FEMIX V4.0. Hence, the main conclusions of the work presented in this document is summarised in the following paragraphs.

In Chapter 3 an overview on the simulation of FRC elements using the multi-fixed smeared crack model (MFSCM) approach available in the FEMIX V4.0 computer code was presented by means of different numerical case studies. Also, the importance of the parameters that govern mode I and mode II was analysed by means of parametric studies. Furthermore, a generalised approach to compute the crack band width (CBW) parameter was described and successfully implemented in FEMIX V4.0 and the influence of mesh refinement and configuration was investigated by means of a numerical case study. The main conclusions of the conducted investigations are summarised as follows:

- The mode I parameters have a significant impact in the structural response and the estimation of such parameters by means of inverse analysis (IA) leads to very good results. Consequently the development of a reliable, robust and automatic approach to conduct IA is of utmost importance for improving the reliability of the simulations of FRC elements.
- The good predictive performance of the available constitutive models in FEMIX V4.0 was demonstrated by the results shown in the prestressed FRC railway sleeper case study, in which the model was able to accurately capture the structural response and the obtained crack patterns were coherent with the observed experimental ones.
- The methodology proposed by Oliver and Idelsohn [205] did not produce significant differences in the results both in terms of force-displacement curves or crack patterns when regular mesh configurations (aspect ratio  $\approx 1$ ) are used.
- The study regarding different mesh configurations with finite elements (FEs) defined by distinct aspect ratios revealed that the implemented CBW approach better captured the experimental response, when compared to the remaining methodologies, and the obtained crack patterns revealed

to be more coherent in terms of crack width uniformity for cracks originated in adjacent elements with distinct aspect ratios producing more realistic crack patterns.

One of the main conclusions that arose from the studies conducted in Chapter 3 was related to the fact that the mode I parameters have a very relevant impact in the results and the determination of such parameters in the best possible manner was key to obtain reliable results.

Hence, the work presented in Chapter 4 is related to the development of a new IA approach for deriving the fracture mode I parameters of FRC from three-point notched beam bending tests (3PNBBT) and round panel tests supported on three points (RPT-3PS). The developed approach was appraised by comparing the obtained numerical predictions with experimental results collected from the literature and the main conclusions are summarised as follows:

- The developed IA approach revealed a very good performance in terms of numerical and experimental prediction and the values obtained for the multi-linear softening diagrams were consistent with the material characteristics;
- The developed tool was able to capture different tensile behaviours (softening and hardening) validating its applicability potential. In addition, the runtimes varied from 1 to 2 minutes approximately, for the case of 3PNBBT and from 4 to 6 minutes in the case of RPT-3PS, which is significantly faster when compared to the conventional FEM approach;
- The results of the impact of the initial variable guess of the multi-linear post-peak diagram demonstrated the robustness of the developed algorithm since the obtained output was not significantly affected by the initial values provided by the user demonstrating the effectiveness of the automatic variable updating procedure;
- The proposed IA methodology revealed to be more accurate, in terms of prediction of the experimental response of 3PNBBT specimens, and simpler when compared to conventional manual FEM IA since no FEM model is required and the fracture parameters are estimated automatically;
- The estimation of the mode I parameters should not be based on the average experimental response of 3PNBBT but instead, i.e., on a 5% fractile, in order to avoid the overestimation of the tensile capacity of FRC;

In some situations it is not possible or very difficult to derive the fracture parameters to conduct reliable simulations. As an attempt to provide an alternative to these situations, a new mixed-mode fracture constitutive model that accounts for the fibre and aggregate interlock resisting mechanisms is proposed in Chapter 5. The model predicts the normal and shear stresses in function of the crack opening and sliding displacements and the fibre and aggregate interlock resisting mechanisms are simulated by means of two well established aggregate interlock models and three fibre pull-out models reported in the literature. The importance of the variables used to define the proposed constitutive model was demonstrated, and its predictive performance was appraised by means of parametric studies and the comparison of the analytical

predictions with experimental results reported in the literature. Considering the results presented in this chapter, the following conclusions can be drawn:

- The parametric study shows that higher fibre volume ratios allow for greater normal and shear stresses to develop. In addition, the concrete compressive strength greatly impacts the maximum normal and shear stress values in both the rough crack model (RCM) and contact density model (CDM) aggregate interlock models. Aggregate size governs the contribution of the aggregate interlock component, especially when greater crack sliding values are considered.
- The results based on the experimental validation show that the RCM gives a better overall agreement with the experimental results comparatively to the CDM. Furthermore, the comparison between fibre pull-out models show that the Pfyl's simple model captures both peak and post-peak response with higher accuracy when compared to the other models. In addition, Pfyl's model has the advantage of requiring less input parameters when compared the simplified diverse embedment model (SDEM).
- The model seems to capture reasonably the peak stresses however, the post-peak response is overestimated in all the experimental tests simulated. This is justified by the fact that both the RCM and CDM were developed for conventional reinforced concrete, where the level of crack width and sliding for the mobilization of cracking resisting mechanisms is much smaller than in case of FRC.
- Both the RCM and CDM were adapted in order to better represent the aggregate interlock mechanisms in FRC. By applying a special sigmoid type function to the original formulation of the RCM and CDM, a much better predictive performance was generally obtained.

In Chapter 6 the implementation of the integrated mixed-mode constitutive model presented in Chapter 5 is detailed. The model was successfully implemented in FEMIX V4.0 and its predictive performance appraised by means of two numerical case studies by comparing the numerical and experimental results found in the literature and provided by the Portuguese civil engineering company CiviTest. Furthermore, modifications to the original formulations of the pullout models were introduced in order to enhance the overall predictive performance of the model and a multi-linear branch constitutive model for simulating the fracture mode I allowing the possibility to use the IA approach developed in Chapter 4. The conclusions of the works conducted in Chapter 6 are the following:

- Regarding the 3PNBBT test, the original formulations of the pullout models provided reasonable estimations of the experimental peak load, however the post-peak trend of the responses exhibited a lower degradation rate than the observed experimental results, leading to overestimations of this phase of the response.
- To mitigate this effect, the original formulations of the pullout models were modified to account for an ultimate pullout value of  $l_f/4$  instead of  $l_f/2$  and the modified version provided better predictions of the experimental responses in all analysed cases.

- To further improve the MMFSCM model predictive performance in mode I, a multi-linear branch constitutive model was implemented. The multi-linear model provided excellent predictions of the experimental results for all 3PNBBT series, after deriving the  $\sigma^{cr} - w^{cr}$  relationship using an inverse analysis tool.
- The multi-linear branch model was able to perfectly capture the experimental results regardless of the experimental response evolution trend.
- Regarding the SFRC panels, The SDEM model in combination with the RCM and CDM models, provided very accurate predictions of the experimental responses of the SFRC panels. Regarding the Pfyl and UVEM models, an overestimation and underestimation of the responses was observed, respectively.
- The importance of the fibre pullout resisting mechanism was shown to contribute up to  $\approx 50\%$  of the shear transferring capacity of the SFRC panel specimens.
- The MMFSCM is able to simulate FRC elements in both fracture mode I and II and its adequacy for estimating the flexural and shear capacity of FRC was demonstrated in the present work.

## 7.2 Recommendations for future works

The objectives initially established for the present PhD work were successfully attained and the conducted research contributed with additional knowledge and tools for the analysis and simulation of FRC structures. In fact, the developed IA methodology demonstrated to be highly effective and efficient in deriving the fracture mode I parameters of FRC from 3PNBBT and RPT-3PS experimental results. Also, the proposed mixed-mode constitutive model was successfully implemented in FEMIX V4.0 computer code and its good predictive performance was demonstrated through a series of numerical case studies. Nonetheless, further research is still required in all investigated topics, and some of the research recommendations that directly arose from the conducted investigations can be summarised in the following key points:

- Implementation of additional analytical models in the developed IA software to extend its applicability to different experimental tests;
- Development of an IA approach for estimating the fracture mode II parameters;
- Extension of the integrated mixed-mode model to the three-dimensional space;
- Implementation of additional fibre pullout and aggregate interlock models to further improve the predictive performance of the mixed-mode model;
- Application of the proposed mixed-mode constitutive model to the development of competitive solutions for FRC structural systems, in particular for the railway field.

# Bibliography

- [1] Donald H. Campbell and Robert T. L. Folk. "Ancient Egyptian Pyramids—Concrete or Rock". In: *Concrete International* 13.8 (1991-01) (cit. on p. 1).
- [2] ACI Committee 544. "State-of-the-Art Report on Fiber Reinforced Concrete". In: *ACI Journal Proceedings* 70.11 (1973-01). doi: 10.14359/7135 (cit. on p. 1).
- [3] Patricia Guerrero and Antoine E. Naaman. "Effect of Mortar Fineness and Adhesive Agents on Pullout Response of Steel Fibers". In: *ACI Materials Journal* 97.1 (2000-01). doi: 10.14359/800 (cit. on p. 1).
- [4] C. Esveld. *Modern Railway Track*. 2. ed. Zaltbommel: MRT-Productions, 2001. isbn: 978-90-800324-3-9 (cit. on pp. 2, 17, 19, 22).
- [5] D. N. Bilow and G. M. Randich. "Slab Track for the next 100 Years". In: *AREMA Proceedings of the 2000 Annual Conference American Railway Engineering and Maintenance-of-Way Association*. 2000 (cit. on p. 2).
- [6] R. Bastin. "Development of German Non-Ballasted Track Forms". In: *Proceedings of the Institution of Civil Engineers - Transport* 159.1 (2006-02), pp. 25–39. issn: 0965-092X, 1751-7710. doi: 10.1680/tran.2006.159.1.25 (cit. on p. 2).
- [7] G. Welch and B. Haisman. "The Application of Fracture Mechanics to Concrete and the Measurement of Fracture Toughness". In: *Materiaux et Construction* 2.3 (1969), pp. 171–177 (cit. on p. 5).
- [8] A. Hillerborg. "The Theoretical Basis of a Method to Determine the Fracture Energy  $G_F$  of Concrete". In: *Materials and structures* 18.4 (1985), pp. 291–296 (cit. on pp. 5, 6).
- [9] S. P. Shah, S. E. Swartz and C. Ouyang. *Fracture Mechanics of Concrete: Applications of Fracture Mechanics to Concrete, Rock and Other Quasi-Brittle Materials*. John Wiley & Sons, 1995 (cit. on p. 5).
- [10] Z. P. Bažant and J. Planas. *Fracture and Size Effect in Concrete and Other Quasibrittle Materials*. First. Routledge, 1998. isbn: 978-0-203-75679-9. doi: 10.1201/9780203756799 (cit. on p. 5).

- 
- [11] M. Kaplan. "Crack Propagation and the Fracture of Concrete". In: *Journal Proceedings*. Vol. 58. 1961, pp. 591–610 (cit. on p. 6).
- [12] M. Elices, J. Planas and G. Guinea. "Fracture Mechanics Applied to Concrete". In: *European Structural Integrity Society*. Vol. 26. Elsevier, 2000, pp. 183–210 (cit. on p. 6).
- [13] C. E. Kesler, D. J. Naus and J. L. Lott. "Fracture Mechanics-Its Applicability to Concrete". In: *Proceedings of the Society of Materials Science Conference on the Mechanical Behavior of Materials*. Conf Paper. 1972 (cit. on p. 6).
- [14] J. Lott and C. Kesler. "Crack Propagation in Plain Concrete". In: *Symposium on Structure of Portland Cement Paste and Concrete*. National Academy of Sciences. 1966, pp. 204–218 (cit. on p. 6).
- [15] Y. Zaitsev and F. Wittmann. "Simulation of Crack Propagation and Failure of Concrete". In: *Matériaux et Construction* 14.5 (1981), pp. 357–365 (cit. on p. 6).
- [16] I. Löfgren. "Fibre-Reinforced Concrete for Industrial Construction". PhD thesis. 2005 (cit. on pp. 6–8, 17, 28, 29).
- [17] V. Cunha. "Steel Fibre Reinforced Self-Compacting Concrete (from Micro-Mechanics to Composite Behaviour)". PhD thesis. University of Minho, 2010 (cit. on pp. 7–11, 106).
- [18] A. E. Naaman and H. Najm. "Bond-Slip Mechanisms of Steel Fibers in Concrete". In: *Materials Journal* 88.2 (1991), pp. 135–145 (cit. on pp. 7, 9, 113, 147, 165).
- [19] A. E. Naaman. "Engineered Steel Fibers with Optimal Properties for Reinforcement of Cement Composites". In: *Journal of advanced concrete technology* 1.3 (2003), pp. 241–252 (cit. on p. 7).
- [20] P. Bartos. "Review Paper: Bond in Fibre Reinforced Cements and Concretes". In: *International Journal of Cement Composites and Lightweight Concrete* 3.3 (1981-08), pp. 159–177. issn: 02625075. doi: 10.1016/0262-5075(81)90049-X (cit. on p. 7).
- [21] M. Maage. "Interaction between Steel Fibers and Cement Based Matrixes". In: *Matériaux et Construction* 10.5 (1977), pp. 297–301 (cit. on p. 8).
- [22] N. Banthia and J.-F. Trottier. "Concrete Reinforced with Deformed Steel Fibers, Part I: Bond-Slip Mechanisms". In: *Materials Journal* 91.5 (1994), pp. 435–446 (cit. on pp. 8, 10).
- [23] V. C. Li and H. Stang. "Interface Property Characterization and Strengthening Mechanisms in Fiber Reinforced Cement Based Composites". In: *Advanced cement based materials* 6.1 (1997), pp. 1–20 (cit. on pp. 8, 9).
- [24] G. Chanvillard. "Analyse Expérimentale et Modélisation Micromécanique Du Comportement Des Fibres d'acier Tréfilées, Ancrées Dans Une Matrice Cimentaire". In: *Etudes et recherches des laboratoires des ponts et chaussees-serie ouvrages d'art OA12* (1993) (cit. on p. 9).

- [25] P. Groth. "Fibre Reinforced Concrete: Fracture Mechanics Methods Applied on Self-Compacting Concrete and Energetically Modified Binders". PhD thesis. Luleå tekniska universitet, 2000 (cit. on pp. 9, 10).
- [26] P. Robins, S. Austin and P. Jones. "Pull-out Behaviour of Hooked Steel Fibres". In: *Materials and structures* 35.7 (2002), pp. 434–442 (cit. on pp. 9–11).
- [27] A. Bentur et al. "Fiber-Matrix Interfaces". In: *Chapter 5 van 'pre-Proceedings 2nd International Workshop 'High Performance Fiber Reinforced Cement Composites (HPF-RCC-95)', Ed. Naaman A. and Reinhardt H., 11-14 Juni Ann Arbor, Michigan, USA. 1995*, pp. 139–182 (cit. on p. 10).
- [28] S. Diamond and J. Huang. "The ITZ in Concrete—a Different View Based on Image Analysis and SEM Observations". In: *Cement and concrete composites* 23.2-3 (2001), pp. 179–188 (cit. on p. 10).
- [29] S. Wei, J. A. Mandel and S. Said. "Study of the Interface Strength in Steel Fiber-Reinforced Cement-Based Composites". In: *Journal Proceedings*. Vol. 83. 1986, pp. 597–605 (cit. on p. 10).
- [30] A. Bentur and S. Mindess. *Fibre Reinforced Cementitious Composites*. Ed. by Routledge. Zeroth. CRC Press, 1990. isbn: 978-0-429-17729-3. doi: 10.1201/9781482267747 (cit. on p. 10).
- [31] A. M. Brandt. "On the Optimal Direction of Short Metal Fibres in Brittle Matrix Composites". In: *Journal of Materials Science* 20.11 (1985-11), pp. 3831–3841. issn: 0022-2461, 1573-4803. doi: 10.1007/BF00552371 (cit. on p. 10).
- [32] J. Barros. "Steel Fibre Reinforced Concrete: Material Properties and Structural Applications". In: *Fibrous and Composite Materials for Civil Engineering Applications*. Elsevier, 2011, pp. 95–155. isbn: 978-1-84569-558-3. doi: 10.1533/9780857095583.2.95 (cit. on pp. 11, 17).
- [33] A. Abrishambaf, M. Pimentel and S. Nunes. "Influence of Fibre Orientation on the Tensile Behaviour of Ultra-High Performance Fibre Reinforced Cementitious Composites". In: *Cement and Concrete Research* 97 (2017-07), pp. 28–40. issn: 00088846. doi: 10.1016/j.cemconres.2017.03.007 (cit. on p. 11).
- [34] C. Kameswara Rao. "Effectiveness of Random Fibres in Composites". In: *Cement and Concrete Research* 9.6 (1979), pp. 685–693 (cit. on pp. 11, 13, 15).
- [35] P. Schumacher. "Rotation Capacity of Self-Compacting Steel Fiber Reinforced Concrete". PhD thesis. 2006 (cit. on pp. 11, 13).
- [36] F. Laranjeira. "Design-Oriented Constitutive Model for Steel Fiber Reinforced Concrete". PhD thesis. Universitat Politècnica de Catalunya, 2010 (cit. on p. 12).
- [37] A. Van Gysel. "Studie van Het Uittrekgedrag van Staalvezels Ingebed in Een Cementgebonden Matrix Met Toepassing Op Staalvezelbeton Onderworpen Aan Buiging". In: (2000) (cit. on pp. 12, 16).

- [38] A. G. Kooiman. “Modelling Steel Fibre Reinforced Concrete for Structural Design”. In: (2000) (cit. on pp. 12, 13, 15, 16).
- [39] D. Dupont and L. Vandewalle. “Distribution of Steel Fibres in Rectangular Sections”. In: *Cement and Concrete Composites* 27.3 (2005), pp. 391–398 (cit. on pp. 12, 15, 16).
- [40] A. B. Álvarez. “Characterization and Modelling of SFRC Elements”. PhD thesis. Universitat Politècnica de Catalunya, 2013 (cit. on pp. 12, 16).
- [41] P. Soroushian and C.-D. Lee. “Distribution and Orientation of Fibers in Steel Fiber Reinforced Concrete”. In: *Materials Journal* 87.5 (1990), pp. 433–439 (cit. on pp. 12, 16).
- [42] P. Stähli, R. Custer and J. G. van Mier. “On Flow Properties, Fibre Distribution, Fibre Orientation and Flexural Behaviour of FRC”. In: *Materials and Structures* 41.1 (2008), pp. 189–196 (cit. on pp. 12, 13, 16).
- [43] B. E. Barragán. *Failure and Toughness of Steel Fiber Reinforced Concrete under Tension and Shear*. Universitat Politècnica de Catalunya, 2002 (cit. on p. 13).
- [44] Å. L. Døssland. “Fibre Reinforcement in Load Carrying Concrete Structures: Laboratory and Field Investigations Compared with Theory and Finite Element Analysis”. PhD thesis. Fakultet for naturvitenskap og teknologi, 2008 (cit. on pp. 13, 16).
- [45] H. Krenchel. *Fibre Spacing and Specific Fibre Surface*. 1975 (cit. on pp. 13, 16).
- [46] F. Laranjeira et al. “Characterization of the Orientation Profile of Steel Fiber Reinforced Concrete”. In: *Materials and structures* 44.6 (2011), pp. 1093–1111 (cit. on p. 13).
- [47] A. Blanco et al. “Assessment of the Fibre Orientation Factor in SFRC Slabs”. In: *Composites Part B: Engineering* 68 (2015-01), pp. 343–354. issn: 13598368. doi: 10.1016/j.compositesb.2014.09.001 (cit. on p. 13).
- [48] S. Grünewald. “Performance-Based Design of Self-Compacting Fibre Reinforced Concrete”. PhD thesis. TU Delft, Delft University of Technology, 2004 (cit. on pp. 13, 16).
- [49] J. P. Romualdi and J. A. Mandel. “Tensile Strength of Concrete Affected by Uniformly Distributed and Closely Spaced Short Lengths of Wire Reinforcement”. In: *Journal Proceedings*. Vol. 61. 1964, pp. 657–672 (cit. on p. 14).
- [50] P. Stroeven. “Morphometry of Fibre Reinforced Cementitious Materials”. In: *Matériaux et Construction* 11.1 (1978), pp. 31–38 (cit. on p. 14).
- [51] M. Alberti, A. Enfedaque and J. Gálvez. “A Review on the Assessment and Prediction of the Orientation and Distribution of Fibres for Concrete”. In: *Composites Part B: Engineering* 151 (2018-10), pp. 274–290. issn: 13598368. doi: 10.1016/j.compositesb.2018.05.040 (cit. on p. 16).



- [52] B. Barr et al. "Round-Robin Analysis of the RILEM TC 162-TDF Beam-Bending Test: Part 3—Fibre Distribution". In: *Materials and Structures* 36.9 (2003), pp. 631–635 (cit. on p. 16).
- [53] R. Gettu et al. "Study of the Distribution and Orientation of Fibers in SFRC Specimens". In: *Materials and Structures* 38.1 (2005), pp. 31–37 (cit. on p. 16).
- [54] J. Michels et al. "Steel Fibers as Only Reinforcement for Flat Slab Construction—Experimental Investigation and Design". In: *Construction and Building Materials* 26.1 (2012), pp. 145–155 (cit. on p. 16).
- [55] M. Alberti, A. Enfedaque and J. Gálvez. "Comparison between Polyolefin Fibre Reinforced Vibrated Conventional Concrete and Self-Compacting Concrete". In: *Construction and Building Materials* 85 (2015-06), pp. 182–194. issn: 09500618. doi: 10.1016/j.conbuildmat.2015.03.007 (cit. on p. 16).
- [56] M. Alberti et al. "Reliability of Polyolefin Fibre Reinforced Concrete beyond Laboratory Sizes and Construction Procedures". In: *Composite Structures* 140 (2016-04), pp. 506–524. issn: 02638223. doi: 10.1016/j.compstruct.2015.12.068 (cit. on p. 16).
- [57] P. Stähli and J. G. Van Mier. "Manufacturing, Fibre Anisotropy and Fracture of Hybrid Fibre Concrete". In: *Engineering fracture mechanics* 74.1-2 (2007), pp. 223–242 (cit. on p. 16).
- [58] M. C. Torrijos, B. E. Barragán and R. L. Zerbino. "Placing Conditions, Mesostructural Characteristics and Post-Cracking Response of Fibre Reinforced Self-Compacting Concretes". In: *Construction and Building Materials* 24.6 (2010), pp. 1078–1085 (cit. on p. 16).
- [59] L. Ferrara, N. Ozyurt and M. Di Prisco. "High Mechanical Performance of Fibre Reinforced Cementitious Composites: The Role of "Casting-Flow Induced" Fibre Orientation". In: *Materials and Structures* 44.1 (2011), pp. 109–128 (cit. on p. 16).
- [60] S. T. Kang et al. "The Effect of Fibre Distribution Characteristics on the Flexural Strength of Steel Fibre-Reinforced Ultra High Strength Concrete". In: *Construction and Building Materials* 25.5 (2011), pp. 2450–2457 (cit. on p. 16).
- [61] A. Abrishambaf, J. A. Barros and V. M. Cunha. "Relation between Fibre Distribution and Post-Cracking Behaviour in Steel Fibre Reinforced Self-Compacting Concrete Panels". In: *Cement and Concrete Research* 51 (2013-09), pp. 57–66. issn: 00088846. doi: 10.1016/j.cemconres.2013.04.009 (cit. on p. 16).
- [62] R. Zerbino et al. "On the Orientation of Fibres in Structural Members Fabricated with Self Compacting Fibre Reinforced Concrete". In: *Cement and Concrete Composites* 34.2 (2012), pp. 191–200 (cit. on p. 16).
- [63] M. di Prisco, M. Colombo and D. Dozio. "Fibre-Reinforced Concrete in Fib Model Code 2010: Principles, Models and Test Validation". In: *Structural Concrete* 14.4 (2013), pp. 342–361 (cit. on p. 16).

- [64] P. Stroeven. "Stereology of Concrete Reinforced with Short Steel Fibres". In: *Heron* 31.2 (1986), p. 15 (cit. on p. 16).
- [65] E. S. Lappa. "High Strength Fibre Reinforced Concrete: Static and Fatigue Behaviour in Bending". PhD thesis. TU Delft, Delft University of Technology, 2007 (cit. on p. 16).
- [66] Y. Zandi, M. Husem and S. Pul. "Effect of Distribution and Orientation of Steel Fiber Reinforced Concrete". In: *Proceedings of the 4th WSEAS International Conference on Energy and Development-Environment-Biomedicine*. World Scientific and Engineering Academy and Society (WSEAS). 2011, pp. 260–264 (cit. on p. 16).
- [67] S.-T. Kang and J.-K. Kim. "The Relation between Fiber Orientation and Tensile Behavior in an Ultra High Performance Fiber Reinforced Cementitious Composites (UHPFRCC)". In: *Cement and Concrete Research* 41.10 (2011), pp. 1001–1014 (cit. on p. 16).
- [68] N. Sebaibi, M. Benzerzour and N. E. Abriak. "Influence of the Distribution and Orientation of Fibres in a Reinforced Concrete with Waste Fibres and Powders". In: *Construction and Building Materials* 65 (2014), pp. 254–263 (cit. on p. 16).
- [69] P. Robins, S. Austin and P. Jones. "Spatial Distribution of Steel Fibres in Sprayed and Cast Concrete". In: *Magazine of Concrete Research* 55.3 (2003), pp. 225–235 (cit. on p. 16).
- [70] L. Ferrara and A. Meda. "Relationships between Fibre Distribution, Workability and the Mechanical Properties of SFRC Applied to Precast Roof Elements". In: *Materials and Structures* 39.4 (2006), pp. 411–420 (cit. on p. 16).
- [71] L. Vandewalle, G. Heirman and F. Van Rickstal. "Fibre Orientation in Self-Compacting Fibre Reinforced Concrete". In: *Proc. of the 7th Int. RILEM Symp. on Fibre Reinforced Concrete: Design and Applications (BEFIB2008)*. RILEM Publications SARL. 2008, pp. 719–728 (cit. on p. 16).
- [72] K. J. Trainor, B. W. Foust and E. N. Landis. "Measurement of Energy Dissipation Mechanisms in Fracture of Fiber-Reinforced Ultrahigh-Strength Cement-Based Composites". In: *Journal of engineering mechanics* 139.7 (2012), pp. 771–779 (cit. on p. 16).
- [73] J. Kaufmann et al. "Rebound and Orientation of Fibers in Wet Sprayed Concrete Applications". In: *Construction and Building Materials* 49 (2013), pp. 15–22 (cit. on p. 16).
- [74] P. Pujadas et al. "Caracterización y Diseño Del Homigón Reforzado Con Fibras Plásticas". PhD thesis. Universitat Politècnica de Catalunya, 2013 (cit. on p. 16).
- [75] R. Deeb, B. Karihaloo and S. Kulasegaram. "Reorientation of Short Steel Fibres during the Flow of Self-Compacting Concrete Mix and Determination of the Fibre Orientation Factor". In: *Cement and Concrete Research* 56 (2014), pp. 112–120 (cit. on p. 16).
- [76] T. Ponikiewski et al. "Determination of Steel Fibres Distribution in Self-Compacting Concrete Beams Using X-ray Computed Tomography". In: *Archives of Civil and Mechanical Engineering* 15.2 (2015), pp. 558–568 (cit. on p. 16).

- [77] N. Ozyurt, T. O. Mason and S. P. Shah. "Non-Destructive Monitoring of Fiber Orientation Using AC-IS: An Industrial-Scale Application". In: *Cement and concrete research* 36.9 (2006), pp. 1653–1660 (cit. on p. 16).
- [78] L. Ferrara, M. Faifer and S. Toscani. "A Magnetic Method for Non Destructive Monitoring of Fiber Dispersion and Orientation in Steel Fiber Reinforced Cementitious Composites—Part 1: Method Calibration". In: *Materials and Structures* 45.4 (2012), pp. 575–589 (cit. on p. 16).
- [79] B. Boulekbache et al. "Flowability of Fibre-Reinforced Concrete and Its Effect on the Mechanical Properties of the Material". In: *Construction and Building Materials* 24.9 (2010-09), pp. 1664–1671. issn: 09500618. doi: 10.1016/j.conbuildmat.2010.02.025 (cit. on p. 16).
- [80] J. M. Torrents Dolz et al. "Surveillance of Steel Fibre Reinforced Concrete Slabs Measured with an Open-Ended Coaxial Probe". In: *XIX IMEKO World Congress. Fundamental and Applied Metrology*. 2009, pp. 2282–2284 (cit. on p. 16).
- [81] G. Roqueta et al. "Microwave Time-Domain Reflection Imaging of Steel Fiber Distribution on Reinforced Concrete". In: *IEEE Transactions on Instrumentation and Measurement* 60.12 (2011), pp. 3913–3922 (cit. on p. 16).
- [82] J. Lataste, M. Behloul and D. Breysse. "Characterisation of Fibres Distribution in a Steel Fibre Reinforced Concrete with Electrical Resistivity Measurements". In: *NDT & E International* 41.8 (2008), pp. 638–647 (cit. on p. 16).
- [83] M. Faifer et al. "Nondestructive Testing of Steel-Fiber-Reinforced Concrete Using a Magnetic Approach". In: *IEEE Transactions on instrumentation and measurement* 60.5 (2011), pp. 1709–1717 (cit. on p. 16).
- [84] S. Nunes, M. Pimentel and A. Carvalho. "Non-Destructive Assessment of Fibre Content and Orientation in UHPFRC Layers Based on a Magnetic Method". In: *Cement and Concrete Composites* 72 (2016-09), pp. 66–79. issn: 09589465. doi: 10.1016/j.cemconcomp.2016.05.024 (cit. on p. 16).
- [85] J. M. Torrents et al. "Inductive Method for Assessing the Amount and Orientation of Steel Fibers in Concrete". In: *Materials and structures* 45.10 (2012), pp. 1577–1592 (cit. on p. 16).
- [86] H. Al-Mattarneh. "Electromagnetic Quality Control of Steel Fiber Concrete". In: *Construction and Building Materials* 73 (2014-12), pp. 350–356. issn: 09500618. doi: 10.1016/j.conbuildmat.2014.09.101 (cit. on p. 16).
- [87] A. Naaman and H. Reinhardt. "Proposed Classification of HPFRC Composites Based on Their Tensile Response". In: *Materials and structures* 39.5 (2006), pp. 547–555 (cit. on p. 16).
- [88] A. E. Naaman. "High Performance Fiber Reinforced Cement Composites". In: *High-Performance Construction Materials: Science and Applications*. World Scientific, 2008, pp. 91–153 (cit. on p. 17).

- [89] A. J. Kozak. *Track and Structure Characterization to Improve Freight Train Performance*. Manual. Association of American Railroads. Colorado, USA, 1992 (cit. on p. 17).
- [90] E. M. C. Fortunato. “Renovação de Plataformas Ferroviárias: Estudos Relativos à Capacidade de Carga”. In: (2005) (cit. on p. 19).
- [91] B. J. Van Dyk, M. S. Dersch and J. Edwards. “International Concrete Crosstie and Fastening System Survey—Final Results”. In: *University of Illinois at Urbana-Champaign* (2012) (cit. on p. 19).
- [92] W. Ferdous and A. Manalo. “Failures of Mainline Railway Sleepers and Suggested Remedies – Review of Current Practice”. In: *Engineering Failure Analysis* 44 (2014), pp. 17–35. issn: 13506307. doi: 10.1016/j.engfailana.2014.04.020 (cit. on p. 19).
- [93] J. Taherinezhad et al. “A Review of Behaviour of Prestressed Concrete Sleepers”. In: *Special Issue: Electronic Journal of Structural Engineering* 13.1 (2013) (cit. on p. 19).
- [94] F. Rezaie, M. R. Shiri and S. M. Farnam. “Experimental and Numerical Studies of Longitudinal Crack Control for Pre-Stressed Concrete Sleepers”. In: *Engineering Failure Analysis* 26 (2012), pp. 21–30. issn: 13506307. doi: 10.1016/j.engfailana.2012.07.001 (cit. on p. 19).
- [95] S. Kaewunruen and A. M. Remennikov. “Effect of a Large Asymmetrical Wheel Burden on Flexural Response and Failure of Railway Concrete Sleepers in Track Systems”. In: *Engineering Failure Analysis* 15.8 (2008), pp. 1065–1075 (cit. on p. 19).
- [96] J. C. Zeman et al. “Investigation of Potential Concrete Tie Rail Seat Deterioration Mechanisms: Cavitation Erosion and Hydraulic Pressure Cracking”. In: *Proceedings of the Transportation Research Board 89th Annual Meeting, Washington, DC*. 2010 (cit. on p. 19).
- [97] J. Sadeghi, A. R. T. Kian and A. S. Khabbazi. “Improvement of Mechanical Properties of Railway Track Concrete Sleepers Using Steel Fibres”. In: (2016). doi: 10.1061/(ASCE)MT.1943-5533 (cit. on p. 20).
- [98] C. L. Hwang et al. “The Material and Mechanical Property of Heavy-Duty Prestressed Concrete Sleeper”. In: *Applied Mechanics and Materials*. Vol. 97. Trans Tech Publ. 2011, pp. 408–413 (cit. on p. 20).
- [99] A. Parvez and S. J. Foster. “Fatigue of Steel-Fibre-Reinforced Concrete Prestressed Railway Sleepers”. In: *Engineering Structures* 141 (2017), pp. 241–250. issn: 01410296. doi: 10.1016/j.engstruct.2017.03.025 (cit. on p. 20).
- [100] J.-M. Yang et al. “Benefits of Blast Furnace Slag and Steel Fibers on the Static and Fatigue Performance of Prestressed Concrete Sleepers”. In: *Engineering Structures* 134 (2017), pp. 317–333. issn: 01410296. doi: 10.1016/j.engstruct.2016.12.045 (cit. on pp. 20, 50, 52).
- [101] H. O. Shin, D. Y. Yoo and Y. S. Yoon. “Enhancing the Resistance of Prestressed Concrete Sleepers to Multiple Impacts Using Steel Fibers”. In: *Construction and Building Materials* 166 (2018), pp. 356–372 (cit. on pp. 20, 21).

- [102] EN13230-2. “Railway Applications-Track-Concrete Sleepers and Bearers Part 2: Prestressed Monoblock Sleepers”. In: (2009) (cit. on p. 20).
- [103] B. Lichtberger. “Track Compendium”. In: *Hamburg, Eurailpress Tetzlaff-Hestra GmbH & Co. Publ* (2005) (cit. on p. 22).
- [104] P.-E. Gautier. “Slab Track: Review of Existing Systems and Optimization Potentials Including Very High Speed”. In: *Construction and Building Materials* 92 (2015), pp. 9–15. issn: 09500618. doi: 10.1016/j.conbuildmat.2015.03.102 (cit. on p. 22).
- [105] C. M. N. A. S. Vale. “Influência Da Qualidade Dos Sistemas Ferroviários No Comportamento Dinâmico e No Planeamento Da Manutenção Preventiva de Vias de Alta Velocidade”. PhD thesis. Faculty of Engineering of the University of Porto, 2010, p. 365 (cit. on p. 22).
- [106] M. Fumey et al. *Feasibility Study Ballastless Track*. Tech. rep. UIC Infrastructure Commission Civil Engineering Support Group, Paris, 2002 (cit. on p. 22).
- [107] G. Michas. “Slab Track Systems for High-Speed Railways”. PhD thesis. School of Architecture and the Built Environment, 2012 (cit. on p. 22).
- [108] J. A. Barros and J. A. Figueiras. “Experimental Behaviour of Fibre Concrete Slabs on Soil”. In: *Mechanics of Cohesive-frictional Materials: An International Journal on Experiments, Modelling and Computation of Materials and Structures* 3.3 (1998), pp. 277–290 (cit. on p. 22).
- [109] T. Takahashi et al. “Study on the Applicability of Short Fiber Reinforced Concrete to Precast Concrete Slabs for Slab Track”. In: *Quarterly Report of RTRI* 49.1 (2008), pp. 40–46 (cit. on p. 22).
- [110] P. Casanova, P. Rossi, et al. “Can Steel Fibers Replace Transverse Reinforcements in Reinforced Concrete Beams?” In: *Materials Journal* 94.5 (1997), pp. 341–354 (cit. on p. 23).
- [111] A. Hillerborg, M. Modéer and P.-E. Petersson. “Analysis of Crack Formation and Crack Growth in Concrete by Means of Fracture Mechanics and Finite Elements”. In: *Cement and concrete research* 6.6 (1976), pp. 773–781 (cit. on pp. 23, 24).
- [112] Z. P. Bažant. “Instability, Ductility, and Size Effect in Strain-Softening Concrete”. In: *Journal of the Engineering Mechanics Division* 102.2 (1976-04), pp. 331–344. issn: 0044-7951, 2690-2427. doi: 10.1061/JMCEA3.0002111 (cit. on pp. 23, 24).
- [113] A. Hillerborg. “Analysis of Fracture by Means of the Fictitious Crack Model, Particularly for Fibre Reinforced Concrete”. In: *International journal of cement composites* 2.4 (1980), pp. 177–184 (cit. on p. 23).
- [114] L. Vandewalle et al. “Recommendations of RILEM TC 162-TDF: Test and Design Methods for Steel Fibre Reinforced Concrete. Design of Steel Fibre Reinforced Concrete Using the Sigma-w Method: Principles and Applications”. In: *Materials and Structures* 35 (2002), pp. 262–278 (cit. on pp. 24, 28).

- [115] J. A. O. Barros. “Comportamento Do Betão Reforçado Com Fibras: Análise Experimental e Simulação Numérica”. PhD thesis. Faculty of Engineering of the University of Porto, 1995 (cit. on pp. 24, 30, 31, 38, 39).
- [116] Z. Bažant. “Fracture Mechanics of Concrete Structures: Part I, State-of-Art Report”. In: *ACI Committee 446* (1992) (cit. on p. 25).
- [117] J. P. Ulfkjær, S. Krenk and R. Brincker. “Analytical Model for Fictitious Crack Propagation in Concrete Beams”. In: *Journal of Engineering Mechanics* 121.1 (1995-01), pp. 7–15. issn: 0733-9399, 1943-7889. doi: 10.1061/(ASCE)0733-9399(1995)121:1(7) (cit. on pp. 24, 25, 27, 34).
- [118] C. M. V. Pedersen and H. Stang. “New Production Processes, Materials and Calculation Techniques for Fiber Reinforced Concrete Pipes”. In: (1997) (cit. on pp. 24–27).
- [119] P. Casanova and P. Rossi. “Analysis of Metallic Fibre-Reinforced Concrete Beams Submitted to Bending”. In: *Materials and Structures* 29.6 (1996), p. 354 (cit. on pp. 24–26).
- [120] M. Maalej and V. C. Li. “Flexural Strength of Fiber Cementitious Composites”. In: *Journal of materials in civil engineering* 6.3 (1994), pp. 390–406 (cit. on pp. 24, 27, 28).
- [121] J. F. Olesen. “Fictitious Crack Propagation in Fiber-Reinforced Concrete Beams”. In: *Journal of Engineering Mechanics* 127.3 (2001-03), pp. 272–280. issn: 0733-9399, 1943-7889. doi: 10.1061/(ASCE)0733-9399(2001)127:3(272) (cit. on pp. 24, 28).
- [122] A. Spasojevic. “Structural Implications of Ultra-High Performance Fibre-Reinforced Concrete in Bridge Design”. PhD thesis. Epfl, 2008 (cit. on pp. 24, 28).
- [123] V. C. Li et al. “Micromechanical Models of Mechanical Response of HPFRCC”. In: *High Performance Fiber Reinforced Cementitious Composites, RILEM Proceedings*. Vol. 31. 1996, pp. 43–100 (cit. on p. 27).
- [124] I. Löfgren. “Analysis of Flexural Behaviour of Reinforced FRC Members”. In: *Workshop Proceeding No. 4: Design Rules for Steel Fibre Reinforced Concrete Structures*. 2003 (cit. on p. 28).
- [125] R. de Borst et al. “Discrete vs Smeared Crack Models for Concrete Fracture: Bridging the Gap”. In: *International Journal for Numerical and Analytical Methods in Geomechanics* 28.78 (2004), pp. 583–607. issn: 0363-9061, 1096-9853. doi: 10.1002/nag.374 (cit. on pp. 29–32, 38).
- [126] Z. P. Bažant and B. H. Oh. “Crack Band Theory for Fracture of Concrete”. In: *Matériaux et Constructions* 16.3 (1983-05), pp. 155–177. doi: 10.1007/bf02486267 (cit. on p. 29).
- [127] J. G. Rots et al. “Smeared Crack Approach and Fracture Localization in Concrete”. In: *HERON*, 30 (1), 1985 (1985) (cit. on pp. 29, 30).
- [128] J. Oliver. “A Consistent Characteristic Length for Smeared Cracking Models”. In: *International Journal for Numerical Methods in Engineering* 28.2 (1989-02), pp. 461–474. issn: 0029-5981, 1097-0207. doi: 10.1002/nme.1620280214 (cit. on p. 30).

- [129] R. Borst and P. Nauta. "Non-orthogonal Cracks in a Smearred Finite Element Model". In: *Engineering Computations* 2.1 (1985-01), pp. 35–46. issn: 0264-4401. doi: 10.1108/eb023599 (cit. on pp. 30, 31).
- [130] M. A. Crisfield and J. Wills. "Analysis Of R/C Panels Using Different Concrete Models". In: *Journal of Engineering Mechanics* 115.3 (1989-03), pp. 578–597. issn: 0733-9399, 1943-7889. doi: 10.1061/(ASCE)0733-9399(1989)115:3(578) (cit. on p. 30).
- [131] O. Dahlblom and N. S. Ottosen. "Smearred Crack Analysis Using Generalized Fictitious Crack Model". In: *Journal of Engineering Mechanics* 116.1 (1990-01), pp. 55–76. issn: 0733-9399, 1943-7889. doi: 10.1061/(ASCE)0733-9399(1990)116:1(55) (cit. on p. 30).
- [132] A. K. Gupta and H. Akbar. "Cracking in Reinforced Concrete Analysis". In: *Journal of Structural Engineering* 110.8 (1984-08), pp. 1735–1746. issn: 0733-9445, 1943-541X. doi: 10.1061/(ASCE)0733-9445(1984)110:8(1735) (cit. on p. 30).
- [133] J. G. Rots. "Computational Modeling of Concrete Fracture". PhD thesis. Delft University of Technology, 1988 (cit. on pp. 30, 33).
- [134] J. Barros et al. "Blind Competition on the Numerical Simulation of Steel-Fiber-Reinforced Concrete Beams Failing in Shear". In: *Structural Concrete* 22.2 (2020-12), pp. 939–967. doi: 10.1002/suco.202000345 (cit. on pp. 30, 89, 92, 98, 104, 150).
- [135] M. S. Jepsen et al. "Adaptive Inverse Analysis (AIA) Applied and Verified on Various Fiber Reinforced Concrete Composites". In: *Materials and Structures* 51.3 (2018-06), p. 60. issn: 1359-5997, 1871-6873. doi: 10.1617/s11527-018-1177-0 (cit. on pp. 30, 35).
- [136] S. J. Stephen et al. "Determination of the Tensile Constitutive Relations of Fiber Reinforced Concrete Using Inverse Analysis". In: *Construction and Building Materials* 195 (2019-01), pp. 405–414. issn: 09500618. doi: 10.1016/j.conbuildmat.2018.11.014 (cit. on pp. 30, 35).
- [137] L. M. Matos et al. "A New Inverse Analysis Approach for Predicting the Fracture Mode I Parameters of Fibre Reinforced Concrete". In: *Engineering Fracture Mechanics* 246 (2021), p. 107613. issn: 0013-7944. doi: 10.1016/j.engfracmech.2021.107613 (cit. on pp. 30, 162).
- [138] A. Pruijssers. "Description of the Stiffness Relation for Mixed-Mode Fracture Problems in Concrete Using the Rough-Crack Model of Walraven". In: *Report Stevin Laboratory, Concrete Structures 5-85-2* (1985) (cit. on p. 30).
- [139] V. Cervenka, H. Pukl and R. Eligehausen. "Computer Simulation of Anchoring Technique and Design of Concrete Structures". In: *Proceedings of the 2nd International Conference on Computer Aided Analysis and Design of Concrete Structures*. Zell am See, Austria, 1990, pp. 1–19 (cit. on p. 30).
- [140] J. G. Rots and R. De Borst. "Analysis of Mixed-Mode Fracture in Concrete". In: *Journal of engineering mechanics* 113.11 (1987), pp. 1739–1758 (cit. on pp. 30, 31).

- [141] A. Ventura-Gouveia. “Constitutive Models for the Material Nonlinear Analysis of Concrete Structures Including Time Dependent Effects”. PhD thesis. School of Engineering of the University of Minho, 2011 (cit. on pp. 30, 31, 38, 39, 101).
- [142] R. Cope et al. “Modelling of Reinforced Concrete Behaviour for Finite Element Analysis of Bridge Slabs”. In: *Numerical methods for non-linear problems 1 1* (1980), pp. 457–470 (cit. on p. 31).
- [143] J. M. Sena-Cruz, J. A. O. Barros and A. F. M. Azevedo. *Elasto-Plastic Multi-Fixed Smeared Crack Model for Concrete*. Tech. rep. Universidade do Minho. Departamento de Engenharia Civil (DEC), 2004 (cit. on pp. 31, 38).
- [144] Y. Rashid. “Ultimate Strength Analysis of Prestressed Concrete Pressure Vessels”. In: *Nuclear engineering and design 7.4* (1968), pp. 334–344 (cit. on p. 31).
- [145] S. Valliappan and T. Doolan. “Nonlinear Stress Analysis of Reinforced Concrete”. In: *Journal of the Structural Division 98.4* (1972), pp. 885–898 (cit. on p. 31).
- [146] M. Suidan and W. C. Schnobrich. “Finite Element Analysis of Reinforced Concrete”. In: *Journal of the Structural Division 99.st1* (1973) (cit. on p. 31).
- [147] M. Divakar, A. Fafitis and S. Shah. “Constitutive Model for Shear Transfer in Cracked Concrete”. In: *Journal of Structural Engineering 113.5* (1987), pp. 1046–1062 (cit. on p. 31).
- [148] M. B. Nooru-Mohamed and M. B. Nooru-Mohamed. *Mixed-Mode Fracture of Concrete: An Experimental Approach*. 1992. isbn: 978-90-90-05047-8 (cit. on p. 31).
- [149] P. Grassl, K. Lundgren and K. Gylltoft. “Concrete in Compression: A Plasticity Theory with a Novel Hardening Law”. In: *International Journal of Solids and Structures 39.20* (2002), pp. 5205–5223 (cit. on p. 31).
- [150] V. K. Papanikolaou and A. J. Kappos. “Confinement-Sensitive Plasticity Constitutive Model for Concrete in Triaxial Compression”. In: *International Journal of Solids and Structures 44.21* (2007), pp. 7021–7048 (cit. on p. 31).
- [151] E. N. B. Pereira. “Processes of Cracking in Strain Hardening in Cementitious Composites”. In: (2012) (cit. on p. 31).
- [152] F. Poltronieri et al. “A Simple and Robust Elastoplastic Constitutive Model for Concrete”. In: *Engineering Structures 60* (2014), pp. 81–84 (cit. on p. 31).
- [153] J. Mazars. “A Description of Micro-and Macroscale Damage of Concrete Structures”. In: *Engineering Fracture Mechanics 25.5-6* (1986), pp. 729–737 (cit. on p. 31).
- [154] A. Brencich and L. Gambarotta. “Isotropic Damage Model with Different Tensile–Compressive Response for Brittle Materials”. In: *International Journal of Solids and Structures 38.34-35* (2001), pp. 5865–5892 (cit. on p. 31).



- [155] H. Kuna-Ciskał and J. J. Skrzypek. "CDM Based Modelling of Damage and Fracture Mechanisms in Concrete under Tension and Compression". In: *Engineering Fracture Mechanics* 71.4-6 (2004), pp. 681–698 (cit. on p. 31).
- [156] J. Mazars, F. Hamon and S. Grange. "A New 3D Damage Model for Concrete under Monotonic, Cyclic and Dynamic Loadings". In: *Materials and Structures* 48.11 (2015), pp. 3779–3793 (cit. on p. 31).
- [157] M. Brünig and A. Michalski. "A Stress-State-Dependent Continuum Damage Model for Concrete Based on Irreversible Thermodynamics". In: *International Journal of Plasticity* 90 (2017), pp. 31–43 (cit. on p. 31).
- [158] P. Grassl and M. Jirásek. "Damage-Plastic Model for Concrete Failure". In: *International journal of solids and structures* 43.22-23 (2006), pp. 7166–7196 (cit. on p. 32).
- [159] L. Jason et al. "An Elastic Plastic Damage Formulation for Concrete: Application to Elementary Tests and Comparison with an Isotropic Damage Model". In: *Computer methods in applied mechanics and engineering* 195.52 (2006), pp. 7077–7092 (cit. on p. 32).
- [160] P. Grassl et al. "CDPM2: A Damage-Plasticity Approach to Modelling the Failure of Concrete". In: *International Journal of Solids and Structures* 50.24 (2013), pp. 3805–3816 (cit. on p. 32).
- [161] J. Zhang, J. Li and J. W. Ju. "3D Elastoplastic Damage Model for Concrete Based on Novel Decomposition of Stress". In: *International Journal of Solids and Structures* 94 (2016), pp. 125–137 (cit. on p. 32).
- [162] A. Edalat-Behbahani, J. A. Barros and A. Ventura-Gouveia. "Three Dimensional Plastic-Damage Multidirectional Fixed Smeared Crack Approach for Modelling Concrete Structures". In: *International Journal of Solids and Structures* 115 (2017), pp. 104–125 (cit. on p. 32).
- [163] D. Ngo and A. Scordelis. "Finite Element Analysis of Reinforced Concrete Beams". In: *ACI Journal*. Vol. 64. 1967, pp. 152–163 (cit. on p. 32).
- [164] A. H. Nilson. "Nonlinear Analysis of Reinforced Concrete by the Finite Element Method". In: *Journal Proceedings*. Vol. 65. 1968, pp. 757–766 (cit. on p. 32).
- [165] A. Ingraffea and V. Saouma. "Numerical Modeling of Discrete Crack Propagation in Reinforced and Plain Concrete". In: *Fracture Mechanics of Concrete: Structural Application and Numerical Calculation*. Springer, 1985, pp. 171–225 (cit. on p. 32).
- [166] T. Belytschko and T. Black. "Elastic Crack Growth in Finite Elements with Minimal Remeshing". In: *International Journal for Numerical Methods in Engineering* 45.5 (1999-06), pp. 601–620. issn: 0029-5981, 1097-0207. doi: 10.1002/(SICI)1097-0207(19990620)45:5<601::AID-NME598>3.0.CO;2-S (cit. on p. 32).

- [167] N. Moës, J. Dolbow and T. Belytschko. “A Finite Element Method for Crack Growth without Remeshing”. In: *International journal for numerical methods in engineering* 46.1 (1999), pp. 131–150 (cit. on p. 32).
- [168] L. Sluys and A. Berends. “Discontinuous Failure Analysis for Mode-I and Mode-II Localization Problems”. In: *International Journal of Solids and Structures* 35.31-32 (1998-11), pp. 4257–4274. issn: 00207683. doi: 10.1016/S0020-7683(97)00313-2 (cit. on p. 32).
- [169] J. Gálvez et al. “A Discrete Crack Approach to Normal/Shear Cracking of Concrete”. In: *Cement and Concrete Research* 32.10 (2002-10), pp. 1567–1585. issn: 00088846. doi: 10.1016/S0008-8846(02)00825-6 (cit. on p. 32).
- [170] J. C. Simo and M. S. Rifai. “A Class of Mixed Assumed Strain Methods and the Method of Incompatible Modes”. In: *International Journal for Numerical Methods in Engineering* 29.8 (1990-06), pp. 1595–1638. issn: 0029-5981, 1097-0207. doi: 10.1002/nme.1620290802 (cit. on p. 32).
- [171] J. Alfaiate, G. Wells and L. Sluys. “On the Use of Embedded Discontinuity Elements with Crack Path Continuity for Mode-I and Mixed-Mode Fracture”. In: *Engineering Fracture Mechanics* 69.6 (2002-04), pp. 661–686. issn: 00137944. doi: 10.1016/S0013-7944(01)00108-4 (cit. on p. 32).
- [172] J. Mosler and G. Meschke. “3D Modelling of Strong Discontinuities in Elastoplastic Solids: Fixed and Rotating Localization Formulations”. In: *International Journal for Numerical Methods in Engineering* 57.11 (2003-07), pp. 1553–1576. issn: 0029-5981, 1097-0207. doi: 10.1002/nme.731 (cit. on p. 32).
- [173] J. Oliver and A. Huespe. “Continuum Approach to Material Failure in Strong Discontinuity Settings”. In: *Computer Methods in Applied Mechanics and Engineering* 193.30-32 (2004-07), pp. 3195–3220. issn: 00457825. doi: 10.1016/j.cma.2003.07.013 (cit. on p. 32).
- [174] D. Dias-da-Costa et al. “A Discrete Strong Discontinuity Approach”. In: *Engineering Fracture Mechanics* 76.9 (2009-06), pp. 1176–1201. issn: 00137944. doi: 10.1016/j.engfracmech.2009.01.011 (cit. on p. 32).
- [175] D. Dias-da-Costa et al. “An Embedded Formulation with Conforming Finite Elements to Capture Strong Discontinuities: Conforming Embedded Approach to Capture Discontinuities”. In: *International Journal for Numerical Methods in Engineering* 93.2 (2013-01), pp. 224–244. issn: 00295981. doi: 10.1002/nme.4393 (cit. on p. 32).
- [176] C. Octávio et al. “Modelling the Behaviour of Steel Fibre Reinforced Concrete Using a Discrete Strong Discontinuity Approach”. In: *Engineering Fracture Mechanics* 154 (2016-03), pp. 12–23. doi: 10.1016/j.engfracmech.2016.01.006 (cit. on p. 32).

- [177] J. Garzon et al. "Improvements of Explicit Crack Surface Representation and Update within the Generalized Finite Element Method with Application to Three-Dimensional Crack Coalescence". In: *International Journal for Numerical Methods in Engineering* 97.4 (2014), pp. 231–273 (cit. on p. 33).
- [178] C. Duarte, I. Babuška and J. Oden. "Generalized Finite Element Methods for Three-Dimensional Structural Mechanics Problems". In: *Computers & Structures* 77.2 (2000-06), pp. 215–232. issn: 00457949. doi: 10.1016/S0045-7949(99)00211-4 (cit. on p. 33).
- [179] A. Simone. "Partition of Unity-Based Discontinuous Finite Elements: GFEM, PUFEM, XFEM". In: *Revue Européenne de Génie Civil* 11.7-8 (2007-08), pp. 1045–1068. issn: 1774-7120. doi: 10.1080/17747120.2007.9692976 (cit. on p. 33).
- [180] D. Dias-da-Costa, V. Cervenka and R. Graça-e-Costa. "Model Uncertainty in Discrete and Smeared Crack Prediction in RC Beams under Flexural Loads". In: *Engineering Fracture Mechanics* (2018) (cit. on p. 33).
- [181] RILEM TC 162-TDF. "Test and Design Methods for Steel Fibre Reinforced Concrete Uni-Axial Tension Test for Steel Fibre Reinforced Concrete". In: *Materials and Structures* 34.235 (2001), pp. 3–6. issn: 1359-5997 (cit. on p. 33).
- [182] EN14651. *Test Method for Metallic Fibered Concrete - Measuring the Flexural Tensile Strength (Limit of Proportionality (LOP), Residual)*. Tech. rep. European Committee for Standardization, Brussels, 2004 (cit. on p. 33).
- [183] ASTM C1550-19. *Standard Test Method for Flexural Toughness of Fiber Reinforced Concrete (Using Centrally Loaded Round Panel)*. Tech. rep. ASTM International: West Conshohocken, PA, 2008 (cit. on p. 33).
- [184] P. Nanakorn and H. Horii. "Back Analysis of Tension-Softening Relationship of Concrete." In: *Doboku Gakkai Ronbunshu* 544 (1996), pp. 265–275. issn: 1882-7187, 0289-7806. doi: 10.2208/jscej.1996.544\_265 (cit. on pp. 33, 34).
- [185] Y. Kitsutaka. "Fracture Parameters by Polylinear Tension-Softening Analysis". In: *Journal of Engineering Mechanics* 123.5 (1997-05), pp. 444–450. issn: 0733-9399, 1943-7889. doi: 10.1061/(ASCE)0733-9399(1997)123:5(444) (cit. on p. 33).
- [186] R. Montagnac et al. "Design of SFRC Structural Elements: Post-Cracking Tensile Strength Measurement". In: *Materials and Structures* 45.4 (2012-04), pp. 609–622. issn: 1359-5997, 1871-6873. doi: 10.1617/s11527-011-9784-z (cit. on pp. 34, 94, 95).
- [187] A. Nour et al. "Development of an Inverse Analysis Procedure for the Characterisation of Softening Diagrams for FRC Beams and Panels". In: *Construction and Building Materials* 94 (2015-09), pp. 35–44. issn: 09500618. doi: 10.1016/j.conbuildmat.2015.06.049 (cit. on p. 34).

- [188] J. Vorel and P. Kabele. “Inverse Analysis of Traction-Separation Relationship Based on Sequentially Linear Approach”. In: *Computers and Structures* 212 (2019-02), pp. 125–136. doi: 10.1016/j.compstruc.2018.10.005 (cit. on p. 34).
- [189] L.-M. Czernuschka, R. Wan-Wendner and J. Vorel. “Investigation of Fracture Based on Sequentially Linear Analysis”. In: *Engineering Fracture Mechanics* 202 (2018-10), pp. 75–86. doi: 10.1016/j.engfracmech.2018.08.008 (cit. on p. 34).
- [190] J. L. A. Oliveira e Sousa and R. Gettu. “Determining the Tensile Stress-Crack Opening Curve of Concrete by Inverse Analysis”. In: *Journal of Engineering Mechanics* 132.2 (2006-02), pp. 141–148. issn: 0733-9399, 1943-7889. doi: 10.1061/(ASCE)0733-9399(2006)132:2(141) (cit. on p. 34).
- [191] C. Pedersen. “New Production Process, Materials, and Calculation Techniques for Fiber Reinforced Concrete Pipes”. PhD thesis. Lyngby, Denmark: Technical University of Denmark, 1996 (cit. on p. 34).
- [192] H. Stang and J. F. Olesen. “On the Interpretation of Bending Tests on FRC-Materials”. In: *Fracture Mechanics of Concrete Structures, Vol. I*. Aedificatio Publishers, 1998, pp. 511–520 (cit. on p. 34).
- [193] H. Stang and J. F. Olesen. “A Fracture Mechanical Based Design Approach to FRC”. In: *Proceedings of the Fifth RILEM Symposium on Fibre-Reinforced Concretes (FRC)*. 2000 (cit. on p. 34).
- [194] H. Salehian, J. A. Barros and M. Taheri. “Evaluation of the Influence of Post-Cracking Response of Steel Fibre Reinforced Concrete (SFRC) on Load Carrying Capacity of SFRC Panels”. In: *Construction and Building Materials* 73 (2014-12), pp. 289–304. doi: 10.1016/j.conbuildmat.2014.09.043 (cit. on pp. 34, 84–86, 88).
- [195] J. A. O. Barros and J. A. Figueiras. “Flexural Behavior of SFRC: Testing and Modeling”. In: *Journal of Materials in Civil Engineering* 11.4 (1999-11), pp. 331–339. issn: 0899-1561, 1943-5533. doi: 10.1061/(ASCE)0899-1561(1999)11:4(331) (cit. on pp. 34, 85).
- [196] H. Mazaheripour. “Structural Behavior of Hybrid GFRP and Steel Reinforced FRC Prestressed Beams”. PhD thesis. University of Minho, 2016-03 (cit. on p. 34).
- [197] R. M. Lameiras. “Sandwich Structural Panels Comprising Thin-Walled SFRSCC and GFRP Connectors: From Material Features to Structural Behaviour”. PhD thesis. University of Minho, 2016-07 (cit. on p. 35).
- [198] M. Alberti et al. “Numerical Modelling of the Fracture of Polyolefin Fibre Reinforced Concrete by Using a Cohesive Fracture Approach”. In: *Composites Part B: Engineering* 111 (2017-02), pp. 200–210. issn: 13598368. doi: 10.1016/j.compositesb.2016.11.052 (cit. on p. 35).

- [199] M. S. Jepsen, L. Damkilde and I. Lövgren. “A Fully General and Adaptive Inverse Analysis Method for Cementitious Materials”. In: *Materials and Structures* 49.10 (2016-10), pp. 4335–4348. issn: 1359-5997, 1871-6873. doi: 10.1617/s11527-015-0791-3 (cit. on p. 35).
- [200] Á. F. M. Azevedo et al. “Software no ensino e no projecto de estruturas”. In: *III Portugal-Mozambique Engineering Conference*. 2003-08, pp. 81–92 (cit. on pp. 38, 84, 92, 98).
- [201] J. M. Sena-Cruz. “Strengthening of Concrete Structures with Near-Surface Mounted CFRP Laminate Strips”. PhD thesis. Guimarães: Universidade do Minho, 2005 (cit. on pp. 38–40).
- [202] A. Edalat Behbahani, J. Barros and A. Ventura-Gouveia. “Plastic-Damage Smeared Crack Model to Simulate the Behaviour of Structures Made by Cement Based Materials”. In: *International Journal of Solids and Structures* 73–74 (2015-11), pp. 20–40. issn: 00207683. doi: 10.1016/j.ijsolstr.2015.07.027 (cit. on p. 40).
- [203] fib. *Fib Model Code for Concrete Structures 2010*. Weinheim, Germany: Wiley-VCH Verlag GmbH & Co. KGaA, 2013-10. isbn: 978-3-433-60408-3. doi: 10.1002/9783433604090 (cit. on pp. 41, 86, 102, 150).
- [204] J. Susetyo, P. Gauvreau and F. J. Vecchio. “Effectiveness of Steel Fiber as Minimum Shear Reinforcement”. In: *ACI Structural Journal* 108.4 (2011). issn: 0889-3241. doi: 10.14359/51682990 (cit. on pp. 45, 107, 150, 163–165).
- [205] J. Oliver and S. Idelsohn. *Modelado de La Fisuración En Estructuras de Hormigón*. Centro Internacional de Métodos Numéricos en Ingeniería, 1993 (cit. on pp. 55–57, 61, 62, 77, 172).
- [206] S. Govindjee, G. J. Kay and J. C. Simo. “Anisotropic Modelling and Numerical Simulation of Brittle Damage in Concrete”. In: *International Journal for Numerical Methods in Engineering* 38.21 (1995-11), pp. 3611–3633. issn: 0029-5981, 1097-0207. doi: 10.1002/nme.1620382105 (cit. on pp. 61–63).
- [207] H. Baghi et al. “Shear Behavior of Concrete Beams Reinforced Exclusively with Longitudinal Glass Fiber Reinforced Polymer Bars: Analytical Model”. In: *Structural Concrete* 19.1 (2018-02), pp. 162–173. issn: 1464-4177, 1751-7648. doi: 10.1002/suco.201700175 (cit. on p. 66).
- [208] J. Červenka, V. Červenka and S. Laserna. “On Crack Band Model in Finite Element Analysis of Concrete Fracture in Engineering Practice”. In: *Engineering Fracture Mechanics* 197 (2018-06), pp. 27–47. issn: 00137944. doi: 10.1016/j.engfracmech.2018.04.010 (cit. on p. 70).
- [209] J. Skoček and H. Stang. “Inverse Analysis of the Wedge-Splitting Test”. In: *Engineering Fracture Mechanics* 75.10 (2008-07), pp. 3173–3188. issn: 00137944. doi: 10.1016/j.engfracmech.2007.12.003 (cit. on p. 79).
- [210] C. B. Markwardt. “Non-Linear Least Squares Fitting in IDL with MPFIT”. In: *Astronomical Data Analysis Software and Systems XVII* (2009-02). arXiv: 0902.2850 (cit. on pp. 79, 80).

- [211] J. J. Moré. “The Levenberg-Marquardt Algorithm: Implementation and Theory”. In: *Numerical Analysis*. Ed. by G. A. Watson. Vol. 630. Berlin, Heidelberg: Springer Berlin Heidelberg, 1978, pp. 105–116. doi: 10.1007/BFb0067700 (cit. on pp. 79, 80).
- [212] K. Levenberg. “A Method for the Solution of Certain Non-Linear Problems in Least Squares”. In: *Quarterly of Applied Mathematics* 2.2 (1944), pp. 164–168. doi: 10.1090/qam/10666 (cit. on p. 79).
- [213] D. W. Marquardt. “An Algorithm for Least-Squares Estimation of Nonlinear Parameters”. In: *Journal of the society for Industrial and Applied Mathematics* 11.2 (1963), pp. 431–441. doi: 10.1137/0111030 (cit. on p. 79).
- [214] R. P. Brent. “An Algorithm with Guaranteed Convergence for Finding a Zero of a Function”. In: *The Computer Journal* 14.4 (1971-01), pp. 422–425. issn: 0010-4620. doi: 10.1093/comjnl/14.4.422 (cit. on p. 86).
- [215] Z. Zamanzadeh, L. Lourenço and J. Barros. “Recycled Steel Fibre Reinforced Concrete Failing in Bending and in Shear”. In: *Construction and Building Materials* 85 (2015-06), pp. 195–207. issn: 09500618. doi: 10.1016/j.conbuildmat.2015.03.070 (cit. on pp. 89, 91).
- [216] F. Soltanzadeh. “High Performance Fiber Reinforced Concrete for the Replacement of Shear Stirrups”. PhD thesis. University of Minho, 2016-06 (cit. on pp. 89, 90).
- [217] F. Soltanzadeh, V. M. Cunha and J. A. Barros. “Assessment of Different Methods for Characterization and Simulation of Post-Cracking Behavior of Self-Compacting Steel Fiber Reinforced Concrete”. In: *Construction and Building Materials* 227 (2019-12), p. 116704. issn: 09500618. doi: 10.1016/j.conbuildmat.2019.116704 (cit. on pp. 89, 90).
- [218] C. Frazão, J. Barros and J. Bogas. “Durability of Recycled Steel Fiber Reinforced Concrete in Chloride Environment”. In: *Fibers* 7.12 (2019-12), p. 111. issn: 2079-6439. doi: 10.3390/fib7120111 (cit. on pp. 94–96).
- [219] J. A. O. Barros. “Debilities and Strengths of FEM-Based Constitutive Models for the Material Non-linear Analysis of Steel Fibre Reinforced Concrete Structures”. In: *Proceedings of the 9th International Conference on Fracture Mechanics of Concrete and Concrete Structures*. IA-FraMCoS, 2016-05, p. 12. doi: 10.21012/FC9.023 (cit. on p. 98).
- [220] J. M. Sena-Cruz. “Strengthening of concrete structures with near-surface mounted CFRP laminate strips”. PhD thesis. Guimarães: Universidade do Minho, 2005 (cit. on pp. 101, 140, 144, 165).
- [221] DIN488. *Germany Standard Ribbed Steel Bars*. Tech. rep. 2009 (cit. on p. 102).
- [222] T. Htut and S. Foster. “Unified Model for Mixed Mode Fracture of Steel Fiber Reinforced Concrete”. In: *Proc. of Fracture Mechanics of Concrete and Concrete Structures– High Performance, Fiber Reinforced Concrete, Special Loadings and Structural Applications* (2010), pp. 23–28 (cit. on pp. 106, 107, 109–111, 147, 165, 201).

- [223] G. Tiberti, F. Minelli and G. Plizzari. "Cracking Behavior in Reinforced Concrete Members with Steel Fibers: A Comprehensive Experimental Study". In: *Cement and concrete research* 68 (2015), pp. 24–34 (cit. on p. 106).
- [224] S. Furlan and J. B. de Hanai. "Shear Behaviour of Fiber Reinforced Concrete Beams". In: *Cement and concrete composites* 19.4 (1997), pp. 359–366. issn: 09589465. doi: 10.1016/S0958-9465(97)00031-0 (cit. on pp. 106, 109).
- [225] C. Cucchiara, L. La Mendola and M. Papia. "Effectiveness of Stirrups and Steel Fibres as Shear Reinforcement". In: *Cement and concrete composites* 26.7 (2004-10), pp. 777–786. doi: 10.1016/j.cemconcomp.2003.07.001 (cit. on pp. 106, 109).
- [226] C. Juárez et al. "The Diagonal Tension Behavior of Fiber Reinforced Concrete Beams". In: *Cement and Concrete Composites* 29.5 (2007-05), pp. 402–408. doi: 10.1016/j.cemconcomp.2006.12.009 (cit. on pp. 106, 109).
- [227] H. H. Dinh, G. J. Parra-Montesinos and J. K. Wight. "Shear Behavior of Steel Fiber-Reinforced Concrete Beams without Stirrup Reinforcement". In: *Structural Journal* 107.5 (2010-09), pp. 597–606. issn: 0889-3241. doi: 10.14359/51663913 (cit. on p. 106).
- [228] B. Boulekbache et al. "Influence of Yield Stress and Compressive Strength on Direct Shear Behaviour of Steel Fibre-Reinforced Concrete". In: *Construction and Building Materials* 27.1 (2012-02), pp. 6–14. doi: 10.1016/j.conbuildmat.2011.07.015 (cit. on pp. 106, 109).
- [229] E. Cuenca, J. Echegaray-Oviedo and P. Serna. "Influence of Concrete Matrix and Type of Fiber on the Shear Behavior of Self-Compacting Fiber Reinforced Concrete Beams". In: *Composites Part B: Engineering* 75 (2015), pp. 135–147. doi: 10.1016/j.compositesb.2015.01.037 (cit. on p. 106).
- [230] J. A. O. Barros et al. "Post-Cracking Behaviour of Steel Fibre Reinforced Concrete". In: *Materials and Structures* 38.1 (2005-01), pp. 47–56. issn: 1871-6873. doi: 10.1007/BF02480574 (cit. on pp. 106, 107, 109, 139).
- [231] F. Soltanzadeh, J. Barros and R. Santos. "High Performance Fiber Reinforced Concrete for the Shear Reinforcement: Experimental and Numerical Research". In: *Construction and Building Materials* 77 (2015-02), pp. 94–109. doi: 10.1016/j.conbuildmat.2014.12.003 (cit. on pp. 107, 108, 128, 130, 131, 135, 139, 149).
- [232] T. Pfyl. "Tragverhalten von Stahlfaserbeton". PhD thesis. ETH Zurich / Eidgenössische Technische Hochschule Zurich, 2003. doi: 10.3929/ethz-a-004501155 (cit. on pp. 107, 109, 117, 128, 139, 200).

- [233] J. Y. L. Voo and S. J. Foster. "Variable Engagement Model for the Design of Fibre Reinforced Concrete Structures". In: *Advanced Materials for Construction of Bridges, Buildings, and Other Structures III*. Vol. P05. Advanced Materials for Construction of Bridges, Buildings, and Other Structures III. ECI Symposium Series, 2003, p. 11 (cit. on pp. 107, 110, 116, 147, 165).
- [234] S. J. Foster, G. G. Lee and T. N. S. Htut. "Radiographic Imaging for the Observation of Modes I and II Fracture in Fibre Reinforced Concrete". In: *The 6th International Conference on Fracture Mechanics of Concrete and Concrete Structures*. 2007, p. 8 (cit. on pp. 107, 139).
- [235] J. C. Walraven. "Aggregate Interlock: A Theoretical and Experimental Analysis". PhD thesis. TU Delft, Delft University of Technology, 1980 (cit. on p. 107).
- [236] A. F. Pruijssers. "Aggregate Interlock and Dowel Action under Monotonic and Cyclic Loading". PhD thesis. Delft University Press / Delft University, 1988 (cit. on p. 107).
- [237] Y. D. Hamadi and P. E. Regan. "Behaviour of Normal and Lightweight Aggregate Beams with Shear Cracks". In: *The Structural Engineer* 58.4 (1980), pp. 71–79 (cit. on p. 107).
- [238] F. Daschner and H. Kupfer. "Versuche Zur Schubkraftübertragung in Rissen von Normal-Und Leichtbeton". In: *Bauingenieur* 57.2 (1982) (cit. on pp. 107, 114).
- [239] S. G. Millard and R. P. Johnson. "Shear Transfer across Cracks in Reinforced Concrete Due to Aggregate Interlock and to Dowel Action". In: *Magazine of Concrete Research* 36.126 (1984-03), pp. 9–21. doi: 10.1680/macr.1984.36.126.9 (cit. on p. 107).
- [240] E. G. Sherwood, E. C. Bentz and M. P. Collins. "Effect of Aggregate Size on Beam-Shear Strength of Thick Slabs". In: *ACI Structural Journal* 104.2 (2007), p. 180. doi: 10.14359/18530 (cit. on p. 107).
- [241] A. Khanlou et al. "Shear Performance of Steel Fibre-Reinforced Concrete". In: *Australasian Structural Engineering Conference 2012: The Past, Present and Future of Structural Engineering*. Engineers Australia. 2012, p. 400 (cit. on pp. 107, 108, 128, 129, 135).
- [242] F. Cavignis, M. F. Ruiz and A. Muttoni. "Shear Failures in Reinforced Concrete Members without Transverse Reinforcement: An Analysis of the Critical Shear Crack Development on the Basis of Test Results". In: *Engineering Structures* 103 (2015-11), pp. 157–173. doi: 10.1016/j.engstruct.2015.09.015 (cit. on pp. 107, 139).
- [243] G. G. Lee and S. J. Foster. "Modelling of Shear-Fracture of Fibre-Reinforced Concrete". In: *International FIB Symposium*. CRC Press, 2008, pp. 493–499 (cit. on p. 107).
- [244] J. Navarro-Gregori et al. "Experimental and Numerical Study on the Behaviour of RC and SFRC Push-off Specimens". In: *Proc. of the FIB Symposium Copenhagen, Denmark*. 2015 (cit. on p. 107).



- [245] T. Soetens and S. Matthys. "Shear-Stress Transfer across a Crack in Steel Fibre-Reinforced Concrete". In: *Cement and Concrete Composites* 82 (2017-09), pp. 1–13. issn: 09589465. doi: 10.1016/j.cemconcomp.2017.05.010 (cit. on pp. 107, 108, 128, 132, 135, 136, 139, 149).
- [246] Z. P. Bažant and P. Gambarova. "Rough Cracks in Reinforced Concrete". In: *Journal of the Structural Division* 106.4 (1980), pp. 819–842 (cit. on pp. 107, 108, 114, 139).
- [247] P. G. Gambarova and C. Karakoç. "A New Approach to the Analysis of the Confinement Role in Regularly Cracked Concrete Elements". In: *Structural Engineering of Prestressed Reactor Pressure Vessels and Other Structures* (1983) (cit. on pp. 107, 114, 139, 199).
- [248] B. Li, K. Maekawa and H. Okamura. "Contact Density Model for Cracks in Concrete". In: *IABSE Colloquium, Delft*. 1987, pp. 51–62 (cit. on pp. 107, 108, 114, 115, 139, 199).
- [249] W. Kaufmann et al. "Shear Transfer across Cracks in Steel Fibre Reinforced Concrete". In: *Engineering Structures* 186 (2019-05), pp. 508–524. doi: 10.1016/j.engstruct.2019.02.027 (cit. on pp. 107, 139).
- [250] S.-C. Lee, J.-Y. Cho and F. J. Vecchio. "Simplified Diverse Embedment Model for Steel Fiber-Reinforced Concrete Elements in Tension". In: *Materials Journal* 110.4 (2013), pp. 403–412 (cit. on pp. 107, 109, 112, 113, 139, 202).
- [251] C. A. N. Da Silva et al. "Analytical Bond Model for General Type of Reinforcements of Finite Embedment Length in Cracked Cement Based Materials". In: *International Journal of Solids and Structures* 167 (2019-08), pp. 36–47. doi: 10.1016/j.ijsolstr.2019.02.018 (cit. on p. 109).
- [252] G. G. Lee and S. J. Foster. *Behaviour of Steel Fibre Reinforced Concrete in Shear III: Variable Engagement Model II*. Tech. rep. UNICIV Report; no. R-448. School of Civil and Environmental Engineering, The University of New South Wales, Sydney, 2007 (cit. on p. 110).
- [253] S.-C. Lee, J.-Y. Cho and F. J. Vecchio. "Diverse Embedment Model for Steel Fiber-Reinforced Concrete in Tension: Model Development". In: *Materials Journal* 108.5 (2011), pp. 516–525 (cit. on p. 112).
- [254] C. Sujivorakul, A. M. Waas and A. E. Naaman. "Pullout Response of a Smooth Fiber with an End Anchorage". In: *Journal of Engineering Mechanics* 126.9 (2000-09), pp. 986–993. doi: 10.1061/(asce)0733-9399(2000)126:9(986) (cit. on p. 113).
- [255] T. Paulay and P. J. Loeber. "Shear Transfer by Aggregate Interlock". In: *Special Publication 42* (1974), pp. 1–16 (cit. on p. 114).
- [256] K. Maekawa, H. Okamura and A. Pimanmas. *Non-Linear Mechanics of Reinforced Concrete*. CRC Press, 2003. doi: 10.1201/9781482288087 (cit. on p. 115).

- [257] A. Saltelli and I. M. Sobol'. "About the Use of Rank Transformation in Sensitivity Analysis of Model Output". In: *Reliability Engineering & System Safety* 50.3 (1995-01), pp. 225–239. issn: 09518320. doi: 10.1016/0951-8320(95)00099-2 (cit. on p. 117).
- [258] B. Iooss and P. Lemaître. "A Review on Global Sensitivity Analysis Methods". In: *Uncertainty Management in Simulation-Optimization of Complex Systems*. Ed. by G. Dellino and C. Meloni. Vol. 59. Boston, MA: Springer US, 2015, pp. 101–122. doi: 10.1007/978-1-4899-7547-8\_5 (cit. on p. 117).
- [259] A. Saltelli. "Making Best Use of Model Evaluations to Compute Sensitivity Indices". In: *Computer Physics Communications* 145.2 (2002-05), pp. 280–297. issn: 00104655. doi: 10.1016/S0010-4655(02)00280-1 (cit. on pp. 117, 118).
- [260] A. Saltelli et al. *Global Sensitivity Analysis. The Primer*. First. Wiley, 2007-12. doi: 10.1002/9780470725184 (cit. on pp. 117, 118).
- [261] I. Sobol'. "Global Sensitivity Indices for Nonlinear Mathematical Models and Their Monte Carlo Estimates". In: *Mathematics and Computers in Simulation* 55.1-3 (2001-02), pp. 271–280. issn: 03784754. doi: 10.1016/S0378-4754(00)00270-6 (cit. on pp. 117, 118).
- [262] A. Saltelli et al. "Variance Based Sensitivity Analysis of Model Output. Design and Estimator for the Total Sensitivity Index". In: *Computer Physics Communications* 181.2 (2010-02), pp. 259–270. issn: 00104655. doi: 10.1016/j.cpc.2009.09.018 (cit. on p. 118).
- [263] L. M. Matos et al. "Constitutive Model for Fibre Reinforced Concrete by Coupling the Fibre and Aggregate Interlock Resisting Mechanisms". In: *Cement and Concrete Composites* 111 (2020-08), p. 103618. issn: 09589465. doi: 10.1016/j.cemconcomp.2020.103618 (cit. on p. 139).
- [264] T. Ng, T. Htut and S. Foster. "Fracture of Steel Fibre Reinforced Concrete—The Unified Variable Engagement Model". In: *UNICIV Rep. No. R-460, May 2012* (2012) (cit. on p. 139).
- [265] Y. Wang. "Mechanics of Fiber Reinforced Cementitious Composites". Thesis. Massachusetts Institute of Technology, 1989 (cit. on p. 145).
- [266] P. SorouShian and C. Lee. "Constitutive Modeling of Steel Fiber Reinforced Concrete under Direct Tension and Compression". In: *Fibre Reinforced Cements and Concretes, Recent Developments*. London & New York: Elsevier Applied Science, 1989, pp. 363–375 (cit. on p. 145).
- [267] J.-Y. C. Seong-Cheol Lee, and Frank J. Vecchio. "Diverse Embedment Model for Steel Fiber-Reinforced Concrete in Tension: Model Verification". In: *ACI Materials Journal* 108.5 (2011-01). doi: 10.14359/51683262 (cit. on pp. 147, 165).
- [268] M. Arrea and A. R. Ingraffea. *Mixed-Mode Crack Propagation in Mortar and Concrete*. Tech. rep. Report n° 81-13. Ithaca, N.Y.: Department of Structural Engineering, Cornell University, 1982 (cit. on pp. 168, 169).



# I

## Annex 1 Aggregate interlock and fibre pullout models expressions

The contribution of the matrix is given by Equation (I.1)

$$\sigma_{n,c}^{cr} (w_n^{cr}) = f_{ct} \cdot e^{-cw_n^{cr}} \quad (I.1)$$

The main equations that define the aggregate interlock and fibre pullout models are summarised in Tables 1 to 4.

Table 1: Summary of the main equations of the RCM and CDM aggregate interlock models.

Expressions	Input Parameters
<b>RCM<sup>(1)</sup></b>	
$\sigma_{n,ai}^{cr} (w_n^{cr}, w_t^{cr}) = -0.62 \cdot \frac{w_t^{cr}}{\sqrt[4]{w_n^{cr2} + w_t^{cr2}}} \cdot \tau_{t,ai}^{cr} (w_n^{cr}, w_t^{cr})$	
$\tau_{t,ai}^{cr} (w_n^{cr}, w_t^{cr}) = \tau_0 \cdot \left(1 - \sqrt{\frac{2 \cdot w_n^{cr}}{D_{max}}}\right) \cdot \frac{w_t^{cr}}{w_n^{cr}} \cdot \frac{\frac{2.45}{\tau_0} + 2.44 \cdot \left(1 - \frac{4}{\tau_0}\right) \cdot \left \frac{w_t^{cr}}{w_n^{cr}}\right ^3}{1 + 2.44 \cdot \left(1 - \frac{4}{\tau_0}\right) \cdot \left(\frac{w_t^{cr}}{w_n^{cr}}\right)^4}$	<ul style="list-style-type: none"> <li>○ <math>f_c</math></li> <li>○ <math>D_{max}</math></li> </ul>
$\tau_0 = 0.30 \cdot f_c$	
<b>CDM<sup>(2)</sup></b>	
$\sigma_{n,ai}^{cr} (w_n^{cr}, w_t^{cr}) = k (w_n^{cr}) \cdot \left(\frac{\pi}{2} - \tan^{-1} \frac{w_n^{cr}}{w_t^{cr}} - \frac{w_n^{cr} \cdot w_t^{cr}}{w_n^{cr2} + w_t^{cr2}}\right)$	
$\tau_{t,ai}^{cr} (w_n^{cr}, w_t^{cr}) = k (w_n^{cr}) \cdot \frac{w_t^{cr2}}{w_n^{cr2} + w_t^{cr2}}$	<ul style="list-style-type: none"> <li>○ <math>f_c</math></li> <li>○ <math>D_{max}</math></li> </ul>
$k (w_n^{cr}) = \left(1 - \frac{2 \cdot w_n^{cr}}{D_{max}}\right) \cdot 3.83 \cdot f_c^{1/3}$	

<sup>(1)</sup> Gambarova and Karakoç [247] | Symbols:  $w_n^{cr}$  and  $w_t^{cr}$  are the crack opening and sliding displacements,  $\sigma_{n,ai}^{cr}$  and  $\tau_{t,ai}^{cr}$  are the normal and shear stresses due to the aggregate interlock effect,  $D_{max}$  is the maximum aggregate diameter and  $f_c$  is the concrete compressive strength;

<sup>(2)</sup> Li et al. [248]

Table 2: Summary of the main equations of the Pfyl's model.

Expressions	Input Parameters
$\sigma_{cf}^{cr}(w^{cr}) = \begin{cases} \left( 2 \cdot \sqrt{\frac{w^{cr}}{w_{c0}^{cr}}} - \frac{w^{cr}}{w_{c0}^{cr}} \right) \cdot \sigma_{cf0}^{cr} & , 0 \leq w^{cr} \leq w_{c0}^{cr} \\ \left( 1 - \frac{2w^{cr}}{l_f} \right)^2 \cdot \sigma_{cf0}^{cr} & , w_{c0}^{cr} < w^{cr} \leq \frac{l_f}{2} \end{cases}$	<ul style="list-style-type: none"> <li>○ <math>l_f</math></li> <li>○ <math>d_f</math></li> <li>○ <math>V_f</math></li> <li>○ <math>E_f</math></li> <li>○ <math>f_{ct}</math></li> </ul>
$w^{cr} = \sqrt{(w_n^{cr})^2 + (w_t^{cr})^2}$	
$\sigma_{cf0}^{cr} = \eta_{\theta f} \cdot \frac{V_f \cdot \tau_{bf} \cdot l_f}{d_f}$	
$w_{c0}^{cr} = \frac{\tau_{bf} \cdot l_f^2}{d_f \cdot E_f}$	
$\tau_{bf} = 2 \cdot f_{ct}$	
$\eta_{\theta f} = \frac{1 + \cos \theta_{w^{cr}}}{\pi}$	
$\theta_{w^{cr}} = \left  \tan^{-1} \frac{w_t^{cr}}{w_n^{cr}} \right $	

(1) Pfyl [232] | Symbols:  $w^{cr}$  is the crack displacement,  $\sigma_{cf0}^{cr}$  is the fibre effectiveness,  $w_{c0}^{cr}$  is the crack opening at which the fibre with the longest embedment length starts to pull-out,  $\eta_{\theta f}$  is the fibre orientation factor,  $V_f$  is the fibre content ratio in volume,  $l_f$  and  $d_f$  are the fibre length and diameter, respectively,  $E_f$  is the fibre elasticity modulus and  $\tau_{bf}$  is the fibre bond strength.

Table 3: Summary of the main equations of the UVEM model.

Expressions	Input Parameters
$\sigma_{cf}^{cr} = \eta_{f,uvem} \cdot l_f / d_f \cdot V_f \cdot \tau_{b,avg}$	
$\tau_{b,avg} = \tau_{b,0} + 0.0625 \cdot \gamma_{crit}^3$	
$\tau_{b,0} = 2.2 \cdot f_{ct}$	○ $l_f$
$\gamma_{crit} = \frac{2 \cdot \gamma_{max}}{\pi} \cdot \tan^{-1} \sqrt[3]{\frac{3.5 \cdot w^{cr}}{d_f}}$	○ $d_f$
	○ $V_f$
	○ $\tau_{b,0}$
$\gamma_{max} =  \phi  - \frac{\pi}{2} \quad , \quad \pi/2 \leq \gamma_{max} \leq \pi$	
$\eta_{f,uvem} = \left( \frac{a+b}{\pi} \right) \cdot p \cdot k_{avg}$	
$a = \min [\gamma_{crit}, \pi/2 -  \phi ]$	
$b = \gamma_{crit}$	
$p = \left( 1 - \frac{2 \cdot w^{cr}}{l_f} \right)$	
$k_{avg} = \frac{1}{2} - \frac{w^{cr}}{l_f}$	

<sup>(2)</sup> Htut and Foster [222] | Symbols:  $\eta_{f,uvem}$  is the fibre orientation factor,  $l_f$  and  $d_f$  are the fibre length and diameter, respectively,  $V_f$  is the fibre volume ratio,  $\tau_{b,avg}$  is the average bond stress of the engaged fibres,  $\tau_{b,0}$  is the bond stress when the fibre alignment coincides with the pull-out loading direction,  $\gamma_{crit}$  is a critical fibre bending angle,  $\gamma_{max}$  is the maximum fibre bending angle.

Table 4: Summary of the main equations of the SDEM model.

Expressions	Input Parameters
$\sigma_{cf,st}^{cr}(w^{cr}) = \sigma_{cf,st}^{cr} + \sigma_{cf,eh}^{cr}$	
$\sigma_{cf,st}^{cr}(w^{cr}) = \eta_{\theta f} \cdot V_f \cdot K_{st} \cdot \tau_{st,max} \cdot \frac{l_f}{d_f} \cdot \left(1 - \frac{2 \cdot w^{cr}}{l_f}\right)^2$	<ul style="list-style-type: none"> <li>○ <math>l_f</math></li> <li>○ <math>d_f</math></li> <li>○ <math>V_f</math></li> <li>○ <math>\tau_{st,max}</math></li> </ul>
$K_{st}(w^{cr}) = \begin{cases} \frac{\beta_f}{3} \cdot \frac{w^{cr}}{s_f} & , w^{cr} < s_f \\ 1 - \sqrt{\frac{s_f}{w^{cr}}} + \frac{\beta_f}{3} \cdot \sqrt{\frac{s_f}{w^{cr}}} & , w^{cr} \geq s_f \end{cases}$	<ul style="list-style-type: none"> <li>○ <math>\tau_{eh,max}</math></li> <li>○ <math>s_{st}</math></li> </ul>
$\sigma_{cf,eh}^{cr}(w^{cr}) = \eta_{\theta f} \cdot V_f \cdot K_{eh} \cdot \tau_{eh,max} \cdot \frac{2 \cdot (l_i - 2 \cdot w^{cr})}{d_f}$	<ul style="list-style-type: none"> <li>○ <math>s_{eh}</math></li> </ul>
$K_{eh}(w^{cr}) = \begin{cases} \beta_{eh} \cdot \left[ \frac{2}{3} \cdot \frac{w^{cr}}{s_{eh}} - \frac{1}{5} \cdot \left( \frac{w^{cr}}{s_{eh}} \right) \right] & , w^{cr} < s_{eh} \\ 1 + \left( \frac{7 \cdot \beta_{eh}}{15} - 1 \right) \cdot \sqrt{\frac{s_{eh}}{w^{cr}}} - \frac{2 \cdot (\sqrt{w^{cr}} - \sqrt{s_{eh}})^2}{l_f - l_i} & , s_{eh} \leq w^{cr} \leq \frac{l_f - l_i}{2} \\ \left( \frac{l_i - 2 \cdot w^{cr}}{2 \cdot l_i - l_f} \right)^2 \cdot K_{eh,i} & , \frac{l_f - l_i}{2} < w^{cr} < \frac{l_i}{2} \end{cases}$	
$K_{eh,i} = K_{eh}(w^{cr} = (l_f - l_i)/2)$	
$\eta_{\theta f} = \frac{1 + \cos \theta_{w^{cr}}}{\pi}$	

<sup>(1)</sup> Lee et al. [250] | Symbols:  $\eta_{\theta f}$  is the fibre orientation factor,  $\tau_{st,max}$  is the maximum frictional bond stress,  $\beta_f$  is a coefficient that compensates for the slip of the longer embedded side of the fibre,  $s_f$  is the slip at maximum frictional bond stress,  $\tau_{eh,max}$  is the maximum bond strength provided by the mechanical anchorage,  $l_i$  is the internal fibre length (excluding hooks),  $\beta_{eh}$  is a coefficient that accounts for the fibres that do not attain the maximum anchorage force, and  $s_{eh}$  is the anchorage slip at maximum bond stress.

## II

# Annex 2 Determination of the $\underline{D}^{cr}$ coefficients

In this Annex the expressions that define the  $\underline{D}^{cr}$  matrix are presented. The coefficients that define the  $\underline{D}^{cr}$  matrix are obtained by computing the partial derivatives of normal and shear stress relative to normal and sliding crack displacements of Equations (5.30) and (5.31) resulting in Equations (II.1) to (II.4),

$$\frac{\partial \Delta \sigma_n^{cr}}{\partial \Delta w_n^{cr}} = \frac{\partial \sigma_{c,m}^{cr}}{\partial w_n^{cr}} + \frac{\partial \sigma_{n,ai}^{cr}}{\partial w_n^{cr}} + \frac{\partial \sigma_{cf}^{cr}}{\partial w_n^{cr}} \cdot \cos \theta_w + \sigma_{cf}^{cr} \cdot \frac{\partial \cos \theta_w}{\partial w_n^{cr}} \quad (II.1)$$

$$\frac{\partial \Delta \sigma_n^{cr}}{\partial \Delta w_t^{cr}} = \frac{\partial \sigma_{n,ai}^{cr}}{\partial w_t^{cr}} + \frac{\partial \sigma_{cf}^{cr}}{\partial w_t^{cr}} \cdot \cos \theta_w + \sigma_{cf}^{cr} \cdot \frac{\partial \cos \theta_w}{\partial w_t^{cr}} \quad (II.2)$$

$$\frac{\partial \Delta \tau_t^{cr}}{\partial \Delta w_n^{cr}} = \frac{\partial \tau_{t,ai}^{cr}}{\partial w_n^{cr}} + \frac{\partial \sigma_{cf}^{cr}}{\partial w_n^{cr}} \cdot \sin \theta_w + \sigma_{cf}^{cr} \cdot \frac{\partial \sin \theta_w}{\partial w_n^{cr}} \quad (II.3)$$

$$\frac{\partial \Delta \tau_t^{cr}}{\partial \Delta w_t^{cr}} = \frac{\partial \tau_{t,ai}^{cr}}{\partial w_t^{cr}} + \frac{\partial \sigma_{cf}^{cr}}{\partial w_t^{cr}} \cdot \sin \theta_w + \sigma_{cf}^{cr} \cdot \frac{\partial \sin \theta_w}{\partial w_t^{cr}} \quad (II.4)$$

where,

$$\sin \theta_w = \frac{w_t^{cr}}{w^{cr}} = \frac{w_t^{cr}}{\sqrt{(w_n^{cr})^2 + (w_t^{cr})^2}} \quad (II.5)$$

$$\cos \theta_w = \frac{w_n^{cr}}{w^{cr}} = \frac{w_n^{cr}}{\sqrt{(w_n^{cr})^2 + (w_t^{cr})^2}} \quad (II.6)$$

The partial derivatives of each resisting mechanism that constitute Equations (II.1) to (II.4) are computed using a Python library for symbolic mathematics computation designated SymPy.